Spectroscopy and Dynamics of Colloidal Particles and Systems at Interfaces

A thesis submitted for the degree of Doctor of Philosophy

Lee James Moore

Balliol College, University of Oxford

Trinity Term 2012

Spectroscopy and Dynamics of Colloidal Particles and Systems at Interfaces

A thesis submitted for the degree of Doctor of Philosophy
Lee James Moore, Balliol College, University of Oxford
Trinity Term 2012

Abstract

This thesis presents an investigation of the dynamic properties of wide range of interfacial systems, from colloidal particles in solution, through the realm of aerosols and onto studies of molecular adsorption at an interface. The primary experimental technique utilized is *optical tweezers*. An exploration of the history of the use of radiation pressure to manipulate matter is presented, followed by an introduction to how optical tweezers work. Some of the more advanced methods of tweezing are discussed, with an emphasis on the use of spatial light modulators (SLMs) to realise *dynamic holographic optical tweezers* (DHOTs), an example of which has been constructed within our laboratory using off-the-shelf optical components, and combined with a spectrometer to facilitate high resolution spectroscopic studies of microscopic systems.

The spectroscopic analysis of microparticles is greatly enhanced by optical feedback generated when the wavelength of light utilized is an integer number of wavelengths around the circumference of the microsphere. Enhanced signal occurs at these wavelengths, termed *whispering gallery modes* (WGMs). The absolute position of these resonances depends strongly upon the shape, size and refractive index of the particle, and is predicted by Mie theory. A discussion of the concepts behind Mie theory, as well as how to use an experimental WGM spectrum to deduce the size and composition of a microparticle, is provided. This technique is then put to use in a detailed study on the properties of single aerosols, comprised of sodium chloride solution, and generated using a handheld medical nebulizer. Studies have been carried out on both evaporating and growing droplets trapped with a Gaussian beam; in the latter case, periods of size stability are observed, owing to resonant absorption of radiation at the trapping laser wavelength. The SLM can be used to change the trapping laser to a Laguerre-Gaussian (LG) mode, and an investigation of how this affects the dynamics of the droplet is presented. It is found that the use of LG modes with $\ell \geq 10$ produced Raman spectra with significantly more intense WGMs, and also suppressed droplet evaporation. Through observations made with fluorescent polystyrene microspheres, it is argued that the LG modes are more efficient at coupling into WGMs of the droplets.

Leading on from these experiments on salt water droplets, experiments have been conducted using ionic liquids (ILs). These fluids have many fascinating properties and potential applications. The optical trapping of droplets comprised of aqueous solutions of the ionic liquid ethylammonium nitrate (EAN) and water has been demonstrated for the first time. These droplets are analysed spectroscopically by illuminating them with the output from a broadband LED; WGMs that are observed in the backscattered light are used to determine their size and composition. The response of the droplets to conditions of varying relative

humidity has also been investigated. In order to characterise the relative humidity experienced by both the salt water and IL droplets, the concentration of water vapour within the trapping cells has been measured using diode laser absorption spectroscopy.

The spatially modulated laser beam is then utilized in a different fashion; instead of optically tweezing a sample, a low numerical aperture objective lens is utilized to focus the laser onto the surface of a gold coated microscope slide. When a colloidal sample is placed on this surface, the thermal gradients cause the particles to form two dimensional crystals. The SLM is utilized to form multiple nucleation sites, and the dynamics of the crystals are directly observed in real time using video microscopy. It is found that grain rotation-induced grain coalescence (GRIGC) occurs, with the rotation of both crystals before coalescence. Control over the grain size is achieved by altering the separation of the laser spots, and shows that the time scale for grain boundary annealing in our system is in good agreement with theoretical expressions formulated for nanocrystal growth.

Finally, as a complimentary technique to the microparticle spectroscopy previously discussed, a bulk interface is probed by using evanescent wave broadband cavity enhanced absorption spectroscopy (EW-BBCEAS) specifically to study the adsorption of cytochrome c (cyt c) to a fused silica surface. Visible radiation from a supercontinuum source is coupled into an optical cavity consisting of a pair of broadband high reflectivity mirrors, and a total internal reflection (TIR) event at the prism/water interface. Aqueous solutions of cyt c are placed onto the TIR footprint on the prism surface and the subsequent protein adsorption is probed by the resulting evanescent wave. The time integrated cavity output is directed into a spectrometer, where it is dispersed and analysed. The broadband nature of the source allows observation of a wide spectral range (ca 250 nm in the visible). The system is calibrated by measuring the absorption spectra of dyes of a known absorbance. Absorption spectra of cyt c are obtained for both S and P polarized radiation, allowing information about the orientation of the adsorbed protein to be extracted.

Acknowledgements

First of all, huge thanks to Dr Grant Ritchie, my trusty supervisor and former undergraduate tutor. He's probably the most guilty for my conversion to pseudo-physicist! All jokes aside, Grant is an incredibly inspiring academic, and has been a tremendous source of enthusiasm, ideas and humour throughout my time in the group. He's also incredibly patient, having tolerated me for so long! For all of your help, Grant, I am extremely grateful. Next up is Dr Michael Summers, who taught me everything I know about optical trapping. Mike has been so much fun to work with, and another great source of ideas, even if some of them didn't quite work (I'm thinking of the Irn Bru laser here). Live long and prosper, my friend! I'm also hugely grateful to Dr Daniel Burnham, who got me started with this SLM malarkey back in 2009. Not only has his software been absolutely fantastic, but the week he spent working with me and getting me up to speed was so useful. Thanks, Dan! Dr Roel Dullens is also deserving of my gratitude, as without his wisdom and expertise in colloids, the GRIGC chapter would never have gotten off the ground.

The Ritchie Group, along with their friends in the Hancock Group, has been my scientific home for the last five years, and hence there are lots of accumulated friends who need thanking for all their support and banter. There is no particular order here, but I'll start with the big man himself, Professor Gus Hancock. It's his fault I got funding to stick around for my DPhil, which I'm still eternally grateful for. Gus is an amazing source of conversation, and legitimately the only person allowed to mock my Northern Irish accent. Cheers, Gus! Various post-docs have been and gone throughout the years, so big thanks to Dr Luca Ciaffoni (*notazione matriciale...*), especially for letting me play with your clever diode-laser box! Dr Graham Richmond for beer and hijinks; Dr Michelle Hamilton for cocktails, pizza, and Legally Blonde; Dr Elin McCormack for being so lovely and eating my baked goods (and also for being the happiest person I have ever met); Dr Jean-Pierre van Helden for all round fun and non-eye safe shirts; and Dr Lineke van der Sneppen for all her help with evanescent wave stuff, the widest variety of swear words I've ever heard, and anatomy lessons.

Noteable alumni over my DPhil have all been a huge contribution to the fun I've had over the last few years. Rich Walker, the driving force behind Pub Mondays (and also the coolest guy ever). Beth Cummings, the Balliolite I overlapped the most with, and good gossip partner. Sarah "Princess" Gowrie, I know I'm a filthy wee pig, but the banter was so much fun! Tom Sharples, yet another Balliolite and loyal office partner (I still miss the Monday morning bitching sessions!). Claire Bell (Mrs B), the most efficient organiser ever and matron of End Lab. Sarah Taylor, another of these pesky people who lead me astray with cocktails. And Stuart Baran. Stuart's been one of my closest friends over the last 4 years, and I definitely wouldn't be where I am today without him. He'll probably tell me off

for being soppy though... But still, thanks for all the banter, food and all around awesome friendship; although I suspect my bank balance won't be thanking you for corrupting me into walking the path of the Mac!

Big thanks to the group as it currently stands: Alex Gilchrist (another key component of Pub Mondays, but also my little lunchtime crew), Ann Bergin, Julian Few (who joins me in Princess baiting), Kimberly Whittaker, James Kirkbride and Helen Lowth. Thanks, guys! I've been fortunate enough to work with some extremely talented Part 2 students over the years, who've definitely made lab sessions so much more enjoyable. So big appreciation to William Partridge, Lucy Fishwick, Andrew Rickards and Will Gault.

Which of course brings me to Rich Dear, who started as another of my Part IIs, and stayed on to do his DPhil. I've been extremely lucky to have gotten so close to Rich these last four years; quite aside from being my MATLAB hero, he's such a dude in the lab, genuinely one of the nicest people I know and is ranked among my closest friends. You're an absolute star, Richard Daniel Dear!

And now we come to my partners in crime: Martin Crow and Katy Langley. You two have arguably known me the longest, from being that loud Irish chap from lectures, to doing our Part IIs together and then coming back for another four years of punishment. Katy, although we do make such a good couple (!), I don't think I'm the man for you! But thank you for all the fun, and the dinner parties (that makes it sound so civilised!), and for being you. And Martin, again I'm sounding soppy, but thank you for everything. I hope its apparent how much you mean to me!

Outside the realm of the group, I've got other friends who I need to say thanks to for their support. Helen Chadwick, who had the misfortune of living with me the last two years. Thanks for the coffee, the bitching and the all round fun! Andrew Iliffe, Jo Wilton, Dermot Green and Sarah Little all need a shout out here for keeping me sane over the last four years. And Alex Robson, another amazing friend and PhD buddy, and loyal Four/Five Pound Thursdays partner! Here's to continuous banter, and plenty of wee nights out at the 2Bs! Awkward spooning is optional.

Finally, I want to acknowledge my entire family. Especially Mum and Dad, for being so supportive. This thesis is for you.

List of Publications

N. J. van Leeuwen, L. J. Moore, W. D. Partridge, R. Peverall, G. A. D. Ritchie and M. D. Summers. "Near-field optical trapping with an actively locked cavity". *Journal of Optics*, **13**, 044007 (2011).
http://dx.doi.org/10.1088/2040-8978/13/4/044007

L. J. Moore, R. D. Dear, M. D. Summers, R. P. A. Dullens and G. A. D. Ritchie. "Direct Observation of Grain Rotation-Induced Grain Coalescence in Two-Dimensional Colloidal Crystals". *Nano Letters*, **10**, 4266–4272 (2010).
http://dx.doi.org/10.1021/nl102786k

L. J. Moore, L. van der Sneppen, R. Peverall, G. Hancock and G. A. D. Ritchie. "Adsorption of cytochrome c to silica surfaces studied using evanescent wave broadband cavity-enhanced absorption spectroscopy." *"Physical Chemistry of Interfaces and Nanomaterials IX"*, p. 77580G. SPIE, San Diego, California, USA (2010).
http://dx.doi.org/10.1117/12.860715

Contents

A very crude water colour painting, of a man in a Bishop's hat

Chapter 1

Introduction

"*Through the looking glass, and what Alice found there.*" The title of this work of literature by Lewis Carroll could easily apply to life as viewed through a microscope. A drop of pond water might seem rather boring on a macroscopic level, but through the looking glass that a microscope affords, a rich and fascinating world is observed. Physics, chemistry and biology intersect within this microscopic world, which is the domain of *colloids*.

1.1 The colloidal domain

A colloid may be defined as a dispersion of small particles of one type of material within another [1]. The precise definition of "small" varies from author to author, but it is generally understood that a colloidal particle will have a diameter ranging from 1 nm to on the order of a few µm. The exact terminology depends upon the nature of the materials comprising the particle and its surroundings, with the term "colloid" and "colloidal suspension" usually interpreted as a collection of solid particles dispersed within a liquid medium. A liquid that is dispersed within another liquid is known as an emulsion, while liquid dispersed within a gaseous medium is known as an aerosol. Colloidal particles play a role in a wide variety of disciplines. Industrially, colloids play an important role within food [2], paints [3] and cosmetics [3] to give a few examples.

Aside from their industrial importance, colloids also play an important role in fundamental condensed matter research. Their characteristic length and timescales are on the order of µm and seconds respectively and hence, provided that there exists a refractive index mismatch between the particle and its surrounding medium, and that its dimensions are greater than the diffraction limit, can easily be observed via conventional, brightfield microscopy [4]. When studying colloids in high concentration, image contrast is limited by

multiple scattering events within the sample. This can be minimized by tuning the refractive index of the solvent to match the particle, rendering them effectively transparent to conventional microscopy. Imaging is usually achieved by fluorescently tagging the particles, and utilizing confocal microscopy to build up a three dimensional picture of the sample [5]. Colloidal suspensions display a rich phase behaviour within the hard sphere model such as fluids, crystals and glasses [6]. Furthermore, their interactions can be tuned by physical or chemical means [7], leading to their application as model systems for physical processes such as phase transitions [8, 9], or systems at interfaces [10, 11]. Indeed, Aarts' use of colloids to study a vapour-liquid interface [10] prompted Poon to describe colloids as "big atoms" [12].

1.2 Outline of the thesis

This thesis explores dynamic properties of some interfacial systems, specifically colloidal particles and aerosols, with a strong emphasis on spectroscopic characterisation. The tools utilized in this investigation all exploit the interaction of electromagnetic radiation with matter, whether that be to simply see what is going on (via microscopy), analysing the composition (via spectroscopy) or actually utilizing light induced forces to manipulate matter on the microscopic level. The advent of optical tweezers [13] has been revolutionary for the study of microscopic systems, and forms the primary experimental technique utilized. Chapter 2 will briefly explore the history behind the development of optical tweezers, as well as describing how they work, and outlining some of their applications in various disciplines. It will then go on to describe how to go about building an optical tweezers from off the shelf optical components. Various methods of creating custom optical potentials will be described, with a focus on the use of spatial light modulators (SLMs) to form *dynamic holographic optical tweezers*, before describing how optical tweezers can be coupled with spectroscopic techniques for the interrogation of microscopic samples.

Chapter 3 describes some of the basics of light scattering (Mie theory), with an emphasis on so called "ripple structure" (also known as morphology dependent resonances, MDRs, or whispering gallery modes, WGMs) apparent within a scattering spectrum. This chapter shall also discuss how spherical particles can act as microcavities, with the cavity modes being the MDRs. A description of how these resonances can be used to obtain accurate information about the size and composition of spherical microparticles shall be provided.

Chapter 4 utilizes optical tweezers and the spectroscopic techniques introduced in Chapter 3 to study aqueous aerosol particles, consisting of solutions of sodium chloride. A review of contemporary interest in aerosols will be provided, as well as an introduction to some of the thermodynamics governing their existence. The specific technique used to study the

aerosols is Raman scattering, which due to the existence of WGMs within the sphere, leads to stimulated Raman scattering at wavelengths associated with WGMs. Initially, the chapter shall focus on the trapping and spectroscopy of droplets using conventional Gaussian beams, exploring both droplet evaporation and growth. During droplet growth, periods of size stability become apparent, termed "locking", and the mechanism behind this is explored. The chapter will then go on to explore the differences in the dynamics of the aerosols when switching the trapping laser's beam profile to that of a Laguerre-Gaussian mode.

Chapter 5 extends this work on the trapping of salt water aerosols to a different class of material, ionic liquids. These exotic fluids have many intriguing properties and potential applications, which shall be discussed. The chapter demonstrates the first known optical trapping of droplets containing ionic liquid, and will focus on their trapping and spectroscopic characterisation within different environments of varying relative humidity, with an ultimate aim of trapping droplets of pure ionic liquid. To quantify the various RH environments, diode laser absorption spectroscopy has been utilized to measure the concentration of water vapour within the trapping chambers.

Chapter 6 marks the beginning of a change of gear for the thesis, where the dynamic holographic optical tweezers experiment is modified to study the formation of colloidal crystals using thermal gradients. A low numerical aperture objective is used, so the term "tweezers" is redundant here, however the use of the SLM allows precisely defined laser spots to be projected onto a gold covered microscope slide, which serve as nucleation spots for the colloidal crystals. An indepth study of the interaction of two colloidal crystal domains is presented, with the crystals being observed to show growth properties analogous to nanocrystals.

Finally, Chapter 7 moves away from the realm of optical trapping and colloids, and focuses on the adsorption of cytochrome c (cyt c) to silica surfaces. This is studied using evanescent wave broadband cavity enhanced absorption spectroscopy (EW-BBCEAS) with a supercontinuum (SC) source, to compliment the microparticle spectroscopic studies of the earlier chapters. By increasing the concentration of cyt c upon the prism surface, a Langmuir isotherm for the adsorption is obtained. Furthermore, selective polarisation of the SC allows a method of determining the mean orientation of the molecules upon the surface.

The thesis closes with some general concluding comments in Chapter 8.

Chapter 2

Fundamentals of Optical Tweezers

This chapter shall introduce optical tweezers, starting with a brief outline of their history and working through to how they function. Some of their many scientific applications shall be explored. The optical components that are required to construct a basic tweezers are discussed, before focusing on more advanced trapping techniques. Finally, a description of the holographic optical tweezers that I constructed for our laboratory will be provided, followed by a discussion of how to integrate tweezers with spectroscopy.

2.1 Arthur Ashkin, and the development of optical tweezers

It is prudent to begin this chapter with an overview of the career of Arthur Ashkin, widely credited as the father of the modern optical tweezers. His question, "is it possible to observe significant motion of small particles using the forces of radiation pressure from laser light?" proved to be a significant driving force in the development of the modern optical tweezer.

2.1.1 Radiation pressure and particle manipulation

It is well known from classical electromagnetic theory that there is a momentum flux associated with electromagnetic radiation, termed *radiation pressure*, given by the ratio of the time-averaged value of the Poynting vector, and the speed of light, i.e. $\langle \mathbf{S} \rangle / c$ [14]. As a student in 1944, Ashkin wondered if one could use the radiation pressure associated with microwaves to apply a force to metallic objects [15]. Obtaining an old telephone earpiece, he fired microwave pulses with a repetition rate of 1000 pulses s^{-1} at the metallic vibration receiver plate. A clear signal at a frequency of 1000 kHz was observed on an oscilloscope, which Ashkin interpreted as radiation pressure. However, no further research in this area was carried out until the late 1960s, when Ashkin carried out some "back of the envelope"

calculations on the magnitude of forces that could be exerted by radiation pressure, which I shall now reproduce.

Consider a beam of light, of power P and frequency ν, incident upon a perfectly reflecting mirror. The number of photons striking the surface per unit time will thus be $P/h\nu$. The momentum p associated with a single photon is given by $h\nu/c$, therefore the force imparted to the surface will be:

$$F = \frac{dp}{dt} = \frac{P}{h\nu} \times \frac{2h\nu}{c} = \frac{2P}{c}$$

With a power of 1 W, a force of 6.67×10^{-9} N will be applied, which is rather small in macroscopic terms. However, if we are dealing with microscopic matter, then forces of this magnitude become much more important. Consider now what would happen if a 1 µm sphere, of mass 1×10^{-14} kg, had the entirety of the 1 W laser incident upon it. The maximum force, $F_{\max}$, that could be applied would be if the incident radiation was perfectly reflected, as in the above situation. The resulting acceleration, given by $F_{\max}/m$, is on the order of $10^6\,\mathrm{m\,s^{-2}}$, which is a large acceleration. Even if the true force was only a tenth of $F_{\max}$, the acceleration is still considerable.

This knowledge inspired Ashkin to attempt to manipulate microscopic particles using radiation pressure alone. His initial experiments consisted of suspensions of latex microspheres (of diameter 0.59, 1.31 and 2.68 µm) in water, illuminated with a weakly focused laser beam operating at 514.5 nm [16]. Both water and latex are weakly absorbing at this wavelength, minimizing any thermal forces that would impede the observation of radiation pressure. While particles were observed to move in the direction of laser propagation and obtain velocities given by Stokes' Law [16], a much more interesting observation was made. Particles were always observed to move along the centre of the beam; if a particle was illuminated by the edge of the laser beam, then it was drawn into the middle. If the laser was blocked when a particle reached the walls of the cell, then its motion reverted to Brownian; when unblocked then the particle returned to the centre of the beam. This remarkable observation suggested a transverse component of the forces related to radiation pressure, that pulled a particle towards the region of highest intensity. This force component has come to be known as the gradient force, and shall be considered in more detail in Section 2.2. The nature of this optical guiding technique suggested that a particle could be stably trapped by arranging two lasers, under identical power and focusing conditions, such that the beams are counterpropagating, i.e. no net radiation pressure acts on the particle in the direction of either laser when it is in mechanical equilibrium. An alternative approach to using counterpropagating beams to achieve equilibrium is to utilize other forces, for instance Ashkin and Dziedzic showed in 1971 that a particle can be trapped by balancing radiation pressure with gravity (the so called optical levitation trap) [17].

2.1.2 Single beam optical trapping

Ashkin's work on trapping of particles with radiation pressure continued through the 1970s and 1980s. For example, it was demonstrated that hollow glass microspheres could be levitated with a TEM_{01}^{*} ("doughnut") laser mode [18]. A modification to the experiment allowed the measurement of forces [19], which lead to the experimental observation of morphology dependent resonances from single particles [20, 21] (as will be discussed further in Section 3.1.3). The work on manipulating microscopic particles lead onto some fruitful research on the trapping and cooling of atoms [15, 22]. In 1986, Ashkin and coworkers reported the development of a single beam gradient force optical trap for dielectric particles [13] which has since become commonly known as *optical tweezers*. Originally proposed as an atom trap [23], it was shown that optical tweezers, which utilize a tightly focused laser beam *via* a microscope objective, could be used to trap particles of a wide size range.

Since then, optical tweezers have become a powerful tool in research laboratories across the world. The fact that tweezers themselves utilize a microscope objective means they can be readily integrated into any experiments that investigate microscopic matter. Ashkin himself was quick to demonstrate the application of tweezers to the trapping of biological cells, such as viruses and bacteria [24]. This paved the way for many biological applications of optical tweezers. The majority of biophotonic measurements utilize the fact that the optical forces (discussed further in Section 2.2) acting on a particle in a single beam trap are such that for small ($<$200 nm) displacements of the trapped particle from its equilibrium position, the restoring force is linear with displacement. This means that the optically trapped particle can be treated as one end of a Hookean spring, and so can be utilized as a sensitive force probe (discussed further in Section 2.2.4). Here, I shall aim to give a flavour of some of the fascinating biological experiments in which tweezers have played a role.

An early experiment that utilized optical forces in a biological context measured the compliance of bacterial flagella [25]. Optical trapping techniques can be used to study single biomolecules, typically by use of a colloidal microparticle to act as a handle for the molecule in question by utilizing surface chemistry techniques to adhere the molecule to the particle [26]. This is very nicely demonstrated in the work of Bockelmann *et al.* where one strand of a DNA molecule was tethered to an optically trapped microsphere, with the other end tethered to the coverslip surface [27]. Position sensitive detection meant that the forces acting upon the DNA strand as the glass slide was moved (relative to the fixed trapping position) could be accurately characterised, ultimately leading to the mechanical unzipping of the DNA molecule. The experiment used had sufficient force resolution (sub pN) to measure extremely high base pair sensitivity, and offered a considerable improvement over their previous measurements on the unzipping of DNA [28]. Optical tweezers have allowed direct measurement of the forces and displacements associated with single myosin molecules

interacting with a single actin filament [29]. The study of the motion of silica nanoparticles that were treated with kinesin along microtubules has also been aided by the use of tweezers [30]. The interaction of dynein (the protein that powers flagellar motion) with individual microtubles was measured directly using tweezers [31]. An excellent introduction to some of the biological applications of optical tweezers in the first 16 years of their history is given by Molloy and Padgett [32]; while a more recent primer on the applications of optical tweezers to single molecule biology is given by Perkins [33].

Of course, it is not just biophysics that has benefited from the development of optical tweezers. As they offer a method of precise particle manipulation, they have found applications in the realm of nanotechnology. Nanofabrication using holographic optical tweezers (Section 2.5) was initially demonstrated by Korda *et al.* [34], and has been utilized in the formation of template structures for photonic band gap materials [35, 36]. The use of tweezers offers an advantage over self assembly of the microparticles, as they offer greater flexibility over the positioning of the microparticles, demonstrated by Benito *et al.* by introducing line defects to the crystals, as well as building 3D cubic structures. Holographic optical tweezers have also been used by Agarwal *et al.* to manipulate and assemble semiconductor nanowires [37].

The ability to apply pico-Newton forces to objects affords a mechanical application for optical tweezers. As an example, Friese *et al.* utilized the torque generated by birefringent particles trapped by circularly polarised laser radiation to drive a second optically trapped "micromachine" element [38]. Carberry *et al.* have developed a series of nanotools, which can be optically trapped and utilized as an alternative method of force measurements (similar to scanning probe microscopy) [39]. Optically trapped microrods [40] offer advantages for force probing measurements, as the trapping laser can be placed at an arbitrary position along the microrod (minimizing optical damage to the sample being probed), and the reduction in symmetry could offer orientational information. Sensitive force measurements mean that optical tweezers are ideal tools for (active) micro-rheology [41], which offers several advantages over bulk rheology such as small sample volumes ($\sim$10 µL), examining the high frequency response of the viscoelastic properties of the sample, and assessing the heterogeneity of the sample [42]. Optical tweezers played an important role in a beautiful experiment by Hertlein *et al.* to directly measure critical Casimir forces between a colloidal silica microparticle, and a planar silica interface [43]. While the measurement itself was performed using total internal reflection microscopy, optical tweezers were utilized to suppress particle diffusion.

Microfluidic chips are readily integrated with optical tweezers [44–46], and indeed other "lab on a chip" type experiments [47]. Optical tweezers also find applications in colloid and interface science [48]. For example, they have been utilized to anneal grain boundaries

within colloidal crystals [49], and to directly measure interactions between colloidal particles [50], such as electrostatic interactions [51, 52] and hydrodynamic coupling [53, 54].

Tweezers are finding increasing applications in chemistry laboratories. For instance, liposomes, which are artificially generated vesicles comprised of a lipid bilayer, can be trapped and manipulated optically. Kulin *et al.* manipulated a pair of lisosomes together, then utilized a pulse of UV laser radiation to break the membrane joining the liposomes and allow the liposomes to fuse into one [55], thus mixing their contents and allowing chemical reactions to occur. Reiner *et al.* were able to generate aqueous droplets which could be trapped with optical tweezers, by generating an emulsion in a low refractive index fluorocarbon [56]. An advantage of this technique over liposomes is that the water droplets, when brought into contact, will spontaneously fuse to form a single droplet. Liquid droplets in air (aerosols) can also be stably trapped and manipulated; this will be given further attention in Chapters 4 and 5.

2.1.3 Non tweezer based particle manipulation

Before proceeding to discuss the physics behind optical tweezers, it is prudent to take a moment to reflect upon the various, non-tweezer based methods of particle micromanipulation, such as the use of evanescent waves, fibre traps and optoelectronic tweezers. An additional method of particle manipulation, which utilizes thermal gradients to transport matter (known as *thermophoresis*) will be discussed in Chapter 6.

2.1.3.1 Evanescent waves

When light that is initially propagating within a high index medium undergoes total internal reflection at an interface between a medium of high and low refractive index, a component of the electric field exists in the optically less dense medium, known as an *evanescent wave* [14]. The evanescent wave propagates in the same direction as the original beam, and has an intensity which decays exponentially away from the surface of the interface (the depth at which the intensity of the wave decays to $1/e$ of its initial value, known as the penetration depth, is on the order of λ). If the surface is perfectly smooth then no energy is transmitted into the second medium; however imperfections (such as scratches, or dust on the surface) will lead to scattering of the evanescent wave and loss of energy. The scattering sites effectively convert the evanescent wave into a traveling wave (alternatively, photons can be thought of as tunnelling across the interface).

In 1992, Kawata and Sugiura showed that an evanescent wave could be used to manipulate micron sized particles (with sizes ranging from 1 µm to 27 µm) across the surface of a

prism/water interface. Scattering of the evanescent wave by the particles is responsible for the transfer of momentum from the evanescent wave to the particles, which obtained velocities of up to $20\,\mu m\,s^{-1}$ [57]. Surprisingly, it took over ten years between this experiment, and the emergence of experiments that utilized counter-propagating evanescent waves, such that no net radiation pressure acts upon the sphere. Garcés-Chávez *et al.* imaged a Ronchi ruling onto a prism surface with counterpropagating evanescent waves, and observed particle sorting into the bright fringes [58]. Mellor and Bain also utilized counterpropagating evanescent waves [59, 60], and observed a rich variety of structures formed by sub-micron sized particles, while for larger particles observed that interference fringes in the evanescent field were important. Concurrent experiments carried out by Šiler *et al.* also showed the sorting of microscopic matter in counterpropagating evanescent waves; they also conducted a more theoretical study on optical forces in the evanescent field [61]. The formation of structures in counterpropagating evanescent waves is reminiscent of optical binding [62], first reported by Burns *et al.* in 1989 [63]. Here, significant optical forces are induced *between* microparticles in intense light fields.

There has been interest in utilizing enhanced evanescent waves for studies of optical binding, as the optical forces due to an evanescent wave are considerably weaker than in conventional optical manipulation techniques. Reece *et al.* utilized a waveguide to enhance the evanescent field, giving a ten-fold enhancement in the evanescent field strength, and large scale arrays of ordered colloidal particles [64]. Research in our group has demonstrated the enhancement of the evanescent wave using an actively locked optical cavity [65]. An interesting application of this technique is the ability to lock to higher order transverse modes of the cavity, giving a different electric field pattern on the prism surface. More recently, our group has utilized an optical tweezers to direct the assembly of such optically bound matter, by loading one particle into the evanescent field at a time and observing the dynamics of the system using single particle tracking [66]; in particular, optical waveguiding effects are found to lead to optically bound structures which are reminiscent of Newton's cradle type motion.

2.1.3.2 Fibre traps

An alternative method of optical trapping, which bears many similarities with Ashkin's counterpropagating beam trap, makes use of optical fibres, first demonstrated by Constable *et al.* [67]. Here, radiation from a pair of infrared diode lasers is coupled into separate single mode optical fibres (which themselves act as spatial filters for the laser light) that can be positioned to act as a counterpropagating trap on the microscopic scale, owing to the highly divergent nature of light emitted from the fibre. This method of particle manipulation offers several advantages over conventional optical trapping. Firstly, the relative position of the

fibres can be altered, to introduce additional forces and torques into the system. Secondly, much greater trapping volumes for sub-micron particles were reported. Finally, the fact that the trap is decoupled from the imaging microscope offers greater flexibility for particle manipulation. An interesting application of fibre traps is the *optical stretcher* of Guck *et al.* [68]. This work exploits the fact that, although the net force on a trapped particle is zero, the surface forces are additive and lead to stretching of the particle along the beam axis. This can therefore be used to measure viscoelastic properties of trapped materials, in particular biological cells. As cancerous tissue have an altered cytoskeleton (relative to a healthy cell), their physical response to the optical forces can be used a method of diagnosis [69].

2.1.3.3 Optoelectronic tweezers

The final non-tweezer based method of particle manipulation that shall be discussed are *optoelectronic tweezers*, based upon dielectrophoresis [70, 71]. The system is based around a pair of electrodes, one of which is transparent (ITO glass), and the other of which is photoconductive. The sample is sandwiched between these two electrode layers, and an a.c. electrical bias is maintained between them. Incoherent light from an LED is then focused onto the photoconductive layer using a low magnification microscope objective. This light is patterned using a digital projector, or indeed any other form of spatial light modulator, and forms what the authors term "virtual electrodes" on the photoconductive layer. The resulting non-uniform field gives rise to dielectrophoresis. Due to the sensitivity of the photoconductive layer, the intensity of light required to achieve the photophoretic effect is on order of 100,000 times smaller than the intensities required for conventional optical tweezers. As extremely well tailored and highly reconfigurable patterns can be formed on the photoconductive substrate, this technique naturally lends itself to manipulation of large numbers of particles, as well as particle sorting and the manipulation of live cells [72]. Recently, the technique has been utilized in assessing the motility of human sperm cells [73].

2.2 Basic physics behind an optical trap

Having explored the history of single particle manipulation with optical tweezers, discussed some of their applications and briefly touched upon some of the other non-contact methods available for particle manipulation, this section shall now focus on how optical tweezers themselves actually work.

Following convention, the optical forces acting on a dielectric microsphere in a laser beam is resolved into two components: the *scattering force* (which acts in the direction of beam propagation) and the *gradient force* (which acts along an intensity gradient in the electric field of the trapping radiation):

$$\mathbf{F} = \mathbf{F}_{\text{scat}} + \mathbf{F}_{\text{grad}} \tag{2.1}$$

These optical forces are readily calculable in the limits where the particle (of radius a) is much larger than the wavelength of the trapping laser (so that geometrical ray tracing can be used to determine the forces), and when the particle is much smaller than the trapping wavelength (so that the particle can be treated as a point dipole). A brief discussion of these limiting forces shall now be provided, which shall also touch upon how the optical forces are calculated when the particle's size is similar to the wavelength of the trapping radiation.

2.2.1 Geometric optics limit, $a \gg \lambda$

The geometric optics limit is an ideal place to discuss the origin of the optical forces, as it can be readily visualised. Furthermore, the forces can be exactly calculated by summing the contributions from all rays incident upon the sphere [26, 74]. Consider the following situation: radiation of a vacuum wavelength λ in a medium of refractive index n_m is incident upon a sphere of refractive index n_s, where $n_s > n_m$. The sphere will act as a weak lens; rays incident upon it will undergo refraction and hence experience a change in momentum due to the change in their direction. Conservation of momentum requires a corresponding transfer of momentum to the sphere, causing an optical force to be exerted. In the case of a homogeneous electric field, a sphere will equally scatter light in all directions. Hence, all horizontal components of the momentum change will cancel, leaving the resultant force acting in the direction of beam propagation, the scattering force, and is analogous with radiation pressure.

If the field is spatially inhomogeneous, e.g. there is a gradient in the electric field across the sphere, then the situation will be somewhat different. This is sketched in Figure 2.1. In this example, the intensity of the light increases from left to right. Upon undergoing refraction, the momentum change due to ray B (for example) will be greater than that of ray A, hence the momentum change (and therefore force) imparted to the sphere for ray B will be greater than ray A. The horizontal components of the momentum change now no longer cancel, and so there will be a net force along the intensity gradient (towards the region of greatest intensity).

The gradient force explains why, in Ashkin's initial optical guiding experiments, the particles always migrated to the centre of the beam. Idealised laser beams have a Gaussian

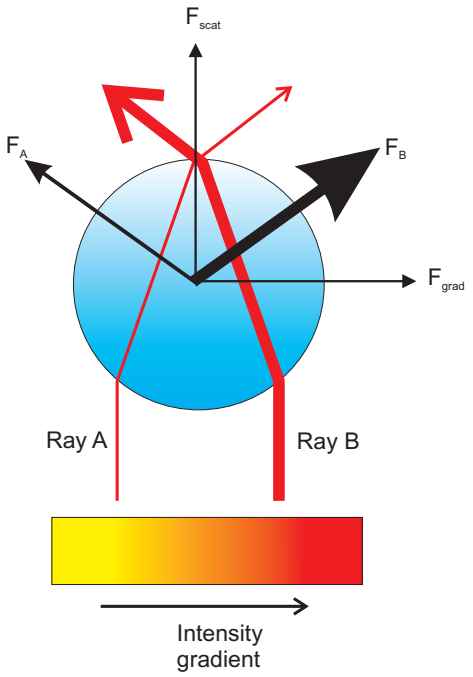

Figure 2.1: Origin of the scattering and gradient forces in the geometric optics limit. Owing to the intensity gradient, ray B is more intense than ray A. Upon refraction, the momentum change for ray B is greater than A, hence the force associated with ray B is greater than ray A. Conservation of momentum results in momentum being imparted to the sphere in the opposite direction to the light's momentum change.

intensity profile, so the most intense region is in the centre. In most circumstances, the scattering force far outweighs the gradient force. However, if the electric field gradient is particularly steep, for instance, in a tightly focused beam, then the influence of the gradient force becomes much more significant, to the extent where the gradient force can be sufficient to overcome the scattering force, holding a particle near the focus. Tightly focused beams are achieved by focusing the beam down with a microscope objective of high numerical aperture (Section 2.3.2), i.e. optical tweezers. An example of a stable trap is sketched in Figure 2.2. Owing to the equilibrium between scattering and gradient forces, the particle sits slightly downstream of the laser focus. Any displacement of the particle from its equilibrium position will result in a large force mismatch, pulling the particle back towards the centre of the beam.

2.2.2 Rayleigh limit, $a \ll \lambda$

When the radius of the particle is much smaller than the trapping wavelength, i.e. the conditions for Rayleigh scattering are satisfied, it may be treated a point dipole and the optical forces directly calculated. In this instance, the two components of the optical force are readily separable. The scattering force arises from the absorption and re-radiation of light by the sphere. It may be calculated by the relation $F_{\text{scat}} = P_{\text{scat}}/c$, where P_{scat} is the

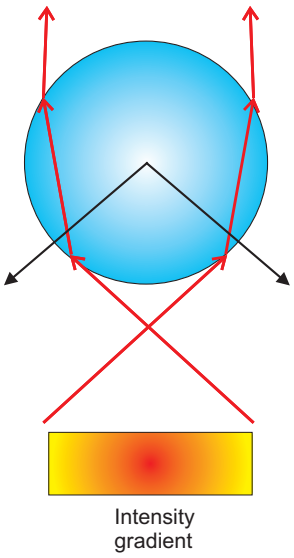

Figure 2.2: A particle in a stable optical trap. Any displacement of the particle from equilibrium results in a strong force imbalance, which acts to pull the particle back to the centre of the beam. The particle sits slightly "downstream" of the focus due to the balancing of the scattering and gradient forces.

scattered power emitted by the dipole, and c is the speed of light. This may be expressed as: [13, 75]:

$$\mathbf{F}_{\text{scat}} = \frac{I_0 \sigma n_m}{c} \tag{2.2a}$$

$$\sigma = \frac{128\pi^5 a^6}{3\lambda^4}\left(\frac{m^2-1}{m^2+2}\right)^2 \tag{2.2b}$$

where I_0 is the intensity of the incident radiation of wavelength λ, σ is the scattering cross section, n_m is the refractive index of the surrounding medium, n_s is the refractive index of the particle, and $m = n_s/n_m$ (termed the refractive index contrast).

The gradient force arises from the interaction of the induced dipole with the inhomogeneous electric field. An electric field induces dipole moments within the sphere; for a field of amplitude $\mathbf{E}$ this dipole is $\mathbf{p} = \alpha\mathbf{E}$, where α is the polarisability of the sphere. The force on a dipole in an inhomogeneous electromagnetic field is $\mathbf{F} = (\mathbf{p}\cdot\nabla)\mathbf{E} + \frac{\partial \mathbf{p}}{\partial t}\times\mathbf{B}$, the gradient force may therefore be written as [13]:

$$\mathbf{F}_{\text{grad}} = \frac{n_m \alpha}{2}\nabla E^2 \tag{2.3a}$$

$$\alpha = n_m^2 a^3\left(\frac{m^2-1}{m^2+2}\right) \tag{2.3b}$$

where α is the polarisability of the sphere. It is clear from Equation 2.3 that if the refractive index of the sphere is greater than that of the surrounding medium, then the gradient force

acts towards the region of highest intensity; otherwise the region of greatest intensity will repel the particle.

2.2.3 Mie, $a \sim \lambda$

Unfortunately, most particles that are used in tweezers experiments fall between these two limits. The optical forces in this regime become difficult to calculate, requiring use of Mie theory to determine the scattering of the laser radiation by the particle. As tweezers utilize highly focused Gaussian beams, classical Mie theory (which is based upon plane wave scattering, and is discussed further in Chapter 3) is insufficient. Generalized Lorenz Mie theory (GLMT) [76] can be used to account for the Gaussian nature of the trapping laser, and has formed the basis of many theoretical descriptions of optical trapping [77, 78]. It is also important to consider that, owing to the refractive index mismatches inherent with oil immersion objectives, the trapping laser will undergo significant aberrations. This will have an influence on the magnitude of the trapping forces. This can be accounted for by utilizing Mie-Debye spherical aberration theory (MDSA) to model the trapping system [79, 80].

2.2.4 Mechanics of an optically trapped particle

As discussed above, a particle confined by optical tweezers experiences a harmonic potential, thus it can be regarded as one end of a Hookean spring (i.e. a damped harmonic oscillator). The implication of this is that optical tweezers may be used as extremely sensitive force probes [81]. To achieve this, it is necessary to utilize a calibrated optical trap, i.e. the force constant, κ (also known as the trap stiffness) for the trap from Hooke's law ($F = -\kappa x$) must be determined. Force measurements are not part of the remit of this thesis, and hence shall only briefly be discussed here.

The one dimensional motion of an optically trapped particle (of radius a and mass m) in a harmonic potential, taking into account its Brownian motion, may be described by the following Langevin equation [82, 83]:

$$\ddot{x}(t) + \Gamma_0 \dot{x}(t) + \Omega_0^2 x(t) = \xi(t) \tag{2.4}$$

where $\Omega_0^2 = \kappa/m$ is the natural frequency of the oscillator, $\Gamma_0 = \gamma_0/m = 6\pi\eta a/m$ describes the damping forces on the system, given by Stokes' Law (with η the dynamic viscosity of the medium). An additional correction factor is required for the proximity to the coverslip. The value $\xi(t)$ represents the stochastic forces present within the system, i.e. Brownian motion.

Taking the Fourier transform of Equation 2.4 yields a *power spectrum* of the time-dependent position of the optically trapped particle:

$$S_x(\omega) = \frac{k_B T}{\pi \kappa} \frac{\Omega_0^2 \Gamma_0}{(\omega^2 - \Omega_0^2)^2 + \Gamma_0^2 \omega^2} \tag{2.5}$$

which can be rearranged as:

$$S_x(\omega) = \frac{k_B T}{\pi \kappa^2} \frac{\omega_c^2 \gamma_0}{\left(\frac{m^2 \omega^4}{\gamma_0^2 - 2\kappa m} \right) + \omega_c^2 + \omega^2} \tag{2.6}$$

where the *corner frequency* is:

$$\omega_c = \sqrt{\frac{\kappa^2}{\gamma_0^2 - 2\kappa m}} \tag{2.7}$$

As the drag (γ_0/m) is given by Stokes' law, measurement of the corner frequency from an experimental power spectrum can be used to retrieve the trap stiffness for a particle, thus allowing the use of the trapped particle as a sensitive force probe.

There are several methods of recording power spectra of trapped particles. Fast cameras (with a frame rates of kHz) can be used to image the particle at a sufficient frequency [84], however a limitation is the amount of computer memory required to store the experimental data. This method also only interrogates two-dimensional displacement of the particle. An alternative method of position detection for particles involves use of a *quadrant photodiode* (QPD) [85]. This consists of four photodiodes, each of which has a unique voltage output. Scattered light from a particle (usually from a source independent from the trapping laser) is imaged onto the QPD array, and Brownian motion of the particle within the trap will result in an inhomogeneous illumination on each of the quadrants. Information about the x, y and z displacements of the particle can be obtained by combining the voltage signals in different fashions.

The form of power spectrum observed for a particle depends upon its surrounding medium. For example, colloidal samples in aqueous solution constitute overdamped systems, and their power spectra show a tail with a gradient of ω^{-2}. If a colloidal sample is suspended in a non-Newtonian fluid, such as an aqueous solution of hyaluronic acid, the gradient of the tail shows a significant deviation from ω^{-2} [86]. Aerosol particles, which are trapped in air, tend to be underdamped oscillators, and in the underdamped regime will show an ω^{-4} dependence in the gradient of the tail in their power spectra [83]. A review of micro-rheological tecnhiques utilizing optical tweezers is provided by Yao *et al.* [41].

2.3 How to build optical tweezers

Having established the basic physics behind how optical tweezers work, I shall now discuss how one actually builds them. For further details, the reader is invited to view the informative protocol produced by Lee *et al.* outlining how to modify a commercial fluorescence microscope to accommodate optical tweezers [87]. This document is also a useful guide for those seeking to build optical tweezers from off-the-shelf optical components, such as the tweezers experiments used in this thesis. Finally, I further note that interest in optical tweezers has developed sufficiently for complete off-the-shelf tweezers systems to have recently become commercially available, for instance a complete optical tweezers (with an optional force measurement module) is available from Thorlabs.

In essence, an optical tweezers system is simply a laser beam, that is directed into a microscope objective using various beam steering optics, shown schematically in Figure 2.3. Each of the components used in a basic optical tweezers shall be described, with a discussion of why these particular components are chosen.

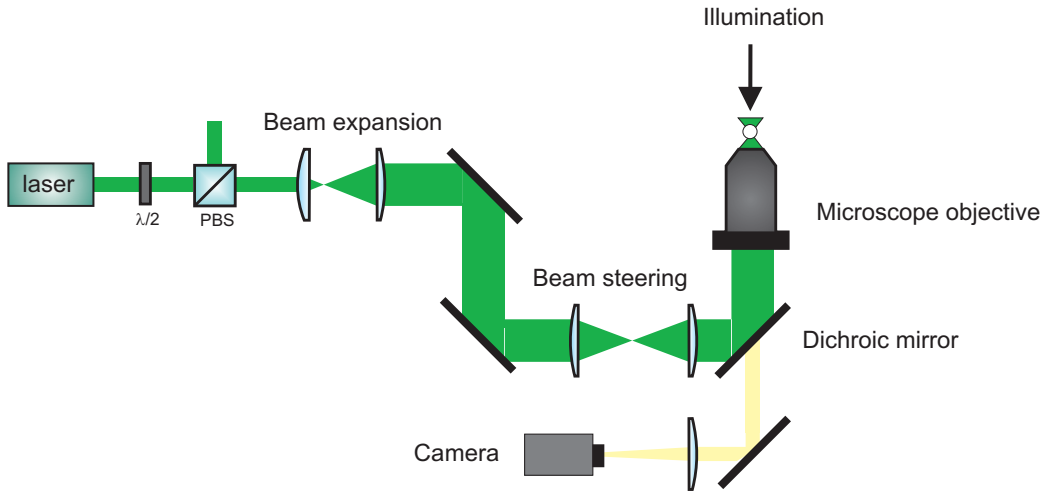

Figure 2.3: A basic optical tweezers experiment.

2.3.1 Lasers

Laser beams are used in optical tweezers for their attractive properties, such as spatial coherence, that allows them to be focused to tight spots using conventional microscope objectives. The high irradiance and Gaussian intensity profile also contribute to good trap performance. The choice of wavelength depends largely on the application; biological trapping experiments tend to be carried out with near infrared beams, as wavelengths in this region are close to the minima in any absorption cross sections for molecules within the

trapping substrate, thus avoiding laser induced damage to the biological specimens (termed *optication* [88]). It is also desirable to avoid a wavelength where water absorbs significantly, to avoid local heating and corresponding transport effects. The output from visible lasers, such as an Argon-ion laser (514.5 nm), or a frequency doubled Nd:YVO_4 (532 nm) are typically used in experiments involving pumping of molecules within the substrate (such as fluorescence, or Raman spectroscopy).

Lasers used in trapping ideally have a good pointing stability, have a stable output power, and have a beam profile with an $M^2 < 1.1$, where M^2 is a parameter that relates a trapping beam's profile to that of a perfect Gaussian beam ($M^2 = 1$). The reason for this is that beams with a good quality beam profile will focus to a diffraction limited spot, thus forming the necessary intensity gradients for three dimensional trapping. It is often the case that lasers only perform to these requirements when operated at maximum driver current. However, as only a few milliwatts are required for optical trapping, a method of power control is thus required. While this could be achieved with neutral density filters, this would lack the ability to fine tune the optical trapping power. The solution is to use a half waveplate (often termed $\lambda/2$) and a polarising beam splitter (PBS). A PBS will transmit polarized laser radiation in accordance with Malus's Law: $I = I_0 \cos^2\theta$, where I_0 is the intensity of the incident laser beam, and θ is the angle of the polarisation of the laser relative to the transmission polarisation of the PBS. Rotation of the waveplate alters the plane of the polarisation, thus affording a method of fine-tuning the optical power directed to the optical trap. An appropriate dichroic mirror is used to direct the laser beam into the objective; this is chosen to have a high reflectivity at the trapping laser wavelength, and transmit all other wavelengths (therefore allowing the same objective to be used for both tweezing and imaging).

2.3.2 Microscope objective

The microscope objective is the centrepiece of an optical tweezers, as it is used to focus down the laser radiation to a diffraction limited spot. Objectives are characterised by their *numerical aperture* (NA), defined as:

$$\mathrm{NA} = n \sin\theta \tag{2.8}$$

where θ is the half angle of the cone of light that can enter/exit the objective, and n is the refractive index of the surrounding medium. The corresponding diameter of a laser beam of wavelength λ focused by the objective is $1.22\lambda/\mathrm{NA}$ [89]. Hence, to minimize the size of the focused laser spot (and hence increase the electric field gradient, as discussed in Section 2.2) an objective with a high NA should be chosen. In order to increase the

NA beyond unity, an immersion fluid must be placed on the exit pupil of the objective. Typically, this is some form of hydrocarbon oil (with $n \sim 1.51$); such objectives are termed *oil immersion* objectives and are by far the most commonly used objectives in optical trapping. However, a disadvantage to using an oil immersion objective is that, owing to the refractive index mismatch between the immersion oil and a (typically) aqueous trapping medium, significant spherical aberrations are introduced into the beam (which increase with increasing depth into the sample). Water immersion objectives can be utilized to reduce the degree of spherical aberration, but these are more expensive than their oil immersion cousins.

Good quality optical traps are produced by expanding the incident beam, such that it overfills the back aperture of the objective. The reason for this is that rays at the periphery of the beam contribute the most to the gradient force, while those in the centre contribute mostly to the scattering force. Therefore, by overfilling the objective, the low intensity rays in the wings of a Gaussian beam profile are removed, increasing the intensity (and hence the optical forces) of the rays associated with the gradient force relative to the core. Gaussian beams are most commonly expanded using a pair of plano-convex lenses with focal lengths f_1 and f_2 in a simple Keplarian telescope, i.e. a distance $f_1 + f_2$ apart. Slight adjustment of the beam expansion lenses can be used to ensure that the microscope imaging plane, and the trapping plane, are coincident.

2.3.3 Beam steering

While an optical tweezers consisting of a laser beam, directed through a pair of lenses and into an objective is technically possible, it would be fairly uninteresting as it would lack maneuverability; "translation" of the trap would only be possible by physically moving the sample stage. Using steering mirrors aids alignment of the tweezers, however simply adding mirrors would not aid in trap maneuverability, as translation of the beam would effect how the beam enters the objective, introducing deleterious clipping of the beam at the back aperture, and aberration. The solution to this is to use another Keplarian telescope in a $4f$ system, as shown in Figure 2.4. The steering mirror M2 is located a distance f_1 from lens L1. Lenses L1 and L2 are separated by the sum of their focal lengths, $f_1 + f_2$, and the distance from L2 to the back aperture of the objective is f_2. Hence, M2 is imaged onto the back aperture (BA) of the objective (termed *conjugate planes*); changing the angular position of M2 will not affect the position of the beam at the back aperture (thus avoiding any negative beam clipping) but will result in a lateral displacement of the trap position, affording a method of manipulating the particle independent of the rest of the sample.

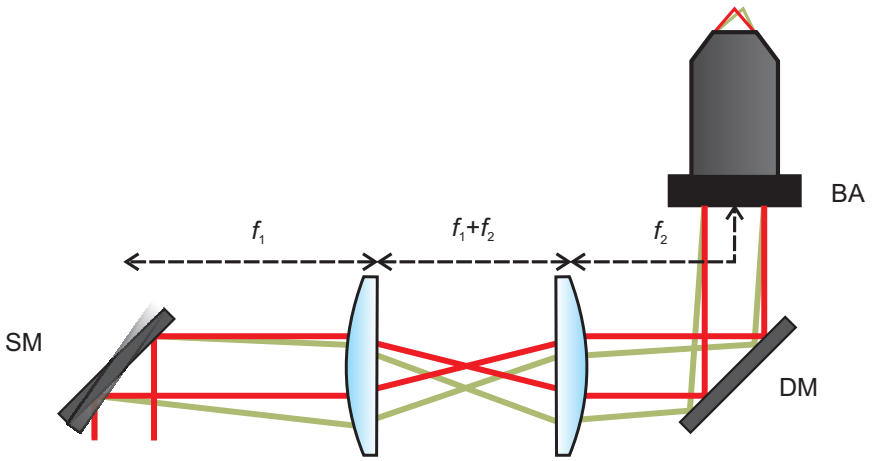

Figure 2.4: A $4f$ beam steering system (not to scale). The steering mirror SM and the back aperture of the objective (BA) form conjugate planes. Angular displacement of SM provides no change to the location of the beam at BA; however the change in angle of the rays corresponds to a lateral shift of the beam focus in the sample plane.

2.3.4 Illumination and imaging

Good microscope illumination is essential for obtaining high quality images and videos of trapped particles. If the tweezers system is a modified microscope then there should already be a good illumination system, however if a custom tweezers set up is being built then extra care needs to be taken. The simplest way to illuminate the sample would be to place a white light source above the sample, and focus it down using a lens, or a second objective. However, much higher quality illumination is achieved by utilising Köhler illumination. This is shown schematically in Figure 2.5. Output from a white light illumination source (I utilize a high intensity fiber coupled light source, Thorlabs OSL1-EC) is collimated using a short focal length (25 mm) lens (L1). This light is then incident upon a pair of lenses (L2 and L3) in a Keplarian telescope arrangement. An iris is positioned at the focus of these lenses, which serves as the *field diaphragm*. An additional lens (L4) forms a second Keplarian telescope with L3, and focuses the white light onto the sample, with the result that the field diaphragm is imaged onto the sample. A second iris is positioned before L4, termed the *condenser diaphragm*. By opening or closing the field diaphragm, the brightness of the image can be adjusted, while the condenser diaphragm will control the contrast of the image.

Most modern objectives are infinity corrected, i.e. their image plane is infinitely far away from the back aperture. To form an image, a tube lens is placed within the beam path, which focuses the light collected by the objective onto the camera. Modern tweezer systems use digital cameras for imaging, with a charge coupled device (CCD) or a complementary metal-oxide semiconductor (CMOS) detector. An appropriate filter is placed before the

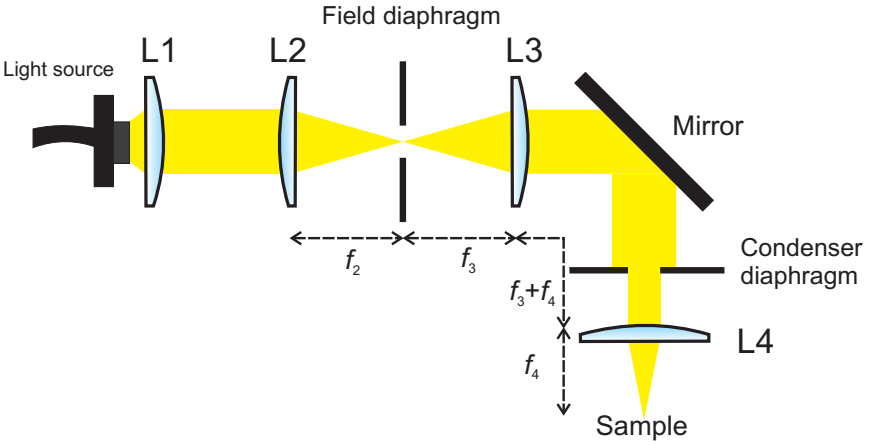

Figure 2.5: Schematic of the configuration of a custom built Köhler illumination. The field diaphragm and the sample form conjugate planes. Adjustment of the field diaphragm alters the brightness of the image, while adjustment of the condenser diaphragm changes the contrast.

camera, to remove any backreflected laser light that is transmitted through the dichroic mirror.

2.3.5 The sample

While this may seem like a trivial topic to discuss, there are several important factors that need to be considered when preparing samples for optical tweezers. Firstly, it is crucial to use the correct thickness of coverslip (borosilicate glass, no. 1 thickness, 0.13–0.17 mm) due to the short working distance of a high NA oil immersion objective. A second consideration, which was alluded to in Section 2.2, is the relative refractive index of the sample, i.e. the ratio of the refractive index of the object and its surrounding medium, $m = n_s/n_m$ (also termed refractive index contrast). In order for an object to be trappable via optical forces, it is necessary that $m > 1$. This is the case for most situations described in this thesis, such as silica microparticles in water, or salt water droplets in air. If $m < 1$, for instance if the sample consists of water droplets suspended in oil, the gradient force will act to push the object away from the region of high intensity. Trapping can be achieved in this instance by using *Laguerre-Gaussian* beams (also referred to as *vortex* beams) [90–92]. A fuller discussion of these beams (and how to generate them) will be given in Section 2.5.4; briefly these modes focus to rings, rather than spots, and so low index particles can be confined to the region of zero intensity.

To prepare liquid samples (i.e. suspensions of microspheres, or emulsions) for tweezing, it is common to sandwich a small volume ($\sim 20\,\mu$L) of liquid between two coverslips. A vinyl spacer (approximately 200 µm thick) is placed on one of the coverslips, to provide a small volume for the sample to occupy. If desired, the edges of the coverslips can be sealed

using transparent nail varnish, minimizing any evaporative losses (and increasing sample lifetime). Custom fabricated cells, such as microfluidic chips, can easily be integrated with an optical tweezers set up provided that a no. 1 thickness coverslip is adhered to the chip. Trapping particles in air can be accomplished by making a simple cell, consisting of a pair of coverslips with a rubber O ring separating them. A small section of the O ring is removed to allow a stream of aerosol to be introduced to the trapping volume.

In all instances, a small volume of immersion oil needs to be applied before the sample can be used on the microscope. This can either be applied directly to the objective, or else to the surface of the coverslip that will be in contact with the objective. It is important to use the correct variety of immersion oil that will give index matching of the glass used in the objective lens (Nikon Type A immersion oil is utilized with the Nikon E-plan objectives utilized in our laboratory), otherwise spherical aberrations will be introduced to the beam. Due to the surface tension at the oil/glass interface, the coverslips will move unless they are appropriately fixed to the microscope translation stage; I commonly achieve this by weighing down the sample with a pair of allen keys, or an empty cage plate (Thorlabs, CP02/M).

2.3.6 Trap characterisation

Although optical tweezers can be utilized as extremely sensitive force probes, they need to be calibrated such that, for a given power incident upon the sample, the magnitude of force imparted to the sample is known. This is achieved by introducing a dimensionless trapping efficiency parameter, commonly given the symbol Q, such that the force acting on a sample may be expressed as:

$$F = Q\frac{n_m P}{c} \tag{2.9}$$

where Q takes a value in the range 0 – 1, and $n_m P/c$ is the total momentum flux incident upon the sample. The trapping efficiency in the axial direction (i.e. parallel to the beam-path) is generally less than the lateral (perpendicular to the beampath) efficiency, and so it is common to only determine the axial value (Q_{axial}). To achieve this, a particle is trapped stably as normal, and then the trapping power is lowered until the particle is observed to *just* fall out of the trap (P_{min}), i.e. the optical forces are equal to the weight of the particle, and any thermal forces on the particle due to Brownian motion. This minimum force may therefore be expressed as [93]:

$$F_{\text{min}} = \frac{\pi d^3 g}{6}(\rho_s - \rho_m) + \frac{2k_B T}{d} \tag{2.10}$$

where d is the diameter of the particle and ρ_s and ρ_m are the densities of the sphere and the surrounding medium respectively. The first time on the right hand side of Equation 2.10 is

the gravitational force acting on the sphere minus its buoyant force, and the second term is the force required to suppress the thermal motion of the particle. As the above minimum force can easily be calculated, and P_{min} can readily be measured, Q_{axial} can therefore be determined. Typical Q_{axial} values for colloidal particles tend to be < 0.1 [94], while for a salt water aerosol they take values around 0.28 [95].

Typically, the minimum trapping power is measured by placing a power meter in the beam dump arm of the PBS. The power incident upon the sample will be equal to the difference between the measured power when the particle falls from the trap, and the maximum value of the power (taking into account the transmission efficiency across the optical train). To give a better discrimination between the small powers that will be measured, a neutral density filter is placed into the trapping laser beam path. The optical losses between the PBS and the microscope objective also need to be characterised; this value is trivial to determine. It involves slightly more effort to determine the losses due to overfilling the objective, and those of the objective itself (owing to the highly divergent nature of the objective, making accurate measurements of power difficult). The former may be determined by setting an iris to the same diameter as the back aperture of the objective and measuring the power before and after the iris. To determine the latter, two identical objectives (with a sample prepared from deionised water sandwiched between them) must be used. Using a translation stage, the relative position of the two objectives is adjusted until the laser is recollimated by the second objective, where the power can then be accurately measured. The transmittance through a single objective is then determined by the square root of the transmittance through both objectives; for the objectives used in this thesis, a transmittance of 0.893 at 532 nm was measured.

2.4 Multiple trapping techniques

The basic tweezers system described above is somewhat limited in the sense that it can only independently trap one object at a time with a Gaussian beam (unless a beam shaping optic, such as an axicon, or a spiral phase plate, is introduced to the beam path). It is therefore desirable to have a system that enables the trapping of multiple particles, which can be moved independently, as this will ultimately improve the flexibilty of the tweezers system. In this section, various methods for achieving multiple trapping of particles shall be discussed.

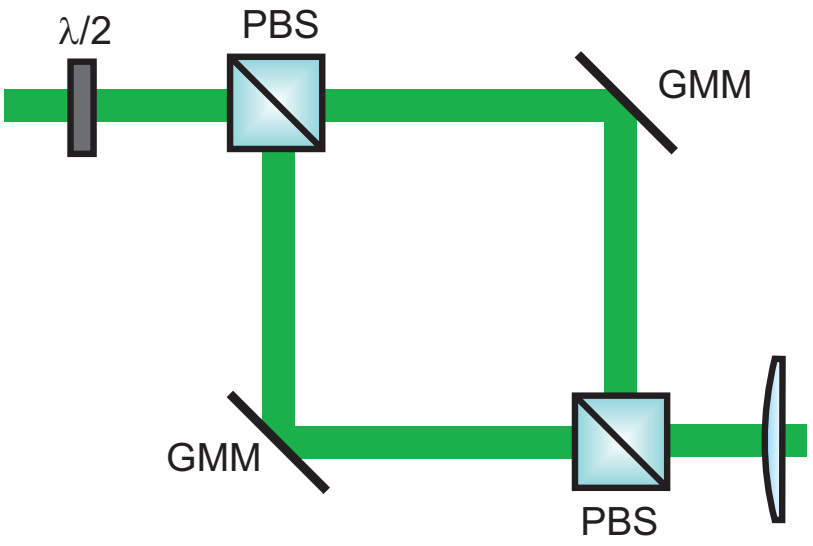

Figure 2.6: Schematic of the beam splitter portion of a basic dual beam tweezers. The lens is chosen such that the gimbal mounted mirrors are imaged onto the back aperture of the objective.

2.4.1 Beam splitters

By far the most simple way to achieve independently steerable traps is to split the beam in two using a polarising beam splitter and a half-waveplate, then recombine them using a second PBS [96], shown schematically in Figure 2.6. Use of gimbal mounted mirrors allows each trap to be steered independently, while using a $4f$ system to image the GMMs onto the normal beam steering mirror allows both traps to be steered simultaneously.

Dual beams have uses in biophysics where two optical handles need to be manipulated independently. For instance, Mammen *et al.* studied the adhesion of a virus coated microsphere with a erythrocyte, both of which were optically trapped, to investigate the effectiveness of viral inhibitors [97]. A review of the applications of dual beam traps in biophysics is given by Sung *et al.* [98]. The manipulation of liposomes described above was achieved using a dual beam trap [55]. The procedure has been employed by Buajarern *et al.* to study the coagulation of aqueous aerosol droplets [99], and is regularly used by the Aerosol Dynamics Group in Bristol to independently trap and spectroscopically characterise a pair of droplets, one of which serves as a control [100].

2.4.2 Acousto-optic deflectors

Acousto-optic deflectors (AODs) operate by generating an acoustic wave within a crystal, thus creating a varying density which acts as an effective diffraction grating for an incident laser beam. The deflection angle for a first order diffracted beam is given by $\theta = \lambda f/v$,

where λ is the wavelength of the incident beam, f and v are the frequency and the velocity respectively of the acoustic wave [101]. The AOD generates "multiple" traps, as it rapidly scans the laser beam between the desired trapping locations (at speeds of several kHz).

To be practical for optical tweezing, a pair of orthogonal AODs are often used to generate optical landscapes in both the x and y directions. There are several drawbacks to the use of AODs; they are reasonably lossy ($< 85\%$ transmission per AOD) and can introduce aberrations to the beam. Furthermore, the diffraction efficiency across the acoustic bandwidth of the AOD is not uniform; there can be a difference of as much as $10 - 15\%$ in the transmitted light levels (which will affect the trap stiffness). Nevertheless, AODs continue to be a popular choice for multiple trap site generation; with digital frequency synthesizers used to control the acoustic wave, high beam pointing stability is achieved (an important consideration for experiments that require nanometre accuracy of the trapping beam, such as biological force measurements) [102].

2.4.3 Diffractive optical elements

Introducing a diffractive optical element (DOE) into the beam path affords a practical method of generating multiple beams [103]. The conceptual idea behind a DOE is quite simple; a handwaving explanation is that the incident beam is split into multiple components (drawing an analogy with a diffraction grating), each of which can be focused to an independent trap. However, unlike in AODs, the laser is not timeshared between the multiple trap sites. A DOE can also be used to alter the wavefront of an incident beam, for instance a discontinuity in a diffraction grating would effectively provide a torque to the wavefronts, changing them from a linear to a helical form, and adding additional angular momentum to the photons.

Diffractive optical elements work by imparting a phase modulation onto an incident waveform, which is decoded by an additional optical element (e.g. a lens). Light propagating through an optical element of thickness d and refractive index n will experience a phase lag given by:

$$\delta = \frac{2\pi n d}{\lambda_0} \tag{2.11}$$

where λ_0 is the vacuum wavelength of the radiation. Thus it is clear that there are two main methods of constructing a phase mask; either alter the local thickness of the substrate (such as in a spiral phase plate, where the thickness increases around the circumference of the plate [104]) or altering the local refractive index. As shall be discussed in the next section, this can easily be achieved by use of liquid crystal displays. Phase masks of the former variety will obviously be static phase modulation devices, while the latter can offer dynamic modulation.

Optical tweezers that utilize DOEs are known as *holographic optical tweezers* (HOTs). Those which incorporate dynamic DOEs that can be altered in real-time are hence known as *dynamic* holographic optical tweezers (DHOTs) [105]. DHOTs are computer driven, hence there is considerable scope for flexibility with the user interface. A particularly user friendly variant on DHOTs combines the output from the camera that images the sample, and the software which drives the optical tweezers, such that optical traps can be generated in the sample via a "point and click" style interface. This progressed to the development of a multitouch console for optical tweezing [106]. With the development and recent popularity of tablet computer devices (most famously, the Apple iPad), the natural progression has been to utilize them as control interfaces for DHOTs [107].

2.5 Holographic Optical Tweezers

This section will expand on the above discussion on diffractive optical elements, with an emphasis on dynamic elements. I am extremely grateful to Dr Daniel Burnham, who provided me with his software for controlling the SLM and generating the necessary kinoforms. Further information regarding how these programmes work can be found in his PhD thesis [108].

2.5.1 Spatial light modulators

An electronic spatial light modulator (SLM) is a device which may serve as a dynamic DOE. The most common form of SLM used in optical tweezers experiments is a *liquid crystal on silicon* (LCOS) display. A schematic of this sort of SLM is shown in Figure 2.7. Briefly, a layer of liquid crystal is sandwiched between two electrode layers. The upper electrode is transparent, while the bottom layer consists of many individual electrodes, which can be individually addressed (pixels). A dielectric mirror is placed over this electrode layer, so that the SLM acts as a reflective optic. The physical properties of liquid crystals allow the phase of the incident light to be modulated by applying an electric field across them. I shall now briefly discuss these properties.

A liquid crystal is an additional state of matter, lying between the solid and liquid phase. They show no positional order, but do have an orientation order. Nematic liquid crystals will tend to align in a certain direction, called the *director* of the liquid crystal (denoted $\mathbf{n}$, not to be confused with refractive index). Nematic liquid crystals display birefringence, with the optical axis dictated by the director [109], meaning that an incident plane polarised wave is split into two orthogonal components: the ordinary ray (o) and the extraordinary ray (e). The electric field vector of the o ray is perpendicular to the optical axis, and so the

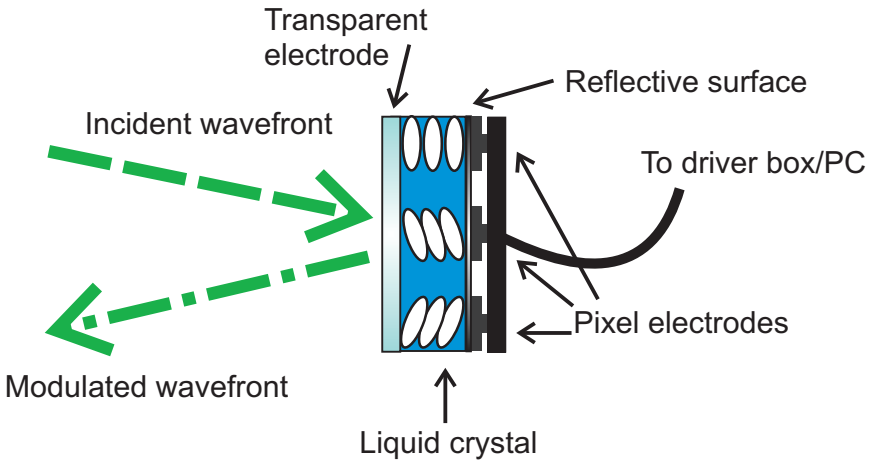

Figure 2.7: A schematic representation of a liquid crystal on silicon (LCOS) SLM. This sort of SLM is used in the holographic optical tweezers described in this thesis.

associated refractive index (n_o) is a constant, independent of the direction of propagation. The electric field vector of the e ray is therefore in a plane which is parallel to the optical axis, and so will display a refractive index (n_e) that depends upon the angle θ the incident ray makes with the optical axis [110]:

$$n_e(\theta)^2 = \left(\frac{\cos^2\theta}{n_o^2} + \frac{\sin^2\theta}{n_e^2} \right)^{-1} \tag{2.12}$$

As a consequence, the effective birefringence for the liquid crystal is given by

$$\Delta n(\theta) = n_e(\theta) - n_o \tag{2.13}$$

and leads to a corresponding phase retardation of a wave incident upon the LC of:

$$\delta = \frac{2\pi \Delta n d}{\lambda_0} \tag{2.14}$$

where d is the thickness of the liquid crystal, and λ_0 is the vacuum wavelength. Nematic liquid crystals also display dielectric anisotropy; the response of the director to an applied electric field is dependent upon the dielectric constants measured parallel ($\epsilon_\parallel$) and perpendicular ($\epsilon_\perp$) to the director. The dielectric anisotropy is given by:

$$\Delta\epsilon = \epsilon_\parallel - \epsilon_\perp \tag{2.15}$$

Applying an electric field across the liquid crystal will therefore cause it to rotate in order to minimize its potential energy, therefore for an ensemble of LC molecules, the director will rotate, thus changing the effective birefringence and hence the phase difference imparted to a wave incident upon the SLM. To achieve efficient phase modulation, it is imperative

that the polarisation of the laser incident upon the SLM is parallel to the optical axis of the liquid crystal, as it is the extraordinary refractive index that is varied when the voltage is applied. This is commonly achieved by using a half-waveplate to alter the polarisation of the laser, prior to the SLM.

An SLM of this variety is somewhat inefficient; $\sim 40\%$ of incident light remains unmodulated (termed the *zeroth order*, borrowing from the language of diffraction gratings) and must be removed, usually by positioning a beam block in the focal plane of a transform lens (see later). Compared to AODs, they are considerably slower (with a typical refresh rate of 75 Hz). However, the advantages they offer when compared to other optical trapping techniques are considerable. These advantages, and how they might be implemented, shall now be briefly discussed.

2.5.2 Beam steering using kinoforms

The easiest place to begin a discussion of DHOTs is to realise how the use of a DOE can manipulate an incoming wave purely by altering its phase. An analogy between a DOE and a diffraction grating was drawn above, although perhaps the simplest optical element to visualise, which can redirect a beam by altering its phase profile, is a prism. Clearly the optical path length of a plane wave travelling through a prism is different depending upon the location at which the wave exits the prism. Similarly, a lens will alter a linear wavefront to a spherical one, again by virtue of the fact that a different points in the lens, some parts of the wave will lag behind others. Phase modulation for beam steering in three dimensions can be adapted from considering the redirection of a wavefront using gratings and lenses, and is hence often referred to as the *gratings and lenses* approach. The appropriate phase modulations, $\Phi(x, y)$, are [111]:

$$\Phi(x, y) = \left(\frac{2\pi}{\Lambda_x} x + \frac{2\pi}{\Lambda_y} y + \Gamma(x^2 + y^2) \right) \bmod 2\pi \tag{2.16}$$

where Λ is the fringe period on the grating comprising the x and y displacements, and Γ controls the axial position of the trap. Should multiple traps be required, the complex sum of the individual phase functions is calculated, and its argument determined:

$$\Phi(x, y) = \arg \left(\sum_j \exp \left[i \Phi_j(x, y) \right] \right) \tag{2.17}$$

The phase only holograms that these modulations describe are examples of *kinoforms*. The method above is somewhat limited, however, as it cannot generate arbitrary trapping patterns. Furthermore, the number of unwanted diffractions (termed *ghost orders*) increases with the number of spots generated.

Curtis and Grier described an algorithm which can produce an arbitrary trapping pattern [105], based upon a Gerchberg-Saxton algorithm. Here, the incident laser field ($E_0(\vec{\rho}) = A_0(\vec{\rho})\exp(i\psi)$, where $\vec{\rho}$ is a point within the DOE aperture, and $A_0(\vec{\rho})$ is the real amplitude of the laser beam) is modelled as having a constant phase in the DOE plane, and of unit intensity. The desired phase modulation imparted by the DOE is denoted $\Phi(\vec{\rho})$. The necessary phase modulation is generally calculated by taking the desired electric field in the sample plane, and working backwards. Fourier optics [14] can be utilized to calculate the relationship between the electric field in the front and back focal planes of a lens; specifically the relationship (if the DOE is located a focal length away from the lens) is a Fourier transform. The modulated field can be written as $E(\vec{\rho}) = A(\vec{\rho})\exp(i\Phi(\vec{\rho}))$. In principle, one can take a desired pattern of traps and work backwards to calculate the necessary kinoform to induce the phase modulation. However, this is a distinctly non-trivial calculation! Inevitable spatial discrepancies between the input laser amplitude, and the calculated amplitude, will result in light being diverted into the ghost orders. However, the kinoform generated by this procedure ($\Phi(\vec{\rho})$) is an ideal starting point for refinement algorithms (such as the Gerchberg-Saxton algorithm). A comprehensive review of various kinoform algorithms (in terms of efficiency, uniformity, etc.) is provided by Di Leonardo *et al.* [112].

The above discussion makes it clear that the DOE needs to be located within a Fourier plane of the objective lens, in order to achieve the dynamic trapping patterns afforded by DHOTs. In practice, this is achieved by utilizing a $4f$ system to image the SLM onto the back aperture of the objective. This is shown schematically in Figure 2.8. A beam block can be positioned at the focus of the $4f$ system to block out the 0^{th} order diffraction.

2.5.3 Aberration correction using kinoforms

A disadvantage of the use of LCOS SLMs is that their surface is not truly flat, which introduces additional, unwanted phase modulation into the beam. In practice, this means that the beam will become further aberrated, reducing trap quality. Typically, an SLM will introduce an astigmatism into the trapping beam.

These aberrations can be corrected for by displaying additional kinoforms on the SLM, which are designed to correct the phase profile of the aberrated beam. These kinoforms are based upon the polynomials devised by Zernike, which describe any form of aberration [113], and operate by imparting an appropriate phase modulation to counteract the aberration introduced by the SLM. Furthermore, they can be used to correct for additional aberration in the beam (such as those arising from misalignment of the optical train).

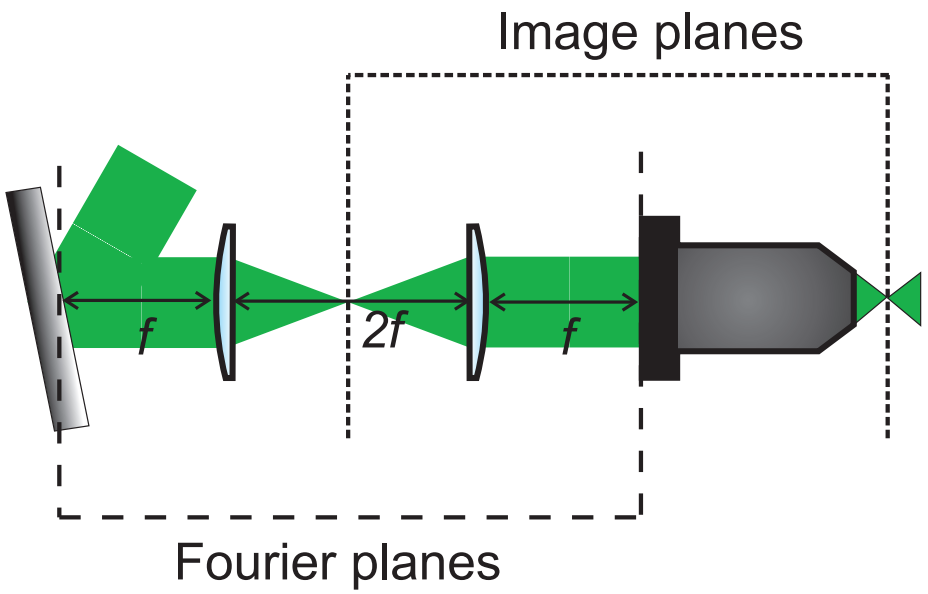

Figure 2.8: Relative positioning of the SLM and the microscope objective, highlighting the Fourier and image planes. Adapted from Padgett and Di Leonardo [47].

Burnham's aberration correction routine precalculates the appropriate kinoforms, each representing the mode of aberration from -2λ to $+2\lambda$ in uniform increments. The kinoform series is displayed sequentially, and an image of the trapping laser (as reflected off a coverslip) is captured using the Firewire camera. To analyse the impact of the correction kinoform on the beam profile, he follows the method of Wulff *et al.* by defining the following metric [114]:

$$M_s = \frac{\left(\sum_{ij} I_{ij}\right)^2}{\sum_{ij} I_{ij}^2} \tag{2.18}$$

where I_{ij} is the intensity of the ij^{th} pixel of the image. The correction kinoform which gives the optimum beam profile will be the global minimum of this metric. Burnham's kinoform generation software incorporate the Zernike correction kinoforms, by adding the phase modulation for the correction kinoform to those which displace the beam's position, modulo 2π. Thus, it is possible to generate multiple diffraction limited spots with the SLM.

2.5.4 Altering the beam profile

A considerable advantage that the use of dynamic DOEs has over other techniques is the ability to alter the beam profile of the trapping laser, to more exotic geometries. This section shall focus on the generation of vortex beams, or Laguerre-Gaussian beams, as experiments have been performed using this beam geometry.

Conventional laser beams, with a Gaussian beam profile, are focused down to small spots. However, if a beam of light has a helical wavefront, it will focus to a ring of light surrounding a region of zero intensity. These are known as *optical vortices* [115], or *Laguerre-Gaussian* (LG) modes. A helical mode $\psi_\ell(\vec{r})$ is distinguished by a phase factor which is proportional to the polar angle θ around the beam axis [115]:

$$\psi_\ell(\vec{r}) = u(r,z)\exp\left[-ikz\right]\exp\left[i\ell\theta\right] \tag{2.19}$$

where $u(r,z)$ is the beam's radial profile at a position z and ℓ is an integer known as the topological charge. Destructive interference is responsible for the regions of zero intensity until a radius R_ℓ is reached, where constructive interference causes the bright ring. Vortex beams may be described in terms of Laguerre-Gaussian modes, which have a radial dependence of [115, 116]:

$$u_p^\ell(r,z) = (-1)^p\left(\frac{\sqrt{2}r}{w}\right)^\ell L_p^\ell\left(\frac{2r^2}{w^2}\right)\exp\left(-\frac{r^2}{w^2}\right) \tag{2.20}$$

where $L_p^\ell(x)$ is a Laguerre polynomial, of radial index p. These can predict the value of R_ℓ as [117]:

$$R_\ell = w\sqrt{\frac{\ell}{2}} \tag{2.21}$$

for a mode with $p = 0$, where w is the corresponding Gaussian beam radius. A vortex beam (also known as an LG beam) may be formed from a Gaussian beam by applying a phase modulation of $\ell\theta$ mod 2π to the incident beam. Examples of the kinoforms required to generate a vortex beam, as well as an image of the resulting beam viewed in the image plane of the objective, are shown in Figure 2.9.

For many applications of vortex beams, it is desirable to know what size of vortex beam with a given value of ℓ will be in the trapping plane. This was achieved by imaging the backreflection off the coverslip of a selection of vortices with differing values of ℓ onto the camera, then analysing the resulting images using commercially available software (National Instruments Vision Assistant) to map the intensity of the pixels within the image (i.e. taking a beam profile). A Gaussian profile was fitted to each region of high intensity; by assuming the diameter of the beam to be the distance between the two Gaussian peaks, the radius of the beam R_ℓ as a function of ℓ can be plotted. This is shown in Figure 2.10. It is apparent that the radius scales linearly with ℓ, not $\sqrt{\ell}$ as is predicted by Laguerre-Gaussian modes. This is consistent with the work of Curtis and Grier [115] and can be attributed to the superposition of higher order p modes within the Laguerre-Gaussian expression. As with Curtis and Grier, additional rings are observed in the LG beam profile, which indicates the superposition of higher order modes.

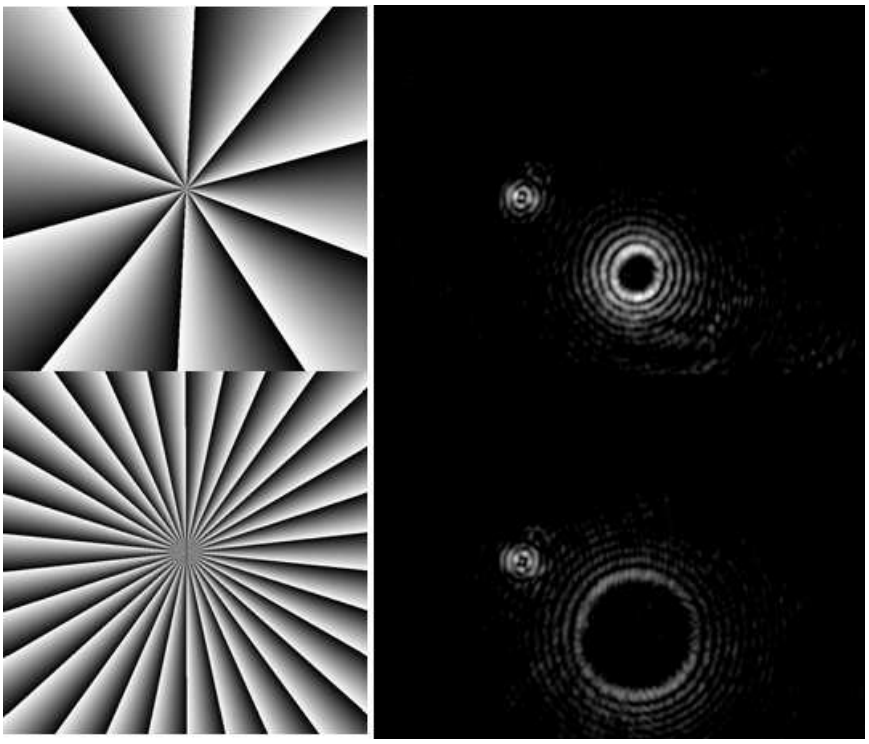

Figure 2.9: Kinoforms required to generate, and corresponding image of LG beams with $\ell = 10$ (top) and $\ell = 30$ (bottom). The kinoform that displaces the beams from the zeroth order has been omitted for clarity; the kinoforms would resemble a diffraction grating with a discontinuity, which imparts the "torque" to the wavefront.

Optical vortices are of interest in optical manipulation for two reasons. Firstly, they carry $\ell\hbar$ units of orbital angular momentum per photon (as opposed to the spin angular momentum associated with circularly polarised light), and these can be transfered to particles with a refractive index higher than the surrounding medium. This is manifested by particles orbiting the region of high intensity. The angular momentum associated with LG modes prompted their use in optical manipulation as an "optical spanner" [118], demonstrating the mechanical equivalence of spin and orbital angular momentum for absorbing spheres. Arrays of LG modes generated with an SLM, and populated with microparticles, can act as an optomechanical micropump [119].

The second reason is that the region of zero intensity allows a method of trapping and manipulating particles that cannot be trapped using conventional Gaussian beams, for instance low index particles (i.e. $n_s < n_m$) such as water droplets in oil, or hollow microbubbles [91], by confining the particle to the region of zero intensity. An recent interesting use of LG modes was demonstrated by Lee *et al.* where they were utilized as an "optical shield" against the influence of other particles in the measurement of fluid viscosity using optical tweezers [120].

Other exotic beam profiles, such as Bessel beams [121], may be generated using the SLM.

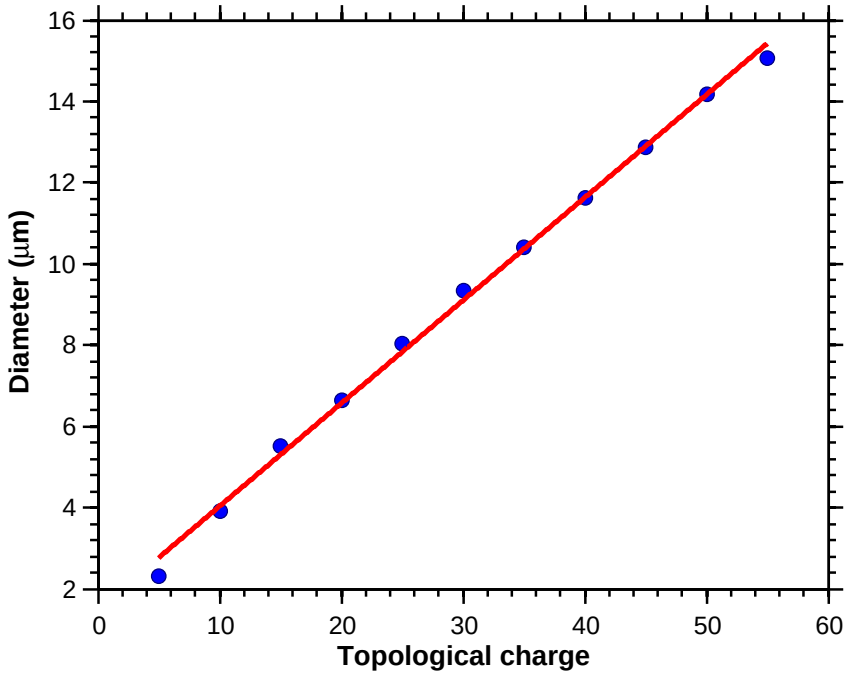

Figure 2.10: The diameter of a vortex beam ($2 \times R_\ell$) as a function of ℓ, highlighting the linear dependence of the beam radius upon ℓ.

It should be noted that, due to the pixelated nature of the SLM, a natural limit is imposed on the efficiency of mode conversion, and that well aligned physical optics (such as axicons in the case of Bessel beams) may be preferable [122]. However, an SLM is not limited to generating laser modes; in principle any electric field distribution can be realised within the trapping plane, and its Fourier transform calculated in order to determine the kinoform required to generate it. Burnham *et al.* used this to great effect in studying the growth of the fungus *Neurospora Crassa* [123]. Custom light patterns generated by the SLM (both multiple Gaussian spots, as well as a continuous extended line) were utilized to influence the hyphal growth. Holographic techniques were also demonstrated to have a use in the thermocapillary control of large ($> 100\,\mu m$) droplets in microfluidic chips [124]; custom beam geometries (such as lines) were more effective at stopping droplets within the flow than Gaussian spots, and also required less laser intensity.

2.6 Experimental configuration of a Dynamic Holographic Optical Tweezers

A schematic of the dynamic holographic optical tweezers set up that I have built and used in this thesis is shown in Figure 2.11. A 532 nm CW solid state laser, operating at a

maximum power of 400 mW (Laser Quantum Torus), is used as the laser source. A half-waveplate (Thorlabs, WPDM05M-532H-1064Q) in a rotation mount (Thorlabs, RSP1/M) and a polarising beam splitter cube (Edmund Optics) are used to finely control the power, as described in Section 2.3.1. A second half-waveplate is used to control the polarisation of the beam incident upon the SLM (Holoeye LC-R 2500), to ensure the maximum efficiency of light directed into the first diffracted order (as discussed previously). This SLM modulates the phase of incident light from 0–2π in 255 discrete levels. It is mounted in a conventional mirror mount, which gives tilt and angular control of the reflected laser radiation. The beam is expanded using a Keplerian telescope, such that the beam overfills the vertical axis of the SLM. Two +400 mm lenses in a $4f$ arrangement are used to image the SLM onto mirror M4. An obstruction (such as a sharpened pencil lead, or an anodized razor blade) is placed at the focus of lens L3 to block out the zeroth order diffraction from the SLM. A second $4f$ lens system is used to image M4 onto the back aperture of a microscope objective (Nikon E Plan, 100×/1.25), as well as simultaneously reducing the size of the beam such that it just overfills the back aperture of the objective. The two $4f$ systems are arranged so that the SLM and the back aperture form conjugate planes. A 532 nm dichroic mirror (CVI Melles-Griot) is used to reflect the laser light into the microscope objective while allowing other wavelengths to pass. The sample is illuminated from above using custom Köhler illumination (Section 2.3.4), and is imaged using the same objective that is used for tweezing. This light is then imaged onto a Firewire camera (PixeLINK PL-A774), with images and videos captured using custom software written in LabVIEW. The entire tweezers section (the section enclosed by a dashed line in Figure 2.11) is constructed using Thorlabs cage systems.

Good alignment of the optical train is crucial for good performance of the holographic optical tweezers, in order to minimize aberration of the beam. The alignment method used involves removing all of the lenses from the optical train, switching off the SLM (so that the system is aligned to the 0^{th} order) and ensuring that the unexpanded beam is passing through the centre of the cage system. This can be checked using commercially available alignment tools, such as the Thorlabs cage alignment plates.[1] The easiest way to align a cage system is to use a pair of mirrors; the mirror closest to the cage system (M4 in Figure 2.11) is used to adjust the position of the beam at the far end of the cage, while the other mirror (M3) is used to align the entrance of the cage. Adjustment of these two mirrors is performed iteratively, until the beam is passing cleanly through the middle of the cage plates. At this stage, the lenses are inserted into the setup, starting with the lens closest to the objective (L6) and working backwards. Each time a lens is inserted, the alignment through the cage system is checked using the alignment plates; if the alignment is off then the position of the lens is changed accordingly. Once all the lenses are in place,

[1] These are affectionately referred to as "T shirts" in our lab.

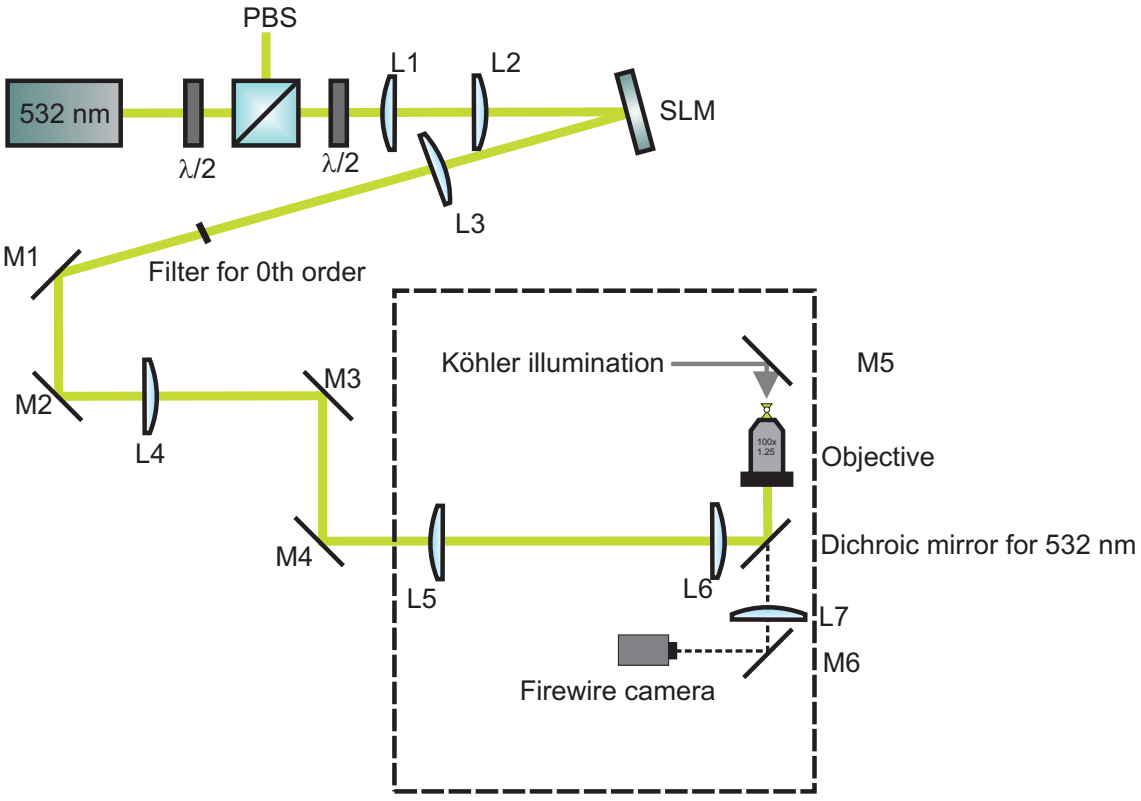

Figure 2.11: Schematic of the experimental setup for dynamic holographic optical tweezers. The area enclosed by the dashed lines refers to a side view of the optical system.

an image of the beam is captured by placing a coverslip onto the sample stage, and lowering to the objective until the Airy disk is observed on the CCD (initially no immersion oil is added). Minor adjustments of the mirror M3 can be used to correct for aberration in the beam (which can be assessed by the appearance of the Airy disk), with M4 (which is in a plane conjugate to the back aperture of the objective) used to return the beam to its initial position. The quality of the beam can easily be assessed by displaying an LG kinoform on the SLM as the LG modes are extremely sensitive to aberration [125]; any misalignment will be manifested in a distinctly non-circular shape of the backreflection off the coverslip. Once satisfactory alignment and beam quality has been achieved, the SLM is switched on, and a beam steering kinoform displayed. The tilt adjustment of the SLM mount is then used to align the 1^{st} order diffraction off the SLM to the position of the 0^{th} order, thus ensuring the optimum alignment of the SLM beam. The Zernike aberration correction procedure is then applied, to correct for the astigmatism introduced by non-uniformities in the SLM.

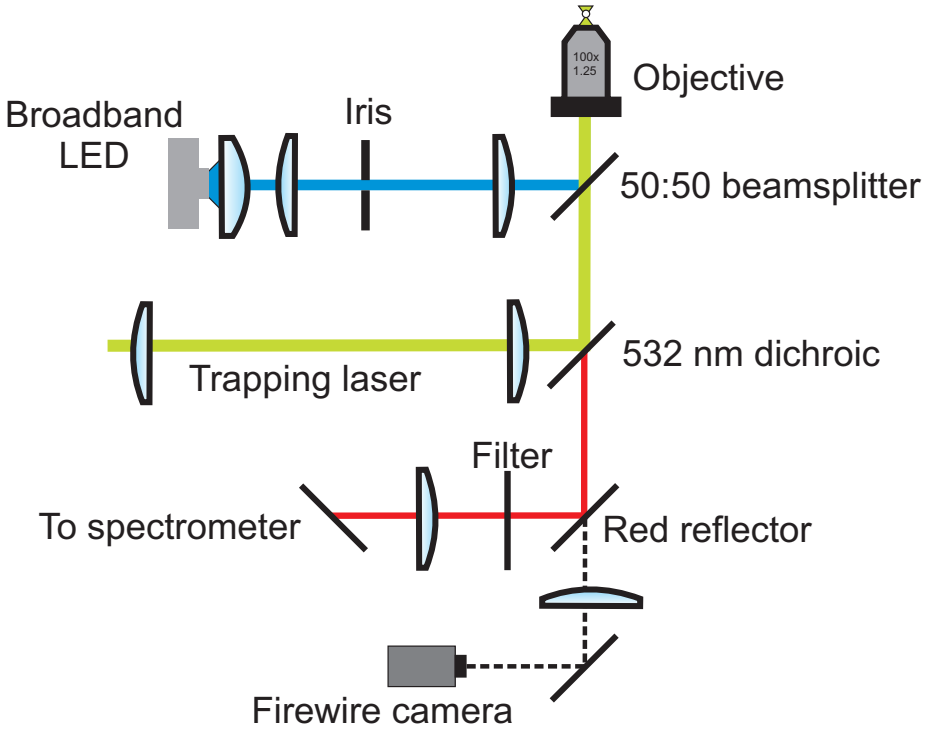

Figure 2.12: Schematic of the arrangement of the tweezers cage system for spectroscopy. A red reflector is used to direct wavelengths $> 600\,\text{nm}$ into the spectrometer. A 550 nm longpass filter cuts out any transmitted laser light. If broadband Mie scattering is desired, an additional arm is added above the trapping laser. The lenses are arranged such that the iris is imaged in the sample plane.

2.7 Combining optical tweezers with spectroscopy

Optical tweezers can readily be combined with a spectrometer, to allow the wavelength-resolved spectroscopy of a sample to be investigated. The work presented in this thesis utilizes two main spectroscopic techniques: spectral analysis of the particle due to molecules within it (such as fluorescence, or Raman spectroscopy) and the scattering of white light from the particle itself. Both of these techniques afford different advantages, depending upon the exact aim of the study being performed. The tweezing objective is also used to collect any emitted/scattered radiation from the trapped sample. An appropriate reflector can be used to remove wavelengths of interest into an extra arm in the tweezers cage assembly, while transmitting all others. The tweezers system described above uses a red reflector (Thorlabs, FM02) to achieve this. A 550 nm longpass filter (Thorlabs, FEL550) is placed in the path of the reflected light to cut out any backscattered laser radiation, before being focused into the entrance slit of a spectrograph (Andor Shamrock SR-303i), coupled with a thermo-electrically cooled CCD detector (Andor iDus DU420A). Spectra are recorded using commercially available software (Andor Solis), which is also used to control the spectrometer. This optical configuration is outlined in Figure 2.12.

Broadband light scattering experiments require an additional arm added to the cage system. Output from a high intensity white LED (1 W Luxeon Star/o LED, LumiLEDs, San Jose, CA) is collimated by a 25 mm lens, and then directed through a Keplarian telescope consisting of a 50 mm and a 100 mm lens, with an iris at the focal plane of the telescope. The 100 mm lens was positioned such that an image of the iris was formed in the focal plane of the microscope objective. A 50:50 beamsplitter (Thorlabs, BSW10) is used to reflect the light into the objective (at the cost of losing $\sim 50\%$ of the incident laser radiation).

2.8 Conclusions and outlook

This chapter has described the basic physics of optical tweezers, as well as outlining more advanced optical trapping techniques. An emphasis has been placed on holographic optical tweezers, as one of these has been constructed for use in our laboratory. Additionally, it has been shown how an optical tweezers experiment can be combined with spectroscopy. Looking ahead, this DHOTs system will be used in three main experiments: Chapter 4 focuses on the spectroscopic studies of aqueous aerosol droplets, utilizing the SLM to generate both conventional Gaussian traps, and LG modes. The primary spectroscopic method employed is Raman spectroscopy of the aerosol droplet; enhanced Raman scattering is observed at discrete wavelengths, and the properties of these resonances afford a highly accurate way to characterize the droplet's size and composition. This resonant behaviour (and its physical origin) will be described in Chapter 3. Chapter 5 looks at the optical trapping and spectroscopy of ionic liquid droplets, and uses broadband Mie scattering to characterise the droplets. Chapter 6 uses the SLM in a somewhat different fashion; instead of a high NA objective, a lower magnification objective with a long working distance is used to focus the 532 nm radiation onto a gold-coated microscope slide. Owing to absorption of the laser radiation, thermally induced forces cause an aqueous suspension of microspheres to self assemble into 2-dimensional colloidal crystals around the laser focus. The SLM is used to generate multiple trapping sites at controlled locations, allowing a study of the interaction of these crystals to be carried out.

Chapter 3

Light Scattering and the Spectroscopy of Microparticles

This chapter will focus on the scattering of light by spherical particles, with an emphasis on so called Mie Theory. A description of how spherical objects can act as spherical microcavities, leading to constructive interference at specific wavelengths and maxima in the measured signal, will be provided. It will be discussed how these resonances are predicted by Mie theory, and can be used to accurately determine both the particle radius and its refractive index, providing the necessary theoretical framework for the data presented in Chapter 4.

3.1 Scattering basics

Consider the following generic system, consisting of an illumination source (say a laser) with an irradiance of I_0, incident upon a photodetector. If we introduce some particles e.g. a fog of aerosols into the system, from intuition it is clear that the irradiance incident upon the detector, I will be less than I_0, i.e. the presence of particles has removed energy from the light source. The main ways that energy can be removed from the beam are (elastic) scattering of radiation, and absorption. This removal of energy is referred to as *extinction*. These processes are quantified by defining an appropriate cross section, i.e. the equivalent area of the light beam that a particle will remove by scattering, conventionally labelled σ_i. However, it is more convenient to work with a dimensionless efficiency; for a sphere of radius a this may be defined as $Q_i = \sigma_i/\pi a^2$. Conservation of energy requires that

$$Q_{\text{ext}} = Q_{\text{abs}} + Q_{\text{sca}} \tag{3.1}$$

where the subscripts ext, abs and sca refer to extinction, absorption and scattering respectively. The scattering of light by a sphere will depend on both the size of the sphere (typically quantified by the radius, a) and the wavelength of the illuminating light, λ (which will depend upon the optical properties of the medium surrounding the sphere). It is therefore convenient to define a parameter which contains these two variables. This is known as the *size parameter*, x, and is defined as:

$$x = \frac{2\pi a n_m}{\lambda_0} \tag{3.2}$$

where n_m is the refractive index of the surrounding medium and λ_0 is the wavelength of the illuminating light in a vacuum. Very small particles ($x \ll 1$) may be treated as point dipoles, and the scattering of light calculated via Rayleigh scattering. Conversely, large particles may be examined via geometric optics, with scattering properties determined by ray tracing. However, as was the case when discussing the physics of optical tweezers, the majority of particles of interest (and all that are relevant to this thesis) lie between these two limits, and therefore require a different theory to describe their scattering properties.

The scattering of light by an arbitrary sized particle is an important problem in many aspects of science. While independently studied by Lorenz [126],[1] Debye [127] and Mie [128], the solution for the scattering of a plane wave is commonly referred to as Mie theory. More recently, the theory has been modified to account for the scattering of a generic light field, known as *Generalized Lorenz-Mie Theory* (GLMT) [129]. However, for the work presented in this thesis, conventional Mie theory provides an adequate description.

In its essence, Mie scattering theory is a solution for Maxwell's equations for a spherical interface, of an arbitrary radius and (complex) refractive index. The theory involves finding a solution to the vector wave equation:

$$\nabla^2 \mathbf{E} = \frac{\epsilon}{c^2} \frac{\partial^2 \mathbf{E}}{\partial t^2} \tag{3.3}$$

that is appropriate for a spherical interface. The boundary conditions for the scattering problem are that the tangential components of the electric and magnetic fields ($\mathbf{E}$ and $\mathbf{H}$ respectively) are continuous across the spherical surface of the particle. A complete and thorough solution can be found in texts such as Bohren and Huffman [130], and van der Hulst [131]. The general solution for Equation 3.3 involves rewriting the Laplacian in terms of spherical polar coordinates, then expanding the incident, internal and scattered fields in terms of an infinite vector spherical harmonic expansion. At this stage, a pair of separation constants m and n (not to be confused with refractive index) appear within the equations.

[1] In a somewhat cruel twist, Lorenz arrived at the solution in 1890, 18 years prior to when Mie and Debye studied the phenomenon. However, his work was buried within a mathematical journal, undiscovered by his younger colleagues.

Applying the boundary conditions to the radial and angular components of the expanded wave yields four coefficients: a_n and b_n, which define the properties of the scattered wave, and c_n and d_n, which describe the internal fields within the spherical object. The scattered field is comprised of a superposition of the vector spherical harmonics $\mathbf{M}_n$ and $\mathbf{N}_n$, known as the electromagnetic normal modes, weighted by the appropriate scattering coefficient. Therefore, for each value of n there is a pair of modes; these are known as the *transverse magnetic* (TM), for which there is no radial component of the magnetic field, and the *transverse electric* (TE), for which there is no radial component of the electric field.

3.1.1 Scattering coefficients

Rewriting Equation 3.3 in spherical polar coordinates then separating the variables into radial and angular components yields a second order differential equation in r, the solutions to which are the spherical Bessel functions. The scattering coefficients are therefore written in terms of spherical Bessel functions, and for a dielectric sphere (which has a relative permeability $\mu_r = 1$) take the form [130]:

$$a_n = \frac{m^2 j_n(mx)[x j_n(x)]' - j_n(x)[mx j_n(mx)]'}{m^2 j_n(mx)[x h_n^{(1)}(x)]' - h_n^{(1)}(x)[mx j_n(mx)]'} \tag{3.4a}$$

$$b_n = \frac{j_n(mx)[x j_n(x)]' - j_n(x)[mx j_n(mx)]'}{j_n(mx)[x h_n^{(1)}(x)]' - h_n^{(1)}(x)[mx j_n(mx)]'} \tag{3.4b}$$

where m is the refractive contrast between the sphere (n_s) and the surrounding medium (n_m), i.e. $m = n_s/n_m$, x is the size parameter and the prime indicates differentiation with respect to the term in brackets. These coefficients are easily calculable in MATLAB, via its built in double-precision Bessel functions, and MATLAB code for calculating the scattering coefficients has been written by Mätzler [132]. The relationship between a Bessel function of the first kind, $J_{n+\frac{1}{2}}(x)$, and the corresponding spherical Bessel function, $j_n(x)$ is:

$$j_n(x) = \sqrt{\frac{\pi}{2x}} J_{n+\frac{1}{2}}(x) \tag{3.5}$$

A similar relationship holds for the Bessel function of the second kind ($Y_{n+\frac{1}{2}}(x)$), i.e.

$$y_n(x) = \sqrt{\frac{\pi}{2x}} Y_{n+\frac{1}{2}}(x) \tag{3.6}$$

The scattering coefficients also make use of the spherical Bessel function of the third kind, i.e. the spherical Hankel function, and may be determined from the spherical Bessel functions of first and second kind, *via*:

$$h_n^{(1)}(x) = j_n(x) + iy_n(x) \tag{3.7}$$

The derivatives of the spherical Bessel functions can be computed via the following recursion relation:

$$[xj_n(x)]' = xj_{n-1}(x) - nj_n(x) \tag{3.8a}$$
$$[zh_n^{(1)}(z)]' = zh_{n-1}^{(1)}(z) - nh_n^{(1)}(z) \tag{3.8b}$$

Often Equations 3.4a and 3.4b are simplified by writing them in terms of Ricatti-Bessel functions: $\psi_n(\rho) = \rho j_n(\rho)$ and $\xi_n(\rho) = \rho h_n^{(1)}(\rho)$. In this notation, the scattering coefficients take the form:

$$a_n = \frac{m\psi_n(mx)\psi_n'(x) - \psi_n(x)\psi_n'(mx)}{m\psi_n\xi_n'(x) - \xi_n(x)\psi_n'(mx)} \tag{3.9a}$$

$$b_n = \frac{\psi_n(mx)\psi_n'(x) - m\psi_n(x)\psi_n'(mx)}{\psi_n(mx)\xi_m'(x) - m\xi_n(x)\psi_n'(mx)} \tag{3.9b}$$

3.1.2 Scattering efficiencies

Now that we have the expressions for the scattering coefficients, the scattering efficiencies Q_{ext} and Q_{sca} can be calculated within Mie theory. These may be expressed as:

$$Q_{\text{ext}} = \frac{2}{x^2}\sum_{n=1}^{\infty}(2n+1)\text{Re}(a_n + b_n) \tag{3.10a}$$
$$Q_{\text{sca}} = \frac{2}{x^2}\sum_{n=1}^{\infty}(2n+1)(|a_n|^2 + |b_n|^2) \tag{3.10b}$$

and Q_{abs} follows from the definition of extinction in Equation 3.1. When calculating the efficiencies, the infinite series may be truncated after $x + 4x^{\frac{1}{3}} + 2$ terms [130, 132]. An example of Q_{ext} as a function of x for a water droplet (assuming a fixed refractive index of 1.33) is shown in Figure 3.1. The trend is apparent; there is an abrupt increase in extinction for small size parameters (owing to Rayleigh scattering). As x increases, the extinction curve undergoes a slow oscillation, tending to a limiting value of 2. The oscillation is known as the *interference structure*. This name originates from the viewpoint of extinction arising due to interference between the incident and scattered fields [130]. The optical path difference between a wave traversing the sphere, and one which bypasses it is $2a(n_s - n_m)$,

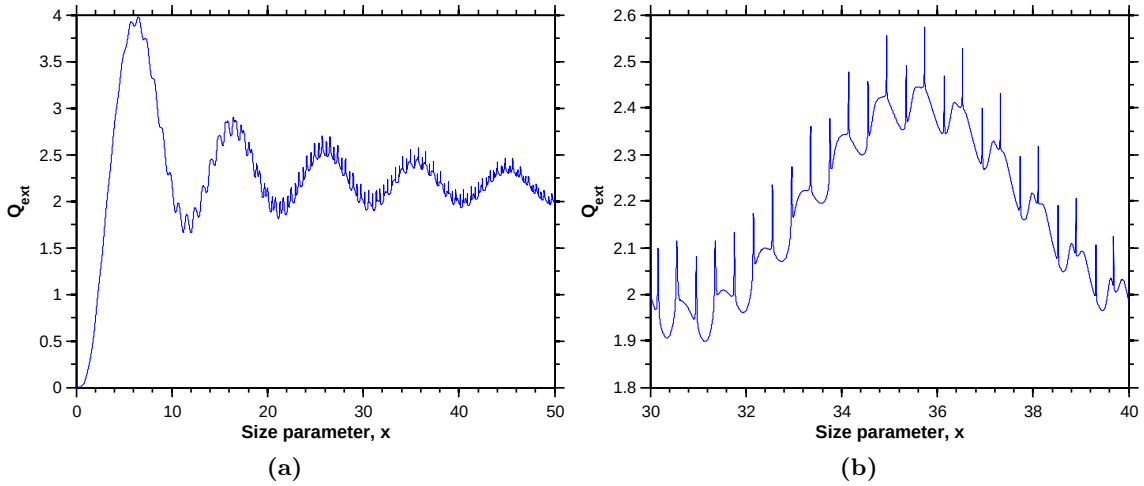

Figure 3.1: An example of an extinction curve for a water droplet in air, with a fixed refractive index contrast of $m = 1.33$. Panel (a) shows the overlying structure of the curve, including the interference structure and the limit of 2. Panel (b) shows a magnified area, highlighting the ripple structure that is imposed onto the extinction curve.

giving a phase difference of $\frac{2\pi}{\lambda}[2a(n_s - n_m)]$, i.e. $2x(m-1)$. Destructive interference will occur between the waves when the phase difference is an odd-integer multiple of π, i.e. $2x(m-1) = (2p+1)\pi$ where p is an integer. For the extinction curve considered above, the difference in x, Δx between successive maxima in the interference structure is calculated to be ~ 9.5. The above expression can also be derived by considering the asymptotic behaviour of the Riccati-Bessel functions comprising a_n and b_n, namely that $\psi_n(\rho) \sim \sin(\rho - \frac{n\pi}{2})$ for $|\rho| \gg n^2$. When this relationship is considered, it is found that the numerators of a_n and b_n both contain a common factor of $\sin[x(m-1)]$, which is independent of n, therefore the maxima in the extinction curve may be approximately located by considering the maxima in the sine function. These occur at $x(m-1) = (2p+1)\frac{\pi}{2}$, which is the same condition that a simple optical model returned.

The limit of 2 (double the prediction from geometric optics), seems counterintuitive; it suggests that a large particle can remove twice the amount of energy incident upon it. This so called "extinction paradox" is resolved by considering diffraction around the edges of the sphere. Effectively, both the physical obstruction by the sphere, and diffraction around its edges, contributes a factor of πa^2 to the extinction efficiency, with the result that the scattering efficiency is twice the geometric cross section. The paradox itself is resolved as diffraction is only observed in the far field.

Of more interest, however, is the "ripple" structure i.e. sharp spikes that are superimposed onto the slow oscillation. These are more apparent in Figure 3.1b, which shows an enlarged section of the extinction curve. A theoretical explanation for the ripple structure, proposed by van der Hulst [131], was interference between the forward scattered field, and surface

waves on the circumference of the sphere. The position of the ripples depends on both the size and refractive index of the scattering object, hence they have come to be known as *morphology dependent resonances* (MDRs).

3.1.3 Morphology Dependent Resonances

The appearance of resonances is unsurprising given the nature of the scattered wave, i.e. it is a superposition of the electromagnetic normal modes. At certain size parameters and for a given value of n, one mode will be dominant in the scattered field; under these conditions the denominator of the appropriate scattering coefficient will be a minimum. The a_n (or TM) mode is dominant when:

$$m^2 j_n(mx)[xh_n^{(1)}(x)]' - h_n^{(1)}(x)[mxj_n(mx)]' = 0 \tag{3.11}$$

Similarly, a b_n mode (TE) will be dominant when:

$$j_n(mx)[xh_n^{(1)}(x)]' - h_n^{(1)}(x)[mxj_n(mx)]' = 0 \tag{3.12}$$

i.e. MDRs are poles in the scattering coefficients. There are an infinite number of solutions to the above equations; each solution is classified by a mode *number*, which is the value of n for the resonance, and a mode *order*, l, which for now we shall describe as an integer which describes which solution of the equations we are referring to (starting with the first order, $l = 1$). Modes of increasing order are broader, to the extent that the full width half maximum of high order modes will be broader than the intermode spacing, and hence will not contribute to the extinction efficiency. A complete label of the resonance would take the form a_n^l and b_n^l, however it is more common to refer to the resonant modes by their polarization, i.e. TM_n^l and TE_n^l. For a given sphere, the frequencies which exactly satisfy Equations 3.11 and 3.12 are complex, with the modes themselves being virtual; the real part of the frequency of the poles is very close to the true resonant mode frequency, while the imaginary part of the pole frequency influences the mode's linewidth [133].

Ripple structure was considered to be "numerically insignificant for practical applications..." by van der Hulst, however it was experimentally observed by Dobbins *et al.* [134] in 1977. This experiment utilized a cloud chamber [135] to generate water droplets with a narrow size distribution, which were illuminated with a helium neon laser. The laser light transmitted through the chamber was detected on a photomultiplier tube, while light scattered at 90° was collected onto a second photomultiplier tube. The size of the droplets was varied by changing the pressure within the chamber, inducing condensation. Low level oscillation observed on the measured signal transmitted through the chamber (as the pressure was varied) was attributed to ripple structure.

Clearly, the observation of MDRs will be difficult for systems with multiple particles (owing to the range of particle sizes), so single particle traps (such as Ashkin's optical levitation experiment [17]) offer benefits for investigating light scattering. This levitation experiment was enhanced in 1977 [19] by introducing an electronic feedback to the laser, which altered the power of the laser (and therefore the height at which a droplet was levitated). This feedback system affords a method for sensitive force measurements, for if the particle's position is perturbed by an external force (for instance, by applying an external field to a charged droplet) then the optical power required to restore equilibrium will be indicative of the force acting on the droplet. It therefore stands to reason that any ripple structure that arises due to dominant modes within scattering should be detectable via this optical levitation experiment. An efficiency for radiation pressure can be defined as $Q_{\mathrm{pr}} = Q_{\mathrm{ext}} - Q_{\mathrm{sca}}\langle\cos\theta\rangle$ [130], where the term $\langle\cos\theta\rangle$ is known as the *asymmetry parameter* and is the average cosine of the scattering angle. Clearly, any ripple structure in the extinction curve will also appear in the radiation pressure curve (recall that Q_{sca} is also defined in terms of the scattering coefficients). Ashkin and Dziedzic [20] investigated this experimentally in 1977, by using a tunable dye laser to scan across size parameters of the droplet under study, and noting the laser power that was required to keep a droplet levitated at a fixed height. Clear resonances were observed in the trapping power, which agreed well with predictions from Mie theory. A further experimental verification within their work was carried out by adjusting the position of the droplet within the beam such that it was near to the focus of the laser (i.e. all of the laser radiation passes through the droplet, and hence cannot be considered as illuminated by plane waves). Under these conditions, no resonances were observed as the wavelength of the laser was scanned. This suggested that edge illumination causes significant numbers of surface waves to propagate around the circumference of the droplet, with the droplet itself functioning as a low-loss optical cavity. A later study directly observed ripple structure in both the near- and farfield backscatter, as well as at 90° [21]. Using these experimental measurements, a theoretical study by Chýlek *et al.* [136] confirmed that the sharp modes were caused by partial wave resonances; furthermore they concluded that first order ($l = 1$) resonances are so narrow that they do not contribute significantly to the radiation pressure and hence were not detected experimentally. A further observation within Chýlek's study was the effect of increasing absorption (quantified by the imaginary part of the refractive index) on the mode structure of a droplet. Increased absorption broadens the resonant modes and decreases their intensity, with the effect being most significant for first order modes. This effect is nicely illustrated on p302 of Bohren and Huffman. A physical interpretation of this is that absorption introduces an additional loss term, which significantly decreases the relevant quality factor of the resonator. This shall be discussed in the next section.

3.2 Spherical particles as optical microcavities

The preceding discussion has introduced the concept of MDRs, however it has lacked a physical interpretation of *why* ripple structure appears in an extinction curve. It was alluded that a droplet can act as an optical cavity in the previous section; this section shall elaborate on this discussion as it plays a significant role in the experimental data presented in Chapter 4, as well as providing a much more physically intuitive picture for the presence of MDRs.

Initially, a discussion of a simple étalon/linear optical cavity will be provided, as there are many useful analogies that can be drawn between the transmission properties of said cavities and their spherical analogues. This then shall lead into a discussion of some of the terminology specific to spherical microcavities, and demonstrate how their resonant modes can be predicted from Mie theory. Finally, an introduction to how this mode structure can be used to determine the radius of a droplet with high precision, as postulated by Ashkin and Dziedzic [20], will be provided.

3.2.1 A Fabry-Pérot optical resonator

Consider a simple example of a Fabry-Pérot optical resonator: a material of thickness L and refractive index n, with a reflectivity of R. A practical realization of this would be a glass coverslip, such as the ones used to make sample chambers described in Section 2.3.5 (thickness 0.15 mm). White light, such as that from the microscope illumination, which is transmitted through this coverslip and focused into a spectrometer will be found to have an oscillating intensity owing to interference effects within the glass. A simple wave picture would suggest that constructive interference will occur when a integer number of half-wavelengths exist between the two surfaces of the coverslip, i.e.: $q\lambda/2n = L$, assuming there is no phase shift due the reflection at the glass/air interface, which is the case for normal incidence. The frequencies that can be supported within the étalon are therefore $\nu_q = qc/2L$, where c is the speed of light. The *free spectral range* is defined as $\nu_{q+1} - \nu_q$ and is equal to $c/2L$. In the context of a linear laser cavity, these frequencies would be referred to as the *longitudinal modes* of the resonator. A more detailed analysis considers the behaviour of a ray incident upon the étalon at an angle θ [137]. A fraction of the ray will be reflected upon hitting the air/glass interface, with the remaining light undergoing refraction and transmission through the glass. Upon hitting the glass/air interface, again most of the light will be transmitted, while some undergoes reflection. This reflected light will then also reflect/transmit through the coverslip, interfering with the incident rays. The

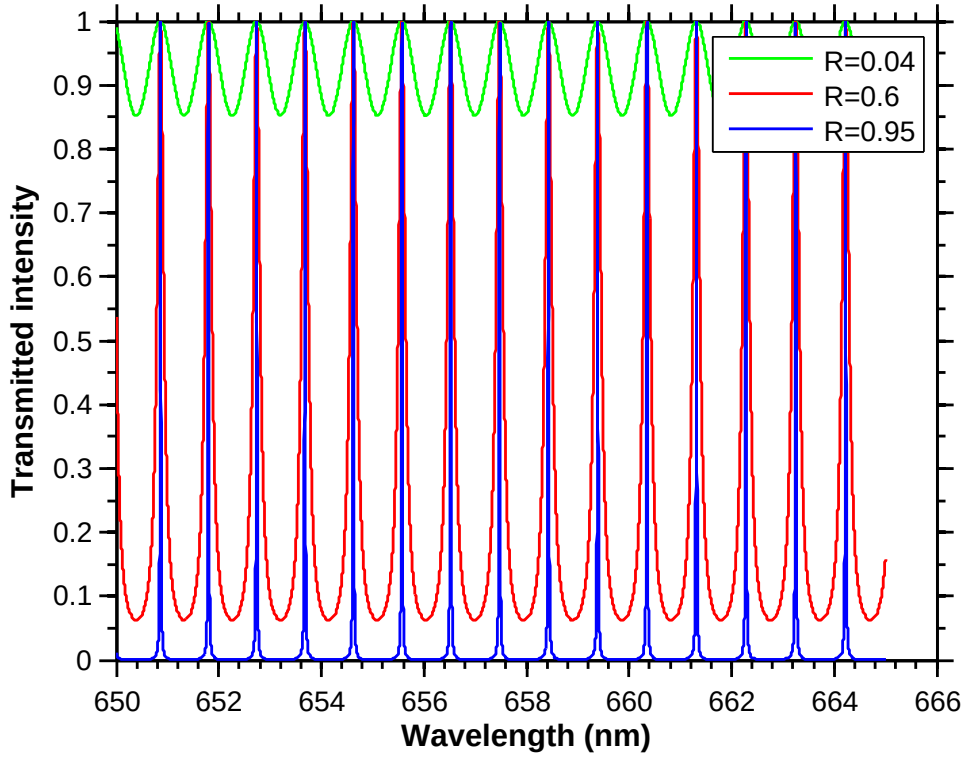

Figure 3.2: A plot of the transmission of a thin (0.15 mm) glass coverslip for various reflectivities. The green line corresponds to the normal case of a $\sim 4\%$ reflective surface. The red and the blue lines show the effect of increasing the reflectivity to 60% and 95% respectively.

phase shift due to the coverslip is:

$$\delta = \left(\frac{2\pi}{\lambda}\right) 2nL\cos\theta \tag{3.13}$$

By summing the contributions from all the waves, it can be shown that the transmitted intensity is given by [137]:

$$T = \frac{1}{1 - F\sin^2\left(\frac{\delta}{2}\right)} \tag{3.14a}$$

$$F = \frac{4R}{(1-R)^2} \tag{3.14b}$$

The factor F is known as the *finesse* of the etalon. A plot of this transmission function is shown in Figure 3.2 for an étalon of thickness 0.15 mm and for three different values of the reflectivity (at normal incidence). The first (green) line corresponds to the normal case of an air/glass interface having a roughly 4% reflectivity. The red and the blue lines show the effect of increasing the reflectivity; the modes sharpen and narrow upon increasing reflectivity. This behaviour may be quantified by defining a *quality factor*, Q, for the

resonator:

$$Q = \frac{\nu}{\delta\nu} \tag{3.15}$$

The quality factor and the finesse are related via the free spectral range of the étalon:

$$Q = F\frac{\nu}{\mathrm{FSR}} \tag{3.16}$$

Therefore, by increasing the reflectivity of the surfaces comprising the étalon, the finesse increases, and therefore Q increases. Furthermore, lengthening the étalon will decrease the FSR of the mode structure, hence leading to an increase in Q.

3.2.2 Whispering Gallery Modes

A famous feature of St Paul's Cathedral in London is the whispering gallery, located within the dome. It gained its name owing to the remarkable feature that a whisper at one part of the gallery could be clearly heard at any other location around the circumference. Lord Rayleigh investigated this phenomenon, providing a mathematical framework for the propagation of sound waves around the gallery [138]. The optical analogue of these acoustic standing waves are the morphology dependent resonances, also termed *whispering gallery modes* (WGMs). Physically, WGMs may be envisaged as rays that are confined to the surface of a sphere by multiple total internal reflections around the circumference. The condition for constructive interference will therefore be that an integer number q of wavelengths must be contained within the circumference of the sphere, i.e.

$$q\frac{\lambda}{n_s} = 2\pi a \tag{3.17}$$

For a sphere of size parameter x, the value of n for a first order ($l = 1$) resonance is approximately $n_s x$ [139] and so the integer q in the above equation may be interpreted as the mode number n. As was the case with MDRs, for a given n there is a pair of WGMs (TE and TM). Within this physical model of a WGM resonance, these modes will not occur at the same wavelength/frequency, owing to the (complex) phase shift associated with total internal reflection. The mode order, l, describes the degree of radial penetration of the WGM (with low order modes being the most confined to the surface). Each WGM has a $2n + 1$ azimuthal degeneracy. This is usually denoted m, and should not be confused with the refractive index contrast defined previously. Any mention of m in this and subsequent chapters should be interpreted as the refractive index contrast, unless otherwise stated.

A WGM has a Lorentzian lineshape; a quality factor Q for a given resonance may be calculated from knowledge of the mode's frequency, ν, and its full width half maximum (FWHM), $\delta\nu$ using Equation 3.15. The value of Q associated with a WGM resonance

defines the lifetime of a photon confined to the surface of the sphere, and may be expressed as [133]:

$$Q = \frac{2\pi \times \text{Energy stored}}{\text{Energy lost per cycle}} \tag{3.18}$$

By analogy with the Fabry-Perot etalon above, a larger sphere will return a larger value of Q owing to the longer optical pathlength. Q is also known to increase with increasing mode number and decrease with increasing mode order [140]. A TE mode exhibits a higher value of Q than a TM mode (attributed to a higher coefficient for total internal reflections, leading to fewer losses per round trip). This may seem initially surprising, as the reflectivity of a total internal reflection event would be equal to 1 when calculated from the Fresnel equations (noting that $R = r^*r$; above the critical angle the Fresnel reflection coefficients are complex) and the resulting evanescent wave carries no power into the second medium. This is only true for a planar interface; for a curved interface such as reflection at a sphere, there will always be some leakage of light into the second medium, as shown by a rigorous ray tracing approach by Ioppolo *et al.* [141]. Theoretical Q values can be very large indeed (e.g. Datsyuk quotes a theoretical Q of 10^{73} [142]) but are experimentally limited to a maximum of $10^8 - 10^9$ [143]. These high Q resonators are of extremely high surface quality and of near perfect spherical form, with very few absorption losses. To put these values in context, typical values of Q for optically trapped aerosol droplets are on the order of $10^3 - 10^4$ [144].

Two examples of WGM spectra are given in Figure 3.3; the left hand figure was taken from an optically trapped salt water droplet of diameter 9.21 µm, with WGMs visible within the Raman scattered light from the water molecules within the droplet. This shall be discussed further in Chapter 4. The right hand figure is a fluorescence spectrum taken from a dye doped polystyrene microsphere (Duke Scientific, 36-3), with a diameter of 10.9 µm and pumped with 532 nm radiation. Again, WGM resonances are visible within the fluorescent emission; these are considerably broader than the salt water droplet due to the lower Q for the resonator. The reason for this is two fold—surface tension will naturally give droplets a more perfect spherical form compared to a manufactured solid microsphere, while the refractive index contrast of the microsphere is lower than that of a droplet (~ 1.2 and 1.33 respectively).

To illustrate the variation in Q between modes of different polarisation, consider the fluorescence spectrum of Figure 3.3b, which has been assigned by the method discussed later. Q for these modes can be determined by fitting a Lorentzian profile to the spectral profile to determine the central wavelength and FWHM, then utilizing Equation 3.15. As a representative, the value of Q for the TM_{83} mode is 2117 ± 68, while for the TE_{83} it is 2408 ± 98, clearly demonstrating the increase in Q for a TE mode.

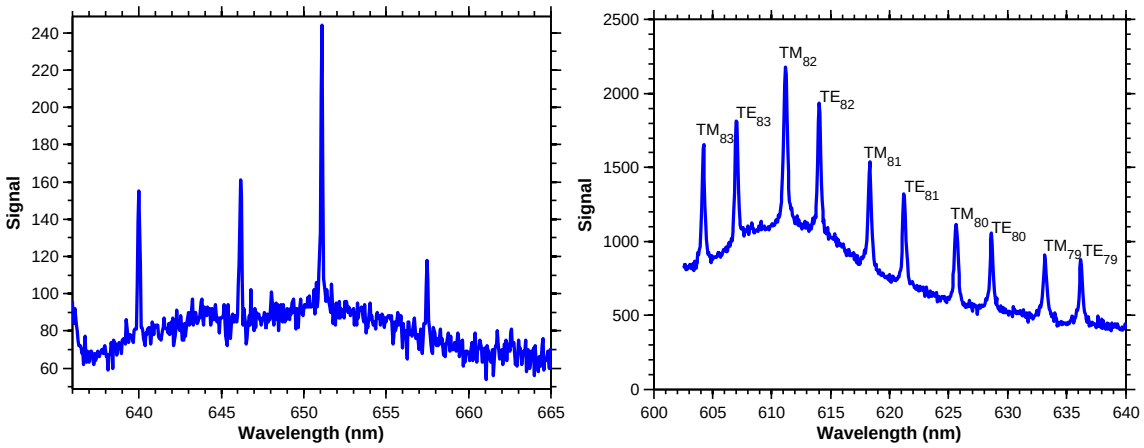

(a) Salt water droplet **(b)** Fluorescent polystyrene sphere

Figure 3.3: Two examples of whispering gallery modes. Figure 3.3a is the Raman emission from an optically trapped salt water droplet. Figure 3.3b is the fluorescence from a dye doped polystyrene microsphere. WGMs are visible in both spectra as local, sharp maxima imposed upon the smooth background emission.

3.2.3 Scattering vs emission

The description of Mie scattering theory, and MDRs in Section 3.1.3 refers to the scattering of a plane wave from a spherical microparticle, with the resulting field being a superposition of the incident and scattered waves. However, the spectra shown in Figure 3.3a are due to emission from *within* a spherical microcavity, with mode structure attributed to WGMs within the sphere. Although these are fundamentally different problems, the physics underlying them is similar. A physical interpretation is that when the molecules emit radiation, some of it will necessarily be coupled into a WGM. Furthermore, the radiation confined in the WGM can stimulate emission at those wavelengths, further increasing the measured signal (see the discussion on *stimulated Raman scattering* in Section 4.4).

Chew [145, 146] has provided theoretical expressions on the transition rates and lifetimes of atoms near spherical surfaces. Consider the power radiated by a dipole $\mathbf{p}$ located at a radial coordinate $\mathbf{r}'$ within a sphere. For radial oscillations of the dipole, the transition rate R (normalized to the transition rate in the absence of a sphere, R_0), which has been rewritten to match the notation given earlier in this chapter, is given by:

$$\frac{R^{\perp}}{R_0^{\perp}} = \frac{3}{2}\frac{n_s n_m^3}{x^2}\sum_{n=0}^{\infty} n(n+1)\times(2n+1)\frac{j_n^2(y_1)}{y_1^2|D_n|^2} \tag{3.19}$$

and for tangential oscillations:

$$\frac{R^{\parallel}}{R_0^{\parallel}} = \frac{3}{4}\frac{n_s n_m^3}{x^2}\sum_{n=0}^{\infty}(2n+1)\times\left(\left|\frac{[y_1 j_n(y_1)]'}{y_1 D_n}\right| + \frac{\mu_m\mu_s}{\epsilon_m\epsilon_s}\frac{j_n^2(y_1)}{y_1^2|D_n'|^2}\right) \tag{3.20}$$

where $y_1 = n_s kr'$, ϵ_m and ϵ_s are the relative permittivities of the medium and the sphere respectively, μ_m and μ_s are the relative permabilities and k is the wavenumber in a vacuum. The factors D_n and D'_n [146], again rewritten to match the earlier notation, are:

$$D_n = n_s^2 j_n(mx)[xh_n^{(1)}(x)]' - n_m^2 h_n^{(1)}(x)[mxj_n(mx)]' \tag{3.21a}$$

$$D'_n = j_n(mx)[xh_n^{(1)}(x)]' - h_n^{(1)}(x)[mxj_n(mx)]' \tag{3.21b}$$

Upon inspection of the factors D_n and D'_n, it is clear that they are identical to the denominators of the scattering coefficients a_n and b_n. This is as expected; the resonance modes should be the same in both theories. Therefore, one is able to make use of the poles of the scattering coefficients as determined from Mie theory to determine the theoretical location of a WGM resonance. Owing to their explicit dependence on the size of the particles, WGMs afford a very accurate method of sizing microparticles (± 1 nm). The next section shall describe how to make such accurate measurements of a particle's size, by utilizing experimentally collected WGM spectra and comparing them to theoretically generated spectra of known input parameters. Their explicit sensitivity to their surroundings also suggests their use as sensors, e.g. *in vitro* biosensing [147].

3.3 Assignment of Whispering Gallery Mode spectra

Having discussed the basic principles of Mie scattering theory, MDRs and their link with WGMs, this section shall now discuss how to assign a WGM spectrum. Here, the term "assignment" means determining the mode number n and mode order l of the resonances, the polarization (TE/TM) of the resonance and hence, the sphere radius and refractive index contrast.

3.3.1 Determining the location of the resonances

The first step of the assignment procedure is to calculate a theoretical WGM spectrum, i.e. determining the location of the resonances of the scattering coefficients in size parameter space. The scattering coefficients are complex parameters; at a size parameter associated with an MDR the real part of the scattering coefficient is equal to one, while the imaginary component equals zero. Thus, to then determine the location of the resonances, it is necessary to solve for the imaginary part of Equations 3.11 and 3.12.

The general procedure adopted for this is as follows. First of all, the real part of the scattering coefficient for a given range of values of size parameter (x), mode number (n) and (complex) refractive index contrast (m) are calculated, for instance as plotted in Figure 3.4.

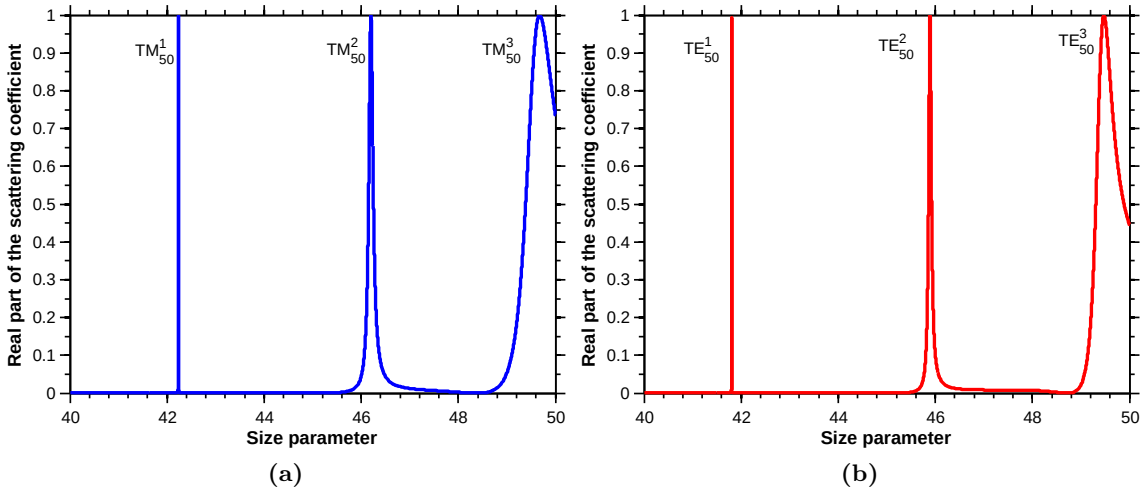

Figure 3.4: A plot of the real part of the scattering coefficients a_{50} and b_{50}, demonstrating the poles in the scattering coefficients at a given size parameter associated with an MDR.

It is clear from this figure that higher order resonances are broader. A simple peak detecting algorithm[2] is used to coarsely determine the location of the first order (and second order, if the spectrum under consideration obviously has second order modes) resonances. A MATLAB script (fzerotx.m) is used to numerically solve the imaginary Equations 3.11 and 3.12 for size parameter, x. The end result is the determination of the location (in size parameter space) of the TE and TM modes for a given refractive index contrast.

3.3.2 Fitting the experimental wavelengths

Having determined the locations of MDRs in size parameter space, the next stage is to match the theoretical resonances to the experimentally measured WGM spectrum, which will thus determine the size of the sphere and therefore give an assignment of the modes observed. The first step is to define the location of the experimental resonance. One way to define these would be to note the most intense pixels recorded on the spectrometer's CCD (see experimental discussion in Chapter 4) for each mode. However, a preferable method would be to fit an appropriate function to the experimental spectrum (subtracting any background signal where necessary) and utilize the central wavelength from this fit as the location of the resonance. The WGMs have a Lorentzian lineshape, whereas the spectrometer's response function will return a lineshape that is approximately Gaussian. Strictly speaking, a Voigt profile with a fixed Gaussian width should be used to fit the resonances. However, if the width of the resonances is narrower than that of the spectrometer's resolution (as is the case for first order resonances in a salt water droplet of diameter $\sim$10 µm) then it is acceptable to fit a simple Gaussian function to the modes.

[2] http://www.billauer.co.il/peakdet.html

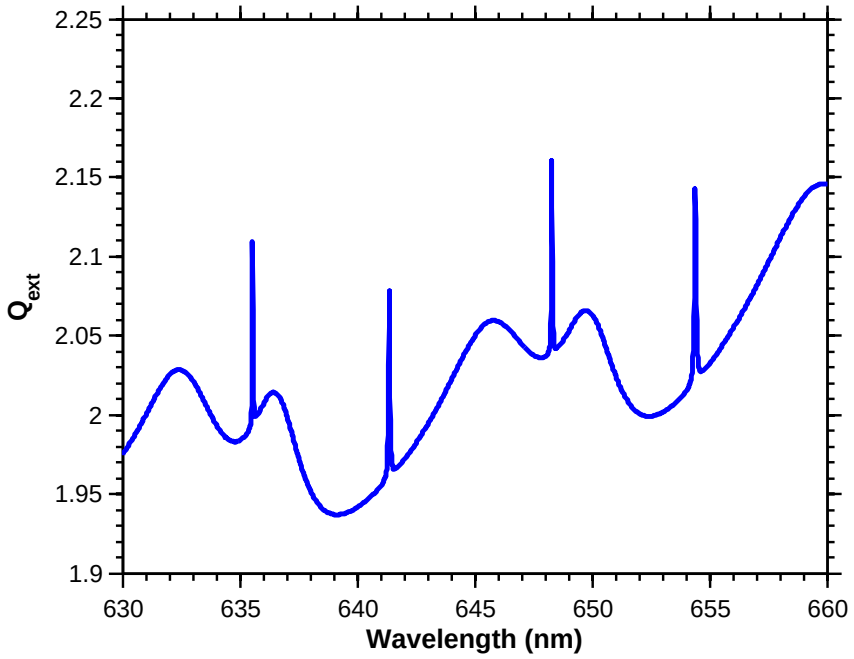

Figure 3.5: Theoretical scattering efficiency for an 8 µm diameter salt water droplet in air, with a salt concentration of $20\,\mathrm{g\,L^{-1}}$.

By considering the wavelength spacing between two adjacent modes of the same polarization (i.e. an effective free spectral range), an initial estimate of the radius can be determined [139, 148]:

$$\Delta\lambda = \frac{\lambda^2 \tan^{-1}[(n_s/n_m)^2 - 1]^{\frac{1}{2}}}{2\pi a n_m [(n_s/n_m)^2 - 1]^{\frac{1}{2}}} \tag{3.22}$$

However, by using theoretically generated spectra (with an exactly defined radius/diameter as the input), it was found that this equation overestimates the size of the sphere. For example, consider the extinction curve, plotted in Figure 3.5. This is a simulated extinction curve for an 8 µm diameter salt water droplet, with a salt concentration of $20\,\mathrm{g\,L^{-1}}$. Dispersion in the refractive index is accounted for by explicitly calculating the refractive index at each wavelength, using the dispersion relationship of Quan and Fry [149],[3] and then using that value for the refractive index when calculating the scattering coefficients that appear in Equation 3.10a. Using Equation 3.22 to determine the size of the droplet yields a diameter of 8.263 µm, $\sim 3\%$ larger than the true value of 8 µm, hence the equation is utilized to provide an initial guess (and upper limit) from which to more accurately determine the radius/diameter. At this point, it is noted that while most equations are written in terms of the radius, it can be more intuitive to think in terms of the particle diameter, hence from here on all references to the particle size shall be to the diameter of a sphere, unless otherwise stated. From this initial guess, a suitable range of "guess" particle

[3] This relationship will be quoted in Chapter 4.

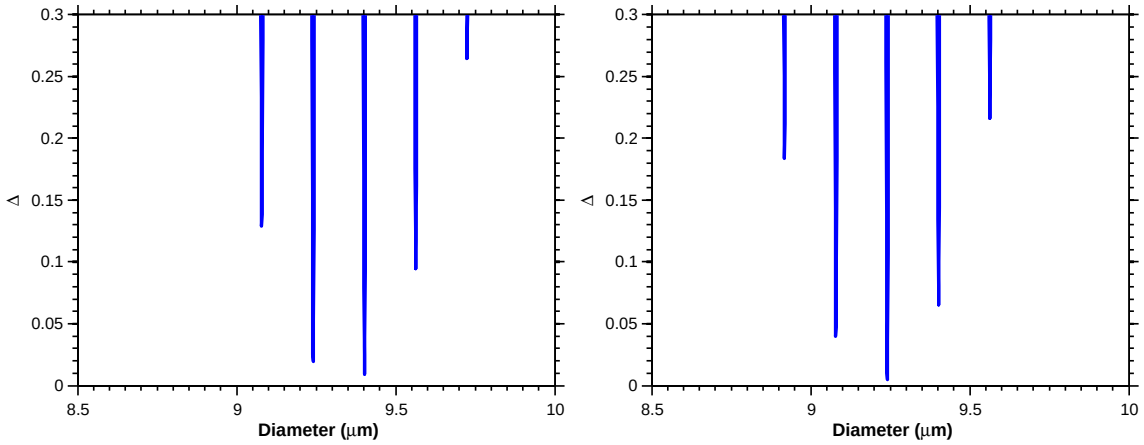

(a) Result from fitting theoretical modes for a fixed refractive index

(b) Result when correcting for refractive index dispersion, clearly showing a less ambiguity in the minimum value of Δ.

Figure 3.6: The result of matching theoretical resonance wavelengths (calculated for a $40\,\mathrm{g\,L^{-1}}$ salt solution) to the experimental spectrum shown in Figure 3.3a, using Equation 3.23.

diameters are determined, and for each of these diameters, use Equation 3.2 (rewritten in the form $x = \pi d/\lambda$) to convert the theoretical resonances calculated earlier from size parameter space into theoretical resonance wavelengths. These theoretical wavelengths are then compared to to the experimentally measured resonance wavelengths (for instance, defined as the central wavelength of the Gaussian fit to each peak in the WGM spectrum) and, provided that a diameter guess will give the correct number of resonances within the experimental range, a residual Δ for that diameter is defined:

$$\Delta = \sum (\lambda_{\mathrm{expt}} - \lambda_{\mathrm{theory}})^2 \tag{3.23}$$

A typical example of this is shown in Figure 3.6a, with reference to the experimental spectrum shown in Figure 3.3a. It is clear from the figure that there are several local minima in the assigned diameter, so care must be taken to ensure that the correct diameter is chosen. Indeed, it is not necessarily the case that the diameter with the lowest associated value of Δ will be the correct value for the diameter, as the theoretical resonances are determined for a fixed wavelength, whereas in reality there will be a variation in the refractive index of the sphere across the relevant emission/scattering band owing to dispersion. This point is best illustrated via a simulation.

Consider again the extinction curve in Figure 3.5 (which took refractive index dispersion into account). Initial fitting of the peaks using the method above would suggest that the best fit diameter is 8.162 µm, rather than the true 8 µm that was used for the input of the simulation, i.e. failure to account for refractive index dispersion will result in oversizing the

sphere. It would be computationally exhausting to recalculate the scattering coefficients for each measured wavelength (and hence refractive index); fortunately there is a simple solution that exploits the fact that the refractive index varies approximately linearly with wavelength over the range considered. Specifically, a linear relationship implies that:

$$\frac{\lambda_{\text{theory}}}{m_{\text{theory}}} = \frac{\lambda_{\text{cor}}}{m_{\text{cor}}} \tag{3.24}$$

where λ_{theory} is the theoretical wavelength returned from Equation 3.2, m_{theory} is the refractive index that was used in the initial calculation of the scattering coefficients, m_{cor} is the refractive index at the experimentally determined resonance wavelength, calculated using an appropriate dispersion relation, and λ_{cor} is the resulting theoretical wavelength that is corrected for refractive index dispersion. Applying these corrected wavelengths to the residual defined in Equation 3.23 results in a plot such as Figure 3.6b. Now there is much less ambiguity in which diameter provides the best fit; furthermore testing this algorithm with the simulated extinction curve returns the exact input diameter of 8 µm.

This initial stage will return the diameter of the sphere, from which the mode number, order and polarization of the resonances can be inferred. However, refractive index has still not been explicitly accounted for; although a refractive index was specified as an input for the fitting programme (in order to generate the theoretical MDR resonances), there are situations where the refractive index of the sphere will not be known. For example, salt water aerosol droplets will have a refractive index that depends on the concentration of sodium chloride present. As shall be discussed in the next chapter, aerosol droplets will change their composition (i.e. grow/shrink) in order to maintain thermodynamic equilibrium with the surrounding environment; therefore as the diameter of the droplet increases/decreases due to condensation/evaporation, the salt concentration (and hence refractive index) of the droplet will decrease/increase respectively. To give a quantitative idea of how the salt concentration affects the refractive index, a difference in salt concentration of $1\,\text{g}\,\text{L}^{-1}$ will result in a difference in refractive index of 2×10^{-4}.

Of course, one solution to determining the refractive index of a droplet would be to simply recalculate all of the theoretical resonances for a range of refractive indices, and determine which refractive index generates a theoretical spectrum that best matches the experimental data. The computational time required to achieve this fitting is greatly reduced if one precalculates the necessary resonances for each refractive index, and saves the values to be read into MATLAB at a later stage. While asymptotic formulae for the positions of the resonance exist [150], the highest accuracy will be obtained from directly solving Equations 3.11 and 3.12.

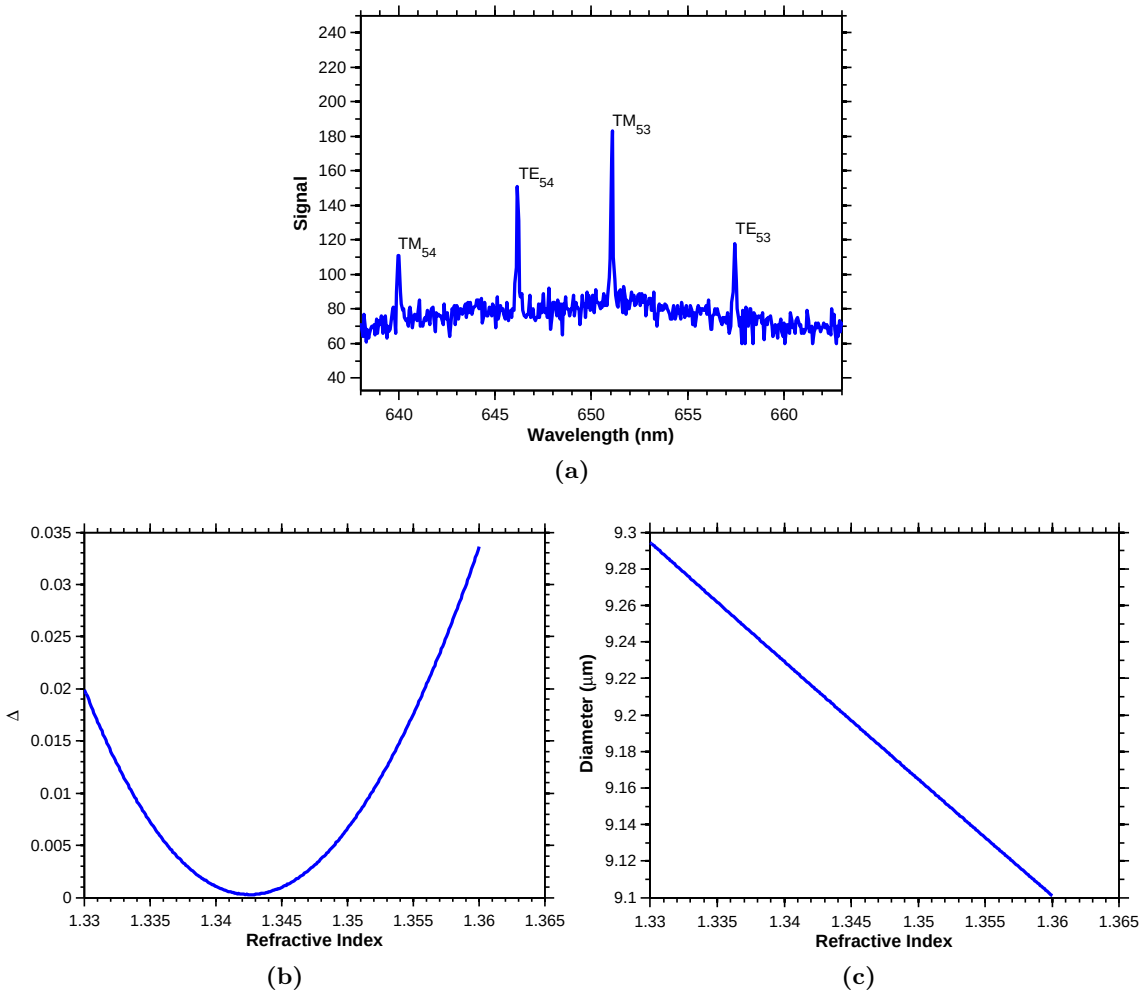

Figure 3.7: An assigned Raman spectrum of a salt water droplet, and the result of fitting the refractive index.

As an example, consider the data presented in Figure 3.7. The spectrum presented was obtained from a droplet generated from a bulk salt water solution of concentration $40\,\mathrm{g\,L^{-1}}$ and was assigned using the method described above. The refractive index is assigned by looping through the various precalulated resonances, as determined by solving Equations 3.11 and 3.12 for refractive indices in the range 1.33–1.36, in 0.0001 increments. The resulting values of Δ are presented in Figure 3.7b, alongside the corresponding best fit diameter in Figure 3.7c. In this instance, the best fit refractive index was 1.3424, and the best fit diameter was therefore 9.2136 µm. This refractive index corresponds to a salt concentration of $63\,\mathrm{g\,L^{-1}}$. This technique shall be utilized significantly in Chapter 4.

3.4 Outlook

This chapter has provided a basic outline of the spectroscopy of microparticles, with an emphasis on the observation of whispering gallery modes within particles, and the use of Mie scattering to assign these resonances and hence determine the size and refractive index of the particle under question. This technique will be put to significant use in the next chapter, which is focused on the study of optically trapped aerosol droplets using cavity enhanced Raman spectroscopy.

Chapter 4

Spectroscopic studies of optically trapped aqueous aerosol droplets

This chapter will apply the concept of WGMs established in the previous chapter to the study of aqueous aerosol droplets. The optical tweezers are used to capture individual aerosol particles, and their growth dynamics interrogated using cavity enhanced Raman spectroscopy. WGM resonances are clearly visible within the OH stretching band of the droplet's Raman spectrum. In addition, differences between trapping an aerosol with a conventional Gaussian beam, and using a Laguerre-Gaussian/vortex beam (Section 2.5.4) are investigated. In both cases, resonant and non-resonant heating effects are observed.

4.1 Why study aerosols?

Aerosols may be defined as a multiphase system, comprising solid or liquid particles suspended in a gaseous medium. They play an important role in many aspects of science, hence it is crucial that they are studied in detail so that their impact within the various fields can be predicted. For instance, aerosol technology plays an important role in drug delivery [151], although perhaps the most relevant contemporary field in which knowledge of aerosols play a role is that of atmospheric physics and chemistry. For example, aerosols serve as a vessel or surface in/on which heterogeneous chemical reactions can occur within the atmosphere [152]. The role that aerosols play in climate change is potentially vast; for example their scattering and absorption properties will have a direct effect on the amount of radiation incident upon the surface of the earth, but they can also have an indirect effect by influencing the properties of clouds and the albedo [153]. Studying aerosol droplets is of interest, as knowledge of their size and composition dependent optical properties (such as the refractive index) is an important consideration in models of climate change [154];

these parameters are necessary to model the absorption and scattering of radiation by the aerosol. Traditionally, aerosols have been studied in the bulk phase, using techniques such as LIDAR [155], while more recently cavity-ring down spectroscopy (CRDS) has been utilized to directly measure the extinction properties of aerosols [156]. Typically these use a single frequency of radiation, and measure a range of size parameters by utilizing a polydisperse sample, although very recent measurements have investigated the scope for the technique to obtain information about the wavelength dependent scattering properties by using a monodisperse sample with a scannable laser source [157]. However, it is of interest to study the dynamics of single aerosol particles, rather than relying on ensemble averaging techniques, owing to the greater quantity of information that can be obtained (and with higher accuracy). To probe the dynamics of single aerosol particles, techniques that can isolate a single droplet from its surroundings are required. Optical manipulation techniques (whether of the single beam gradient force trap, counterpropagating beams trap or optical levitation) are ideally suited towards this goal [158, 159]; practical features of tweezing aerosols shall be discussed in Section 4.2. Prior to the widespread use of aerosol optical tweezers, electrostatic levitation (in a similar fashion to the Millikan experiment) was a commonly used technique to isolate individual droplets [160], however an obvious disadvantage to this technique is the requirement that the aerosol acquire a charge prior to levitation [161].

Aerosols are classified by their size distribution. Particles with radii less than 0.05 µm are known as *nucleation mode* aerosols. Those with a size range between 0.05 µm to 1 µm are known as *accumulation mode*, while those with a radius greater than 1 µm are known as *coarse mode*. Accumulation mode aerosols are of most interest, due to their dominance in the atmosphere [162]. Considerable progress has been made in utilizing CRDS to interrogate bulk volumes of accumulation mode aerosols [154, 157]. However, these are difficult to capture and interrogate with conventional optical trapping techniques. Sub-micron droplets can be optically guided using a Bessel beam [163], while counter-propagating Bessel beams can be utilized to confine droplets and probe them using elastic light scattering [164], with optical characterisation recently demonstrated for accumulation mode particles [165]. Dear *et al.* have experimentally demonstrated that it is possible to trap smaller droplets ($a > 0.5\,\mu m$) with single beam gradient force traps by utilizing an annular beam, which was realised by simply blocking the central core of a Gaussian beam [166]. Furthermore, they also reported an increase in the axial:lateral trap stiffness ratio when compared to Gaussian trapping. These observations are in excellent agreement with theoretical predictions by Burnham and McGloin [167].

While this section has predominantly focused on contemporary interest in aerosols within other disciplines, from a purely physical viewpoint aerosols are interesting to study as they form easily reconfigurable microcavities. As shall be explained in Section 4.3, the size

of the aerosol can be controlled by adjusting the local relative humidity. Changing the morphology in this fashion would be the microcavity equivalent of scanning a linear optical cavity *via* a piezoelectric transducer on one of the cavity mirrors. This chapter shall focus on the dynamic response of droplets to changes in the beam geometry and power of the trapping laser, specifically with respect to droplet heating mechanisms (both resonant, and non-resonant). Initially, the focus shall be on the use of Gaussian beams, as the majority of previous measurements reported in the literature were performed under those conditions (e.g. [158]) . The SLM shall then be utilized to change the trapping laser to an LG mode, to determine how the microcavity responds to these changes in trapping and excitation geometry.

4.2 General considerations for optically trapping aerosols

The optical trapping of aerosol particles is rather different to trapping in an aqueous medium (as is the case with conventional colloidal samples). The first obvious difference is that the surrounding medium is air, therefore an optically trapped aerosol particle can constitute an underdamped system. This has important consequences for force measurements and other experiments which measure the dynamics of optically trapped aerosols [83]. Another consequence of the surrounding medium being air is that, due to the refractive index mismatch between a glass coverslip ($n \sim 1.5$ for borosilicate glass) and air ($n \sim 1$), the critical angle at the interface is $\sim 42°$. Any incident rays at an angle greater than this will be reflected at the interface, this means that the numerical aperture of the objective lens is effectively limited to 1, therefore weakening the gradient force relative to the scattering force [95].

The art of trapping in air is very different from trapping in aqueous media. In the latter situation, it is relatively easy to seek out and trap the particles of interest by moving either the trap (with steering mirrors) or the sample itself. As water is more viscous than air, the distance over which the particles will diffuse in a given time interval is comparitively small,[1] allowing a somewhat active method to trap particles. To tweeze particles in air, the trap itself must be held stationary, while aerosols are introduced into the trapping cell. This makes trapping in air a much more passive (and often quite laborious) process. As a consequence of this, the fog of aerosols will settle onto the lower surface of the trapping chamber. These would form small droplets, which would impart severe aberrations onto the trapping beam (as well as distorting the image of the trapped particle). To minimize this negative beading, the coverslips which form the lower surface of the trapping chamber are soaked in a solution of 50% Decon 90 for at least one week [108]. Before being used, they are thoroughly rinsed with Milli-Q water, then carefully dried using a piece of lens

[1] The mean square displacement, $\langle x^2 \rangle$, is related to the diffusion coefficient by $\langle x^2 \rangle = 2Dt$. The diffusion coefficient is inversely proportional to the solvent viscosity (Stokes-Einstein relationship).

tissue. This treatment increases the hydrophilicity of the glass, which will result in droplets spreading out into a thin layer when they settle on the surface.

In this chapter, aerosols are generated using a handheld medical nebulizer (Omron, U22 Micro A-I-R) with a custom manufactured glass nozzle. This nozzle serves two purposes; it aids conditioning of the aerosol droplets but also focuses the stream, to allow the aerosols to be introduced to the sample chamber [95]. Other common techniques utilized to generate aerosols include the use of vibrating orifice aerosol generators [168], and ultrasonic nebulizers [169]. The solutions nebulized are aqueous sodium chloride, henceforth referred to as salt water. The concentrations of bulk solution varied depending on the specific experiment performed, but varied from $20\,\mathrm{g\,L^{-1}}$ to $80\,\mathrm{g\,L^{-1}}$. Salt water is utilized as the salt lowers the vapour pressure of the droplet, allowing it to achieve equilibrium at relative humidities lower than 100% (as shall be discussed more thoroughly in Section 4.3). The relative humidity is defined as:

$$\mathrm{RH} = 100 \times \frac{p}{p^{\circ}} \tag{4.1}$$

where p is the partial vapour pressure of atmospheric water vapour, and p° is the saturated vapour pressure at that temperature. The majority of the experiments in this thesis utilize a very basic aerosol chamber, consisting of a rubber O-ring with a small section of its circumference removed, adhered to a circular coverslip, 30 mm in diameter and of no. 1 thickness (VWR, ECN 631-1585). A second circular coverslip is applied (with immersion oil) to the microscope objective (which has been treated with surfactant, as discussed above), and the cell is placed on top. Although crude, this type of chamber provides protection from local air currents in the laboratory, as well as providing a region where a high concentration of aerosols can be contained (to aid trapping, and growth of droplets). Compared to the outside lab air, the relative humidity will be greater within this chamber owing to the layer of water that settles on the surface of the cell. When working with aqueous aerosols, a piece of moist tissue (soaked in deionised water) is inserted into the cell, to further increase the local relative humidity.

Experimentally, optically trapped aerosol droplets show many interesting properties that are somewhat counterintuitive. For example, the size of droplet that can be trapped shows a linear dependence upon the trapping power [159]. However, simply increasing the trapping power does not increase the ease with which a droplet can be trapped; in fact stable trapping is not possible with high powers [170]. Another interesting observation for aerosols is that their axial trapping position depends on the trapping power, with higher trapping powers "pushing" the droplet out of the focal plane, eventually pushing the droplet out of the trap altogether. These peculiar observations motivated Burnham and McGloin to rigorously model the optical forces acting upon a droplet, utilizing Mie-Debye spherical

aberration theory (MDSA) to account for the refractive index mismatches between the objective optics/oil, the glass coverslip, the thin water layer and the surrounding air [167]. An important prediction of this model is that removal of the central portion of the Gaussian beam profile (an *annular* beam) enhances the performance of the air based tweezers (similar to Ashkin's demonstration that a doughnut mode enhances the trapping of a colloidal/biological specimen [74]), experimentally verified by Dear *et al.* [166].

4.3 Thermodynamics of a single aerosol droplet

Before introducing spectroscopic studies of aerosols, it is prudent to consider some of the thermodynamic properties governing their existence. The basis for this discussion is that the droplet will remain in thermodynamic equilibrium with its surroundings. In this instance, there is an interface between liquid and air, and so we must consider the vapour pressure of the liquid component. For the pure liquid at a planar interface, this may be quantified using the Clausius-Clapeyron equation:

$$\frac{d\ln p}{dT} = \frac{\Delta_{\text{vap}}H}{RT^2} \tag{4.2}$$

An excellent (and comprehensive) discussion on the thermodynamics of aerosol droplets is provided in Seinfeld and Pandis [162], and is the source upon which the following discussion is based.

4.3.1 The Kelvin effect

A liquid will tend to adopt a shape that minimizes its surface area to volume ratio; this ensures that the majority of the molecules are in the bulk phase (as opposed to being at an interface) and thus lowers the free energy of the system. For a droplet, the morphology with the lowest surface area to volume ratio is a sphere, hence the existence of spherical droplets. The work required to form a droplet with a radius of curvature a is $4\pi a^2\sigma$, where σ is the surface tension of the liquid. The surface tension for pure water as a function of temperature over the range $-40\,^{\circ}\text{C}$ to $40\,^{\circ}\text{C}$ can be described via [171]:

$$\sigma_w = 0.0761 - 1.55 \times 10^{-4}(T - 273) \tag{4.3}$$

where T is the temperature in K. At typical laboratory temperatures ($23\,^{\circ}\text{C}$), the surface tension of water is $72.5 \times 10^{-3}\,\text{N m}^{-1}$. To quantify the effect on the vapour pressure over this curved interface, it is necessary to consider the change in the Gibbs free energy for the formation of a droplet from the pure vapour, i.e. $\Delta G = G_{\text{droplet}} - G_{\text{pure vapour}}$. It can be

shown that resulting vapour pressure over a water droplet (p) of diameter D_p, relative to the vapour pressure over a corresponding flat interface (p°) is given by the *Kelvin equation*:

$$\frac{p_w(D_p)}{p^\circ} = \exp\left(\frac{4M_w\sigma_w}{RT\rho_w D_p}\right) \tag{4.4}$$

where M_w is the molar mass of water, σ_w is the surface tension of water and ρ_w is the density of water. Thus, the vapour pressure of a liquid above a curved interface will always be greater than the corresponding bulk medium; this means that a pure water droplet will only be stable in supersaturated conditions. Indeed, this is in fact a metastability; slight perturbations to the system will result in either perpetual growth or evaporation of the droplet. Note that the Kelvin effect is most significant for small (<100 nm) droplets.

4.3.2 The solute effect

Atmospheric aerosols are often composed of solutions of inorganic salts, as well as various other chemicals. Therefore, the vapour pressure of these solutions must be determined when considering the thermodynamic properties of the droplet. Consider the equilibrium of a (planar) liquid interface with its surrounding vapour. By definition, the chemical potential, μ, of the liquid and vapour phases will be equal, i.e. $\mu_w(\mathrm{g}) = \mu_w(\mathrm{aq})$. Assuming that water vapour behaves as an ideal gas, its chemical potential can thus be written as $\mu_w(\mathrm{g}) = \mu_w^\circ + RT\ln p^\circ$ where, as before, p° refers to the partial vapour pressure of water vapour over the interface. Similarly, we can write for the liquid component $\mu_w(\mathrm{aq}) = \mu_w^* + RT\ln(\gamma_w x_w)$, where μ_w^* is the chemical potential of the pure liquid, γ_w is the activity coefficient for water and x_w is the mole fraction of water in the solution [162]. It follows that the vapour pressure of the solution (p_s°) is related to the vapour pressure of pure water (p°) via:

$$p_s^\circ = \gamma_w x_w p^\circ \tag{4.5}$$

Note that Equation 4.5 does not assume ideality, and reduces to Raoult's Law in the limit of infinite dilution ($\gamma_w \to 1$).

4.3.3 Köhler theory

The two above effects may be combined to describe the vapour pressure of an aerosol comprising of an aqueous solution of a given solute. Substituting Equation 4.5 into Equation 4.4, we find that a droplet of diameter D_p, comprising of n_w moles of water and n_s moles of an involatile salt (such as sodium chloride), will have a vapour pressure described by:

$$\frac{p_w(D_p)}{p^\circ\gamma_w x_w} = \exp\left(\frac{4\overline{v}_w\sigma}{RTD_p}\right) \tag{4.6}$$

where $\overline{v}_w$ is the partial molar volume of water within the droplet. The total droplet volume will satisfy:

$$\frac{\pi D_p^3}{6} = n_w \overline{v}_w + n_s \overline{v}_s \tag{4.7}$$

For a dilute solution, $n_s \overline{v}_s \ll \pi D_p^3/6$, $\sigma \approx \sigma_w$, $\overline{v}_w \approx M_w/\rho_w$ (where ρ_w is the density of water) and $\gamma_w \to 1$. With these approximations, Equation 4.6 can be expressed as:

$$\ln\left(\frac{p_w(D_p)}{p^\circ}\right) = \frac{4M_w\sigma_w}{RT\rho_w D_p} - \frac{6n_s M_w}{\pi\rho_w D_p^3} \tag{4.8}$$

Plots of the vapour pressure of the droplet vs their diameter are known as Köhler curves. Equation 4.8 shows that there are two main components to describe the vapour pressure of a droplet; the Kelvin effect, which increases the vapour pressure relative to the bulk phase, and a solute effect, which decreases the vapour pressure. The presence of solute therefore means that a droplet can achieve thermodynamic equilibrium with its surroundings at relative humidities lower than 100%.

4.3.4 Heating effects

An optically trapped droplet sits slightly downstream of the waist of the tightly focused laser beam, hence it is sensible to assume that all of the laser radiation passes through it. As the imaginary part of the refractive index will be non-zero, some degree of absorption of the laser radiation will occur. This absorption may be quantified by the Beer-Lambert law (see Section 4.7). The pathlength can be approximated as the diameter of the droplet, giving an absorption of αd, where α is the absorption coefficient and is related to the imaginary part of the refractive index,[2] *via* $\alpha = 4\pi k/\lambda$. Therefore, for a given trapping power P, the temperature elevation induced by absorption may be stated as [100]:

$$\Delta T = P\frac{(1 - \exp[-\alpha d])}{2\pi d K_a} \tag{4.9}$$

where K_a is the thermal conductivity of the surrounding air, and takes the value of $2.62 \times 10^{-2}\,\mathrm{W\,m^{-1}\,K^{-1}}$ at 298 K and 1 atmosphere [172]. The magnitude of the imaginary part of the refractive index at 532 nm is 1.8×10^{-9} for pure water, and for salt water solutions lies within the range of 9.2×10^{-9} to 14.8×10^{-9} for the range of concentrations used [173]. Thus, the influence of trapping power on the equilibrium size of a droplet can be described; increasing the power will increase the amount of absorption, and hence increase the temperature of the droplet. This temperature increase will lead to an increase the vapour pressure of the droplet. In order to regain equilibrium with the surroundings, the

[2] The complex refractive index is expressed as $\tilde{n} = n + ik$, where n is the real part of the refractive index, which describes the dispersion properties, and k is imaginary part of the refractive index, which describes absorption of radiation.

droplet must increase its salt concentration in order to lower its vapour pressure to equal the partial pressure of water vapour in the surroundings, i.e. water must be lost from the droplet. Conversely, if the trapping power is lowered, then the amount of heating decreases. The droplet will then have a lower vapour pressure than the partial pressure of water in the surroundings, and so must decrease its salt concentration by the uptake of additional water molecules. To give a feel for the magnitude of temperature changes, for a trapping laser wavelength of 532 nm, with 5 mW of power incident upon the droplet and the imaginary components of the refractive index quoted above, a 9 µm diameter droplet (a typical value for the droplets discussed in this chapter) will experience a temperature increase of 1.3 mK, 6.6 mK and 10.6 mK respectively.

4.4 Raman spectroscopy of aqueous aerosols

The primary analytical technique utilized within this chapter is vibrational Raman spectroscopy, utilizing the trapping laser as a source of pump photons. Briefly, when electromagnetic radiation is scattered by a molecule, some of the photons will have a different energy to the input field (i.e. inelastic scattering), known as Raman scattering. The difference in energy between the pump and scattered photons correspond to molecular transitions within the molecule. The pump photon excites the molecule to a "virtual state"; if the molecule relaxes back to its initial state (so no change in energy) then the scattered photon is equivalent to Rayleigh scattering. If the molecule relaxes to a higher energy state, the scattered photons have a lower energy than the pump, and are referred to as *Stokes* scattered. Conversely, if the molecule returns to a lower energy state, the photons increase in energy relative to the pump, and are *anti-Stokes* scattered. For a vibrational transition to be Raman active, it is necessary that the molecular polarisability changes with vibrational coordinate. Generally speaking, only Stokes emission is observed in vibrational Raman scattering, as the majority of molecules are in the ground vibrational state at room temperature. This type of Raman scattering process is referred to as linear Raman spectroscopy, or spontaneous Raman scattering. Raman scattering is widely used in chemical analysis; as an example pertinent to the study of aerosols, Rosen and Novakov demonstrated the use of Raman scattering in the analysis of atmospheric aerosols (with an emphasis on the particles found in urban environments) [174].

The presence of intense electromagnetic fields, such as within pulsed laser beams, not only enhances the Raman effect but can result in significant non-linear effects. For example, a Stokes photon, coupled with a pump photon, can stimulate another Raman transition, generating a second Stokes photon at that frequency. This amplification process is known as *stimulated Raman scattering* (SRS), and is considerably more efficient than spontaneous

Raman scattering. The stimulated Raman emission intensity increases exponentially with propagation distance within the scattering medium (z), and may be expressed as [175]:

$$I_s(z) = I_s(0) \exp(GI_0 z) \tag{4.10}$$

where I_s is the flux density of the Stokes scattered radiation, and I_0 is the flux density of the pump source. The factor G is the Raman gain factor, and is proportional to the concentration of scattering species, the Raman scattering cross-section and the spontaneous lineshape function [176].

Spherical particles can form microcavities where the resonant modes of the cavity are the whispering gallery modes, and at a wavelength concomitant with a WGM, a large enhancement in the optical pathlength and internal electric field occurs, which can provide the necessary feedback for coherent, nonlinear processes within the microcavity [177, 178]. When the electric field exceeds a certain threshold value, the resulting gain will amplify any spontaneous processes, leading to stimulated Raman scattering within the cavity. The SRS process begins when molecules emit spontaneous Stokes scattered light into a WGM, which is then confined to the surface of the microparticle via multiple total internal reflections. The threshold for SRS occurs when the gain per round trip exceeds the losses. Although a rigorous theoretical framework of SRS within microparticles is incomplete, approximations have been formulated, for instance [175]:

$$I_s(a\Phi) = I_s(0) \exp[(\kappa \cdot GSI_{\text{res}} - L)a\Phi] \tag{4.11}$$

where a is the radius, and the coordinate $a\Phi$ describes the angular variation during propagation around the circumference of the droplet. Quantum electrodynamic (QED) enhancement of the Raman gain is described by the Purcell factor, κ. The value this takes depends upon the cavity mode spacing, $\Delta\nu$ and the homogeneous line width of the spontaneous Raman line, Γ [179]. If $\Delta\nu > \Gamma > \nu/Q$, where Q is the droplet quality factor, then $\kappa \approx \Delta\nu/\Gamma$ [175]. Conversely, if $\Delta\nu < \Gamma$, then $\kappa \approx 1$. For the spectroscopic studies in this chapter, the width of the spontaneous Raman line in water is $\sim 800\,\text{cm}^{-1}$, while the mode spacing is $\sim 240\,\text{cm}^{-1}$. Therefore, $\kappa \approx 1$.

The radiation circulating within the microcavity, I_{res}, may be expressed as:

$$I_{\text{res}} \approx I_0 \cdot f_v \cdot f_b \tag{4.12}$$

where f_v is the fraction of laser radiation coupled into the input resonance, and f_b is the cavity build up factor, which (for plane wave excitation) is a function of the droplet radius, quality factor, refractive index and illuminating wavelength. If a multimode laser is utilized, then the laser bandwidth will often be greater than the linewidth of the WGM resonance,

hence only a fraction of the laser power can be amplified within the droplet.[3] However, even if $\Delta\nu_{\text{laser}} < \Delta\nu_{\text{droplet}}$, it will not necessarily be the case that $f_v = 1$, i.e. spatial overlap between the input and output resonances is important. This is quantified by the factor S. The losses per unit length, L, are linked to the quality factor of the droplet, Q, by [180]:

$$L = \frac{2\pi n_s}{\lambda_s Q} \tag{4.13}$$

where λ_s is the WGM wavelength, and n_s is the refractive index at that wavelength. It follows that the threshold circulating intensity, I_{th}, within the droplet may be expressed as:

$$I_{\text{th}} = \frac{L}{\kappa G S} \tag{4.14}$$

Previous spectroscopic studies of SRS in droplets utilized a vibrating orifice aerosol generator to generate a flow of droplets, which fall through the beam path of a pulsed laser source [177, 181]. These droplets were considerably larger than the droplets captured using tweezers (diameters on the order of 40 µm; tweezed droplets tend to have diameters on order of 10 µm), although the size of the droplets could be altered by changing the vibrational frequency of the aerosol generator. More recently, it has been shown that the combination of optical tweezers with spectroscopy is beneficial as it allows probing of single particle dynamics over extended time periods [158]. Furthermore, multiple trapping techniques mean that droplets of a different composition can be individually trapped and coagulated [99].

4.4.1 General comments on the analysis of SRS spectra

Raman spectra from the aerosol droplets are induced using the same laser used for trapping, i.e. operating at a wavelength of 532 nm. The observed spontaneous Raman band arises due to the fundamental OH stretching vibration in the water molecules of the aerosol, and ranges from 630 nm to 660 nm, which corresponds to an energy in the frequency range $\sim$2900 cm^{-1} to 3700 cm^{-1} being removed from the pump. A typical example of this is shown in Figure 4.1. The extremely broad shape of the Raman band is due to the large rotational constants of water, and to hydrogen bonding between the water molecules [182]. The maximum in the spontaneous Raman signal occurs at approximately 650 nm. SRS resonances, corresponding to WGMs within the droplet, are observed over the spontaneous Raman signal, and their intensity mirrors the intensity of the spontaneous signal. However, a strong spontaneous Raman signal, corresponding to CH stretches in the (hydrocarbon) immersion oil, is observed between 630 nm to 638 nm, and obscures any SRS modes from water occurring in that wavelength range.

[3] A droplet with a Q on the order of 10^4 would have a linewidth on the order of 60 GHz. Note that our solid state laser has a linewidth that is $\sim$ 5 MHz.

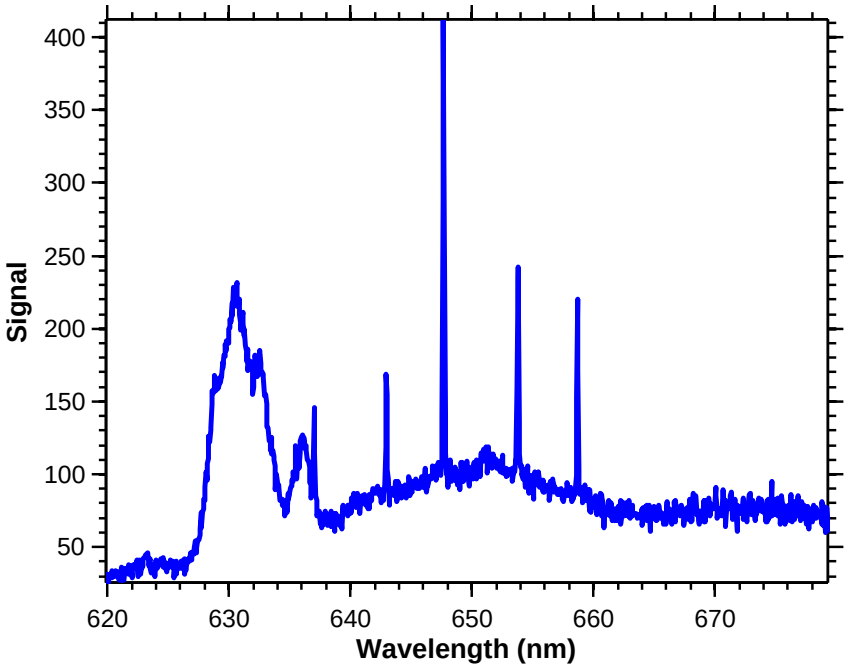

Figure 4.1: Typical example of raw data from the spectrometer, showing the Raman band of water molecules with WGMs superimposed upon it, and Raman scattered light due to the immersion oil between 630 and 638 nm.

In order to utilize WGMs for quantitative measurements of the size of a droplet, it is necessary that a sufficient number of resonances occur within the bandwidth of the spectral region of interest. The physical size of the droplet puts a natural limit on the number of WGMs present; if it is too small then there will be too few resonances lying within the spectral range (a minimum of three modes need to be present to confidently assess the diameter). Conversely, if the droplet is too large, then higher order WGMs become increasingly narrow (i.e. show a higher value of Q); if these higher order modes are so narrow that they too are spectrometer limited then accurate assignment of the modes is extremely difficult.[4] The optimum size range for aerosols is thus 8–10 µm in diameter.

The important parameter for assigning a WGM spectrum is the location of the WGMs themselves. The procedure for determining this was alluded to in Section 3.3; an appropriate lineshape is fitted to the resonance modes in the experimental spectrum and the central wavelength from the fit is used as the experimentally determined WGM resonance. While a WGM itself has a Lorentzian lineshape, the response function of the spectrometer returns a lineshape that is approximately Gaussian. Therefore, the choice of which function to fit

[4] This is only a problem with techniques that involve buildup of radiation within the microcavity; in Chapter 5 it will be experimentally shown that within Mie scattering, narrow resonances are not detected by the spectrometer.

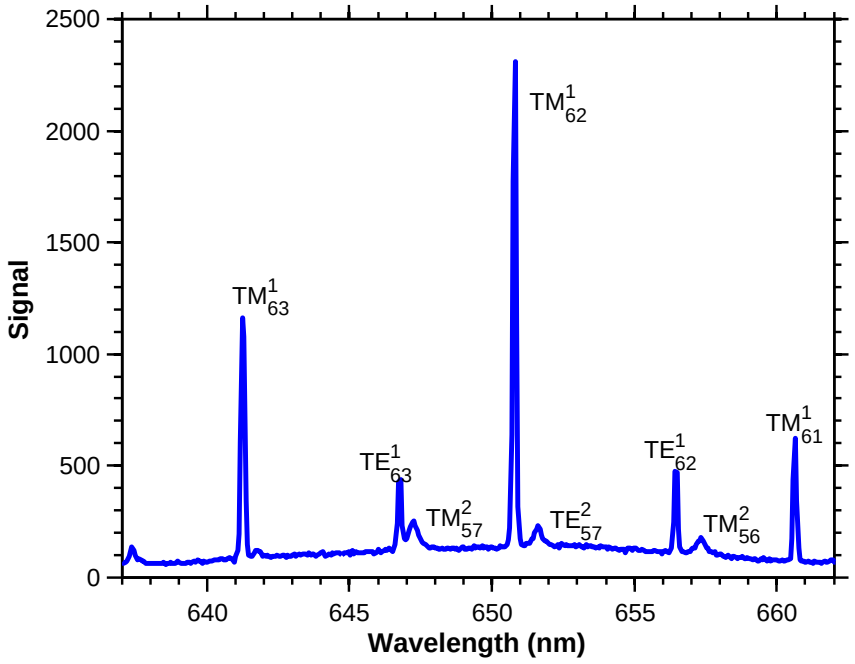

Figure 4.2: A fully assigned SRS spectrum for a typical water droplet, showing both first and second order modes. In this instance, the diameter is 10.63 µm.

with depends upon how narrow the resonance is. The Gaussian function used for fitting is:

$$y = y_0 + \frac{A}{w\sqrt{\pi/2}} \exp\left(\frac{-2(\lambda - \lambda_c)^2}{w^2}\right) \tag{4.15}$$

where A is the area under the Gaussian curve, λ_c is the central wavelength and w is the width, related to the full width half maximum (FWHM) via $w = \mathrm{FWHM}/\sqrt{\ln 4}$. The Lorentzian function used is:

$$y = y_0 + \frac{2A}{\pi} \frac{w}{(4(\lambda - \lambda_c)^2 + w^2)} \tag{4.16}$$

where the width in this instance is equal to the FWHM. In both cases, the area of the function may be interpreted as the integrated intensity of the WGM resonance; hence from here on, use of the term "intensity" should be interpreted as the integrated area of the WGM resonance.

To put these fitting routines into context, consider the spectrum shown in Figure 4.2. In this case the droplet is sufficiently large to show both first and second order resonances, while not so large that the second order widths become spectrometer resolution limited. Example fits to the resonances are shown in Figure 4.3. From the fitting parameters, values of the quality factor Q can be obtained. For the second order resonance, Q takes the value of 1650 ± 160, while for the first order resonance $Q = 5070 \pm 80$. Note that the true value of Q for the first order resonance will be considerably higher (on the order of 10^4).

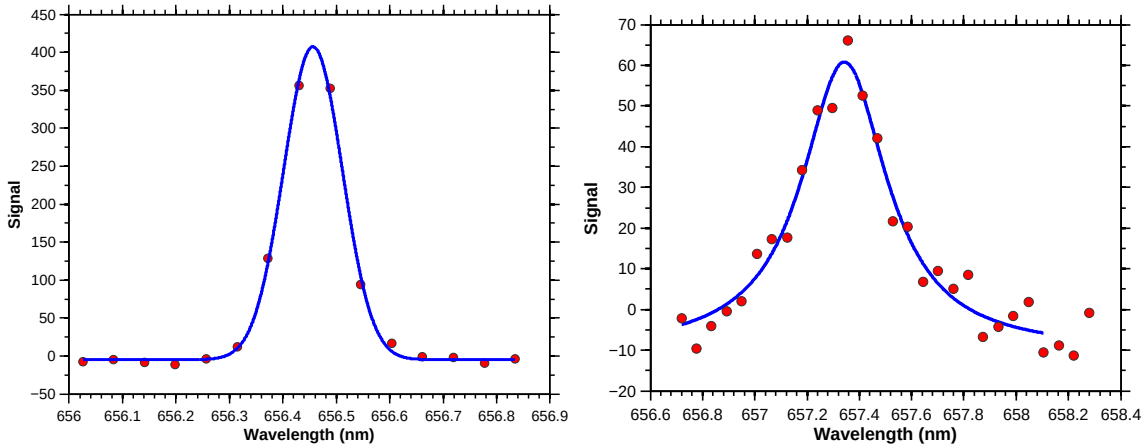

(a) **(b)**

Figure 4.3: Examples of fits to the experimental data, in this case referring to Figure 4.2. Panel (a) shows the TE^{1}_{62}, which is spectrometer limited, and has a Gaussian function fitted. Panel (b) shows the TM^{2}_{56}, whose width is not limited by the spectrometer and has been fitted with a Lorentzian function.

As the aerosol droplet used consist of nebulised aqueous sodium chloride solutions (herein referred to as salt water solutions), the real part of the refractive index is determined using the algorithm of Quan and Fry [149], which is an empirical equation for the refractive index of sea water. Adapting notation to suit this thesis, it is expressed as:

$$n(S,T,\lambda) = n_0 + (n_1 + n_2 T + n_3 T^2)S + n_4 T^2 + \frac{n_5 + n_6 S + n_7 T}{\lambda} + \frac{n_8}{\lambda^2} + \frac{n_9}{\lambda^3} \qquad (4.17)$$

where S is the salt concentration in $\mathrm{g\,L^{-1}}$, T is the temperature in °C and λ is the wavelength in nm. The coefficients are presented in Table 4.1.

Table 4.1: Coefficients for the refractive index algorithm of Quan and Fry [149], given in Equation 4.17, for the refractive index of salt water solutions.

n_1	1.31405
n_2	1.779×10^{-4}
n_3	-1.05×10^{-6}
n_4	-2.02×10^{-6}
n_5	15.686
n_6	0.01155
n_7	−0.00423
n_8	−4382
n_9	1.1455×10^{-6}

4.5 Optically trapped aerosols in a Gaussian beam

Having established the thermodynamic properties of aerosol droplets pertinent to single droplet studies, and reviewed the analysis procedure, the dynamics of droplets trapped by a conventional Gaussian laser beam are now considered. Performing experiments with a Gaussian beam also affords a method of testing the validity of the results obtained with LG mode illumination presented later, and corroborates some of the previous studies of droplets trapped with optical tweezers which have been performed in a very small number of laboratories [100, 158, 183–185].

4.5.1 Evaporating droplets

The aerosol cell described in Section 4.2 has no method of fine RH control, and as it is exposed to the lab atmosphere it is expected that droplets should, on the whole, evaporate due to the decreasing RH conditions within it. As an example, consider the spectrum shown in Figure 4.4. The WGMs can be observed to blueshift, which is characteristic of droplet evaporation. This is because the size parameter x of a resonance[5] (for a given refractive index contrast) is a constant; hence as the diameter decreases, λ must also decrease. As a consequence, the wavelength of the resonances should be expected to track the size of the droplet, i.e.:

$$\frac{\Delta\lambda}{\lambda} = \frac{\Delta a}{a} \tag{4.18}$$

where $\Delta\lambda$ and Δa are the changes in resonance wavelength and radius respectively. The time dependent wavelengths of the TM_{58} and TE_{58} resonance are plotted in Figure 4.4c and 4.4d; both show an identical trend (and indeed, all the modes within the spectrum show this behaviour). Note that there is slight variation in the position of the wavelengths at around 50 and 80 s; this is a real phenomenon that was observed in the time resolved spectrum, and is not an artifact in the fit to the experimental data, likely caused by slight variations in the local relative humidity of the laboratory air. A linear fit to the data in Figure 4.4b yields a gradient of $-0.88 \pm 0.01\,\mathrm{nm\,s^{-1}}$. The diameter of the droplet decreases by 0.12 µm over the 128 s period presented; the change in volume is therefore 19 fL, giving a net loss of 6.3×10^{11} water molecules. The net evaporation rate under these conditions is therefore $4.9 \times 10^{9}\,\mathrm{molecules\,s^{-1}}$.

The evaporation rate of the droplet depends upon a balance between the rate at which water molecules leave the surface of the aerosol, and the collision frequency of gas phase water molecules with the droplet. The latter can be estimated using a simple kinetic model

[5] Recall the definition of the size parameter was $x = 2\pi a/\lambda$

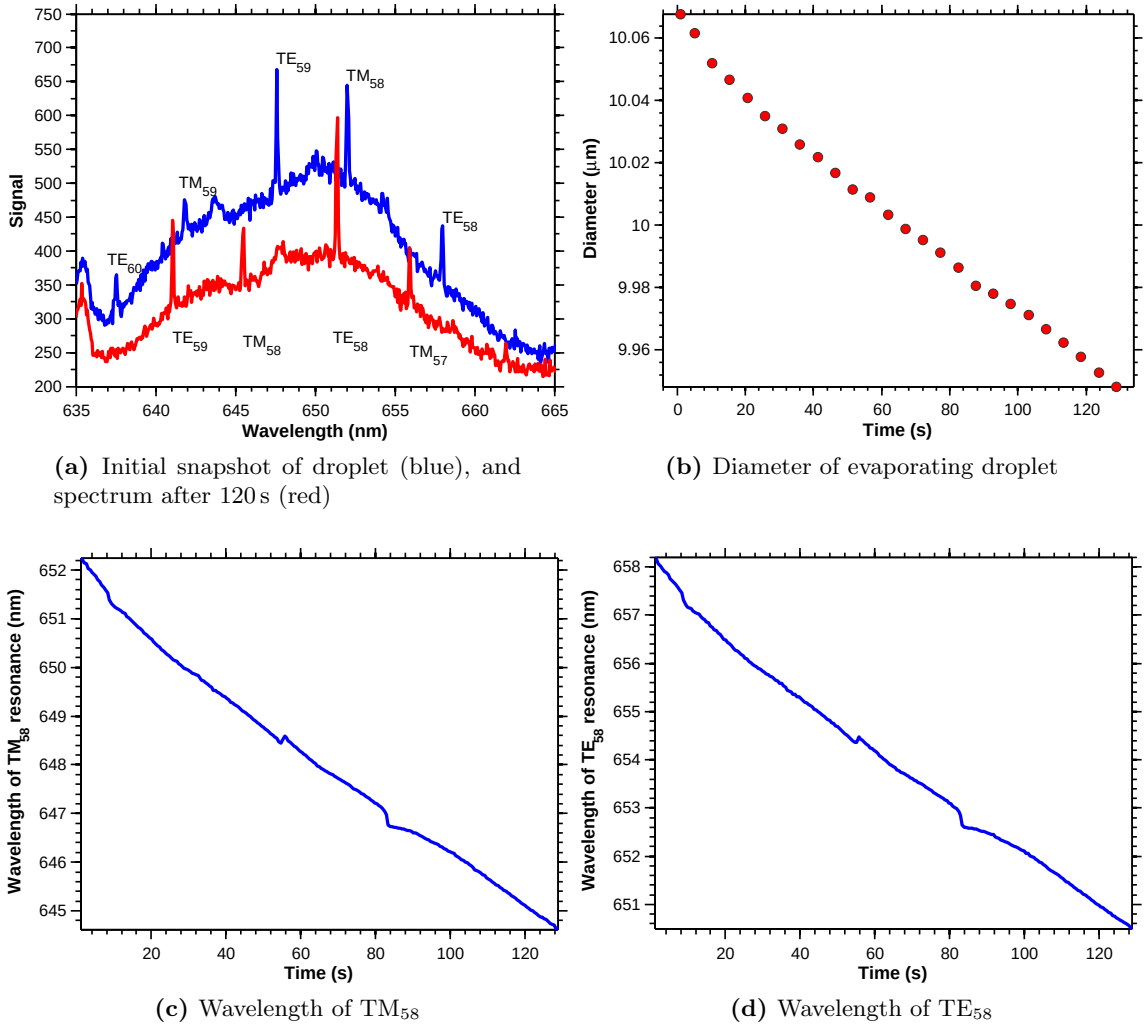

(a) Initial snapshot of droplet (blue), and spectrum after 120 s (red)

(b) Diameter of evaporating droplet

(c) Wavelength of TM_{58}

(d) Wavelength of TE_{58}

Figure 4.4: SRS spectrum of an evaporating droplet. The modes are clearly observed to blueshift, which is characteristic of droplet evaporation. Assignment of the modes allows the diameter of the droplet to be tracked through time (assuming a constant refractive index, in this case).

of the collision frequency of gas phase molecules (Z_w) with a surface of area A:

$$Z_w = \frac{p_w A}{\sqrt{2\pi m_w k_B T}} \tag{4.19}$$

where p_w is the partial pressure of water vapour in the environment surrounding the aerosol, m_w is the mass (in kg) of a water molecule and $A = 4\pi a^2$, i.e. the surface area of the droplet. If we assume that every collision of a water molecule with the surface of the droplet results in the uptake of that molecule into the droplet, then the condition for net evaporation (which is what is measured experimentally) will be that Z_w must be less than the rate at which molecules evaporate from the surface, which in turn will depend on the vapour pressure due to the solute effect and net heating of the droplet due to absorption of the

trapping laser. As an example, a droplet of diameter 10 µm in an environment of relative humidity of 90% will experience a collision frequency of 2.9×10^{16} molecules s^{-1}.

4.5.2 Growing droplets

If the local relative humidity increases, it should be expected that an equilibrium condition will exist, where the rate of evaporation is balanced by the rate at which water molecules are uptaken by the droplet, followed by droplet growth. The driving force behind growth of a droplet will be an increase in the vapour pressure at the droplet interface, by decreasing the concentration of salt within the droplet. To encourage observation of growing droplets in a low RH environment offered by the trapping cell, a more concentrated salt solution was nebulized.

When an aerosol droplet is growing, the WGMs will be expected to redshift for the same reason as outlined above. However, instead of constantly changing (in time) like in the spectra from evaporating droplets in Figure 4.4, the modes are observed to "lock" at certain wavelengths for extended periods of time. Furthermore, the intensity of the SRS modes increase dramatically during these periods. As an example, consider the spectra shown in Figure 4.5. It is clear from this figure that the wavelength position of the WGMs in the droplet are stable in time.

Two subtly different cases of droplet growth have been observed in these experiments. The first bears more similarity to the evaporating case, where the individual modes can be observed to red shift. Upon reaching a size associated with locking, the modes then fix their wavelength and grow in intensity. After an intensity maximum is reached, a sudden loss of all SRS intensity occurs. Low intensity SRS modes then reappear, at further redshifted wavelengths, where the process then repeats. The second observed case is similar, except that instead of the droplet's modes being observed to redshift before coming onto a locking period, the spectrum shifts from one locked state to another. This is termed *mode hopping*, to draw an analogy with the operation of single mode lasers.

While the intensity of the SRS modes increases during the locked period, the wavelength of the resonance also subtly redshifts. This is shown clearly in Figure 4.6, and is characteristic of all periods of locking. The magnitude of this shift is extremely small (0.01 nm), and indeed would not be observed if the lineshape was not fitted with a Gaussian/Lorentzian profile. The corresponding change in diameter is approximately 0.2 nm (the initial diameter of this droplet was 11.2479 µm), i.e. a change in volume of 40 aL. This volume change corresponds to a net uptake of 9.8×10^9 molecules, i.e. a growth rate of 7.3×10^6 molecules s^{-1}. To put this figure in context, consider the number of molecules striking the droplet per

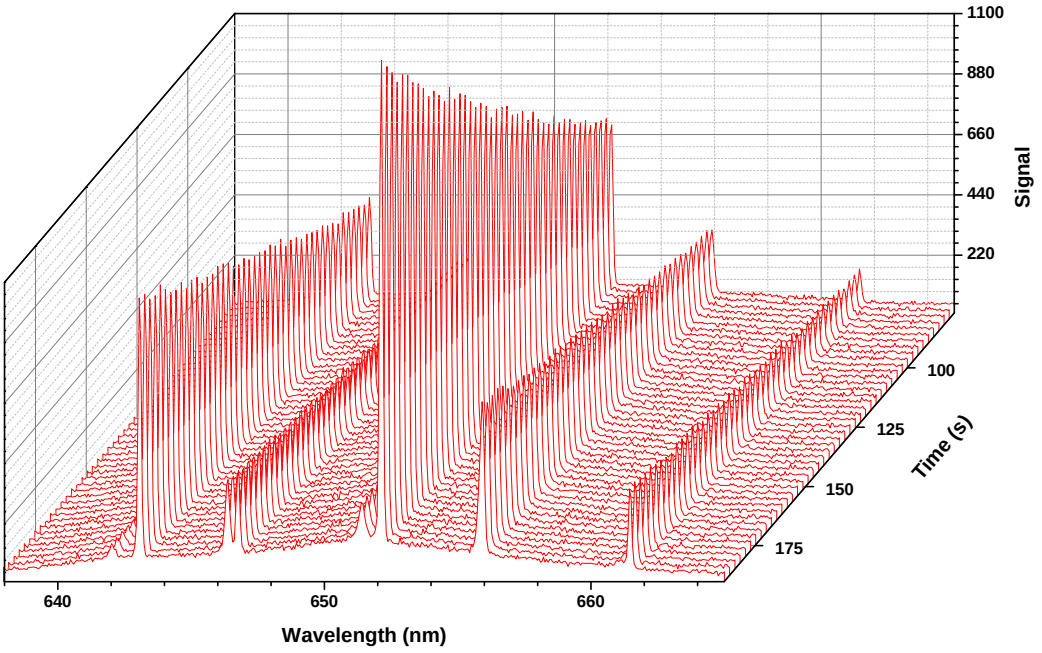

Figure 4.5: Time invariance of WGMs during a Gaussian locking period.

unit time. If we assume an ambient relative humidity of 90%,[6] the corresponding partial vapour pressure of water is 25.3 mbar. For the droplet considered above, Equation 4.19 yields a collision frequency of 3.4×10^{16} molecules s^{-1}, which is considerably greater than the measured growth rate.

However, before moving onto discuss the implications of these results, it is important to confirm that the observations are indeed due to droplet growth, and not due to drifting of the laser frequency. Recall that the bandwidth of a WGM at the trapping laser wavelength is on the order of 60 GHz, and that the laser utilized has a bandwidth of $\sim$ 5 MHz. The measured shift in wavelength of the TE_{66} resonance is approximately 0.01 nm over a 110 s period. The fractional change in wavelength, $\Delta\lambda/\lambda$ is therefore 1.5×10^{-5}. Assuming this can be related to a change in the laser frequency, the corresponding drift would be 8.5 GHz over the whole time period, hence 77 MHz s^{-1}. A drift of this magnitude does not correspond to the experimental behaviour of the laser, and hence it is concluded that droplet growth is occurring during the locking periods.

[6] This number was chosen as a representative value using the results of Section 4.7.

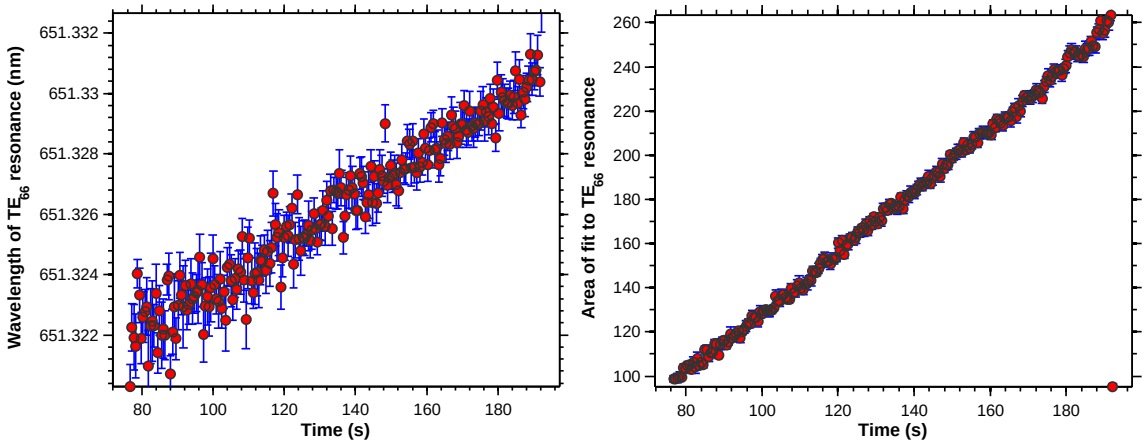

(a) Central wavelength **(b)** Integrated intensity

Figure 4.6: Central wavelength (a) and area (b) of an SRS resonance during a locked period (in this instance, corresponding to the spectra shown in Figure 4.5). The growth in intensity is accompanied by redshifting of the resonance frequency.

4.5.3 Discussion

Clearly, the phenomenon of locking must suppress droplet growth, i.e. there must be an enhanced evaporation during the locking period. These observations are consistent with a previous study by Miles *et al.* [173], who observed similar mode locking for an optically trapped aerosol in an environment of increasing RH, where active control over the local RH was provided by flowing wet nitrogen through the trapping chamber. It is interesting that locking periods are observed even in the open cell utilized in this work, suggesting that the moist tissue is indeed providing a greatly increased local relative humidity within the trapping cell.

The periods of size stability indicate that there is an additional heating contribution to the droplet, arising from resonant absorption of the trapping laser radiation. This can be justified by considering the absorption efficiency, Q_{abs}, of a droplet illuminated by 532 nm radiation, such as in Figure 4.7. Here, Q_{abs} is plotted as a function of the droplet diameter, for a droplet consisting of a $40\,\text{g}\,\text{L}^{-1}$ salt water solution, with an imaginary part of the refractive index of $9 \times 10^{-9}i$ (a typical value for the imaginary part of the refractive index for a salt water solution at this wavelength; 532 nm is near the minimum in the absorption spectrum of water). Ripple structure is observed in the absorption efficiency; the diameters at which a resonance occurs correspond to a resonance wavelength of 532 nm, i.e. there is *resonant* absorption of the laser. Note that Q_{abs} is calculated assuming plane wave illumination, and so will be an overestimate of the true absorption efficiency for a Gaussian beam illuminating a spherical droplet. The temperature change, in terms of Q_{abs}, may be

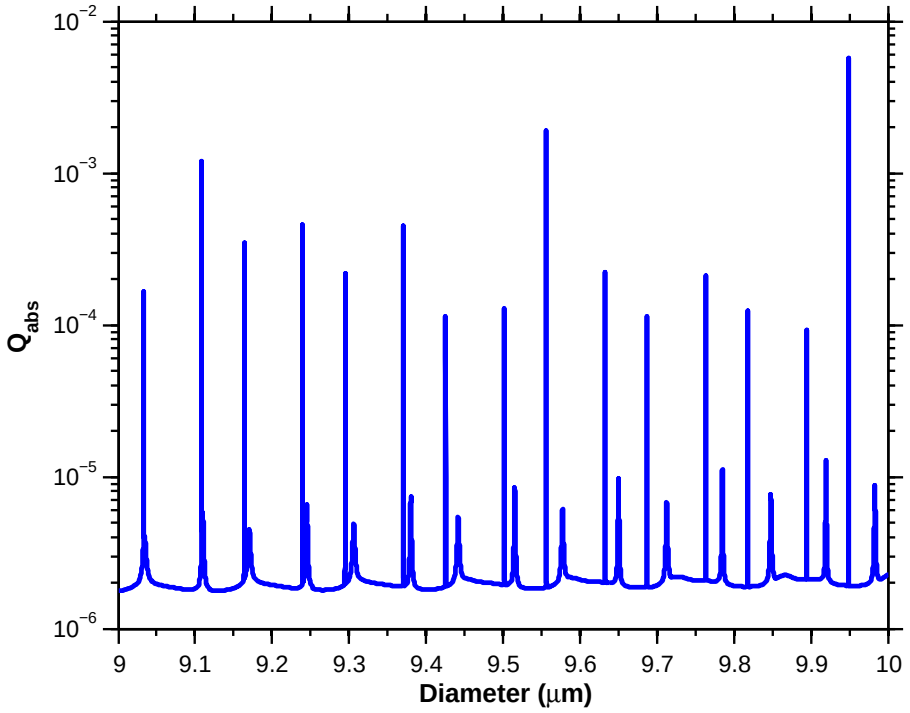

Figure 4.7: Plot of the absorption efficiency for a droplet, comprised of a $40\,\mathrm{g\,L^{-1}}$ salt water solution, where the imaginary part of the refractive index is $9 \times 10^{-9}i$, illuminated by radiation of wavelength 532 nm.

expressed as:

$$\Delta T = \frac{IQ_{\mathrm{abs}}a}{4K_a} \tag{4.20}$$

where I is the laser irradiance, expressed in $\mathrm{W\,m^{-2}}$. Guillon *et al.* [144], who also contributed to the study of Miles, showed that the temperature rise of the droplet can be factorised into two components: a non-resonant contribution that depends solely on the degree of absorption, and a resonant contribution that depends on the fraction of radiation that is able to couple into a WGM. The increase in temperature is therefore expressed as :

$$\Delta T = \frac{PQ_{\mathrm{abs}}}{4\pi K_a a} = \frac{\alpha P}{2\pi K_a}\left(1 + \frac{fQ}{2ka}\right) \tag{4.21}$$

where Q is the quality factor for the droplet, $k = 2\pi/\lambda$, and f is the fraction of light coupled into a WGM at the trapping laser wavelength.[7]

The mechanism behind locking again relies on the droplet being in thermodynamic equilibrium with the surrounding gas. As the local relative humidity increases, the droplet will absorb water to grow and increase its vapour pressure by diluting the salt present (the solute effect). However, as the droplet's size tunes towards a WGM resonance at the wavelength of the trapping laser, it will suddenly experience a (large) temperature change associated

[7] Note that this equation, as originally formulated in Guillon's paper, contained an erroneous factor of a.

with resonant heating. For instance, the droplet that provided the data for Figure 4.6 was trapped with 20 mW of laser power.[8] Using the calculated value of Q_{abs} (assuming plane wave illumination) of 1.3×10^{-3} gives a temperature increase of 28 K using Equation 4.21. Note that this is exceptionally high value for the temperature rise, owing to the calculation of Q_{abs} assuming plane wave illumination. A later study by Miles *et al.* utilized Mie-Debye spherical aberration theory (MDSA) to calculate Q_{abs}, returning a much smaller value of $\sim 3 \times 10^{-6}$ [186]. This value suggests that the fractional degree of light coupled into a WGM should be on the order of 2×10^{-3}. Using this value for Q_{abs} gives $\Delta T = 65$ mK. Note that utilizing Equation 4.9 with the above parameters yields a non-resonant contribution to the droplet temperature of 26 mK, i.e. resonant heating is *at least* as important as non-resonant heating when determining the equilibrium response of the droplet.

The increase in temperature will be responsible for an increase in the vapour pressure of the droplet without the need to absorb water to dilute the salt. The red shift of the resonant modes in the SRS spectrum, along with the increase in intensity, are characteristic of the droplet's size tuning closer to a wavelength where a WGM exists for the trapping laser wavelength. Figure 4.7 shows that the first order resonances are very sharp, and so once the droplet's size passes through the maximum, there will be a sudden drop in the droplet temperature. To compensate for this decrease in droplet vapour pressure, the droplet will quickly grow to restore equilibrium with the surroundings via the solute effect. According to this mechanism, the two distinct growth regimes described above are actually identical; in the latter case, the slow growth period must be happening faster than the spectrometer's temporal resolution (1.94 Hz). This resonant heating mechanism also explains why no locked periods are observed for droplet evaporation; approaching a resonance will simply drive off more molecules due to the temperature increase, meaning the droplet's size will never lock to the trapping laser wavelength. It is, however, possible to tune an evaporating droplet to a resonance at 532 nm by lowering the trapping power, which reduces the degree of non-resonant heating and encourages droplet growth. The droplet will not stay on resonance, however; it will then rapidly evaporate (characterised by blue shifting of the resonance wavelengths in the SRS spectrum, accompanied by a reduction in the intensity of the SRS signal).

To further confirm that the droplet is indeed locking to the trapping laser, via a WGM at 532 nm, consider the following pieces of data. First of all, the diameter assigned to a growing droplet (in the limit where the sudden growth at the end of a locking period occurs at a timescale that is shorter than the spectrometer's temporal resolution) during successive locking periods is shown in Figure 4.8. Note that these diameters were inferred by assuming a constant refractive index, equal to the bulk solution that was nebulised to form the droplets. In reality, the refractive index of the droplet will decrease as the droplet

[8] This is on the higher end of the range of trapping powers.

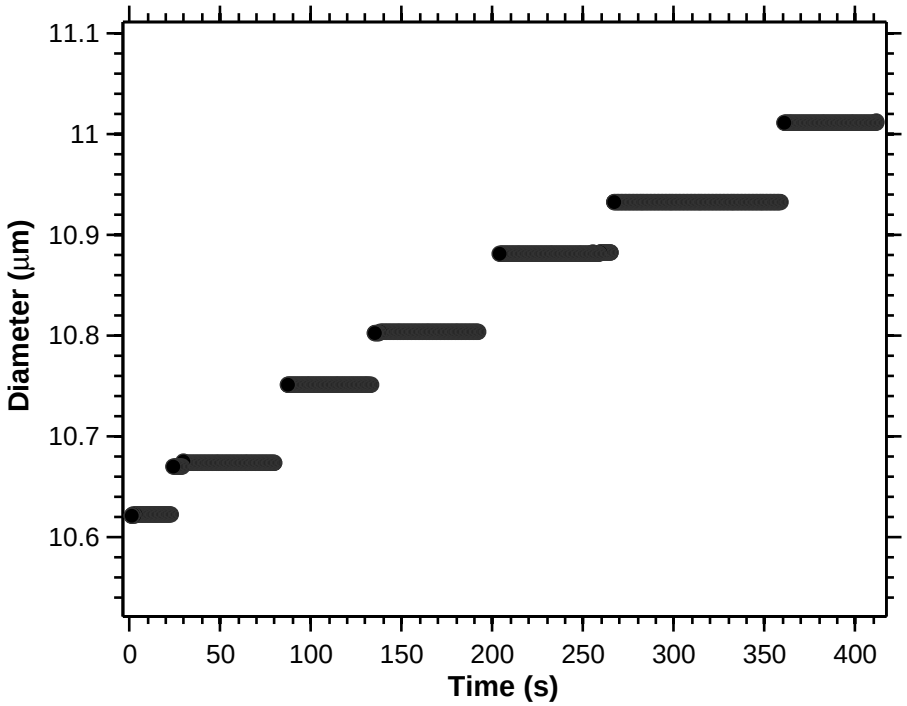

Figure 4.8: Assigned diameter of a droplet during successive locking periods, in this case with where the sudden growth occurs faster than the spectrometer resolution. The diameters in this plot were inferred by assuming a constant refractive index, corresponding to a concentration of $80\,\mathrm{g\,L^{-1}}$.

gets bigger, due to the reduction of the salt concentration. The size stability is apparent; furthermore, the magnitude of the change in droplet diameter alternates reproducibly between the different locking periods as a function of the polarisation of the locking mode. This data is presented in Table 4.2, along with a comparison of the diameter that would return a resonance with the trapping wavelength. The difference between diameters of consecutive locked periods is also computed. The agreement between the theoretical resonances and experimentally measured diameters does indeed suggest that resonant heating is responsible for the observed locking periods. However, it is stressed that no refractive index fitting is considered for this table; variation in the refractive index is presented in Table 4.3 where the diameter and refractive index quoted is those which provide the best fit to the experimental data. Using this refractive index, the wavelength that the spectrometer grating is centred at (650 nm, and assuming the droplet is at the same temperature as the ambient conditions in the laboratory, 23 °C), a value for the salt concentration (in $\mathrm{g\,L^{-1}}$) for each period is estimated. This salt concentration is then used to determine the droplet size for a resonance at 532 nm.

At this point, it is appropriate to comment on the subtle differences between the theoretical diameter, and the experimentally measured value. The first point to note is the uncertainty in the assigned salt concentration. To quantify this, a change in the assigned

salt concentration of $1\,\mathrm{g\,L^{-1}}$ results in a change in the refractive index of 0.0002. While this is perhaps a very slight change, it corresponds to a roughly 1 nm change in the diameter for a resonance at 532 nm. Secondly, it is noted that the algorithm used to determine the refractive index of the salt water solution comprising the droplets also has temperature as an input. If the temperature used is increased by 2 °C, the refractive index increases by 0.0003, which again alters the resonance diameter by approximately 1.7 nm. Finally, it is noted that the trapping laser does not operate at exactly 532 nm. The wavelength of our frequency doubled Nd:YVO_4 was measured using a wavemeter (Coherent Wavemaster); the exact wavelength varied according to which specific longitudinal mode of the resonator that the laser driver locks to, but was always observed to lie within the range of 532.054 nm to 532.106 nm (the value quoted is the wavelength in air). Hence, from here onwards, the resonant diameter at a wavelength of 532.1 nm will be considered.

Further evidence for locking comes from the relative intensities of the SRS resonances. Consider Figure 4.9, in which the intensities of a pair of WGMs of the same mode number and order are plotted as a function of time (the integrated areas have been normalised to

Table 4.2: Comparison between the diameter which would give a resonance at 532 nm, and the experimentally measured diameters at the beginning of a locking period. Additionally, the difference in size between consecutive locked periods is considered.

Locking resonance	Theoretical diameter (µm)	Difference (µm)	Measured diameter (µm)	Difference (µm)
TM_{77}	10.6233	0.0522	10.6213	0.0530
TE_{78}	10.6755	0.0777	10.6742	0.0768
TM_{78}	10.7531	0.0521	10.7510	0.0508
TE_{79}	10.8052	0.0777	10.8018	0.0793
TM_{79}	10.8830	0.0520	10.8811	0.0511
TE_{80}	10.9349	0.0778	10.9322	0.0789
TM_{80}	11.0127		11.0111	

Table 4.3: Analysis of the data in Table 4.2, taking into account the variation in the refractive index. Note the anomalous value TE_{80}, this is likely due to a second order SRS mode overlapping with a first order resonance at this diameter, introducing an error into the fit.

Locking resonance	Diameter (µm)	Refractive index	Salt concentration ($\mathrm{g\,L^{-1}}$)	Resonance Diameter (µm)
TM_{77}	10.5462	1.3555	135.88	10.5463
TE_{78}	10.5985	1.3553	134.77	10.5985
TM_{78}	10.6897	1.3536	125.33	10.6898
TE_{79}	10.7418	1.3533	123.66	10.7430
TM_{79}	10.8157	1.354	127.55	10.8157
TE_{80}	10.9347	1.3452	78.65	10.9369
TM_{80}	10.9585	1.3522	117.55	10.9589

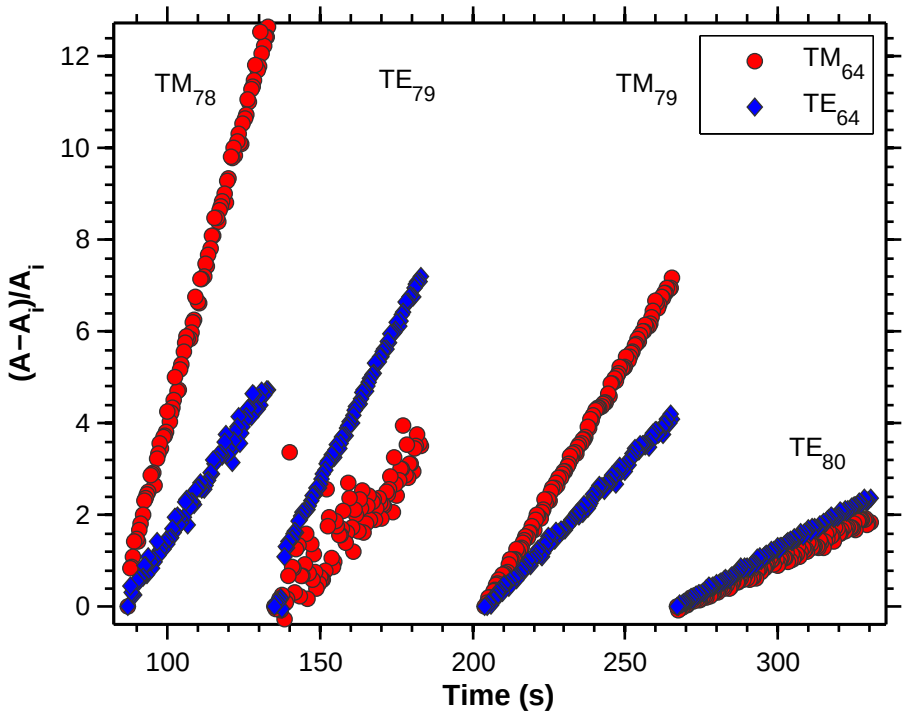

Figure 4.9: The areas of the TM_{64} and TE_{64} resonances, normalised to their area at the start of each locking period. The mode with a polarisation which matches the locking mode at 532 nm, indicated above each set of data, grows in intensity quicker, and shows a higher overall intensity.

their initial value at the start of the locking period). As the assignment of the modes also returned a diameter, the resonance that occurs at the trapping laser wavelength is also quoted. It is clear from this figure that the mode whose polarisation matches the resonance at 532 nm grows in intensity faster, and reaches a higher overall intensity.

As a final piece of evidence that the droplet is indeed optically locking to the trapping laser wavelength, consider the data shown in Figure 4.10. In Figure 4.10b, which is a zoomed in portion of Figure 4.8, there is clearly a period at earliest times where the droplet locks to a smaller size. Upon considering the resonant diameters at 532.1 nm, it is apparent that a TE^2_{72} resonance occurs at 10.6719 µm, while the TE^1_{78} resonance occurs at 10.6775 µm. The difference of 5.7 nm is consistent with the experimental data, which has a difference of approximately 4 nm. Furthermore, it is clear from the spectra shown in Figure 4.10a that the second order WGMs (just short of 645 and 655 nm) are more intense than the first order WGMs in the same spectrum (the spectrum resulting from locking to the first order resonance is also shown, vertically offset for clarity). The observation of locking to a second order resonance is likely due to the low bandwidth of the frequency doubled Nd:YVO_4 laser used in these experiments (sub 1 MHz according to the manufacturer's specifications, although measured to be < 5 MHz *via* high resolution spectroscopy measurements conducted within our group [187]); furthermore the short period of time associated with locking is

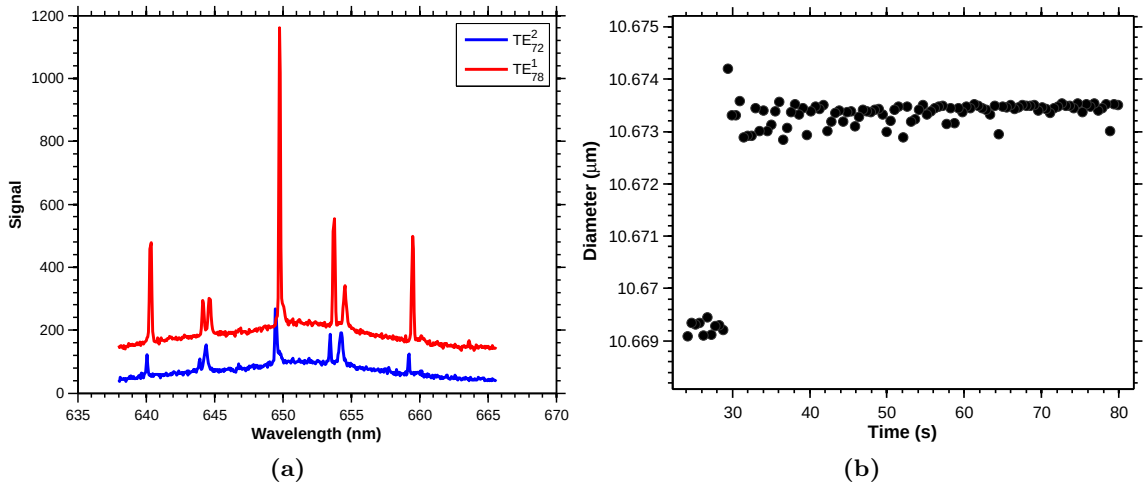

Figure 4.10: Evidence of locking to a second order resonance at 532.1 nm. In panel (a), note that the second order WGMs short of 645 and 655 nm are as intense as the first order. The subsequent first order locking spectrum is also shown, and is vertically offset for clarity. Panel (b) is a zoomed in version of Figure 4.8, showing that there is clearly a period (before 30 s) where the droplet is locked to a smaller size.

explained by both the low value of Q_{abs} for a second order resonance (see Figure 4.7), and the close proximity of the first order resonance.

4.6 Optically trapped aerosols in a Laguerre-Gaussian beam

Having established the general properties of optical trapping of aerosols with Gaussian laser beams, their Raman spectroscopy and the phenomenon of size locking, this section shall now consider what happens to the dynamics of optically trapped aerosol particles when the illuminating light field is changed, specifically from a Gaussian beam to an LG mode.

4.6.1 Trapping with an LG beam

Aerosol droplets were generated as above, and initially trapped with Gaussian beams. Generally, the kinoforms which produced the LG mode were generated in advance, using an additive adaptive algorithm [188], and displayed on the SLM using a custom LabVIEW interface. The kinoforms themselves were a superposition of the $\ell\theta$ phase modulation hologram, which generates the LG mode, and a grating element to displace the trapping beam from the zeroth order (which was blocked using a fine pencil lead).

Example images of a trapped droplet of approximately 9.6 µm are shown in Figure 4.11. When trapped with a Gaussian beam, the droplet lies within the image plane of the microscope objective, and when low values of ℓ were utilized, the droplet's axial position did

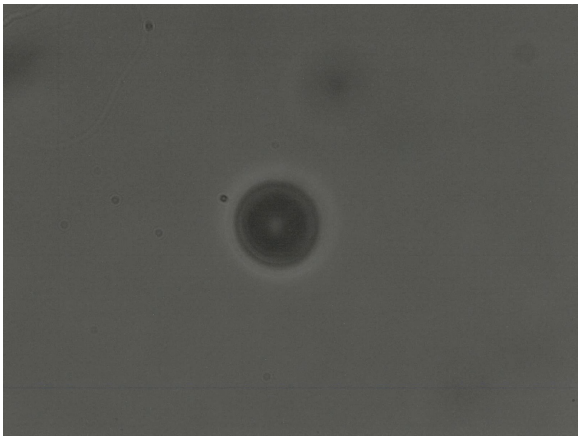

(a) Gaussian

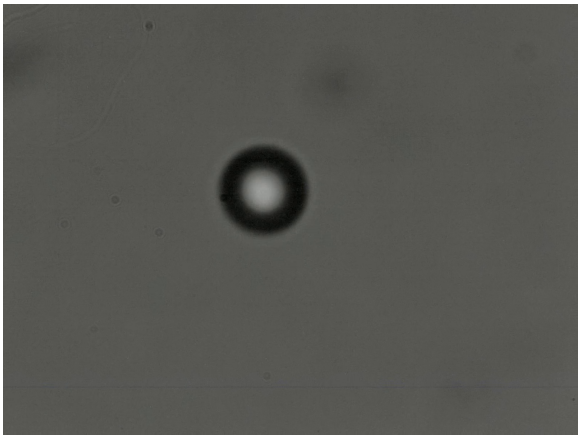

(b) $\ell = 10$

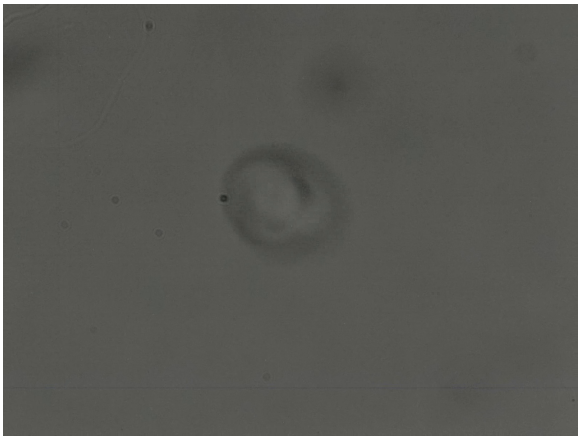

(c) $\ell = 20$

Figure 4.11: Video microscopy images of an optically trapped aerosol particle of approximately 9.6 µm in diameter. Upon switching the laser geometry, a clear "jump" in axial position occurs. At higher values of ℓ, the droplet orbits the region of high intensity.

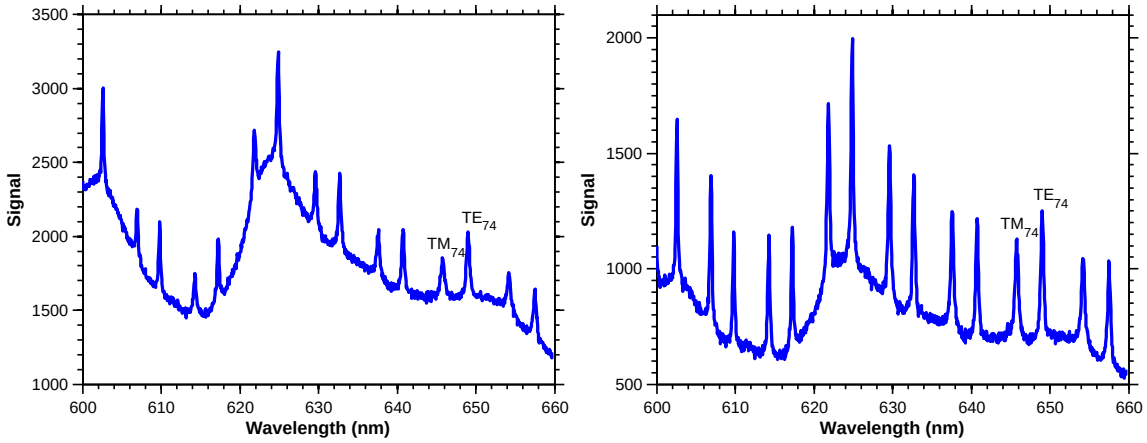

(a) Gaussian **(b)** $\ell = 30$

Figure 4.12: Fluorescence spectra from a dye-doped polystyrene microsphere. Upon changing excitation geometry from Gaussian to LG, a clear increase in the WGM intensity (relative to the background fluorescence) is observed.

not appear to alter. However, upon switching to $\ell = 10$, the droplet jumped slightly out of focus, as shown in Figure 4.11b. If ℓ was further increased (hence increasing the size of the LG mode, see Figure 2.10), the droplet could be observed spinning as in Figure 4.11c, i.e. angular momentum is being imparted to the droplet. Note, however, that LG modes are highly susceptible to aberration; it is feasible that a slight imperfection in the optical alignment causes a hotspot to develop within the focused beam, in which the droplet will preferentially sit. This is confirmed by observing an increased degree of lateral motion of the droplet in the $\ell = 10$ mode. Upon increasing the topological charge of the mode, the intensity distribution of the beam becomes more uniform, allowing the particle to freely orbit around the beam axis.

4.6.2 Spectroscopy with LG modes

To begin to consider the differences between spectroscopy utilizing conventional Gaussian beams and LG modes, spectra were taken from a fluorescent polystyrene microsphere, utilizing the green laser as an excitation source (rather than trapping, as the increased absorption due to the fluorescent dye lead to short microsphere lifetimes when the laser powers associated with trapping were incident upon the sphere) positioned at the centre of the particle. The SLM was then used to change the illumination geometry, with a spectrum recorded for increasing values of the topological charge ℓ. Two example spectra are shown in Figure 4.12; panel (a) corresponds to Gaussian illumination, while panel (b) refers to excitation with an $\ell = 30$ mode. The assigned diameter of this sphere is 10.46 µm. The differences between these two spectra are immediately clear; while the Gaussian spectrum has

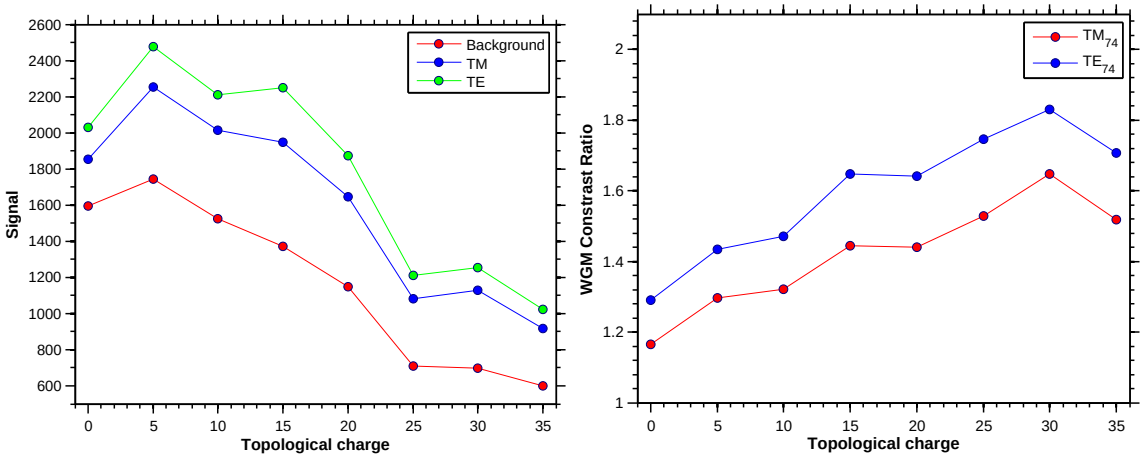

(a) Raw data **(b)** Corresponding contrast ratio

Figure 4.13: Variation of the WGM contrast ratio with topological charge, where the Gaussian mode is taken to have a topological charge of zero. A clear increase is observed, with the maximum corresponding to an LG size that best matches the circumference of the microsphere.

a higher overall signal (owing to the laser radiation passing through the entire diameter of the microsphere), the WGMs are less pronounced upon the background fluorescence signal when compared to the LG spectrum. To confirm this, a WGM contrast ratio was defined, being equal to the ratio of the height of the WGM to the background fluorescence signal. This was calculated for a range of LG modes, and the results are plotted in Figure 4.13, specifically for the TE and TM_{74} modes, but the trend is identical across all modes. A clear increase in the contrast ratio is observed as the topological charge is increased, reaching a maximum value before rapidly decreasing. This maximum corresponds to the size of LG mode that best matches the circumference of the microsphere; the rapid decrease in intensity occurs as the mode becomes too large to illuminate the particle.

While it is known that edge illumination provides better coupling into WGMs [181], edge illumination of the microparticle with the Gaussian beam did not provide the same level of contrast enhancement that the high LG modes demonstrated (contrast ratio measured to be 1.57 for Gaussian edge illumination on the TE_{74}, vs 1.29 for Gaussian centre illumination, and 1.83 for $\ell = 30$). These observations indicate that illumination with an LG mode provides better overlap between the input excitation field and the output WGMs.

4.6.3 Mode hopping with LG modes

Having established that LG illumination results in a higher contrast ratio for WGMs within a fluorescent polystyrene sphere when compared to utilizing a Gaussian beam, the spectroscopic response of aerosol droplets shall now be considered. Especially pertinent here is

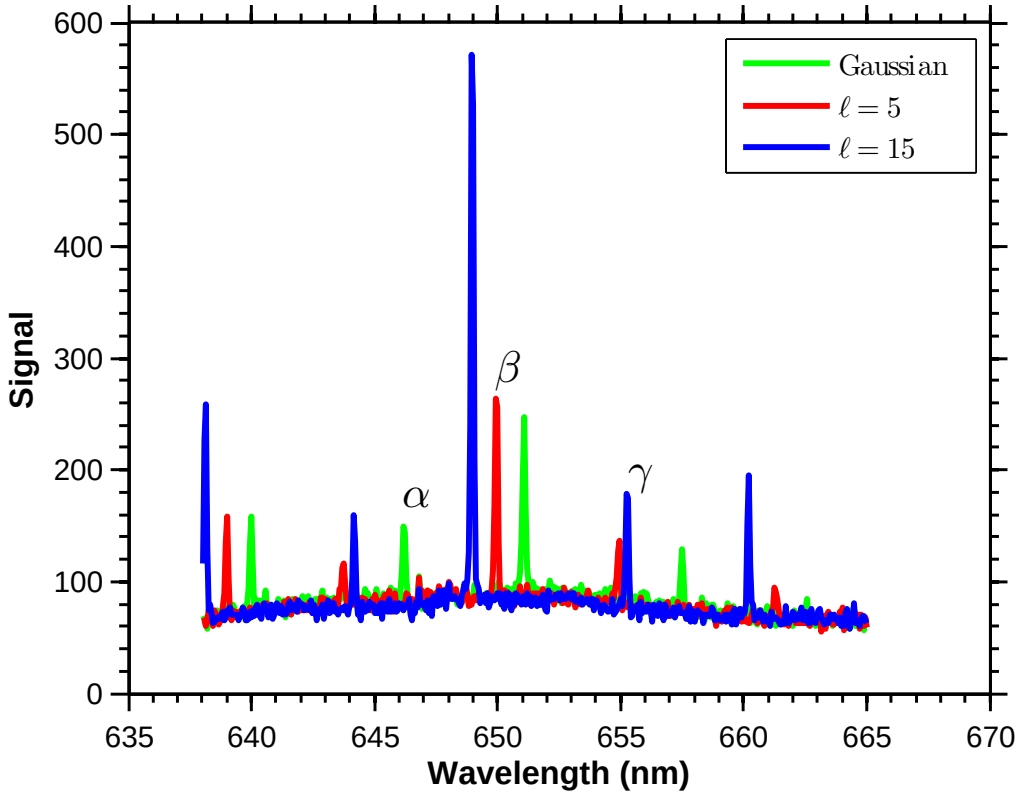

Figure 4.14: "Mode hopping" upon switching between Gaussian and LG illumination. The droplet was initially stable when trapped with a Gaussian beam. The location of the TE_{54} resonance within a Gaussian beam and LG beams with $\ell = 5$ and $\ell = 15$ are marked with an α, β and γ respectively.

that, unlike a solid microsphere, an aerosol can change its size depending on the degree of resonant and non resonant heating.

The first condition to consider is a droplet, trapped in a Gaussian beam and showing WGMs in its Raman spectrum, such as in Figure 4.14 (green line). The assigned diameter of this droplet is 9.218 µm and the corresponding best-fit refractive index is 1.3418. This implies a salt concentration of 59.6 g L^{-1}. Note that this salt concentration suggests that a TM_{66} resonance occurs at 532.1 nm for a diameter of 9.2181 µm. The droplet was stable at this size for around 15 minutes prior to the recording of the above spectra, suggesting that the droplet is in a stable equilibrium with its surroundings.

The trapping laser is then changed to an $\ell = 5$ mode, and an instant "mode hop" is observed. To quantify this, consider the location of the TE_{54} resonance. For Gaussian illumination, it occurs at 646.18 nm (indicated by α in Figure 4.14). Assignment of the LG spectrum shows that the resonance has shifted to 649.96 nm (indicated by β). By applying $\Delta\lambda/\lambda = \Delta d/d$, the expected change in diameter should be a growth of 53.9 nm. The diameter returned from the assignment is 9.275 µm, with a new refractive index of

Table 4.4: The data described in the text, for the first set of mode hopes for LG excitation. The resonance diameter is the closest match to the experimental diameter, that gives a WGM at 532.1 nm; the difference between these two is also tabulated.

Excitation mode	Assigned diameter (µm)	RI	Salt conc ($g\,L^{-1}$)	Resonance diameter (µm)	Difference (nm)
Gaussian	9.218	1.3418	59.6	9.2181	0.1
$\ell = 5$	9.275	1.3413	57	9.2756	0.6
$\ell = 10, 15$	9.358	1.3403	51.43	9.3588	0.8
$\ell = 20$	9.403	1.3417	59.2	9.4035	0.5

1.3413 (salt concentration of $57\,g\,L^{-1}$), corresponding to a Δd of 59 nm. Note that if the refractive index was not allowed to vary, then the value of Δd from assignment would be 55.9 nm. The droplet was illuminated by the $\ell = 5$ mode for ∼90 s, before switching to an $\ell = 10$ mode. Another mode hop was observed, with the TE_{54} resonance now located at 655.24 nm (indicated by γ). The new diameter (from assignment) is 9.358 µm, with a salt concentration of $51.43\,g\,L^{-1}$. Of more interest, though, is the behaviour of the SRS line intensities; upon switching to $\ell = 10$ illumination, the modes have become more intense. No further changes were observed in the SRS spectrum when ℓ was changed from 10 to 15, with no appreciable change in the spontaneous Raman signal. Finally, a further mode hop occurred upon changing to $\ell = 20$, though this did not happen instantly (as was the case when switching from Gaussian to $\ell = 5$, and to $\ell = 10$). Instead, the droplet remained size stable for ∼10 s before mode hopping to a diameter of 9.4 µm, with a refractive index of 1.3417 (a corresponding salt concentration of $58.9\,g\,L^{-1}$). For ease of reference, this data is presented in Table 4.4, along with the closest theoretical resonance diameter for 532.1 nm.

This stepping series (Gaussian, $\ell = 5$, $\ell = 10$, $\ell = 15$, $\ell = 20$) was then repeated with the same droplet. Upon switching back to the Gaussian illumination, the droplet lost its previous size stability. The initial diameter and refractive index for this second Gaussian period are 9.385 µm and 1.342 respectively (i.e. the droplet has shrunk, relative to the previous period of LG excitation), giving a salt concentration of $61.1\,g\,L^{-1}$. Tracking the wavelength of the TE_{55} mode shows that the droplet then proceeds to grow, as shown in Figure 4.15. When the beam was changed to an $\ell = 5$ mode (at approximately 310 s), a sudden jump in the position of the wavelength occurred. The wavelength fluctuates for a while, before continuing to increase. Note that although both illumination geometries display a plateau wavelength, the intensity is the same throughout this period, and small. Immediately before switching to higher ℓ modes, the assigned diameter is 9.429 µm with a refractive index of 1.3398, giving a salt concentration of $48.5\,g\,L^{-1}$. A comparison of these sizes with the closest resonant diameter is presented in Table 4.5. Sharp SRS resonances were again observed for $\ell = 10$, 15 and 20, though in this instance there was no variation in

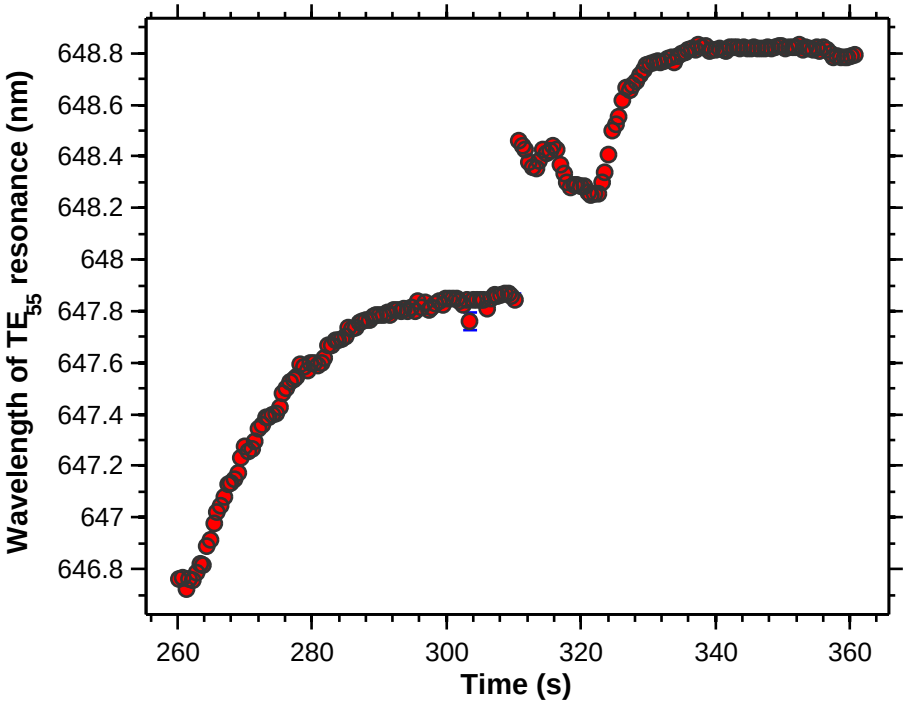

Figure 4.15: Tracking the wavelength of the TE_{55} resonance, upon switching back to Gaussian illumination, followed by a switch to $\ell = 5$ at approximately 310 s.

the position of the SRS resonances upon increasing ℓ, indicating size stability for this period. In all cases, the droplet's diameter is observed to tune closer to the resonant diameter.

Table 4.5: Data for the continuation of the Gaussian/LG stepping series that was presented in Table 4.4. This time, assignment data from the beginning and end of each period are considered.

Excitation mode	Assigned diameter (µm)	RI	Salt conc ($g\,L^{-1}$)	Resonance diameter (µm)	Difference (nm)
Gaussian (initial)	9.385	1.342	61.1	9.4011	16.1
Gaussian (final)	9.409	1.3407	53.7	9.4103	1.4
$\ell = 5$ (initial)	9.427	1.3392	45.8	9.4202	-7.2
$\ell = 5$ (final)	9.429	1.3398	48.5	9.4168	-12.2
$\ell = 10$ (initial)	9.492	1.3399	48.8	9.4929	0.9
$\ell = 10$ (final)	9.489	1.3403	51.4	9.4896	0.2
$\ell = 15$ (initial)	9.489	1.3403	51.0	9.4901	0.8
$\ell = 15$ (final)	9.490	1.3402	50.9	9.4903	0.3
$\ell = 20$ (initial)	9.491	1.3401	49.9	9.4915	0.8
$\ell = 20$ (final)	9.487	1.3406	53.1	9.4876	0.3

It is clear from the above spectra that illumination with higher ℓ modes results in significantly more intense SRS peaks. To investigate this further, spectra were recorded from a trapped droplet while ℓ was incrementally stepped up on the SLM. The resulting spectra

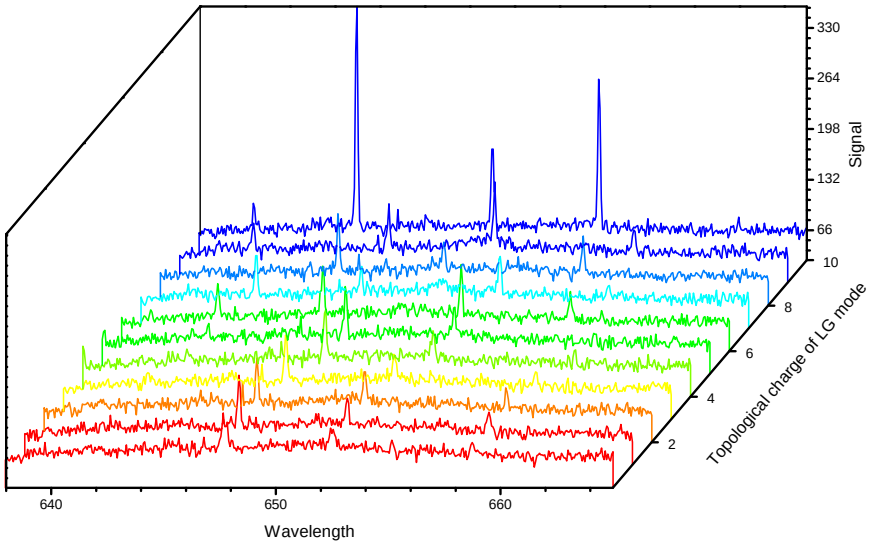

Figure 4.16: An illustration of the effect of stepping up the values of ℓ which form the kinoform displayed on the SLM. Note that there appears to be a transition at $\ell = 10$, where the intensity of the WGMs increases.

are shown in Figure 4.16. It is immediately clear that there is not much variation between the intensities of the SRS modes for a Gaussian beam, and the low values of ℓ (1–9). However, upon switching to $\ell = 10$, the intensity of the modes increases and the droplet became size stable. Furthermore, the droplet was observed to "jump" out of focus in the trap, as discussed in Section 4.6.1. The assigned diameters are presented in Table 4.6; generally the diameter increases as ℓ increases.

Table 4.6: Assigned diameters from the spectra resulting in stepping up the value of ℓ displayed on the SLM. A clear transition to more intense SRS peaks was observed at $\ell = 10$, and remained size stable.

Excitation mode	Assigned diameter (µm)
Gaussian	9.412
$\ell = 1$	9.409
$\ell = 2$	9.408
$\ell = 3$	9.414
$\ell = 4$	9.427
$\ell = 5$	9.428
$\ell = 6$	9.490
$\ell = 7$	9.503
$\ell = 8$	9.545
$\ell = 9$	9.565
$\ell = 10$	9.621
$\ell = 15$	9.621

Table 4.7: Assigned diameter of a droplet trapped in various LG modes, corresponding to the data in Figure 4.17. A constant refractive index, corresponding to an $86.6\,\mathrm{g\,L^{-1}}$ salt solution was assumed. This gives a resonant diameter of 9.1895 µm, i.e. a TM_{66} resonance at 532.1 nm. The difference between the assigned diameter, and the resonant value, is also tabulated.

Excitation mode	Assigned diameter	Difference (nm)
$\ell = 5$	9.1850	0.87
$\ell = 10$	9.1854	0.54
$\ell = 15$	9.1855	0.40
$\ell = 20$	9.1856	0.35

4.6.4 Enhanced SRS spectra with LG excitation

The observations presented above suggest that enhanced SRS spectra from droplets can be observed by using a high (≥ 10) value of ℓ for the LG mode that constitutes the trapping and excitation beam. The data presented in Figure 4.17 is a further illustration of the positive effects on the stimulated Raman spectrum that LG illumination offers. The first point of interest was that, for this droplet, low intensity WGMs were observed when the particle was trapped with a Gaussian beam, with the wavelengths slowly redshifting (but not showing any sign of locking due to resonant heating). Slightly more intense WGMs were observed for $\ell = 5$, and once again with an associated increase in signal for $\ell = 10$, 15 and 20. Looking at the raw spectral data, it again appears the resonances are occurring at the same wavelength (the maximum in each WGM is detected by the same pixel on the spectrometer's CCD) for the three LG excitation geometries. In Figure 4.17a, the central wavelength of a Gaussian fit to the WGMs is noted (for the TM_{53} resonance in this case, but an identical trend is shown in all the modes). The larger uncertainties (and scatter in the position) in the central wavelength for the $\ell = 5$ data is attributed to the lower intensity modes in the spectrum (giving a greater standard error in the lineshape fit). However, there is still an obvious shift in the wavelength upon switching between the different topological charges. The modes are observed to redshift, implying that the LG mode illumination leads to droplet growth. The increase in intensity as ℓ is increased suggests better overlap of the input and output fields, however an increase in intensity may also indicate that the droplet is tuning closer to a resonance at the trapping laser wavelength. To quantify this, a representative of the assigned diameter for each LG mode, and theoretical resonant diameter for 532.1 nm, are presented in Table 4.7. Due to the very small shift in the SRS wavelengths, a constant refractive index corresponding to a salt concentration of $86.6\,\mathrm{g\,L^{-1}}$ has been used (the refractive index which gave a best fit to an $\ell = 5$ spectrum) in calculating the assigned diameters.

Of more interest is that, for this droplet (and under the ambient conditions at the time), the system is highly reversible. This is best illustrated by Figure 4.18a, where the droplet

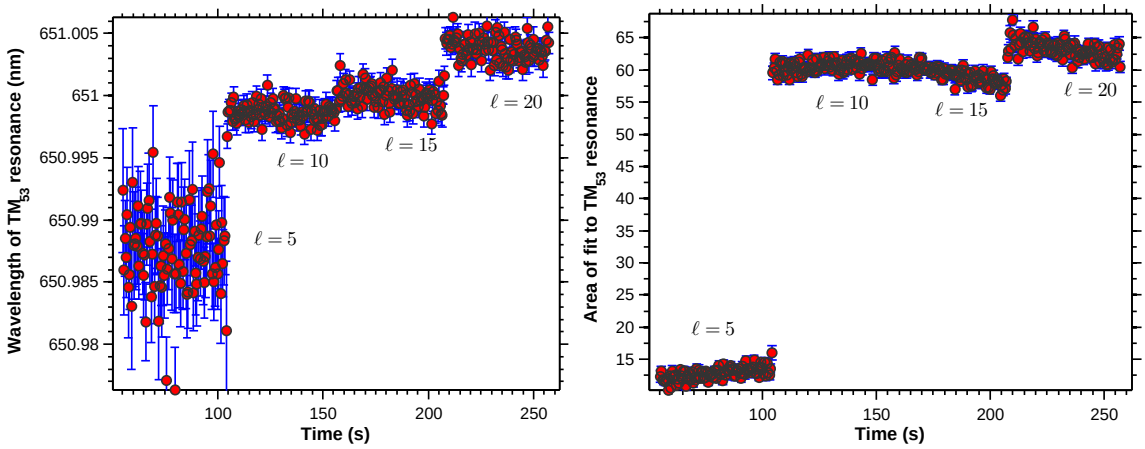

(a) Wavelength **(b)** Intensity

Figure 4.17: A demonstration of observed effects when switching between low and high values of ℓ in an optically trapped droplet. Note that for $\ell = 20$, angular momentum was clearly imparted to the droplet.

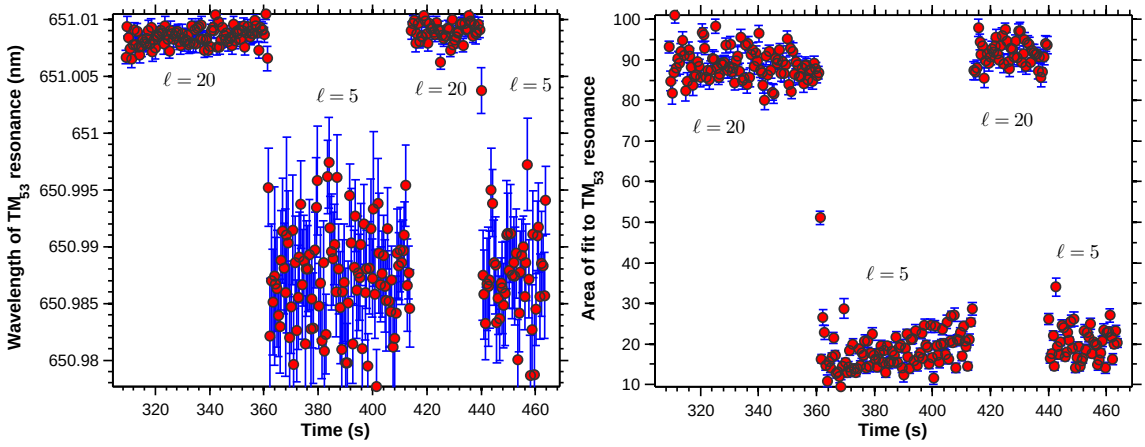

(a) Wavelength **(b)** Intensity

Figure 4.18: Data from the same droplet as Figure 4.17, at a later time.

is modulated between $\ell = 20$ and $\ell = 5$ illumination. The droplet was trapped with a Gaussian beam for the minute between Figures 4.17 and 4.18, and no WGMs were observed in its spectrum; furthermore the droplet itself was moving quite wildly in the trap, its axial trapping position fluctuated between different positions (perhaps indicating bistability in the trapping position, as in the work of Knox *et al.* [189]). Upon switching back to $\ell = 5$, the droplet's axial position stabilised. While there is a very slight (but noticeable) redshift of the $\ell = 20$ central wavelength, the central wavelength for $\ell = 20$ and $\ell = 5$ is essentially unaffected by switching between the two. It is therefore concluded that the higher ℓ modes are tuning the droplet closer to the diameter corresponding to a WGM at the trapping laser wavelength.

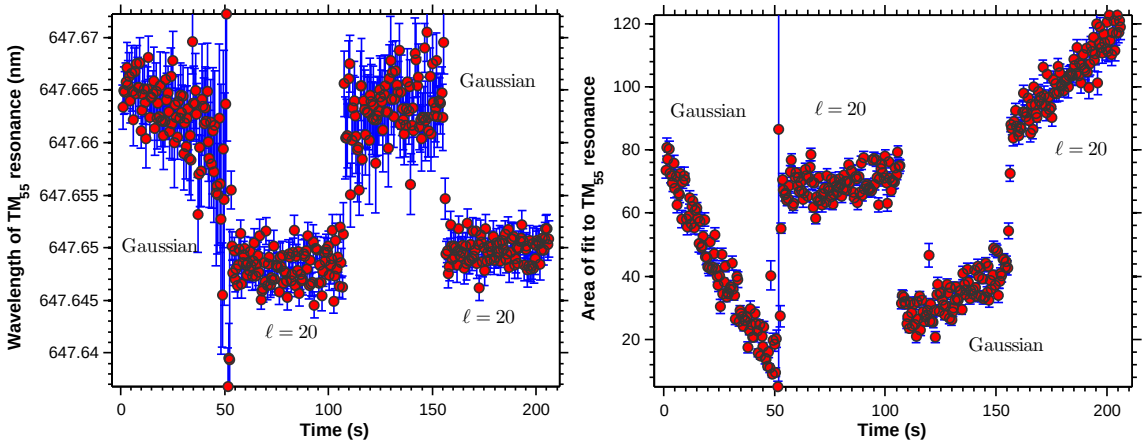

(a) Wavelength **(b)** Intensity

Figure 4.19: Evaporating Gaussian followed by LG switch.

4.6.5 Changing excitation geometry during Gaussian locking periods

The response of changing the beam geometry for a droplet coming off resonance with a Gaussian beam is now considered. The data at early times (<50 s) presented in Figure 4.19 corresponds to this scenario, as evidenced by the blueshifting of the central wavelength of the mode, and its decrease in intensity. Upon switching to an $\ell = 20$ beam, the mode further blueshifts (i.e. the droplet shrinks), but the intensity of the mode increases. Switching back to a Gaussian causes an increase in the resonance wavelength and an overall decrease in the intensity, however the intensity of the mode now grows with time. Finally, another switch back to $\ell = 20$ shifts the resonance wavelength back towards the blue end of the spectrum, and the intensity continues to increase.

Clearly, there is a subtle combination of processes occurring within this system. The assignment of this data presents some curious findings. Again, due to the small variations in the position of the resonances, a constant refractive index shall be assumed. At the beginning of the dataset, the droplet's size is 9.5014 µm, and is coming off a TM_{68} resonance (the resonant diameter is 9.5037 µm, a difference of 2.3 nm). Upon switching to the LG mode, the droplet's size remains steady at 9.5012 nm, which is still displaced from the resonance condition. Even if the refractive index is allowed to vary, the assigned diameter is still smaller than the resonant diameter by ~ 2.5 nm. This is puzzling, as the intensity of the SRS modes has increased relative to the Gaussian excitation.

As was discussed in Section 4.5.3, misassignment of the salt concentration can induce refractive index changes that will change the resonance diameter, and if the temperature

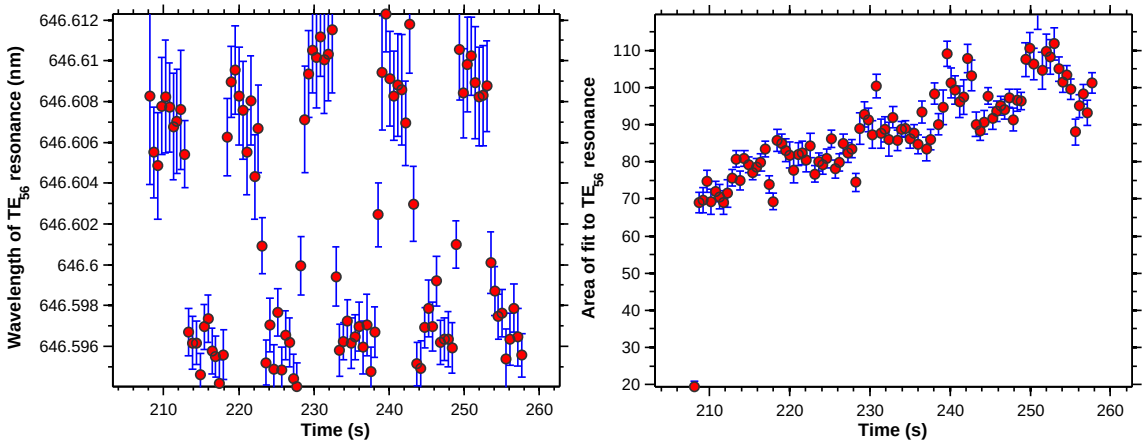

(a) Wavelength **(b)** Intensity

Figure 4.20: A continuation of the data presented in Figure 4.19b. After a mode hop caused by switching back to a Gaussian profile, the beam was modulated between a Gaussian and an $\ell = 20$ mode every 10 frames ($\sim$5 s).

quoted is incorrect then this too will offset the resonance diameter[9] (indeed, these two quantities are intrinsically linked, as a temperature was required to determine the salt concentration, based upon the best fit refractive index). However, the droplet's diameter is clearly decreasing away from a resonant diameter during the Gaussian period (as evidenced by the blueshifting and decrease in SRS intensity), and the SRS wavelengths for the LG period are both stable in position and shorter than the initial Gaussian data but yet show an clear increase in intensity. This suggests that there must be an additional consideration rather than resonant heating associated with WGMs at the trapping laser wavelength.

Continuation of the data accumulated from this droplet is presented in Figure 4.20. After a mode hop induced by switching back to a Gaussian profile, which changed the size of the droplet to 9.556 µm (a TE_{69} resonance would require a diameter of 9.5583 µm) the droplet was modulated between Gaussian and $\ell = 20$ every 10 frames (roughly every 5 s.) Again, the difference in resonance wavelength is reversible, although note that the diameter for LG periods is 9.5558 µm, i.e. further from the resonant diameter.

Next, consider what happens to the spectrum of a droplet that is switched from a Gaussian beam to an LG mode during a Gaussian locking phase (Section 4.5.2). The first ten seconds of data in Figure 4.21 correspond to Gaussian excitation; the increasing intensity and the minimal redshifting of the resonance wavelength are characteristic of a Gaussian locking period. During the first minute of spectral acquisition, there were two typical Gaussian mode hops; the data in Figure 4.21 is therefore from the third growth period. The initial diameter of the droplet during this period is 10.7327 µm (tuning towards a TE_{77} resonance

[9] Note that temperature changes on the order of 50 mK only affect the refractive index beyond the fifth significant figure.

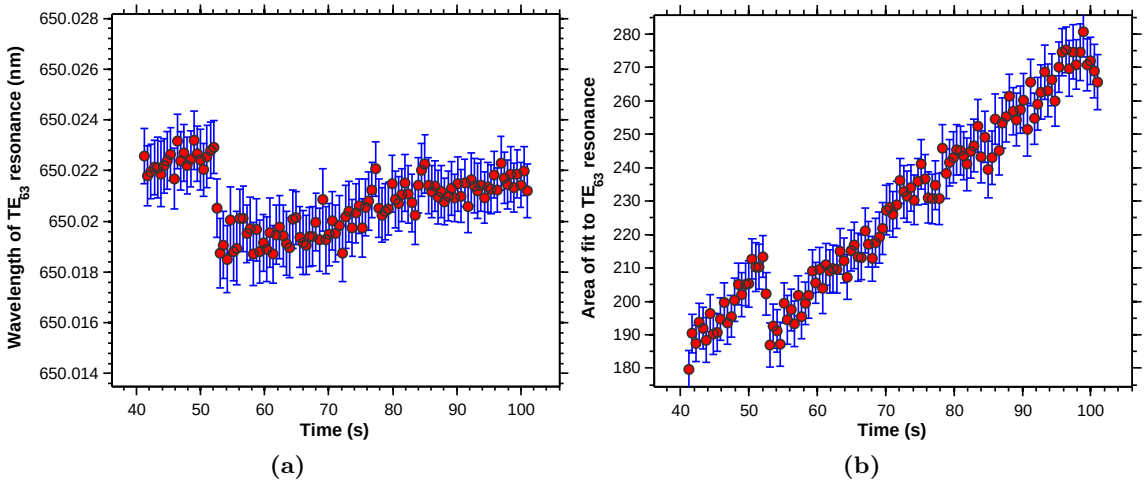

Figure 4.21: A growing Gaussian droplet, switched to an LG mode.

at 10.7344 µm). Upon switching to the LG mode ($\ell = 20$), the intensity immediately drops by $\sim 10\%$, but then continues to grow. The wavelengths of the SRS modes also blue shift immediately upon mode shifting (implying a droplet contraction of 0.1 nm), before red shifting in a similar fashion to spectra of growing droplets from Gaussian illumination. It is of interest to note that, despite the intensity of the SRS modes exceeding those of the Gaussian as the droplet grows, the droplet doesn't reach the same size as with Gaussian excitation (as evidenced by the position of the WGMs), again suggesting that the droplet has not reached the resonance condition.

4.6.6 Using LG modes to suppress droplet evaporation

An interesting feature of LG illumination is that it appears to suppress the evaporation of the droplet. This was apparent during the Gaussian unlocking in Figure 4.19, however it is also observed when the SRS modes are blue shifting. For instance, in the spectra shown in Figure 4.22, it is clear that the SRS modes are blue shifting during periods of Gaussian trapping. Upon switching to LG illumination, the spectra snapped back to a pattern that is consistent with a resonance at the wavelength of the trapping laser (with the associated increase in WGM intensity). This is most clearly illustrated in Figure 4.22b, which plots the diameter of the droplet as a function of time.

As a further investigation, the trapping power was varied for a droplet while trapping with an $\ell = 20$ mode. The effects of the power shifts on the wavelength and intensity on the TE_{63} mode are shown in Figure 4.23. Upon increasing the trapping power (by a relatively large amount, 17.5 mW), a blueshift of the resonances occurred, i.e. increasing the power has caused the droplet to slightly evaporate. In real terms, the droplet's size has changed

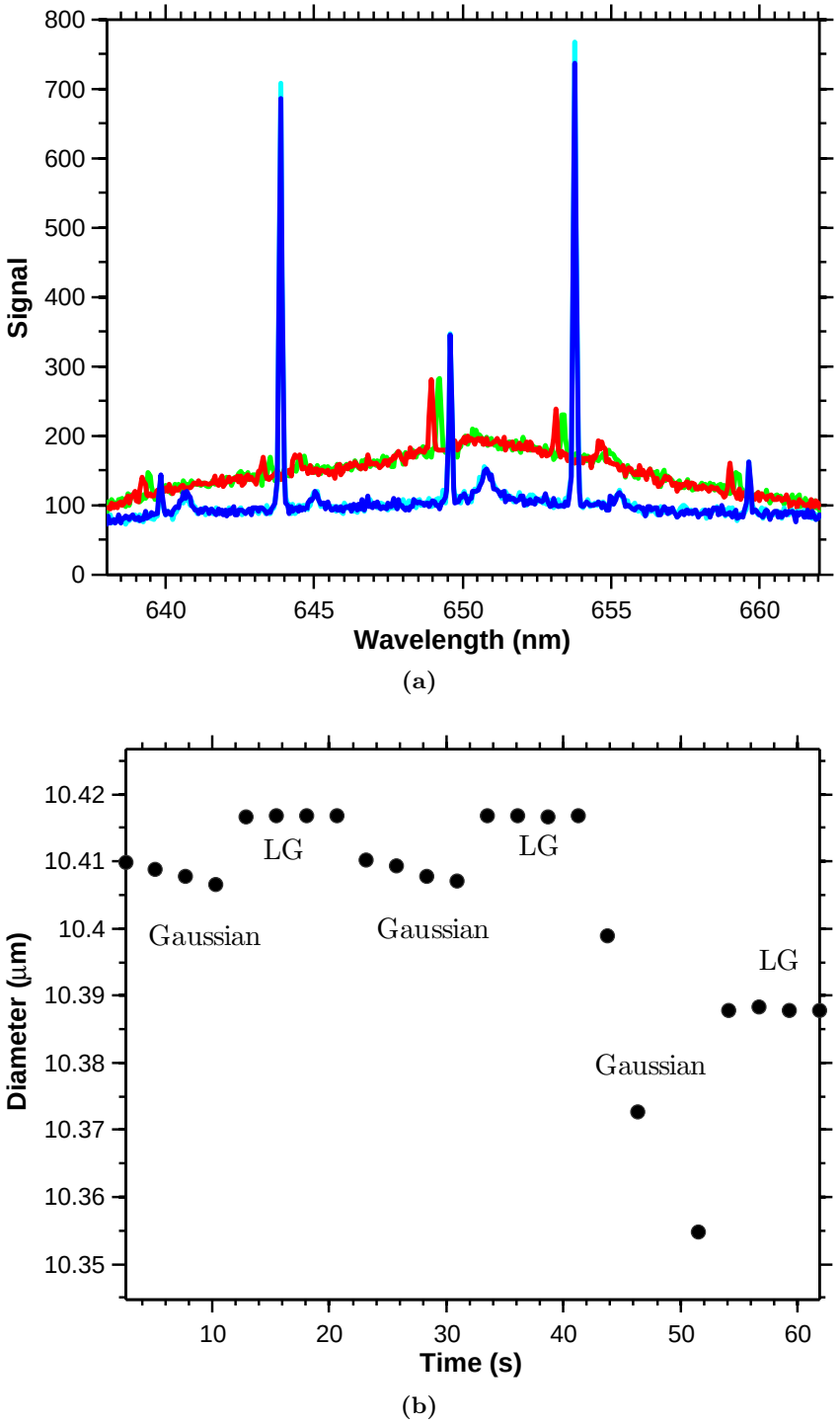

Figure 4.22: A demonstration of the observation that switching from an Gaussian beam to an LG beam ($\ell = 15$ in this case) suppresses evaporation of the droplet. In panel (a), there is a 10 s time period between the two Gaussian spectra (red and green), and a 10 s period between the two LG spectra (blue and cyan). Panel (b) shows the temporal variation in diameter, over a longer time period.

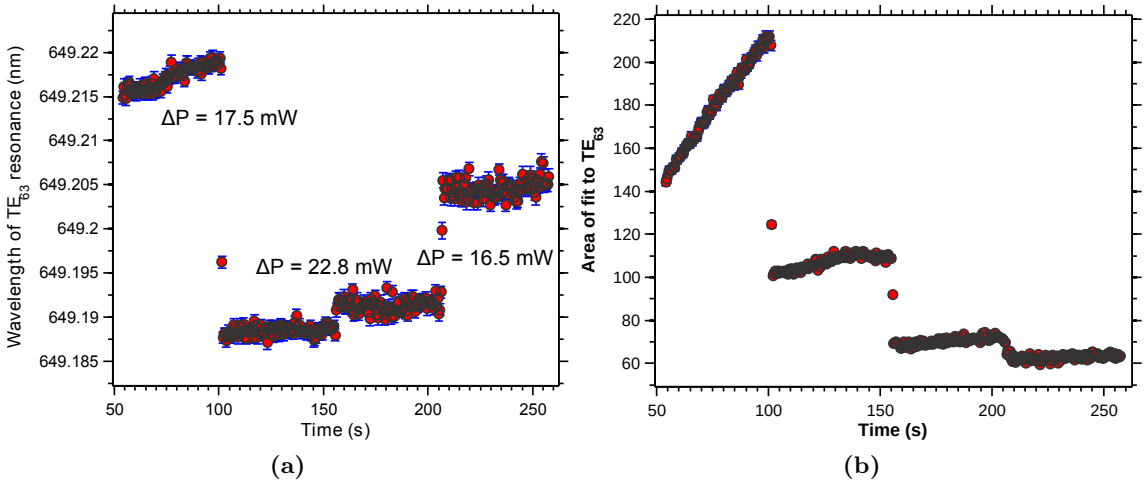

Figure 4.23: Effect of altering the trapping power on the central wavelength and intensity of the TE_{63} resonance while trapping with an $\ell = 20$ mode.

from 10.7326 µm to 10.7322 µm, i.e. a shrinkage of 0.4 nm. This corresponds to a loss of $\sim$ 2000 water molecue. Droplet evaporation is be expected due to the increase in laser absorption, i.e. non-resonant heating, however this is a surprisingly small change, given the magnitude of the change in power. It was also noted that the lateral position of the droplet, as observed via video microscopy, changed when the power was changed, with the droplet observed to spin at the highest trapping powers. Further increasing the trapping power in this instance *increases* the droplet size. However, as the droplet's position changed within the beam, the irradiance will be diminished, decreasing the degree of non-resonant heating and encouraging the modes to redshift. Generally note, however, that the intensity of the SRS signal decreases with increasing power; this is likely to be due to poorer overlap of the input and output fields due to the change in axial position of the trapped droplet. Previous measurements on SRS spectra also showed a decrease in SRS intensity as trapping power was increased [144], which was attributed to the increase in power driving the droplet further from the resonance condition.

While LG illumination clearly has been shown to suppress droplet evaporation, it should be noted that LG illuminated droplets themselves are not completely immune to evaporation. This is illustrated in Figure 4.24. Initially this droplet was 10.0698 µm in diameter, with a refractive index of 1.3502, and a corresponding salt concentration of 106 g L^{-1}. The closest 532.1 nm resonant diameter is 10.0707 µm (TM_{73}). Upon the switch from Gaussian to $\ell = 15$, the resonant modes blue shift (shown for a TM_{59} resonance) and increase in intensity, however this rapidly depletes as the modes continue to blue shift further until the modes are barely discernible over the spontaneous Raman signal.

In contrast, however, is Figure 4.25. This droplet was held stable in an $\ell = 15$ beam for

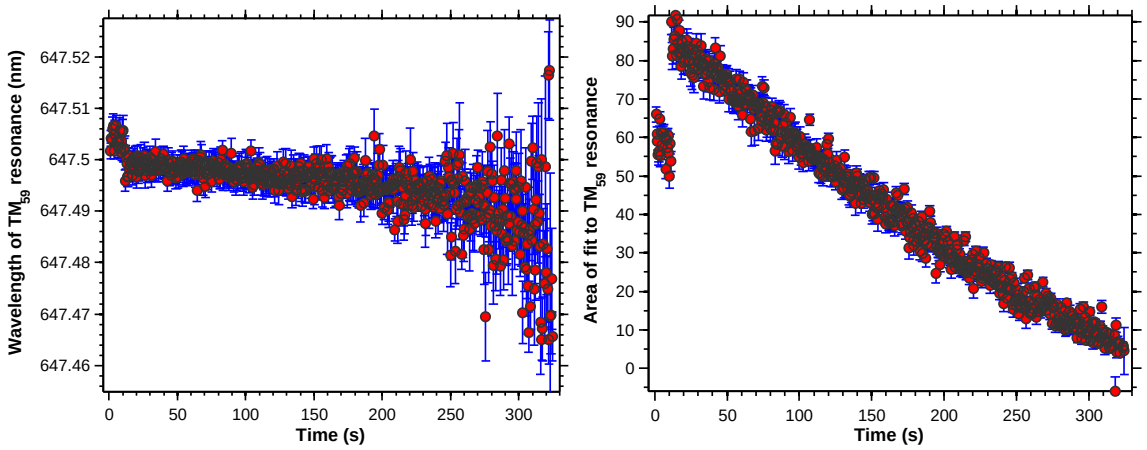

Figure 4.24: Unlocking of a droplet (i.e. evaporation) trapped with an $\ell = 15$ mode, that was initially trapped with a Gaussian beam.

nearly 2.5 hours, in a cell without active relative humidity control. To put this figure in context, no salt water droplets trapped with a Gaussian beam have been stably trapped in such a cell within our laboratory, for a time period of that magnitude. Initially, the droplet has a diameter of 9.759 µm, with a refractive index of 1.3466 and a salt concentration of 86.6 g L^{-1}. The closest resonance at the trapping laser wavelength is the TE_{71} resonance, which gives a diameter of 9.7596 µm (this value is obtained by utilizing a wavelength of 532.1 nm). Assuming that the refractive index is constant across the time period (owing to the very small changes in the resonance wavelengths), the diameter of the droplet as a function of time is plotted in Figure 4.25c. Note that the diameter of the droplet is decreasing as the integrated intensity of the modes increases, which is contrary to the observations for Gaussian locking periods, although the precise value of this diameter change is very small (< 1 nm). Even slight uncertainty in the trapping laser wavelength will change the theoretical resonant diameter to lie within/beyond this experimentally measured diameter range.

4.6.7 General Discussion

The data presented above has made it clear that changing the trapping beam profile from a conventional Gaussian beam to a Laguerre-Gaussian mode has a measurable effect on the stimulated Raman spectra of optically trapped aerosol droplets. This section shall attempt to rationalise the observations, in light of the observations made for a fluorescent microsphere in Section 4.6.2. As ever, the discussion begins by assuming that the droplet is in equilibrium with its surroundings, and that any external perturbation to the droplet will result in a change in its composition to restore equilibrium.

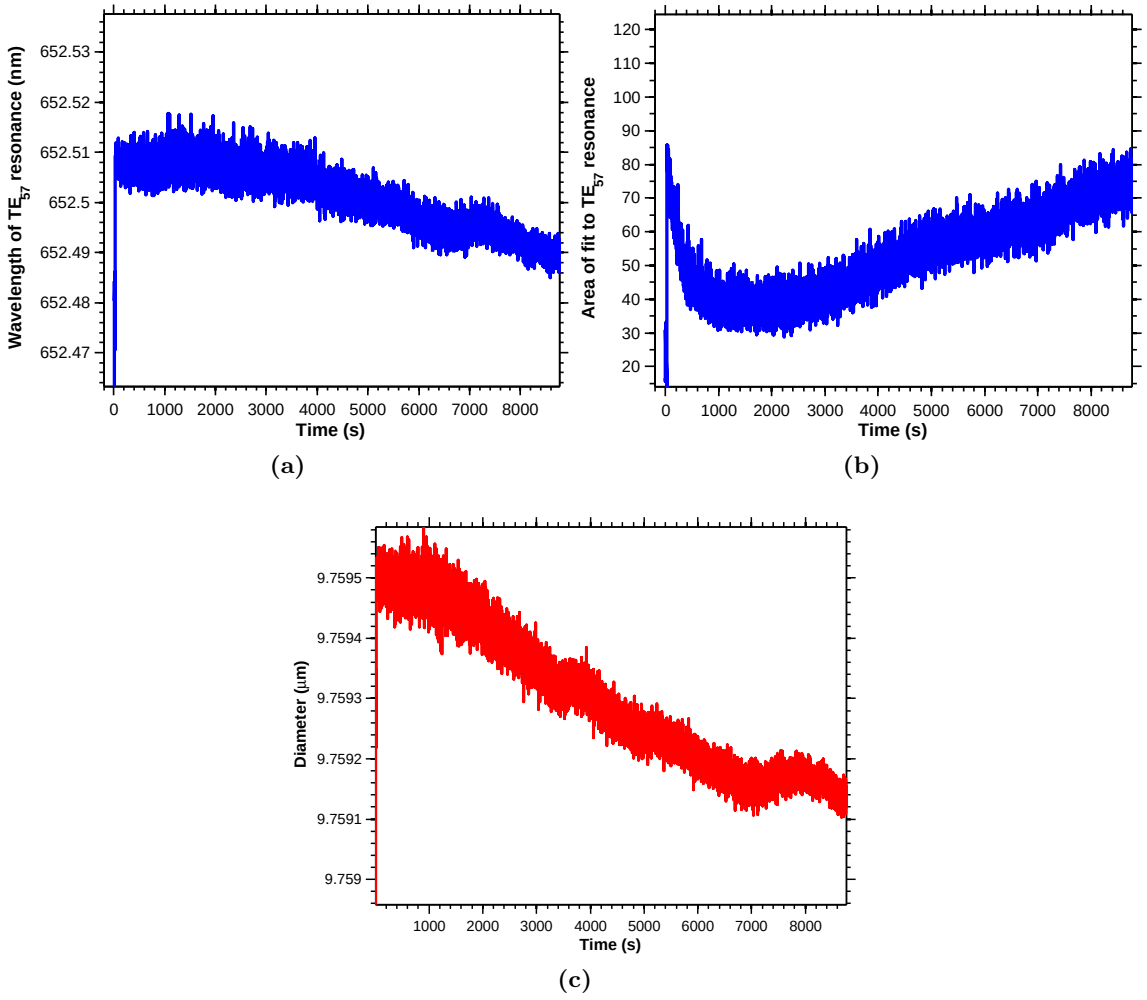

Figure 4.25: Spectral data for a droplet that was trapped in an $\ell = 15$ mode. The wavelength stability of this droplet is impressive for a non-RH controlled cell.

The first consideration is the effect on non-resonant heating upon switching to an LG mode. As the size of the LG mode scales linearly with ℓ, and assuming that the efficiency of the first order diffraction from the SLM is independent of the value of ℓ (this assumption is validated by a lack of observable change in the magnitude of the Raman signal of the immersion oil upon mode switching), progressive increases in ℓ simply results in a decrease in the overall intensity of laser radiation incident upon the particle. This conclusion is supported by the decrease in the integrated bulk fluorescence from dye doped polystyrene microparticles by a factor of 2–3 as ℓ is changed from 0–30 (see Section 4.6.2). Thus the temperature rise associated with non-resonant heating effects should be roughly half that for an LG mode compared to a Gaussian and, all other things being equal, a droplet should grow when the illumination mode is switched from Gaussian to LG; this behaviour is generally observed in much of the data with growth occurring on a timescale faster than the time response of the spectrometer.

While the non-resonant heating effects are diminished when using LG beams, coupling into WGMs is more efficient for this illumination mode than for Gaussian with the result that the SRS signals are of comparable magnitude for both cases despite the total illumination power being different by a factor of 2 or so. This observation indicates that resonant heating will be generally at least as large for the case of LG modes. Given that resonant heating generally dominates non-resonant heating in these systems, and locking is readily observed, it seems entirely reasonable that only small increases in droplet size will be observed when switching illumination modes and this is indeed the case where the changes are of the same order as those observed when the polarization of the locking mode changes. Once, again it should be emphasised that all of these changes correspond to very small number of added water molecules, in comparison to the average rate at which water molecules collide with the droplet surface, and these subtle but reproducible effects are only discernible given the high sensitivity of WGMs to changes in droplet size.

It should however be emphasised that switching to LG mode illumination does not always promote growth; the droplet dynamics also depend upon the direction and rate of size change prior to switching illumination modes as well as the polarisation of the locking mode as this also changes the magnitude of resonant heating. The above discussion also ignores the fact that the position of the droplet within the trap is clearly affected by switching to an LG mode—indeed the particle orbits within the trap for high ℓ modes. While SRS spectra are still readily observable with LG mode illumination, a change of trap position also subtly changes the coupling efficiency into WGMs, an effect that requires high level modelling to quantify. Note that similar SRS studies were conducted using sodium dodecyl sulphate solutions, which have a lower surface tension than salt water solutions; these measurements could not discern any effects of droplet deformation induced by trapping with LG modes.

4.7 Determining the local relative humidity using laser absorption spectroscopy

The work in the previous sections have been related to the dynamic properties of an aerosol droplet with respect to changing the trapping geometry. During the experimental runs, the ambient relative humidity was not characterised. This section aims to provide a measure of the relative humidity within the aerosol cell while a droplet is trapped, and investigate whether there are any measurable changes in this property during droplet growth/evaporation.

Previously reported measurements utilize different methods to determine the RH. For instance, experiments conducted at the University of Bristol utilize a capacitive RH probe

within the sample chamber to monitor the RH to an accuracy of ±2% [190]. Alternatively, the Raman spectrum of a control droplet (which has been trapped with the second beam of a dual-beam tweezers configuration), along with knowledge of the mass of solute present within the droplet, can be utilized to monitor the RH [100]. For a droplet of radius a in equilibrium with its surroundings, the RH may be expressed as [191]:

$$\mathrm{RH} = a_w \exp\left(\frac{2\overline{V}_w\sigma}{RTa}\right) \tag{4.22}$$

where $\overline{V}_w$ is the partial molar volume of water, and a_w is the activity of water in the solution comprising the droplet. However, if a droplet is not in equilibrium with the surroundings (e.g. it is growing or evaporating), then this method would not be valid.

This section shall present an alternative method of determine the relative humidity by utilizing diode laser absorption spectroscopy to determine the concentration of water vapour present within the sample cell. A brief overview of absorption spectroscopy will be provided, followed by measurements of water vapour in both the background laboratory air and in the aerosol cell. Concentration gradients within the cell shall be characterised, and the water vapour concentration monitored while a droplet is trapped.

4.7.1 Laser absorption spectroscopy

Consider two quantum states of a molecule, $|m\rangle$ and $|n\rangle$, separated in energy by $\Delta E = E_n - E_m = h\nu$. At this stage, the states are completely generic; they could refer to vibrational, rotational, electronic energy levels or combinations thereof. Interaction of electromagnetic radiation of frequency ν can result in the promotion of the molecule from state m to n (absorption). This excited state can reemit a photon to relax to m (spontaneous emission), alternatively the electromagnetic field can induce the emission of a photon and cause relaxation of the system back to m (stimulated emission). The rate of these processes are described by the *Einstein coefficients* B_{mn} (absorption), B_{nm} (stimulated emission) and A_{mn} (spontaneous emission) [192]. In fact, if $|m\rangle$ and $|n\rangle$ have the same degeneracy, the two Einstein B coefficients are equal, and at thermal equilibrium, A_{nm} is related to B_{nm} by $A_{nm} = 8hv\tilde{\nu}^3 B_{nm}$, where $\tilde{\nu}$ is the wavenumber of the transition. The transition between m and n will be optically allowed provided that the transition dipole moment integral (TDM), defined as $\mathbf{R}_{nm} = \langle n|\hat{\mu}|m\rangle$, is non zero. The rate of a transition is proportional to the square modulus of the TDM, hence providing the link between the Einstein B factor and the wavefunctions of the upper and lower states ($B \propto |\mathbf{R}_{nm}|^2$). Absorption of electromagnetic radiation will attenuate its intensity, providing the basis for experimental *absorption spectroscopy*. As the energy difference between the upper and lower states are determined by the molecular properties, absorption spectroscopy can provide a high degree

of specificity for molecular detection. Furthermore, it can give quantitative information about the absolute amount of molecular species present.

Absorption spectroscopy is quantified by the *Beer-Lambert law* [193]. Radiation incident of intensity I_0, incident upon a region of pathlength L containing a homogeneous distribution of absorbing species will have its intensity attenuated to an intensity I, via:

$$\ln \frac{I_0}{I} = \alpha(\nu)L \tag{4.23}$$

where $\alpha(\nu)$ is the frequency dependent absorption coefficient of the species. This is often written in the form $\alpha(\nu) = \sigma(\nu)C$, where $\sigma(\nu)$ is the absorption cross section of the species, present in a concentration[10] C. The absorption cross section is proportional to the Einstein B factor for that transition [194]. As absorption profiles have a finite linewidth, it is typical to integrate the absorption profile and quote the *integrated* absorbance, and hence describe a transition in terms of its *integrated* absorption cross section, σ_{int}. The units of the absorption cross section are usually quoted as $\text{cm}^2\,\text{cm}^{-1}\,\text{molecule}^{-1}$. In this work, a diode laser operating at $\sim 1.37\,\mu\text{m}$ is utilized to probe a strong vibrational transition in the water molecule at this wavelength; specifically the $v_1 + v_3$ combination band. The rotational transition $(3,1,3) \leftarrow (2,1,2)$ used occurs at $7306.75\,\text{cm}^{-1}$,[11] with $\sigma_{\text{int}} = 1.795 \times 10^{-20}\,\text{cm}^2\,\text{cm}^{-1}\,\text{molecule}^{-1}$.

4.7.2 Experimental method

To carry out these experiments, a different aerosol chamber was constructed. This was based upon a Thorlabs cageplate, which had three holes drilled through its sides to provide an aerosol inlet port, and two apertures for the laser radiation. The chamber was created by adhering two circular coverslips to the top and bottom of the cage plate using transparent nail varnish. As before, the coverslip forming the bottom surface was pre-treated with Decon 90 solution. A piece of moist tissue was inserted into the cell to replicate the conditions of the experiments described above.

The diode laser system utilized, comprising of laser, detector, driver electronics and acquisition software, is part of the *laser gas analyser* (LGA) developed within our group for breath diagnostics [195, 196]. Briefly, a 1368 nm fibre coupled diode laser (NTT Electronics, NLK1E5EAAA), controlled by commercially available current and temperature drivers (Thorlabs, LDC205B and TED200C respectively) is utilized as the source. The output

[10] For gaseous samples, the term concentration is often synonymous with the number density, N/V, where N is the number of molecules within a volume V.

[11] The terminology for a rotational transition is $(J', K'_a, K'_c) \leftarrow (J'', K''_a, K''_c)$, where K_a and K_c describe projections of J on the molecular rotational axis a and c respectively.

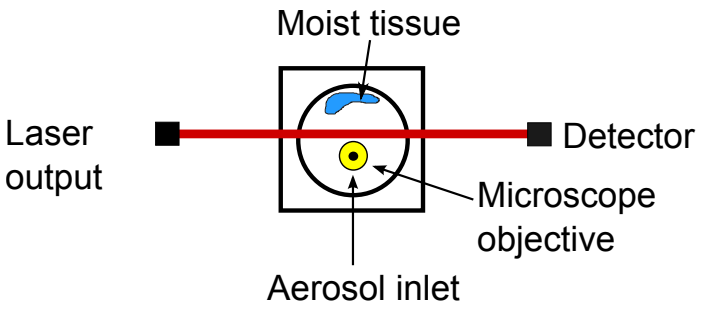

Figure 4.26: Experimental configuration of the laser-absorption spectroscopy experiment, as viewed from above.

of this laser is directed through the aerosol chamber, onto an InGaAs photodiode (Hamamatsu, G8372-01). The laser current is altered in order to scan the laser wavelength across the transition, and data acquisition is carried out by a custom written LabVIEW software. The response time of the water analyser was set to 20 ms. The cell is oriented on top of the microscope objective such that the diode laser beam is probing the air between the piece of tissue paper, and the droplet. This is shown schematically in Figure 4.26; the output coupler for the fibre-coupled diode laser is positioned outside the cell. The total pathlength traversed by the laser is 7.5 cm, of which 4.06 cm corresponds to the aerosol chamber.

An example of the raw data is shown in Figure 4.27a. This specific set of data was taken without the aerosol cell in place, and hence corresponds to the absorption of water vapour in the laboratory air. The plotted signal is an average over a 5 s acquisition time; each individual acquisition spanned 20 ms. The absorption due to water vapour in the atmosphere can clearly be observed over the background laser signal, which increases in intensity (reflecting a greater output power) as the laser is scanned. To define I_0 for the absorption, a second order polynomial was fitted to the background signal. The absorbance for each data point was then calculated *via* $\ln(I_0/I)$. The x axis of this graph is in time, and must be converted to a frequency scale before quantitative measurements on the absorption can be made. This was achieved with an optical spectrum analyser with a FSR of 7.5 GHz (CVI, 35AE036). The conversion from time (t) to relative frequency ($\tilde{\nu}$) is performed by the following polynomial:

$$\tilde{\nu} = -0.005515 + 610.1t + 62823t^2 + 5.935 \times 10^6 t^3 \tag{4.24}$$

The resulting absorption spectrum is shown in Figure 4.27. A Lorentzian profile is fitted to this spectrum, as at atmospheric pressures the lineshape will be dominated by pressure broadening (the Doppler width is $0.02\,\mathrm{cm}^{-1}$ at 298 K, while the width of the line in Figure 4.27 is $0.2\,\mathrm{cm}^{-1}$). The resulting area from the fit defines the integrated absorbance, which is equal to $\sigma_{\mathrm{int}}CL$. The corresponding water concentration is $(3.96 \pm 0.03) \times 10^{17}$ molecules cm^{-3}, where the uncertainty comes from the standard error in the Lorentzian fit,

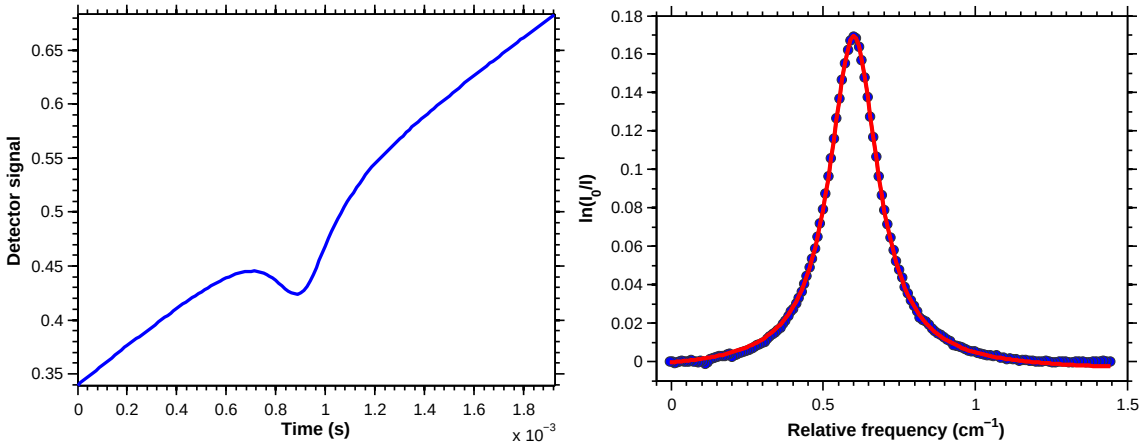

(a) Raw data **(b)** Absorption spectrum

Figure 4.27: Example of the data produced by the LGA for laboratory air. The red line in panel (b) is a Lorentzian fit to the experimental spectrum.

as well as uncertainty in the laser pathlength. Assuming that the water vapour behaves as an ideal gas, the partial pressure of water vapour is 16.2 ± 0.1 mbar.

To convert this partial pressure into a value of RH, the saturated water vapour pressure (p°) needs to be calculated. An empirical formula for this was determined by Lowe and Fick [197], and is given by:

$$p^\circ(T) = a_0 + a_1 T + a_2 T^2 + a_3 T^3 + a_4 T^4 + a_5 T^5 + a_6 T^6; \tag{4.25}$$

where the pressure is in mbar, and T is the temperature in °C. The coefficients are given in Table 4.8. During these measurements, the laboratory temperature was measured to be 23.7 °C, giving a saturated vapour pressure of 28.1 mbar, i.e. a relative humidity of $55.3 \pm 0.4\%$.

Table 4.8: Parameters to determine the saturation vapour pressure of water from Equation 4.25.

Parameter	Value
a_0	6.1078
a_1	$4.436518521 \times 10^{-1}$
a_2	$1.428945805 \times 10^{-2}$
a_3	$2.650648471 \times 10^{-4}$
a_4	$3.031240396 \times 10^{-6}$
a_5	$2.034080948 \times 10^{-8}$
a_6	$6.136820929 \times 10^{-11}$

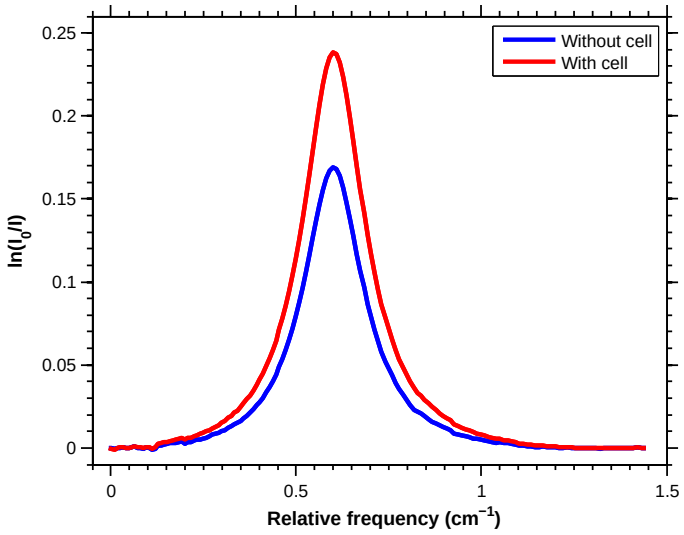

Figure 4.28: Absorption spectrum of water vapour, both without and with the aerosol cell in place. The increase in the total absorption when the cell is present, owing to the presence of the moist tissue and the thin water layer on the lower surface of the chamber, is apparent.

4.7.3 Results and discussion

Having established the water concentration in the laboratory air, it is now possible to insert the aerosol chamber (containing the moist tissue and a thin layer of water on the lower surface) to determine the increase in water vapour concentration that an optically trapped aerosol will experience. The resulting spectrum (alongside the background spectrum, for comparison) is shown in Figure 4.28. The increase in absorption due to the higher concentration of water vapour along the pathlength of the laser is apparent; the integrated absorbance is now 0.0774, compared to the background absorbance of 0.0533. Using the Beer-Lambert Law, the resulting water concentration with the cell in position is $5.75 \pm 0.04 \times 10^{17}$ molecules cm^{-3}, an increase of 1.8×10^{17} molecules cm^{-3} over the background air. This would equal a partial pressure of 23.5 ± 0.2 mbar, hence an RH of $80.36 \pm 0.59\%$, averaged over the whole pathlength of the cell. It is noted, however, that this is a lower bound on the RH within the cell. As the laser apertures and aerosol inlet port are unsealed, water molecules will necessarily diffuse out of the aerosol cell and along the beampath of the probe laser. As a consequence, it is not possible to infer a water concentration within the dimensions of the cell itself.

The next stage in characterising the water vapour within the cell is to determine the variation in the concentration across the cell, perpendicular to the probe laser propagation axis. This was achieved by positioning the cell on the tweezers translation stage with the laser beam at the edge of the window closest to the moist tissue, such that the beam was not clipping the edge of the window. The stage position was then manipulated using the

micrometers, in 0.5 mm increments, with an absorption spectrum recorded at each position. The resulting integrated absorbances are plotted in Figure 4.29a. A clear decrease in signal is observed as the laser is moved away from the tissue and towards the aerosol inlet window (which is exposed to laboratory air), with the absorbance decreasing by $\sim$ 10% over a distance of $\sim$ 1 cm. The resulting water vapour concentration is plotted in Figure 4.29b.

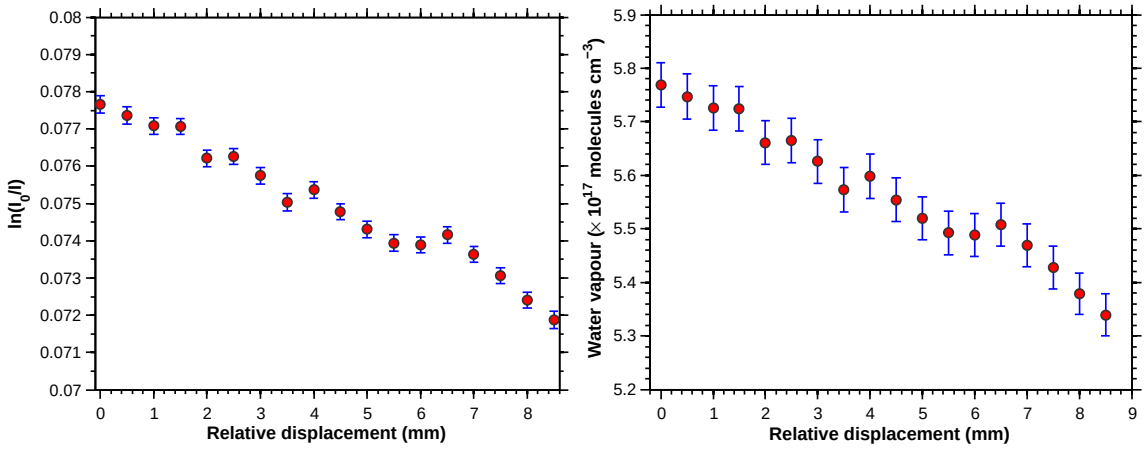

(a) Absorption over whole path length.

(b) Water vapour concentration.

Figure 4.29: Variation of the laser absorption (and hence water vapour concentration) over the dimensions of the window in the cell.

The next stage of these measurements is to follow the water concentration while an aerosol droplet is trapped. The SLM was not utilized for these measurements; trapping was carried out with a basic tweezers, such as in Figure 2.3. The background water vapour concentration while the droplet was trapped was measured to be $4.39 \pm 0.03 \times 10^{17}$ molecules cm^{-3}, hence the RH was 61.4 $\pm$ 0.46%. A representative Raman spectrum of the droplet is shown in Figure 4.30a, and the variation of the WGM positions plotted in Figure 4.30b. The clear blueshifting indicates droplet evaporation, which is unsurprising given that three of the cell walls are open to the laboratory atmosphere. To characterise the local humidity while the droplet was trapped, an absorption spectrum was recorded every 20 ms for the duration of the experimental run (8.5 min); ten consecutive spectra were recorded, and their signals averaged. The resulting variation in water concentration (again, relative to the background air in the laboratory) is plotted in Figure 4.30c. A near constant water vapour concentration of $6.05 \pm 0.02 \times 10^{17}$ molecules cm^{-3} is observed,[12] despite the droplet overall evaporating. The overall decrease in droplet diameter over the course of the measurement is 62 nm. The fact that a bulk measurement of the water vapour concentration reveals a near constant concentration over the result of the measurement, while the measured SRS wavelengths clearly indicate evaporation, highlights the exquisite sensitivity of WGMs to the surrounding environment. This is unsurprising; the change in droplet diameter

[12] The quoted value is mean $\pm$ standard deviation.

during this measurement corresponds to a volume change of $9.2 \times 10^{-18}\,\mathrm{m}^3$. The change in droplet mass would be approximately $9.2 \times 10^{-12}\,\mathrm{g}$, corresponding to a difference of 3×10^{11} molecules, i.e. considerably less than the concentration of water vapour present within the air.

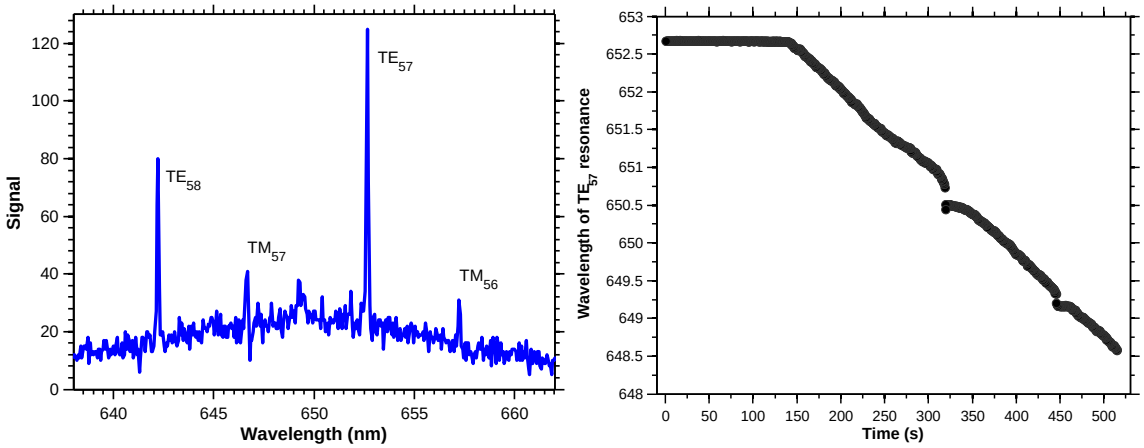

(a) Assigned WGM spectrum of droplet (at $t = 0$.

(b) Variation in WGM position.

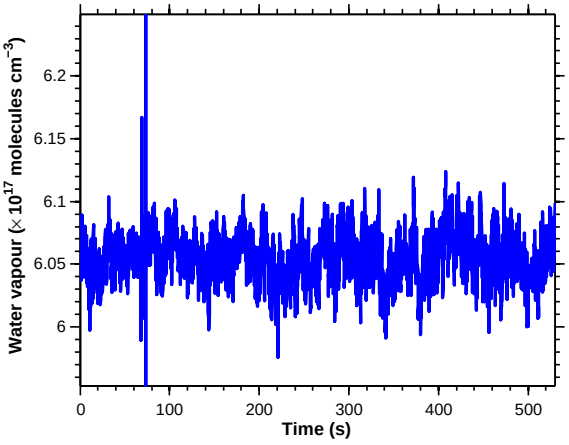

(c) Increase in water vapour, relative to background laboratory air

Figure 4.30: Variation in the water concentration increase, with an optically trapped aerosol.

For a final set of measurements, an attempt was made to increase the local relative humidity by adhering thin glass coverslips to the sides of the cell with transparent nail varnish, over the probe laser entrance and exit windows. While glass is not wholly transparent to infrared radiation, the attenuation over the wavelength range of the diode laser was a constant and should not affect the absorbance measurements. While this droplet was trapped, the laboratory air concentration was determined to be $4.06 \pm 0.03 \times 10^{17}\,\mathrm{molecules\,cm}^{-3}$, corresponding to a lab RH of 56.8 ± 0.4 %. With the cell in place, the RH measured across

the whole pathlength is 91.3± 0.7%, highlighting that the glass coverslips are effective at containing the water vapour within the cell.

4.7.4 Conclusions and future work

This section has applied laser absorption spectroscopy towards the measurement of absolute water vapour concentration within an aerosol cell whilst a droplet is optically trapped, with a higher accuracy than conventional capacitive probe measurements. Even without a relative humidity controlled cell, high water vapour concentrations were measured within the cell. Additionally, concentration gradients due to the open cell have been measured. Aerosol dynamics are not changed by the range of bulk RH values within the cell, and none of the subtle growth/evaporation dynamics observed are determined by long term changes in the RH within the cell.

Future measurements should aim to measure the absolute water concentration within the cell. The first step towards this is to minimize the path length between the laser output and the detector. The cell itself should be extremely well sealed with windows that are transparent to IR radiation, such that no water can diffuse from the sealed sections.

4.8 General Conclusions

This chapter has provided an in-depth study of some characteristics of the Raman spectroscopy of optically trapped salt water droplets. Droplets that were trapped with a conventional Gaussian beam within a non-RH controlled cell were shown to both evaporate and grow, depending upon the specific conditions within the cell. The growing periods are dominated by periods of droplet size stability, termed locking, and the observed measurements are consistent with previous measurements reported in the literature, thus confirming that the custom constructed optical tweezers/spectroscopy set up is functioning correctly. The diameter difference between successive modes is a function of the polarisation of the locking mode, and further evidence for the locking phenomenon comes from the observation of transient locking to a second order resonance. The SLM was then utilized to investigate the spectral response of a droplet to LG trapping/excitation. Switching between Gaussian and LG illumination was observed to cause the droplet to "mode hop" between different diameters. LG modes with a topological charge > 10 were observed to give much more intense SRS spectra, and could be utilized to suppress evaporation of the droplet by locking to a resonant diameter at the trapping laser wavelength. Finally, laser absorption spectroscopy was applied to the aerosol cell in an effort to determine the local relative humidity experienced by a trapped droplet and to determine the extent of any spatial gradients in

the RH. These latter experiments will be of use in interpreting the experimental results presented in the next chapter.

Chapter 5

Optical trapping and spectroscopy of Ionic Liquids

Salts which exist in the liquid phase at room temperature are known as *ionic liquids* (ILs). These liquids have many fascinating properties and potential applications in chemistry. In this chapter, these properties and applications shall be briefly reviewed, followed by a demonstration of the optical trapping and spectroscopy of aqueous solutions of the ionic liquid *ethylammonium nitrate* (EAN), as a first step towards the trapping and characterisation of pure ILs. This is of interest from a "lab on a chip" analysis context to assess the purity of an IL sample, owing to the very small volumes involved for an optically trapped droplet. Furthermore, the trapping and analysis of individual droplets of pure ILs would be crucial for investigating their potential to sequester industrial and greenhouse gases.

5.1 History and properties of ionic liquids

Ionic liquids were first developed in 1914 with the synthesis of ethylammonium nitrate (EAN) by Walden [198], however they remained largely ignored for the majority of the 20^{th} century, until the discovery of binary ILs that were made from mixtures of aluminum (III) chloride and N-alkylpyridinium in 1975 [199] and with 1,3-dialkylimidazolium chloride in 1982 [200]. The structure of an IL typically consists of bulky organic cations and anions [201], with no requirement for a molecular solvent. They exhibit an extremely low volatility compared to traditional organic solvents, with an almost immeasurable vapour pressure [202], and are highly effective solvents in their own right [203], hence are widely touted as 'green' solvents [204]. Further attractive properties include low flammability [205], high thermal stability and a large liquidus region (where the term liquidus is defined as the range of temperatures between the normal melting and boiling points) [206]. It should

be stressed, however, that ILs themselves are *not* inherently "green" liquids (they could easily be designed to utilize toxic compounds such as cyanides); their attraction lies in their potential to contribute to green chemistry by, for instance, reducing the amount of volatile organic compounds (most conventional solvents fall into this category) discharged into the atmosphere.

The physical properties of ILs, such as viscosity, hydrophobicity, density and melting point can be altered by changing the composition of the ions [205], hence ILs have developed the label of "designer solvents" [207]. For instance, the melting points of 1-alkyl-3-methylimidazolium tetrafluoroborates depend on the length of the alkyl chain [208]. As a flavour of some of the wide applications of ILs, they have been utilized in organic synthesis [209], synthesis of nanoparticles [210], industrial lubricants (where their high thermal stability and neglible vapour pressure make them ideal for extreme environments) [211] and chemical processing [206]. They have extensive uses in materials science, both as advanced materials in their own right, and as advanced media for further material production [212]. An interesting and relevant property of ILs is their ability to sequester gases such as CO_2 [213–215], SO_2 [216] and N_2O [217]. These gases are particularly relevent as they are post-combustion waste products, and are greenhouse gases. Two recent comprehensive, open source volumes of research stand as a testament to the vast amounts of contemporary interest in ILs in chemical and materials science [218, 219]. As well as being readily synthesised in house, ILs are widely available commercially; however a serious limitation is the difficulty of obtaining highly pure IL samples in large volume [220].

Optical tweezers are a prime candidate for the characterisation and analysis of IL samples, particularly those only produced in small quantities, owing to their ability to perform micro-rheology as well as being readily coupled with spectroscopic techniques, yet there appears to have been little research done on the properties of ILs using tweezers. Recently, forces between single negatively charged microspheres within aqueous solutions of water miscible IL solutions have been measured utilizing optical tweezers [221]. Micro-rheology utilizing tweezers would provide a useful method of assessing the local physical properties (such as viscosity, and any micro-heterogeneity) of ILs; the small volumes ($\sim 10\,\mu$L) of IL required also provide a significant advantage over bulk techniques [222], as a smaller amount of pure IL would need to be synthesized. The generation and trapping of IL droplets is of interest as the volume scales involved are further reduced (fL), and the exquisite sensitivity afforded by a combination of Raman spectroscopy and WGMs would provide an excellent method for assessing the purity of the liquid. Furthermore, droplets of different composition could be coagulated to initiate chemical reactions within a micro-reactor, with the extent of reaction monitored via conventional spectroscopic techniques (such as Raman spectroscopy), or through the use of WGMs (exploiting their sensitivity to local refractive index variations). The uptake of gases could also be monitored, to assess the viability of IL droplets in

sequestering post-combustion flue gases, again utilizing changes in the droplet's spectrum to measure the change in composition of the droplet.

The work in this chapter presents the first known trapping of aqueous ionic liquid solutions, specifically of EAN. These droplets are characterised using broadband Mie scattering, to determine their size and composition. Their response to different relative humidity environments is investigated, and compared with the results of conventional salt water droplets from Chapter 4. Finally, a comparison between Mie scattering and cavity-enhanced Raman spectroscopy (CERS) is presented.

5.2 Optical trapping of ethylammonium nitrate solutions

The ionic liquid used for this study was ethylammonium nitrate (EAN), and was obtained from a specialist IL manufacturer (io-li-tec) and utilized without further purification. The SLM was not used for optical trapping; droplets were trapped using the 532 nm laser in a basic optical tweezers configuration, such as that presented in Figure 2.3. Owing to their high viscosity, it was not possible to nebulize pure ILs with the handheld nebulizer utilized in the work presented in the previous chapter. As a workaround, it was decided to dissolve the IL within a solvent as a carrier, taking inspiration from commercial aerosol cans. Ethanol was a good solvent for EAN, however its own viscosity (which is greater than water) made nebulization difficult. Organic solvents like acetone, and ethyl acetate, were also good candidates for dissolving ILs, and their lower viscosities means that nebulization should not be problematic. However, these organic solvents were not compatible with the plastic of the handheld nebulizer, resulting in complete disintegration of the nebulizer head. As a result, water had to be used as the solvent for the IL.

Pure ILs have relatively high refractive indices; for instance, EAN has a refractive index of 1.452 [223]. To characterise the refractive index of aqueous solutions of EAN, bulk solutions were made by diluting pure EAN with MilliQ water by volume. The refractive indices were measured using an Abbe refractometer (Reichert, Mark II Plus), and are plotted in Figure 5.1 as a function of the mole fraction of EAN (which was determined using the density of EAN, $1.2191\,\mathrm{g\,cm^{-3}}$ [223]); the results are consistent with the data for mixtures of other ILs with water and ethanol of Cabeza *et al.* [224]. A fit to the resulting data was performed via the following equation:

$$n_{\mathrm{sol}} = n_0 + (n_\infty - n_0)\frac{x}{k + x} \tag{5.1}$$

where x is the mole fraction of EAN in the bulk solution, and n_0, n_∞ and k are fitting parameters. The best fit values for these parameters are tabulated in Table 5.1.

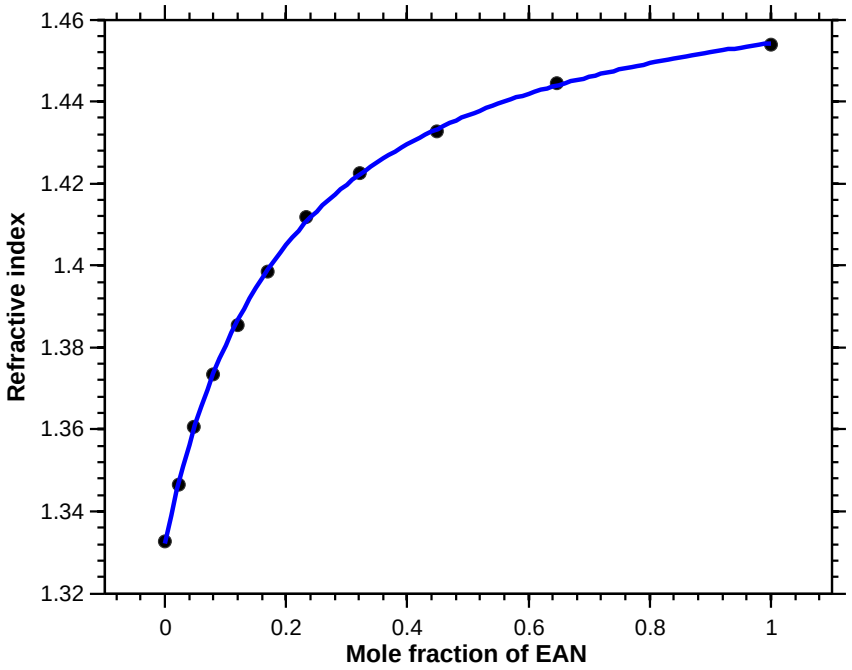

Figure 5.1: The refractive index of bulk solutions of EAN and water, as a function of the mole fraction of EAN. The fit to the data is described in the text.

Table 5.1: Values of the fitting parameters in Equation 5.1 for the data presented in Figure 5.1.

Parameter	Value	Standard error
n_0	1.33204	8.57×10^{-4}
n_∞	1.47903	0.00111
k	0.20288	0.00597

The viscosity of EAN solutions increases with mole fraction of EAN [225], and it was found experimentally that concentrations greater than 50% by volume EAN (corresponding to a mole fraction of 0.17) were too viscous to be nebulized with the handheld nebulizer. As a result, all of the following experiments utilize 50% EAN as the most concentrated solution.

Once a solution was nebulized, droplets could readily be trapped using optical tweezers. The axial trapping efficiency, Q_{axial}, was determined for a series of different EAN concentrations by trapping the droplet and then slowly reducing the trapping power (utilizing the half-waveplate/PBS) until the droplet *just* falls out of the trap. The power was measured on the beam dump arm of the PBS; the difference between the power measurement when the droplet falls out of the trap, and the maximum power, corresponds to the minimum trapping power propagating through the optical train of the trapping arm. To facilitate this measurement, a neutral density filter (with OD = 1, Thorlabs NE10A) was positioned within the trapping arm of the PBS output. This allows a greater discrimination between the small minimum trapping powers. By accounting for the optical losses across the optical

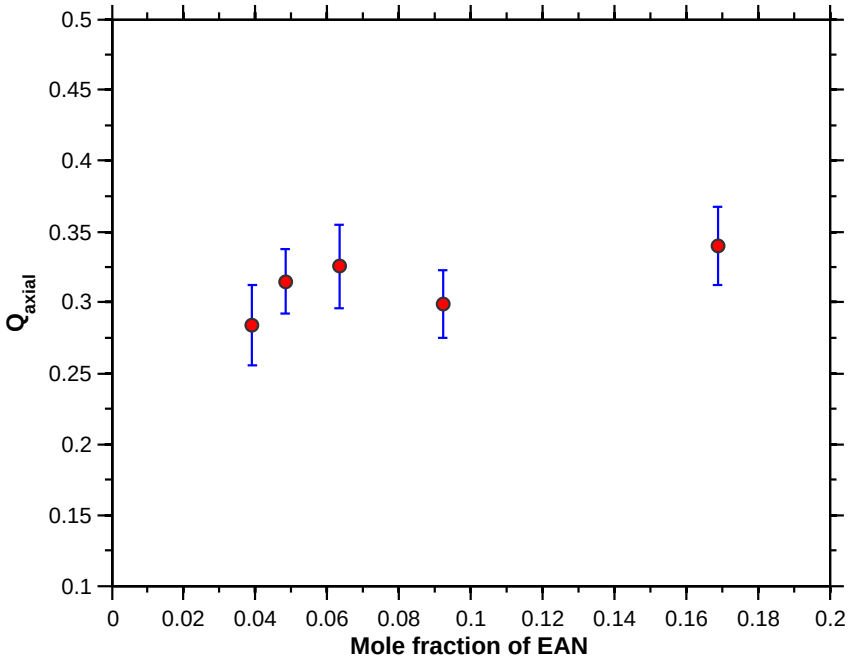

Figure 5.2: Experimentally measured Q_{axial} values for different concentrations of EAN solution. A value for Q_{axial} was determined for ten droplets at each concentration, and the average value quoted. The error bars are the standard error in the mean.

train (including the loss due to the ND filter, and the objective), the minimum trapping power (P_{min}) was determined. This value was utilized in Equations 2.9 and 2.10 to determine Q_{axial} for that droplet. The droplet's diameter was measured using calibrated video microscopy, and its density was estimated by assuming it to be equal to the bulk solution comprising the droplet. For each concentration, ten droplets were trapped, and their Q_{axial} values determined. The resulting average values are plotted in Figure 5.2, where the error bars are the standard error in the mean. Surprisingly, there appears to be little difference between the measured values of Q_{axial}, and previous measurements of salt water droplets [95], despite the increase in refractive index (a dependence of trapping efficiency upon refractive index would be expected as the optical forces, calculated within the ray optics limit, depend upon the Fresnel coefficients of reflection and transmission, which in turn depend upon the refractive index contrast). To confirm these measurements, theoretical plots of F_{min} *vs* droplet diameter were determined, utilizing the model of Burnham and McGloin [167] (which calculates the efficiency of momentum transfer from the laser to the particle; the resulting minimum trapping force calculated *via* Equation 2.9), accounting for both the increase in refractive index and density for the EAN solutions. Two such plots are shown in Figure 5.3, alongside the experimentally measured data. A good agreement between the theoretical plot and the experimental data is observed; furthermore the invariance of the axial trapping efficiency with droplet composition is confirmed by the theoretical plots.

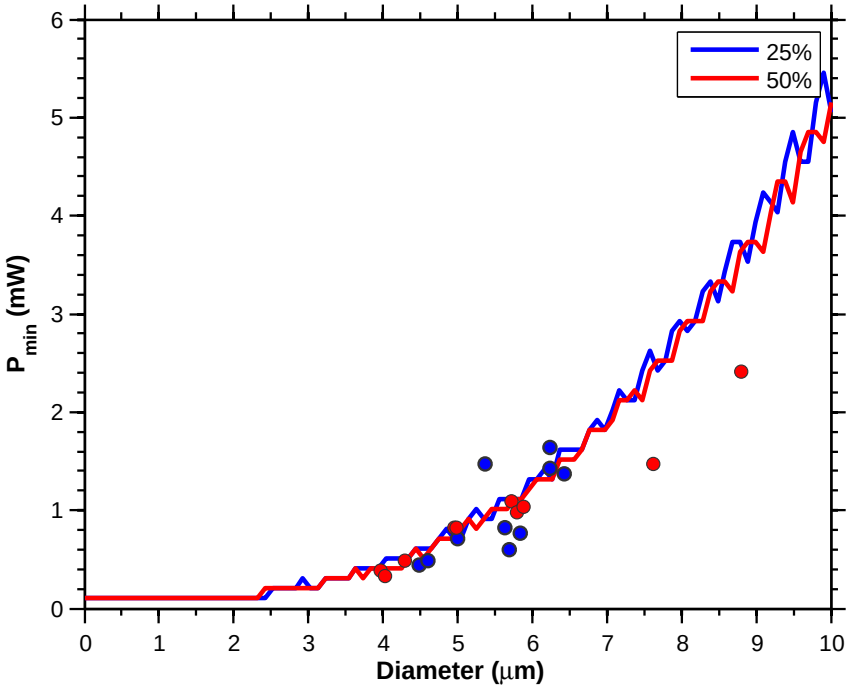

Figure 5.3: The minimum trapping power versus droplet diameter for two different concentrations of EAN. The circles are experimentally measured values, while the solid line is calculated using the model of Burnham and McGloin [167].

5.3 Spectroscopy of EAN droplets

Having established that droplets of EAN solution can be stably trapped, the focus is now shifted towards characterising these droplets spectroscopically. Cavity enhanced Raman spectroscopy on droplets of pure EAN of the sizes readily trapped by optical tweezers ($d =$ 5 µm to 10 µm) would be limited by the fact that, unlike in water molecules, the Raman bands of EAN are relatively narrow. Therefore, a minimal number of WGMs would be observed in its spectrum. Furthermore, the band with the highest gain is the C-H stretch, which overlaps with the spontaneous Raman emission from the immersion oil utilized for the microscope objective. To overcome this, it was decided to utilize broadband Mie (BB-Mie) scattering to characterise the droplets. Ward *et al.* have previously used this technique in studies of optically trapped salt water droplets [226], illuminating the droplet with the emission from a broadband LED and analysing the backscattered light from the droplet. The morphology dependent resonances (MDRs) from the droplet were clearly visible, and assigned using a similar strategy to that outlined in Chapter 3. The spectrometer configuration utilized for these experiments was described in Section 2.7, and is as shown in Figure 2.12. Two examples of BB-Mie spectra, obtained from solutions of EAN utilizing the tweezers/spectroscopy arrangement, are presented in Figure 5.4. Theoretical scattering efficiencies are also presented for comparison; note that the difference between the baseline

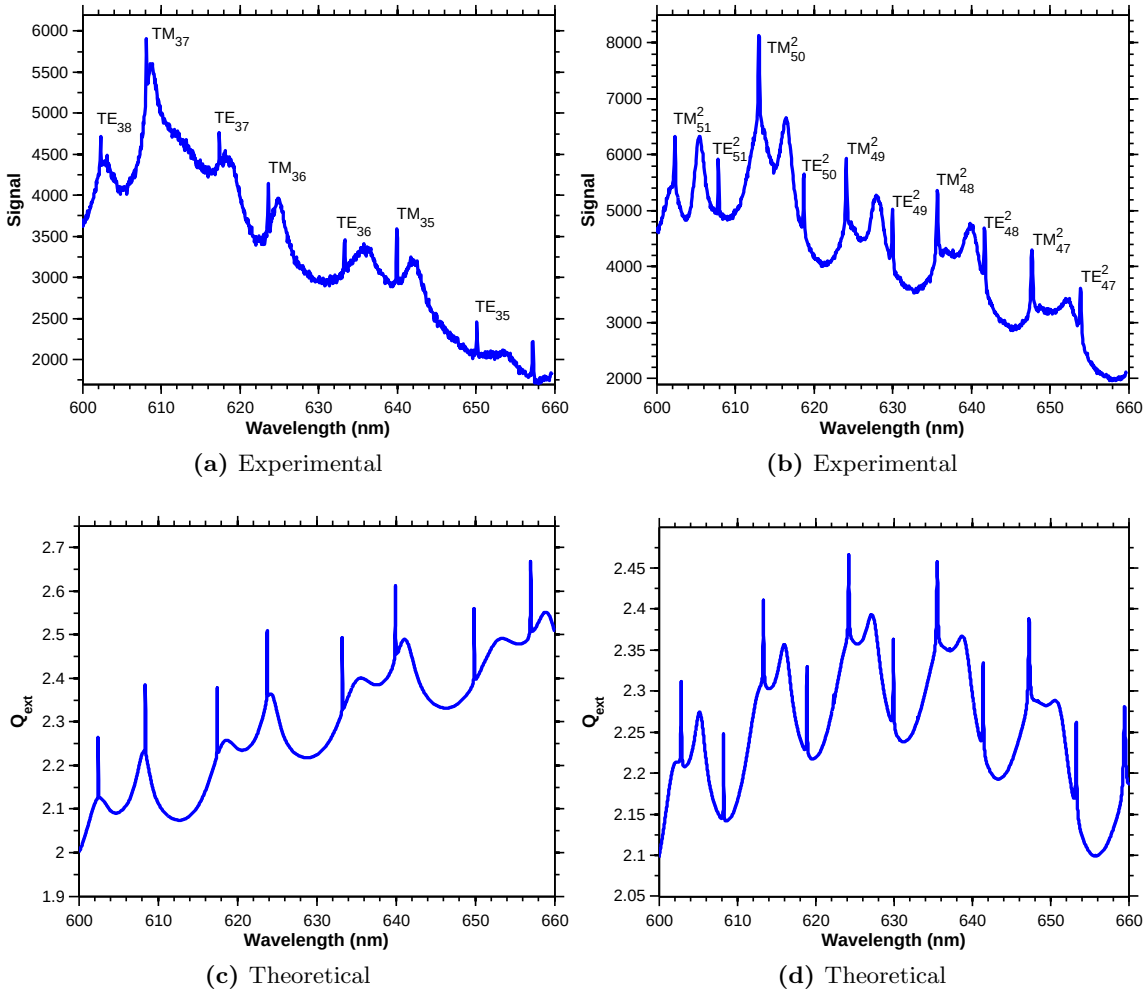

(a) Experimental **(b)** Experimental

(c) Theoretical **(d)** Theoretical

Figure 5.4: Two examples of broadband Mie scattering spectra from aqueous EAN droplets. Panel (a) corresponds to a droplet of 5.88 µm in diameter, with sharp first order resonances. Panel (b) shows a droplet of 8.53 µm diameter; here the sharp resonances are second order, with no visible first order modes. Panels (c) and (d) show theoretical extinction efficiencies, generated using the assignment parameters.

between theory and experiment is a consequence of the LED's spectral profile, and the reflectance of the red reflector utilized in the spectrometer arm of the cage system.

5.3.1 Spectroscopy of EAN droplets under conditions of varying relative humidity

Initial experiments were performed under conditions of varying relative humidity, to investigate the response of the droplet to different environments. This characterisation is an important step towards measuring the uptake of water and other impurities by IL droplets.

5.3.1.1 General comments on the MDR assignment

Before proceeding to discuss the BB-Mie spectroscopy of EAN droplets, it is prudent to take a moment to discuss how the assignment procedure for these droplets is different to the Raman studies of Chapter 4. The first, most obvious difference is the much wider spectral window; for BB-Mie the entirety of the spectrometer CCD (which spans 60 nm with the specific grating utilized) is illuminated by scattered light from the droplet, therefore there are more MDRs present to facilitate analysis. In contrast, there is only an approximately 30 nm envelope within the Raman band of water in which to observe WGMs. This is not to say that BB-Mie spectroscopy is inherently superior to CERS; one advantage that CERS has over BB-Mie is that the intensity of the SRS resonances is a function of the Raman gain profile and degree of overlap between input and output fields, as was demonstrated by the increase in SRS intensity during Gaussian locking periods in Chapter 4. No such information is available from BB-Mie resonances, as their intensity will show no variation owing to the technique relying on light scattered by the droplet.

Due to the strong dependence of the refractive index on droplet composition, the position of the MDRs (in size parameter space) will show a considerable variation as the droplet changes size. In order to facilitate a full MDR assignment, a two stage process was adopted. Initially, the resonances for a coarse range of refractive indices (1.34–1.45, in 0.01 increments), which were precalculated and called into the assignment script, were utilized to gain a rough estimate of the droplet diameter and refractive index. A refined value of the diameter and the refractive index (to an accuracy of 10^{-4}) are obtained in the second stage of the analysis procedure. The refined refractive index will lie within ± 0.01 of the coarse value, but rather than precalculating the necessary resonances, a function that describes the location of a resonance of a given mode number and polarisation as a function of the refractive index was determined by fitting second order polynomials to the coarse dataset. Therefore, the variation of the resonance size parameters with refractive index can easily be determined without requiring copious amounts of computational time.

As a final note specific to the analysis of IL droplets, there are no reported measurements of the refractive index dispersion of EAN solutions. Therefore, the correction procedure outlined in Section 3.3.2 cannot be utilized. Dispersion effects on the fitting residual Δ will be more pronounced due the broadband nature of the LED, although the greater number of resonances does provide a more rigorous test of the best-fit diameters. As a consequence, all analysis in the following section has been performed without considering dispersion. Simulations for a salt water droplet, such as Figure 3.6, suggest that the assigned diameters will be around 100 nm larger than their true size.

5.3.1.2 Trapping under low relative humidity

Low relative humidity conditions were achieved by adhering some silica gel particles to the upper surface of the aerosol trapping cell. The initial aim for this conditioning was to drive off as much water from the EAN solution as possible. The degree of dehumidification was determined by utilizing diode laser absorption spectroscopy (Section 4.7). Without the cell in place, the water vapour concentration was $4.32 \pm 0.03 \times 10^{17}$ molecules cm^{-3}, corresponding to an RH of $60.3 \pm 0.4\%$. When the cell containing silica gel was positioned within the diode laser beam path, the measured water vapour concentration fell to $3.67 \pm 0.03 \times 10^{17}$ molecules cm^{-3}, i.e. an RH of $51.5 \pm 0.4\%$. As noted in the previous chapter, this measurement was performed over the entire path length that the diode laser traverses (~ 7 cm) with an unsealed cell, hence it is likely that the RH within the cell (~ 4 cm) will be even lower.

Upon capture of the droplet by the tweezers beam, rapid evaporation was observed as red shifting of the resonant modes in the scattered spectrum. The initial evaporation rate was more rapid than the temporal resolution of the spectrometer, and hence initial spectral characterisation of the trapped droplet was not possible. To facilitate analysis, it was therefore assumed that the initial composition of the droplet is identical to the bulk solution in the nebuliser. The evaporation rate slows down as the concentration of EAN in the droplet becomes greater, at which point the spectra could be accurately recorded and assigned. To gain an initial appreciation of the dynamics of the droplet, consider the wavelength of a single resonance. Recall that the definition of the size parameter implies that $\Delta\lambda/\lambda = \Delta a/a$. Thus, the behaviour of a resonance will indicate changes in droplet size (it should be noted, however, that if the change in wavelength is large then this relationship will be approximate, owing to the change in refractive index associated with change in aerosol size).

Figure 5.5 shows example data for a droplet initially comprised of a 25% EAN solution. In 5.5a, the time dependent position of a MDR resonance is plotted (determined by subtracting the background signal, then fitting a Gaussian lineshape to the MDR). At early times, the steep gradient indicates rapid evaporation, at an average rate of -1.8×10^{-4} µm s^{-1}. However, the mode then begins to slightly redshift, suggesting that the droplet is then growing. This must be due to the uptake of water vapour, owing to the negligible vapour pressure of ILs [203]. Assignment of the spectrum confirms this growth, and the diameter is plotted in Figure 5.5b, with an average growth rate of 1.4×10^{-5} µm s^{-1}. The assigned refractive index of the droplet is plotted in Figure 5.5c, and shows an increase at early times that is correlated with droplet evaporation, as should be expected due to the increasing mole fraction of EAN. It is interesting to note that, even at the earliest analysable times, the assigned refractive index ($n \sim 1.42$) is considerably higher than the bulk solution that

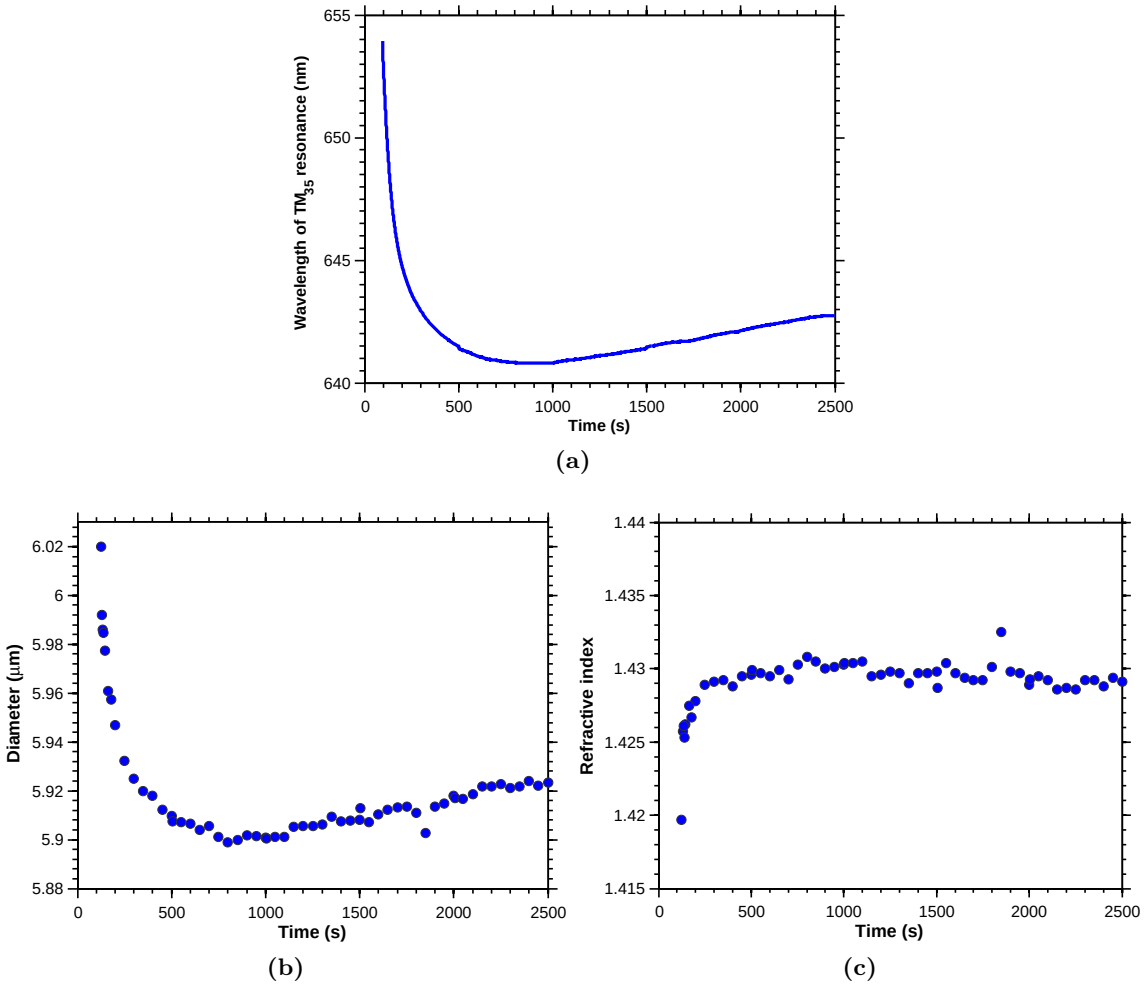

Figure 5.5: Spectral data for a droplet, initially comprised of a 25% by volume EAN solution, in a low RH environment.

was nebulized ($n \sim 1.37$). This large discrepancy suggests that, in addition to the rapid initial evaporation upon capture of the droplet, the individual droplets within the nebulizer stream are rapidly losing water as they try to equilibrate with the surroundings.

The response of a more concentrated droplet (50% by volume EAN) to the low RH environment is presented in Figure 5.6. This droplet was larger than the 25% droplet, hence showed second order MDRs within its scattered spectrum (a typical example of which is shown in Figure 5.4b). The temporal variation of the resonance wavelengths is similar to the 25% case, i.e. a rapid blueshift, followed by a slow redshift as the droplet reabsorbs water vapour. The shifting of the resonance wavelengths once again correlates with the assigned diameters. The assigned refractive index is also high, starting at 1.422 for initial times, increasing to 1.431 by the end of the acquisition time. The final composition is therefore concluded to be similar to that for the 25% droplet after its equilibration with the surroundings, with a higher value of the refractive index due to the higher initial

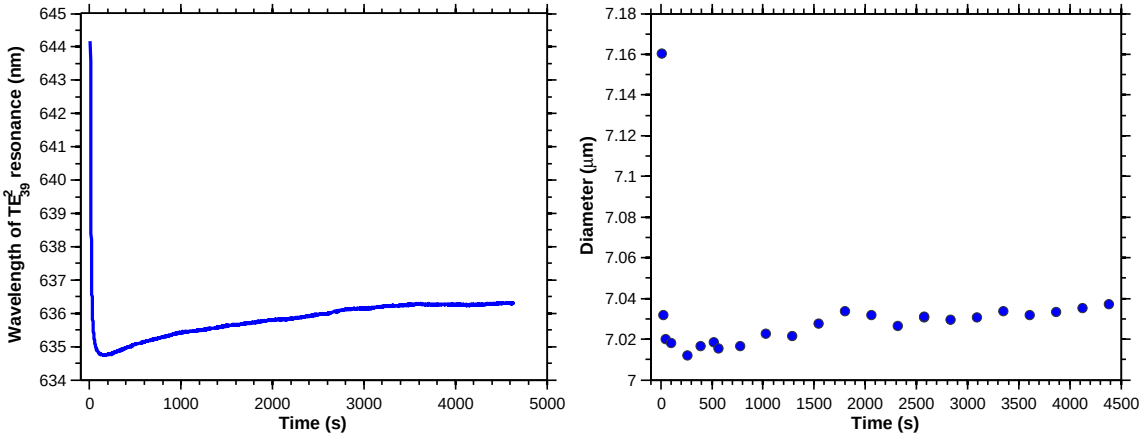

Figure 5.6: Spectral data for a droplet, initially comprised of 50% by volume EAN solution, in a low RH environment.

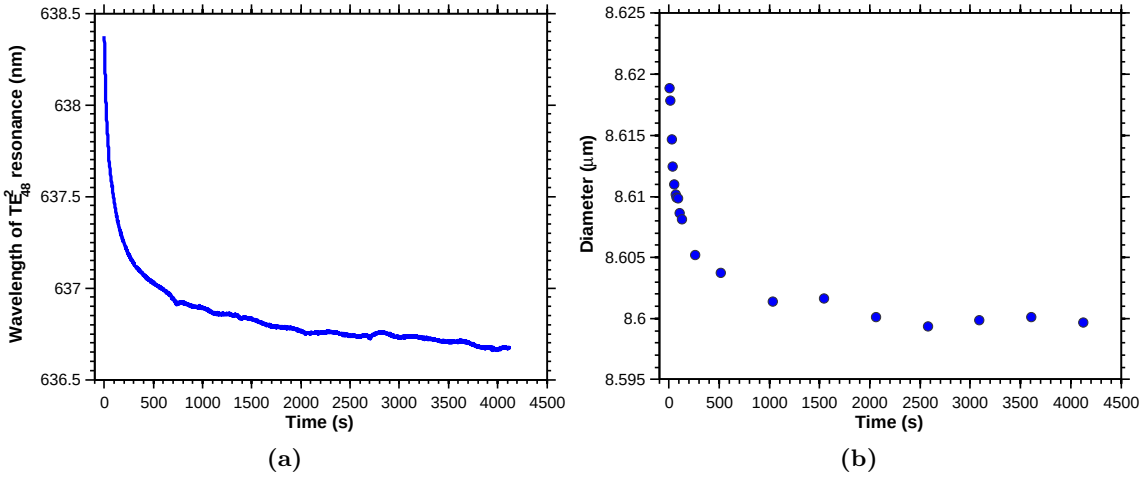

Figure 5.7: Data for an additional 50% by volume EAN droplet in a low RH environment. Note that the early portion of this spectrum was not available, owing to the droplet's initial capture taking place at the end of a spectrometer kinetic acquisition series.

concentration of EAN within the droplet.

Figure 5.7 shows the time dependence of the TE^2_{48} resonance associated an additional 50% droplet, of diameter $\sim 8.6\,\mu m$. In this case, the droplet constantly evaporates (indicated by the resonance wavelengths blueshifting). The assigned refractive index did not show much variation around 1.4. It is likely that the silica gel was starting to saturate at this point, reducing its effectiveness in providing a low RH environment. Furthermore, the fact that the droplet itself is considerably larger means that comparitively more water molecules must be lost to achieve the compositions observed within the earlier droplets. A continuation of the spectral data for this droplet is provided in Figure 5.8, clearly showing

that the modes continue to blueshift, and the droplet continues to reduce in size at a rate of $-2.8 \times 10^{-6}\,\mu\mathrm{m\,s^{-1}}$. Note the unusual response of the resonance wavelengths at 1500 s, likely a fluctuation in the laboratory relative humidity. This again highlights the exquisite sensitivity of MDRs to changes in their environment.

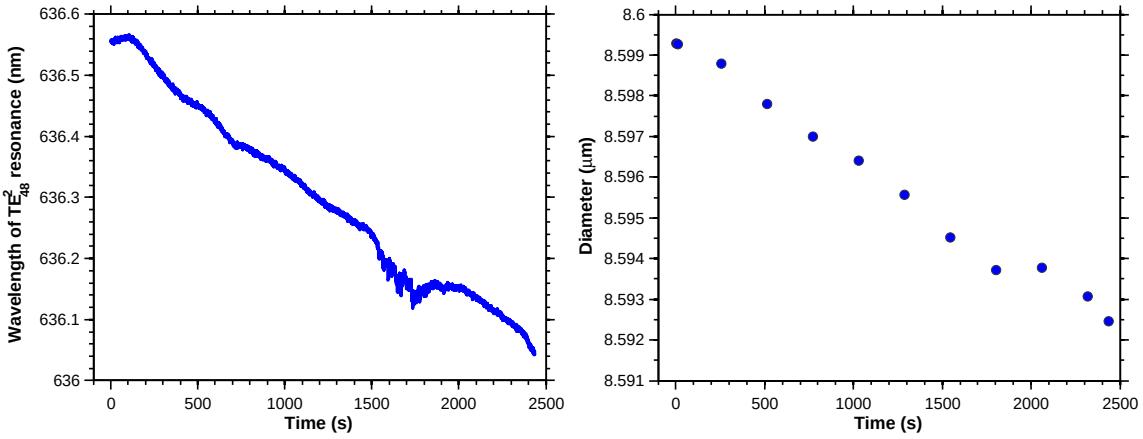

Figure 5.8: Continuation of the droplet from Figure 5.7, showing that the resonance modes continue to blueshift, and the droplet continues to evaporate at a rate of $-2.8 \times 10^{-6}\,\mu\mathrm{m\,s^{-1}}$.

5.3.1.3 Trapping at ambient relative humidity

For these experiments, no additional agents were added to the trapping cell; thus the air droplet is effectively open to the laboratory. The RH in the laboratory air is approximately 10% larger than in the low RH environment provided by the silica gel, as confirmed by diode laser absorption spectroscopy, hence it is expected that the EAN solutions will again evaporate, but at a slower rate than in the low RH environment. Owing to the similar behaviour between 25 and 50% solutions, only the higher concentration was utilized from here onwards. An example of the observed data is shown in Figure 5.9, and it is immediately clear that the spectral response in this instance is much less extreme than in the low RH environment. While droplets did evaporate, they did so at a much slower rate, such that they could be characterised upon initial trapping (once the fog of aerosol within the chamber settled down, such that additional coagulation with the trapped droplet did not occur). In this instance, the droplet grew slightly before continuing to evaporate (although the gradual shift would suggest that coagulation is not the responsible factor), most clearly shown by Figure 5.9b, which plots a numerical derivative of the MDR position with respect to time, as this will be proportional to the evaporation rate. The fitting of the refractive index of this droplet was curious; the RI was tending towards 1.422 during the first 200 s of the dataset (consistent with the asymptotic values presented in the previous section), at which point

the analysis routine started returning an RI which tended towards 1.39. This is puzzling, as the values of the diameter fit with the trend provided by the resonance wavelength. It is likely that the particular combination of resonance wavelengths from the droplet lies within a local minimum of the fit to the theoretical size parameters, hence returning a false refractive index, as it would not be possible for the refractive index of the droplet to decrease as it loses water molecules by evaporation. This is quite likely, owing the known problems with the assignment procedure (namely the lack of dispersion data, resulting in a misassignment of the best fit diameter, and hence best fit refractive index). An alternative explanation could be that phase separation, or a concentration gradient, exists within this droplet, with more water molecules existing at the surface and hence lowering the measured refractive index.

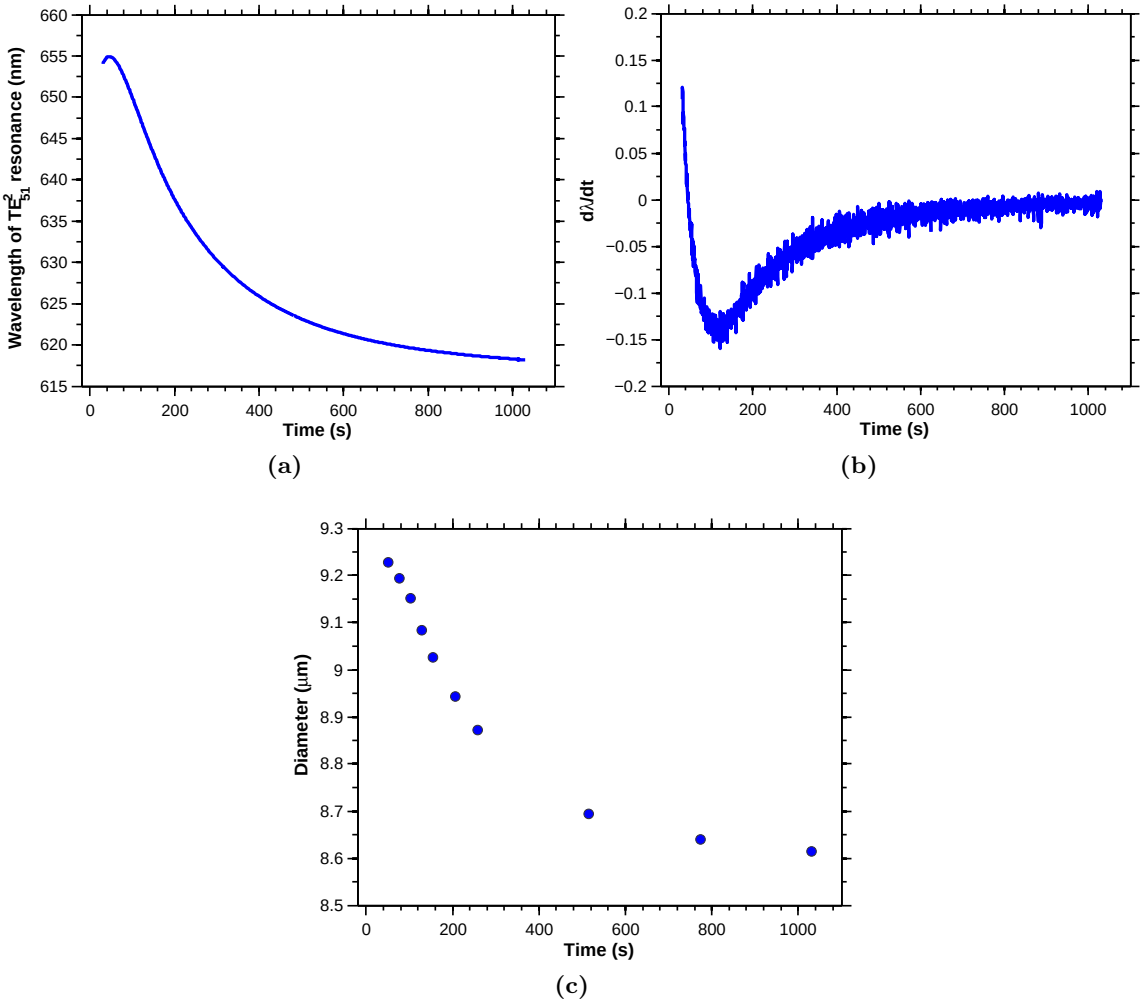

Figure 5.9: Data for a droplet that is initially comprised of 50% by volume EAN, in a cell that is open to the ambient laboratory conditions.

A study of an additional droplet is provided in Figure 5.10. A similar trend in the wavelength is observed, i.e. a slight growth followed by evaporation. This droplet is much smaller than the previous one (6.255 µm initially, vs 9.25 µm), and equilibrates to a refractive index of 1.4255. The acquisition is continued in Figure 5.11, which shows that the droplet's resonance modes continue to blueshift as the droplet is slowly evaporating. The final refractive index of this droplet is 1.4279. This high value of the refractive index is consistent with the work performed in the low RH environment, and further confirms that smaller droplets will equilibrate towards more concentrated EAN solutions in a shorter timeframe.

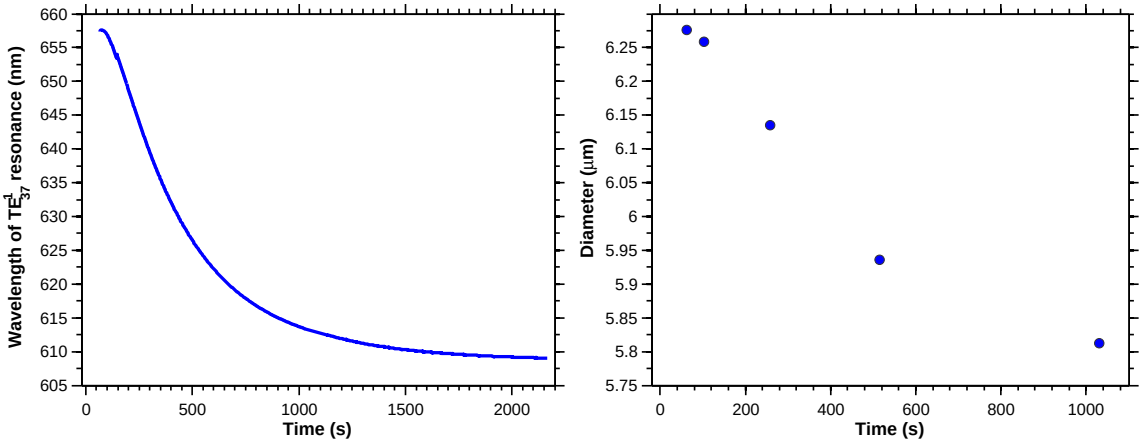

Figure 5.10: An additional 50% by volume EAN droplet in a cell open to the ambient laboratory conditions.

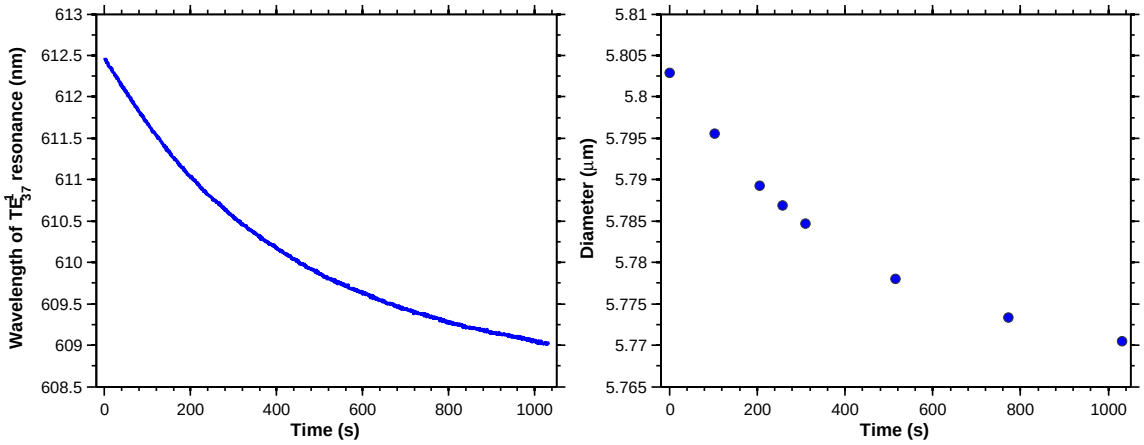

Figure 5.11: Continuation of the data shown in Figure 5.10, on a new spectral acquisiton.

5.3.1.4 Trapping at high ambient relative humidity

As a final test case, a high relative humidity environment was obtained in a similar fashion to Chapter 4, namely that a piece of moist tissue paper was inserted into the trapping cell. This will provide the droplet with an environment with an RH that is greater than 80%. As 50% EAN solution is utilized, it is expected that the droplet will absorb water from the surroundings in an effort to dilute the EAN further.

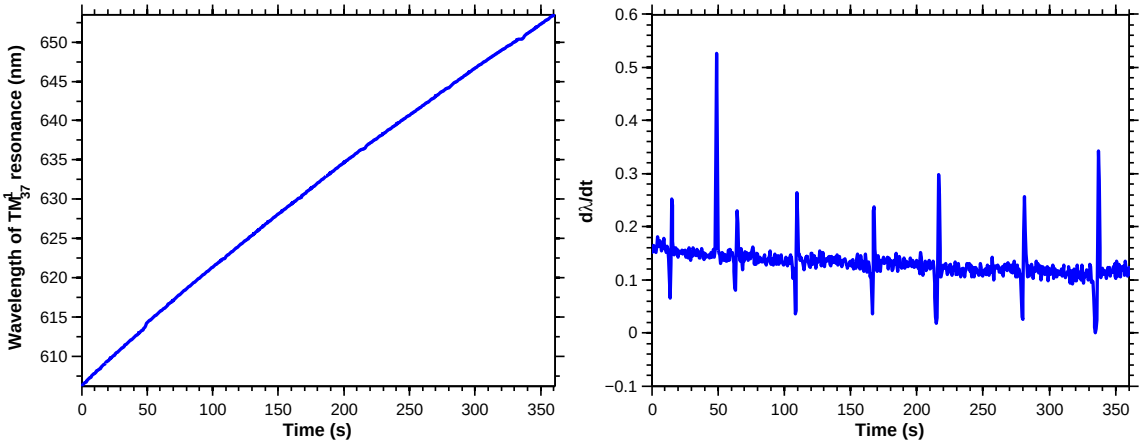

Figure 5.12: Spectral data for a droplet, initially composed of 50% EAN by volume, in an environment of high RH.

The first set of experimental data from these conditions is presented in Figure 5.12. The droplet's initial diameter is 5.63 µm, and it can be clearly seen from the time dependence of the central wavelength that the droplet grows, at a near constant rate of $1.3 \times 10^{-3}\,\mu\mathrm{m\,s^{-1}}$. Barely discernible on the wavelength variation are slight jumps in the position of the wavelength. These are more clearly observable in Figure 5.12b, where the time derivative of the resonance wavelength is plotted. The feature at 512 s is likely due to a variation in the laboratory environment. Of more interest are the quasi-periodic ripples, which resemble the derivative of a Lorentzian profile. It is hypothesised that these spectral features are a consequence of the droplet passing through resonances at the trapping laser wavelength, with the solute effect dominating droplet growth and pushing the droplet through the resonance. As the concentration of EAN at this time is still relatively high, resonant heating will be insufficient to increase the vapour pressure of the droplet, hence the continual growth. (Recall that, for a salt water droplet approaching resonance, the droplet remained approximately size-stable as its diameter tuned closer to the diameter concomitant with a WGM at the trapping laser wavelength, as resonant heating was responsible for an increase in the droplet vapour pressure.)

As the droplet further increases in size, resonant heating effects start to become more apparent, as is clear from Figure 5.13. In 5.13a, periods of wavelength stability are observed in between periods of constant growth. These growing periods become progressively shorter, until the droplet jumps between resonant spectra, similar to the Gaussian locking periods of Section 4.5.3. This trend is continued in Figure 5.13b, albeit referring to a different mode (TE^1_{38}) owing to the previous resonance shifting to outside of the spectrometer's range. At this stage, it is concluded that the droplet is acting almost entirely like a conventional salt water solution. Evidence for this comes from the value of $\Delta\lambda$ for the successive periods of constant wavelength; these oscillate between $\sim 7.1\,\text{nm}$ and $\sim 5.6\,\text{nm}$, which is consistent with the Gaussian growth data of Chapter 4 and reflects the polarisation of the locking mode.

To characterise the changes in size and refractive index, let us assume that the composition of the droplet upon capture by the trapping laser is identical to the bulk solution. Using this value of the refractive index to assign the initial spectrum yields a diameter of $5.29\,\mu\text{m}$, meaning that the droplet contains $4.37 \times 10^{-13}\,\text{mol}$ of EAN and $2.16 \times 10^{-12}\,\text{mol}$ of water ($x_{\text{EAN}} = 0.17$). Assigning the modes at the end of Figure 5.13b yields a diameter of $6.91\,\mu\text{m}$ and a refractive index of 1.3579. The difference in volume corresponds to an absorption of $5.29 \times 10^{-12}\,\text{mol}$ of water. This increase in water means the diluted mole fraction of EAN is now 0.056, which when substituted into Equation 5.1 yields a refractive index of 1.3636. The assigned refractive index is smaller than this (1.3579), a likely reason for this discrepancy is the assumption that the initial composition of the droplet is equal to that of the bulk.

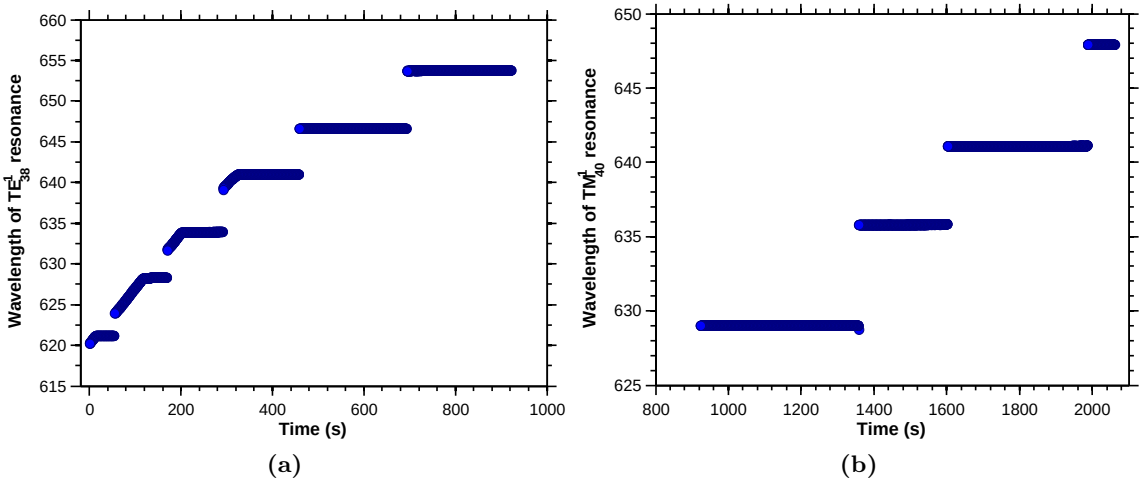

Figure 5.13: Continual growth of an EAN droplet in a high RH environment. The droplet is now displaying evidence of resonant heating, judging from the periods of size stability that are inferred from the time-constant resonant wavelengths.

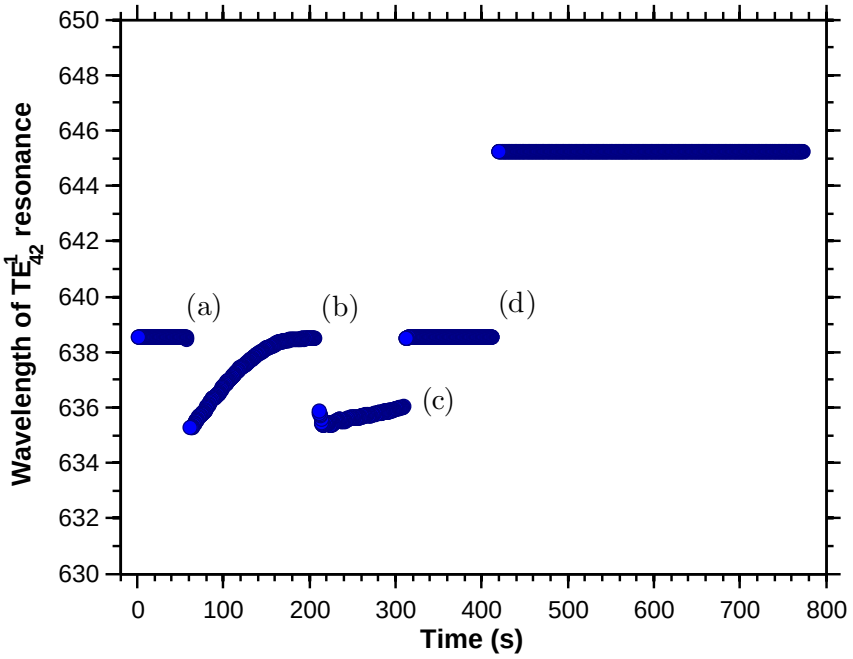

Figure 5.14: "Unlocking" of an EAN droplet in a high RH environment, induced by changing the power of the trapping laser.

5.3.2 Spectroscopy of EAN droplets under conditions of varying trapping power

Experiments were also conducted to investigate the response of the trapped EAN droplet to changes in the trapping power, which alters the degree of non resonant heating of the droplet. This was performed with droplets under the three different RH environments considered above. For the low and ambient RH conditions, no changes in the droplet spectra were observed. This is unsurprising given the composition of the droplet; the high concentrations of IL will mean that the reduction of vapour pressure via the solute effect will be the dominant process, compared to the effect of temperature changes due to non resonant heating.

A much more dynamic response was observed under high RH conditions. The experiment was performed once the droplet had achieved a composition at which it was displaying locking behaviour. The droplet had gone through several locked diameters, which were stable for a few minutes. The effect of changing the power while a droplet is locked is shown in Figure 5.14. Initially the resonance wavelengths were size stable, with a trapping power of 12.2 mW. At (a), the power incident upon the droplet was increased to 27.2 mW. The droplet instantly unlocked, with the modes blueshifting due to water being driven off from the droplet. However, the droplet then grew again (as demonstrated by the redshifting modes), returning to its initial size. A further power increase at (b) again unlocked the

droplet, with 31.3 mW incident upon the droplet, and this time some additional evaporation was observed before the droplet started to grow. At (c), the power was decreased to 27.2 mW, and the droplet relocked to its initial size. At (d), the power was further decreased back to 12.2 mW, taking the droplet to an additional locking diameter, larger than its initial state.

5.3.3 Broadband Mie scattering, vs Raman spectroscopy

As a comparison between the use of Raman spectroscopy to study droplets, as in Chapter 4, versus the broadband Mie scattering that has been utilized in this chapter, consider the spectra shown in Figure 5.15. These spectra were captured from a droplet whose initial composition was 50% EAN, and had been trapped in a low RH environment. Both spectra have been normalized to 1 (although the most intense part of the Mie spectrum lies off the x axis, which has been focused on the Raman bands of the droplet) so that comparisons between the two can be drawn. Firstly, note that the highly intense SRS modes in the Raman spectrum suggest that the droplet's diameter is resonant with a WGM at 532 nm. The most intense SRS modes would correspond to first order resonances, whose widths are limited by the spectrometer resolution. The presence of C-H stretches of EAN in the Raman spectrum is obvious, owing to the fact that SRS modes are observed within the range 630 nm to 640 nm, although these do occur at the same frequency as C-H stretches of the immersion oil. Interestingly, although WGMs are observed in the water region (640 nm to 660 nm), the spontaneous Raman signal is barely discernable, and reflects the higher Raman gain coefficient for the IL in comparison to water. The assigned refractive index is less than that of pure EAN, so water must still be present within the droplet.

The first order resonances do not appear in the BB-Mie spectrum, which consists wholly of second order resonances. It is clear that these second order MDRs in the BB-Mie spectrum occur at the same wavelength as the second order resonances in the Raman spectrum. As an example, the widths of the TE^2_{50} and the TM^2_{49} resonances within the Raman spectrum are 0.127 nm and 0.304 nm respectively, while within the BB-Mie spectrum they are 0.112 nm and 0.164 nm. The values for the TE resonance are near the spectrometer resolution, while for the TM resonance, the higher width for the Raman spectrum would imply a lower Q for that resonance (consistent with the theory presented in Chapter 3). The implication of this lies within the fundamental differences between SRS spectroscopy, and Mie scattering; clearly the TM resonance for Raman gain is lossier. From an analytical viewpoint, the much greater number of resonances in the Mie spectrum (the spectral range of the spectrometer CCD is ~ 60 nm) as well as the lack of congestion within the spectrum (first order MDRs are not detectable if their linewidth is narrower than the spectrometer's resolution) highlight

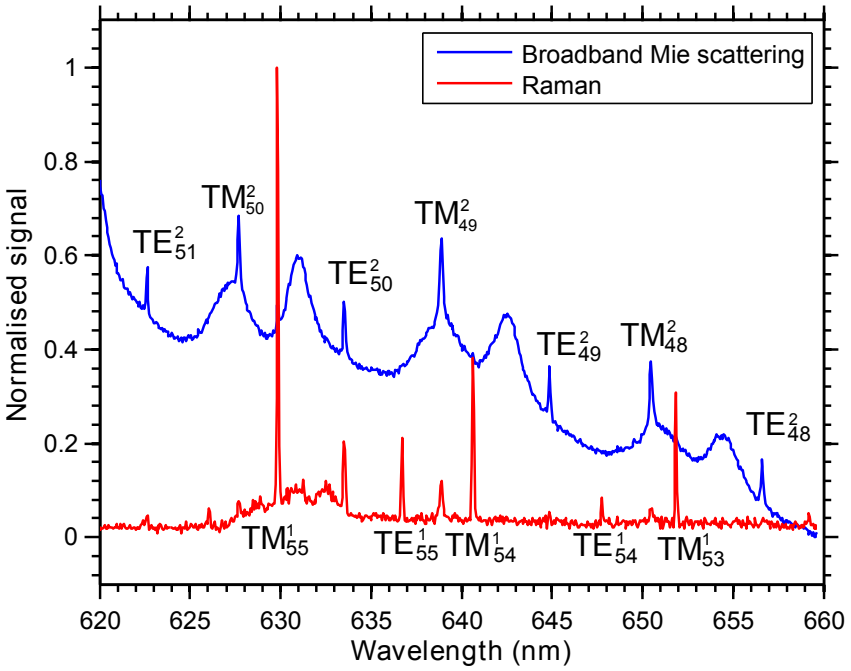

Figure 5.15: Comparison of the Raman spectrum from an aqueous EAN droplet, and the broadband Mie scattering spectrum. Note the intense SRS peaks, which suggest the droplet's diameter is resonant with a WGM at the trapping laser wavelength.

that BB-Mie is a more suitable technique for analysing these droplets of high refractive index.

5.4 Conclusions and future work

This chapter has introduced the optical trapping of ionic liquid droplets, and begun to characterise them via analysis of morphology dependent resonances present in backscattered light from an LED which illuminated the droplets. Droplets comprised of the ionic liquid ethylammonium nitrate in aqueous solution have been demonstrated to be optically trappable, and axial trapping efficiencies have been obtained as a function of concentration. The composition of these droplets has been assessed utilizing the MDRs present within a broadband Mie scattering spectrum, with a specific emphasis on exploring how the droplets respond to environments of differing relative humidity. A comparison between the complimentary techniques of BB-Mie scattering, and cavity-enhanced Raman spectroscopy (CERS) has been presented.

The next step for this project would be to nebulize and trap droplets of pure ionic liquid. The technical difficulties involved with this arise from the high viscosity of the ILs, meaning that vibrating orifice, ultrasonic, and handheld nebulizers will not be able to generate aerosol from the liquid. It is, however, possible to generate droplets of IL using a pneumatic

nebulizer. The primary disadvantage of this technique is that the droplets generated by this method are small, and have a high velocity. Both of these factors make it difficult to trap the droplets using optical tweezers. Solutions to these problems include a suitable design for a nozzle, which would allow the droplets to coagulate within the flow. Alternative methods of generating aerosols could also be explored, for example via electrospray [227], a technique that is commonly used to vapourise liquid biological samples for mass spectrometry characterisation [228].

The trapping and characterisation of pure ionic liquids would be very interesting; for instance, introducing controlled amounts of impurities into the system should be easily detectable via the slight changes in the refractive index that these impurities will induce (which will be manifested in the position of WGMs). A most interesting experiment will be the trapping of a droplet, composed of an IL which is known to sequester CO_2 (such as [EMIM][Tf_2N]). The uptake of CO_2 could be monitored by Raman spectroscopy (by observing the Fermi resonance [229]) or by observing changes in the refractive index via BB-Mie spectroscopy. This could then be compared to the uptake of CO_2 by the bulk solution, to investigate if the increased surface area of the droplet offers advantages for CO_2 capture, which would have important consequences for the carbon economy. The uptake of other greenhouse gases as a function of IL composition (particularly water content) may also be of particular practical importance.

Chapter 6

Microscopy studies of thermophoretically assembled 2D colloidal crystals

This chapter marks a change of gear for the thesis, in so far as optical tweezers are no longer used. Here, a different method of particle manipulation is exploited, which transports matter along thermal gradients and is known as thermophoresis. The thermal gradients are generated by focusing the laser onto a gold coated microscope slide, using the SLM to position heating spots at precisely defined locations. The combination of thermophoresis, and convection currents within the cell, results in 3.5 µm silica particles forming two-dimensional colloidal crystals. The two crystals grow into each other, and video microscopy used to observe the mechanism of crystal growth. It is found that the two crystals merge to form a crystal with a single orientation, via *grain rotation induced grain coalescence* (GRIGC). The observed annealing lifetimes are found to be in excellent agreement with theoretical models for the growth of nanocrystals. The work in this chapter forms the basis of a publication in Nano Letters [230].

6.1 Particle manipulation via thermal gradients

A particle subject to a thermal gradient moves along this gradient, and this is known as *thermophoresis* [231]. Particles subjected to a temperature gradient of ∇T will move with a velocity $v = -D_T \nabla T$, where D_T is the thermophoretic mobility of the particle (sometimes referred to as the thermal diffusion constant), given by $D_T = S_T D$ (where S_T is the Soret coefficient of the particle, and D the diffusion coefficient). The sign of the Soret coefficient dictates the direction of the thermophoretic force; a particle with a

Soret coefficient that is greater than zero will migrate towards the colder region. This thermal transport property has found numerous uses. For example, in 2002 Braun and Libchaber demonstrated that thermophoresis can be used to deplete DNA from a hotspot which, in combination with induced convection currents, lead to accumulation of DNA at the bottom of their cell chamber [232]. This is believed to be an important mechanism at hydrothermal vents. The combination of thermophoresis and convection can also be used to form two dimensional colloidal crystals, as demonstrated by Duhr and Braun in 2005 [233]. In this case, an aqueous suspension of 2 µm polystyrene spheres (which have a positive Soret coefficient) formed crystals at the bottom of a cell consisting of a upper layer of glass and a lower layer of sapphire, separated by a 500 µm thick silicone spacer, which was heated using an infrared laser. Crystallization was attributed to convection currents transporting the particles beneath the heated spot, and a strong downwards thermophoretic force (due to the high thermal gradient from the cooling sapphire window) causing the particles to aggregate. Later work [234] demonstrated that, for high thermal gradients, a slip flow was induced and this was responsible for crystallization.

More recently, Di Leonardo *et al.* [235] demonstrated the formation of colloidal crystals confined to a wall by heating an absorbing surface. They placed a sample of 2 µm silica spheres (in a glycerol/water mixture) into a cell consisting of a lower layer of transparent coverglass and an upper layer of a yellow colour glass filter. Holographic Optical Tweezers [105] were used to generate a pattern of laser spots on the upper filter (in order to generate the thermal gradients) and additionally to measure the forces between individual colloidal particles. Particle accumulation was attributed to a hydrodynamic attraction (such an attraction was predicted by Squires in 2001 [236]) driven by long range Marangoni-like forces.

6.2 Mechanisms of crystal growth

Nanocrystalline materials have attracted much interest due to their size and shape dependent properties, and have found uses in many applications including optics, electronics and materials [237]. The mechanism by which a nanocrystal grows is an important factor in determining its morphology and mechanical properties. There are two main mechanisms for nanocrystal growth. The first is known as *Ostwald Ripening* [238], and is the classical mechanism for growth, in which larger crystals grow at the expense of smaller ones. The driving force for this growth is that larger crystals are more favored energetically, due to the reduction of the surface to volume ratio. However nanocrystals display many peculiarities that cannot be explained by the Ostwald Ripening mechanism, such as unusual structures

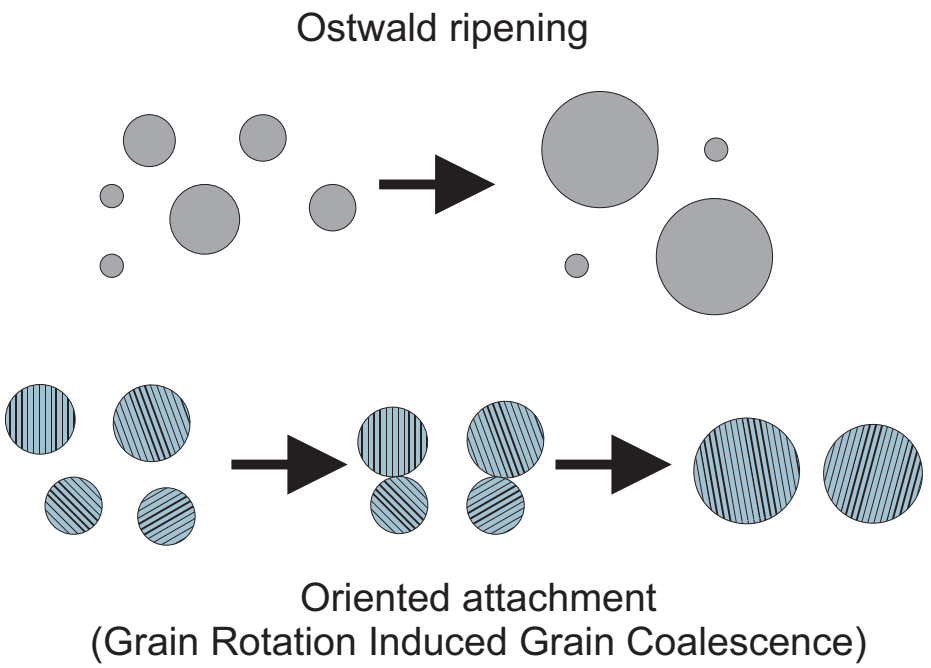

Figure 6.1: Crystal growth mechanisms.

or anisotropic morphologies within the crystal [239]. An alternative mechanism is required to explain these observations.

The so called *oriented attachment* mechanism was first reported in 1998 [240, 241]. In oriented attachment, adjacent grains rearrange themselves so that they share a common crystal orientation, followed by coalescence of the grains. If the individual grains do not share a common crystallographic orientation prior to coalescence, they can still form a crystal with a single orientation through a process termed *grain rotation induced grain coalescence* (GRIGC) [242]. In this mechanism, the driving force is the elimination of the grain boundary between the domains, lowering the free energy of the crystal. Although high-resolution electron microscopy studies have provided much of the present experimental evidence for the occurrence of GRIGC [243, 244], the dynamics at the single atom level in nanocrystals is difficult to observe. It is often the case that intermediate steps in the mechanism are simply not captured by these imaging techniques due to the rapid self-recrystallization of two grains that are just touching [245]. As a consequence, quantitative and microscopic details of GRIGC, such as the lifetime of the grains, the effect of the grain size and the particle rearrangement processes at the surfaces of the grains, are cumbersome to establish.

In this chapter, colloidal silica microspheres, grown into crystals by the combination of thermophoresis and convection described above, are used as an analogue of a nanocrystal system to directly observe the GRIGC mechanism at the simplest level of two grains. As their characteristic time and length scales are on the order of seconds and micrometers

respectively, the interaction between the crystalline grains in real space and time can be directly observed *via* optical microscopy. The size of the grains is controlled by tuning the position of the nucleation sites using the SLM. This allows a direct and quantitative investigation of how the grain size affects the lifetime of the grains, which is of central importance for the growth of nanocrystalline systems via GRIGC [242]. As will be shown, excellent agreement with theoretical predictions for nanocrystal growth from the work of Moldovan *et al.* [242] is found. Additionally, it is observed that both grains rotate before coalescence. Rather surprisingly, only minimal particle rearrangements at the surface of the small crystallites are observed during GRIGC, while surface melting seems to become more important for larger grains.

6.3 Materials and methods

6.3.1 Optical components and sample preparation

The experimental setup used in this chapter is the DHOTs setup referred to in Figure 2.11. The sample in this instance is placed upon the surface of a gold coated microscope slide. This is used to generate the thermal gradients, as the modulated 532 nm laser beam is focused onto the gold surface, where it is absorbed. Use of the SLM allows fine control over the position of multiple heating spots in the sample plane, in both lateral and axial directions. The microscope slides were prepared by thoroughly cleaning using Decon 90, followed by coating with a 2 nm thick chromium layer (to aid adhesion of the gold) and a 25 nm thick gold layer using an Edwards Auto 306 Cryo Evaporator. The absorption of the gold layer is 0.7 at 532 nm. Colloidal samples were prepared by diluting a stock suspension of 3.5 µm silica spheres (Bangs Laboratories, SS05N) with Milli-Q water (Millipore) in a 1:50 ratio. No salt was added to the suspension as it is known that this diminishes the thermophoretic force [232, 246]. 20 µL of this suspension was sandwiched between a glass coverslip and the gold coated slide, separated using a vinyl spacer, with the gold layer forming the bottom surface of the cell.

When operating the laser, it was found that laser powers greater than ∼2.5 mW incident upon the sample caused local boiling of the water. Power control was achieved by combining the waveplate/PBS attenuator, described in Section 2.3.1, and a neutral density filter with an optical density of 1 (Thorlabs, NE10A-A). An iris was positioned at the focus of lens L3 in such a way as to block out the zeroth order diffraction (and the higher order "ghost" diffractions, which caused unwanted nucleation sites) from the SLM while allowing the first order diffraction to pass unobstructed. The SLM was imaged onto the back aperture of the microscope objective (Nikon M Plan 40/0.4 SLWD) via a $4f$ lens relay system. The chosen

objective gave a wide field of view and, due to the low numerical aperture, minimized any optical trapping gradient forces.

The sample was illuminated from above using Köhler illumination, as it is important for particle tracking purposes that the illumination is uniform and of high contrast. The system was imaged using the same objective used for focusing the laser. This white light was then imaged onto a Firewire camera (PixeLINK PL-A774), with images and videos captured using software written in LabVIEW (National Instruments). Kinoforms were generated and displayed on the SLM using a custom LabVIEW program [188] using an additive adaptive algorithm. Appropriate virtual lens elements were added to the kinoform to axially displace the focus of the laser, such that the laser was optimally focused on the surface of the slide while the particles themselves are in the image plane of the objective. The kinoform generation program was calibrated by imaging a stage micrometer and using this to equate the camera pixels to a real distance.

6.3.2 Video analysis

Videos were recorded at a resolution of 1600×1200, with a frame rate of 6 fps. Video frames were extracted and analyzed using MATLAB particle tracking routines,[1] based upon the algorithms originally developed by Crocker and Grier [247]. The particle tracking routine takes an image as an input, and then applies a filter algorithm to reduce any noise and distortions. Particles are detected by seeking pixels with a certain threshold intensity; spurious results are avoided by defining the maximum size of particle in terms of pixels. The routine then calculates the centroids of the detected particles to subpixel accuracy, outputting the x and y coordinates of the centroids of the particles. This output can then be processed in MATLAB to give a wide variety of parameters of interest for the image. In the case of crystals, Delaunay triangulations and Voronoi diagrams that are colour coded to depict the coordination of particles within the crystal [248] can be obtained. The particle tracking output was further processed to give information on the local orientation bond order parameter, ψ_6, defined as [249]:

$$\psi_6 = \frac{1}{N}\sum_{j=1}^{N} \exp[6i\theta(\vec{r_j})] \tag{6.1}$$

where the sum is taken over all N nearest neighbors of the particle in question. The angle $\theta(\vec{r_j})$ is defined as the angle between the vector connecting the particle to its neighbor j and an arbitrary axis, in this instance it is defined as the angle relative to the vertical axis of the images. This is shown schematically in Figure 6.2. In the remainder of this chapter,

[1] http://physics.georgetown.edu/matlab/

ψ_6 represents the absolute value of ψ_6 averaged over all particles, $\langle|\psi_6|\rangle$, which equals unity for a perfect hexagonal crystal. In the context of these experiments, the *orientation* of a particle is taken to be the value of $\theta(\vec{r_j})$ that lies between -30° and +30°. The Voronoi diagrams are then replotted, colour coding the polygons that correspond to 6 fold centers according to their orientation (herein referred to as an orientation Voronoi diagram). The individual orientations are also binned into 1° intervals, and plotted as a histogram, to easily observe the spread of orientations present in a given image of a crystal.

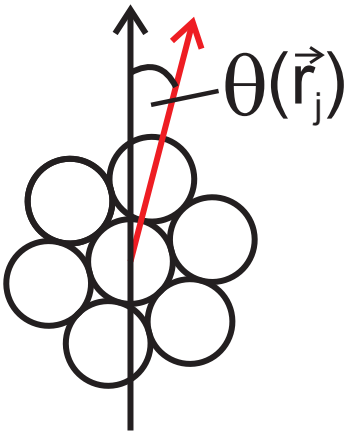

Figure 6.2: Definition of the vectors and angles used to calculate ψ_6.

6.4 Results and discussion

In order to study the mechanism of GRIGC, it is important that the crystals generated by the thermal gradients are of a single-crystalline nature, and that their size remains constant during the rotation and coalescence process. To verify this, initial experiments were performed using a single spot focused onto the gold surface of the microscope slide. When the heating laser is switched on, particles immediately drift towards the focus of the beam and organize themselves into a hexagonal close packed (HCP) lattice. Figure 6.3 shows two examples of the crystals formed after 30 minutes of heating the gold surface with different incident laser powers, along with orientation Voronoi plots and histograms. When the laser is switched off, the crystal immediately begins to melt, with the particles composing the crystal undergoing free Brownian motion. The crystals, on the whole, grow with a single orientation, as is indeed confirmed by the orientation Voronoi diagrams and histograms presented in Figure 6.3, a crucially important observation for the study of GRIGC. Deviations occurred when defects were introduced to the crystal, for example, a deformed particle may be present within the lattice. It is also noted that, at higher laser powers, stacking of the particles around the focus of the laser beam occurred during the initial crystal growth period, attributed to the increased strength of convection at these

higher incident laser powers. This effect is responsible for the defect region at the center of the crystal in Figure 6.3d. Therefore, the laser power was carefully controlled to ensure that this deleterious stacking did not occur, and that all studies of grain coalescence were conducted with the same incident laser power.

The growing technique affords a method of controlling the size of the individual grains. The number of particles in the crystal is defined as the total number of particles within a crystal that have a coordination number of 4 or higher, and have a local ψ_6 greater than 0.7. It was found the number of particles within the crystal at a given time increases with the laser power at a constant particle number density in the sample. The ψ_6 values of the crystal also increases as the power incident on the gold slide increases; after 30 minutes of heating for 6 different incident laser powers, ψ_6 increases from 0.74 to 0.87. This increase is attributed to two factors: the stronger thermal gradients causing stronger forces in the system, and the associated increased size of the crystal. The values of ψ_6 and the grain size after 30 minutes of heating with a range of laser powers are documented in Table 6.1.

The rotational motion of the single grains after growth is characterized by computing the mean square angular displacement, $\langle \Delta\theta^2 \rangle$, which for a particle undergoing rotational

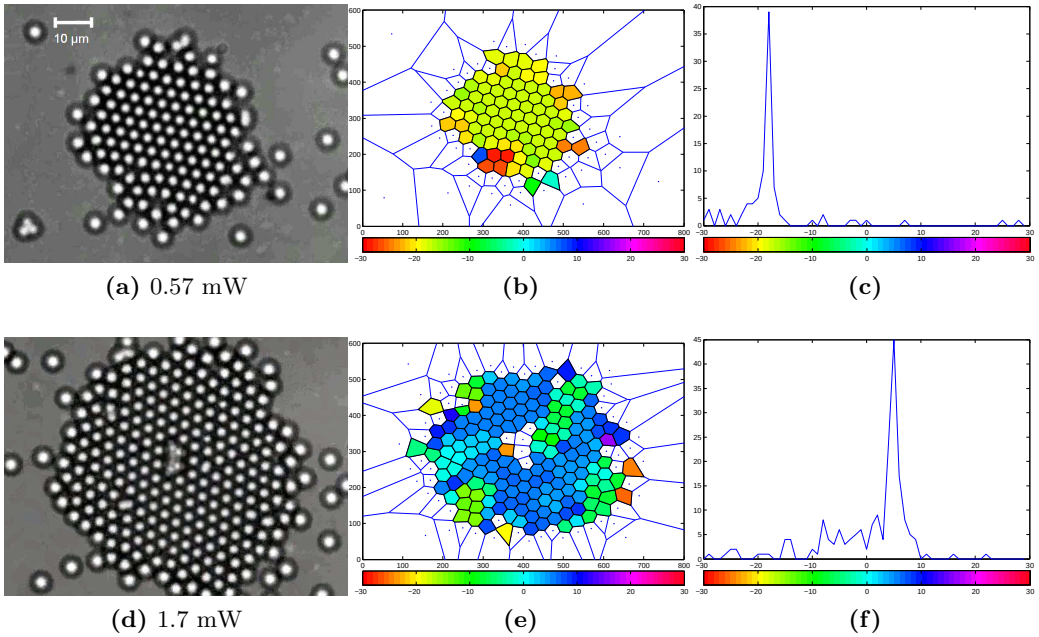

(a) 0.57 mW **(b)** **(c)**

(d) 1.7 mW **(e)** **(f)**

Figure 6.3: Examples of crystals formed after 30 minutes of heating the gold surface with a single laser spot. The power quoted corresponds to the power incident upon the gold surface. The defect region at the center of 6.3d is due to particle "stacking" during initial crystal growth, attributed to increased strength of convection currents at higher incident laser powers. Orientation Voronoi diagrams and histograms are presented, revealing that the crystals grow with a single orientation (limited by defects within the system).

Table 6.1: Values of ψ_6 and number of particles in the crystal after 30 mins of heating the gold surface with the quoted laser power.

P / mW	ψ_6	Number of particles
0.32	0.742	67
0.57	0.773	88
1.2	0.757	123
1.7	0.823	183
2.2	0.819	197
2.3	0.866	280

diffusion in a single plane is given by: [250]

$$\langle \Delta\theta^2 \rangle = 2D_r t \tag{6.2}$$

Here, the rotational diffusion constant D_r is given by the Debye-Stokes-Einstein relation [250]:

$$D_r = \frac{k_B T}{8\pi\eta a^3} \tag{6.3}$$

where T is the temperature, η is the dynamic viscosity of the solvent and a is the radius of the particle undergoing diffusion. The rotational mean square displacement of a grain was determined by taking the maximum value in the orientation histogram at time t as the average orientation for the crystal. Note that for this measurement, the crystal did not grow significantly while the video was being recorded i.e. this a quasi-equilibrium measurement. The resulting data is plotted in Figure 6.4. Fitting a straight line to the data gave a value for the rotational diffusion constant of 0.108 $\mathrm{deg}^2\ \mathrm{s}^{-1}$, from which a crystal radius of approximately 17 µm can be deduced using Equation 6.3. The fact that this value is consistent with the measured radius of the crystal (on the order of 16 $\pm$ 0.7 µm, as measured from calibrated video microscopy), confirms the quasi-equilibrium nature of the single grains and suggests that the rotation of the grains is well described by the equilibrium rotational diffusion of a two dimensional circular particle.

Having established the feasibility of this technique to generate colloidal single crystalline grains with a tunable size, the SLM was utilized to generate multiple spots at a controlled separation. Thus, grains were grown at precise locations, and their real-time interactions directly observed via standard optical microscopy. Figure 6.5 shows an example of a typical annealing process. Two spots were located 7 particle diameters apart, which corresponds to a distance of 24.5 µm. It is clearly observed that grains first rotate to align their orientations and then coalesce to form one single crystallite, consistent with the GRIGC mechanism. To quantitatively analyze this process, the mean orientation of each grain was measured, as shown in the corresponding orientation Voronoi diagrams in Figure 6.5. It was found that both grains contribute to the rotational alignment, with the orientation of the resultant

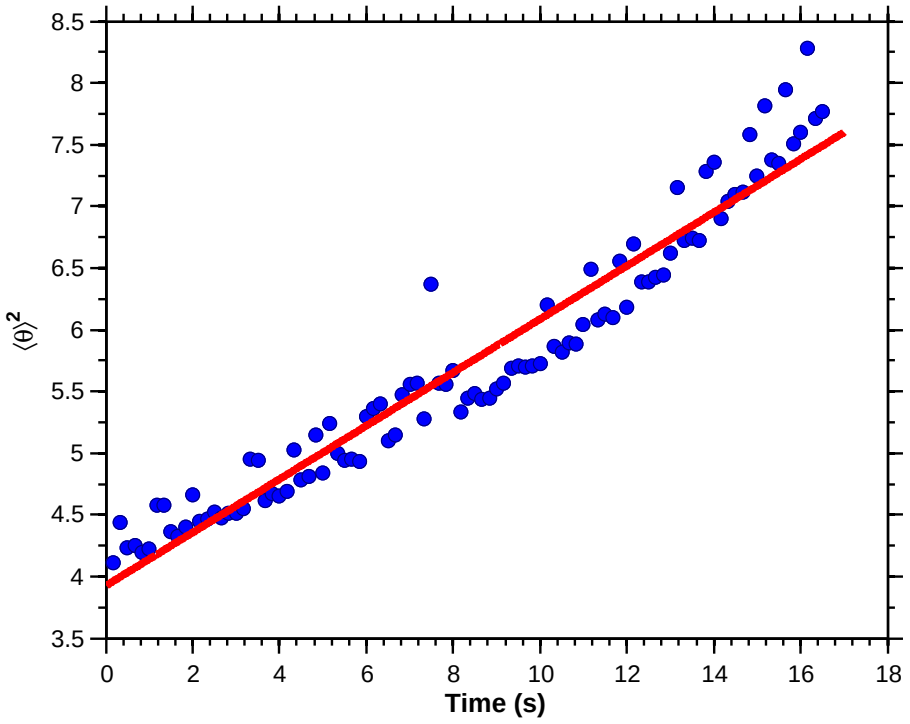

Figure 6.4: Mean square displacement for a crystal undergoing rotational diffusion. The red line is a straight line fit to the data, from which a value of the rotational diffusion constant can be obtained using Equation 6.2.

crystal lying between the values of the individual grains. This is shown more clearly in Figure 6.6, where the orientations of the individual grains are plotted as a function of time. Defining the lifetime of a grain t_L as being the time between when the individual grains first touch, t_0, to the time when they anneal to form a single crystal, the lifetime in this case was measured as 100 s. It is important to emphasise that the data shows that timescale over which the grains rotate and anneal is significantly shorter than the time taken for the grains to grow (which is on the order of multiple minutes), suggesting that grain size is effectively constant during the annealing process.

The lifetime of a grain t_L is an important parameter in grain rotation induced grain growth and should sensitively depend on the grain size and misorientation between grains [242]. The grain size can be controlled by varying the laser spot separation, which is demonstrated in Figure 6.7, however the initial orientations of the individual grains are completely random. Performing multiple repetitions of the experiment for a fixed spot separation, i.e. a fixed grain size, gave a wide range of orientation mismatches and corresponding lifetimes. It was observed that the average lifetime remains essentially constant for any orientation mismatch at a fixed grain size; this surprising result is believed to be due to the fact that only two grains are coalescing. Assuming that the frequency of coalescence events is proportional to the average rate of grain rotation, the average lifetime is inversely proportional

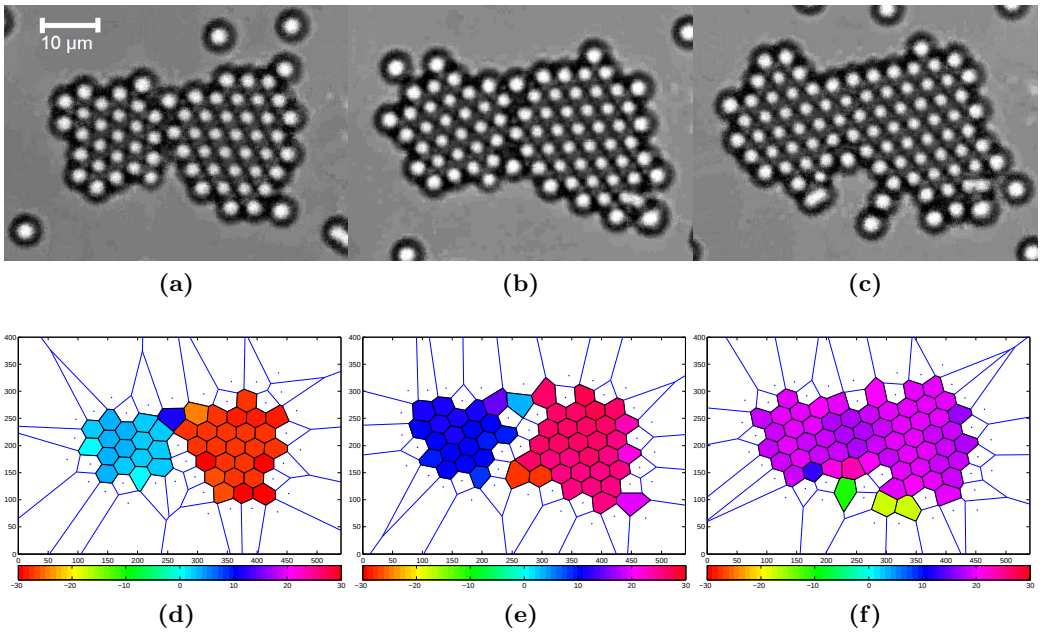

Figure 6.5: A typical annealing process, corresponding to two laser spots separated by 24.5 µm, along with orientation Voronoi plots, showing the two grains with different orientations merging to form a grain boundary, before rotating to form a crystal with a single orientation.

to the average angular velocity, i.e. $t_L \sim \langle\omega\rangle^{-1}$. The driving force for grain rotation is a torque τ with respect to the center of mass. This torque is related to the grain boundary length, L, energy per unit length, γ, and the orientation mismatch, θ, by the following expression [242, 251]:

$$\tau = \sum_j L_j \frac{d\gamma_j}{d\theta_j} \tag{6.4}$$

The angular velocity of the rotation is then related to the torque via $\omega = M(R)\tau$, where $M(R)$ is the rotational mobility, which is a function of the grain size. In the case of two grains, there is only one orientation mismatch and the grain boundary length is a constant. To a first approximation, the grain boundary energy depends linearly upon the orientation mismatch [242], and so the derivative in Equation 6.4 will be a constant. Hence, for a fixed grain size, the angular velocity (and therefore the lifetime of the grain) is not expected to depend upon the orientation mismatch.

A consequence of this is unprecedented access to study the grain size dependence of the annealing lifetime. To investigate this, measurements were taken for a range of grain sizes by varying the spot separations from 17.5–42 µm (the actual distances corresponded to integer and half integer multiples of the mean particle diameter) and the average observed annealing lifetimes determined. The results are plotted in Figure 6.8. There is a clear non-linear dependence on the annealing time upon the spot separation, which is itself related

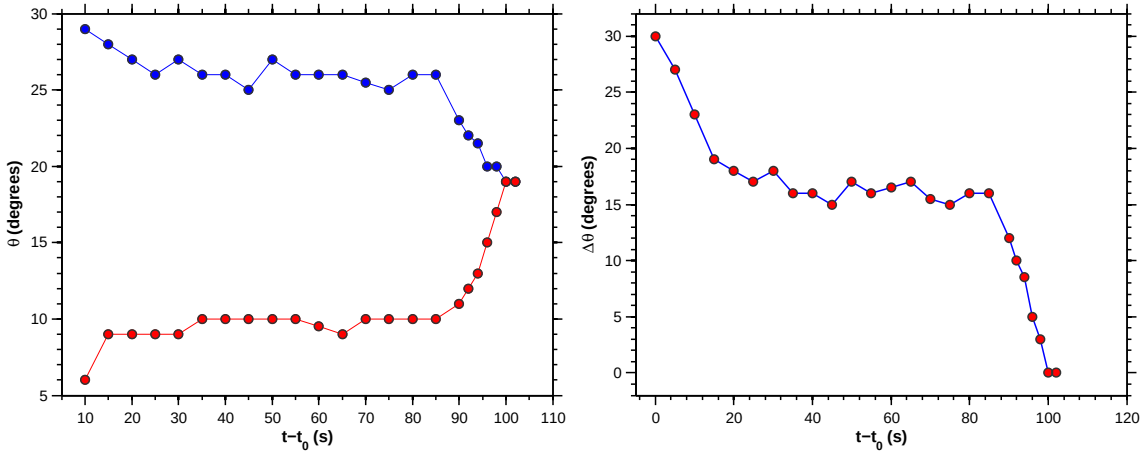

(a) (b)

Figure 6.6: Plot of the variation in the orientation for the annealing process depicted in Figure 6.5. t_0 is the time at which the two grains make contact. Figure 6.6a shows the variation of the orientation of the individual grains, showing that both grains rotate in the annealing process.

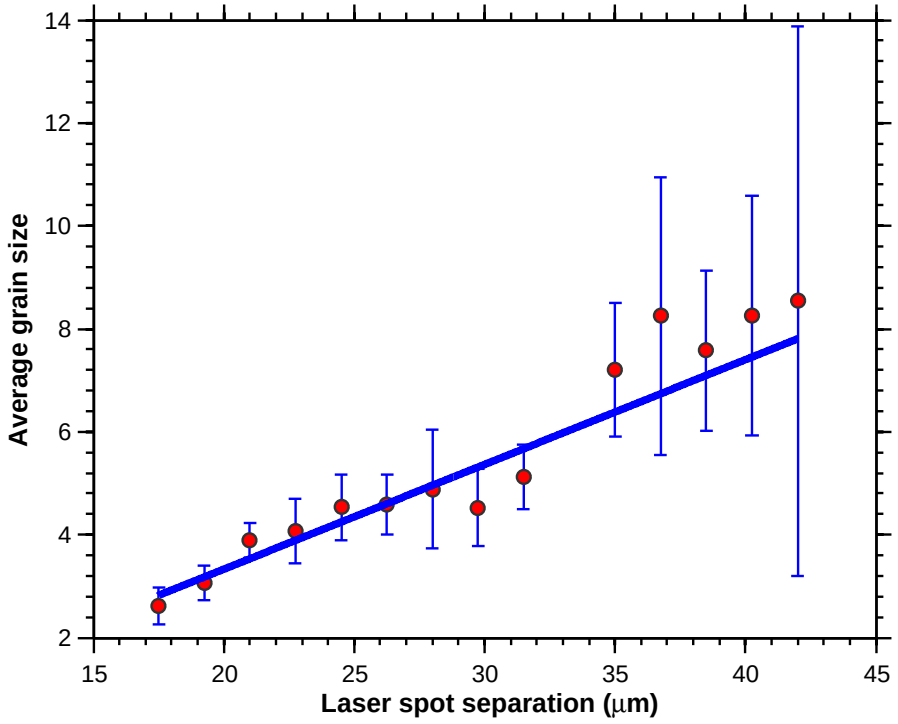

Figure 6.7: Variation of the average grain size (defined as $\sqrt{N/2}$, where N is the size of the crystal as defined in the text) with laser spot separation. The error bars are the standard error in the mean.

to the grain size as shown in Figure 6.7. The grain size is defined as $\sqrt{N/2}$, where N is the total number of particles (as defined above) in the individual crystals. To explain the observed dependence of lifetimes upon grain size, consider the work of Moldovan *et*

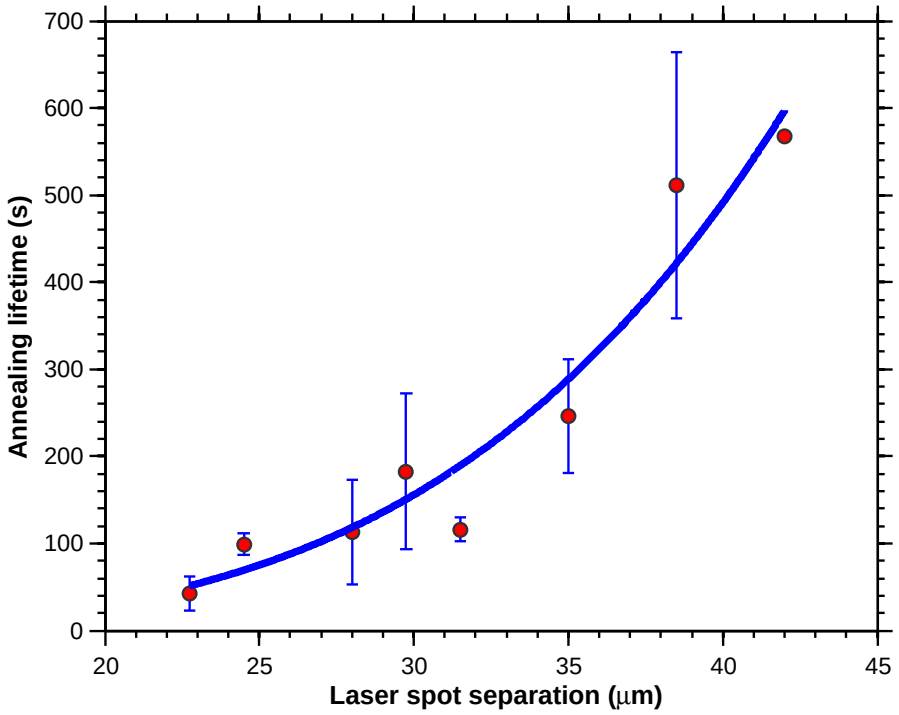

Figure 6.8: Average annealing lifetime as a function of spot separation, R. The line corresponds to a fit of $t_L = aR^4$ where a is a constant. The error bars are the standard error in the mean.

al. on the scaling behavior of grain rotation induced grain growth [242]. The rotational mobility depends sensitively on the grain size: $M(R) = C/R^p$, where C is a parameter which depends upon the physical properties of the system. The exponent p depends on the mechanism for the grain rotation; for accommodation by grain boundary diffusion $p = 5$ while for accommodation by lattice diffusion, $p = 4$ [252]. For small grain sizes, there is minimal particle rearrangement at the grain interface, while for larger grains, local melting of the crystal along the grain boundary was observed prior to grain rotation. Moldovan *et al.* show that the torque is proportional to the grain area (A) by a power law, $\tau \sim A^{(1+2q)/2}$, where the exponent q links the average grain area to the gradient of the grain boundary energy [242]. Hence, as the grain size is related to the area by $A = R^2$, the lifetime scales as:

$$t_L \sim R^{(p-1-2q)} \tag{6.5}$$

Simulations by Moldovan *et al.* showed that $q \ll 1$, (and in the steady state regime, the value of q is zero). The measured data clearly shows diffusion of defects along the grain boundary, hence the value of $p = 5$ should be utilized. Thus, for a negligible value of q, Equation 6.5 reduces to a R^4 dependence; a fit to this dependence is shown in Figure 6.8. This suggests that these observations do correspond to the GRIGC mechanism, and that for the simplest level of two grains, both grains rotate during the annealing process.

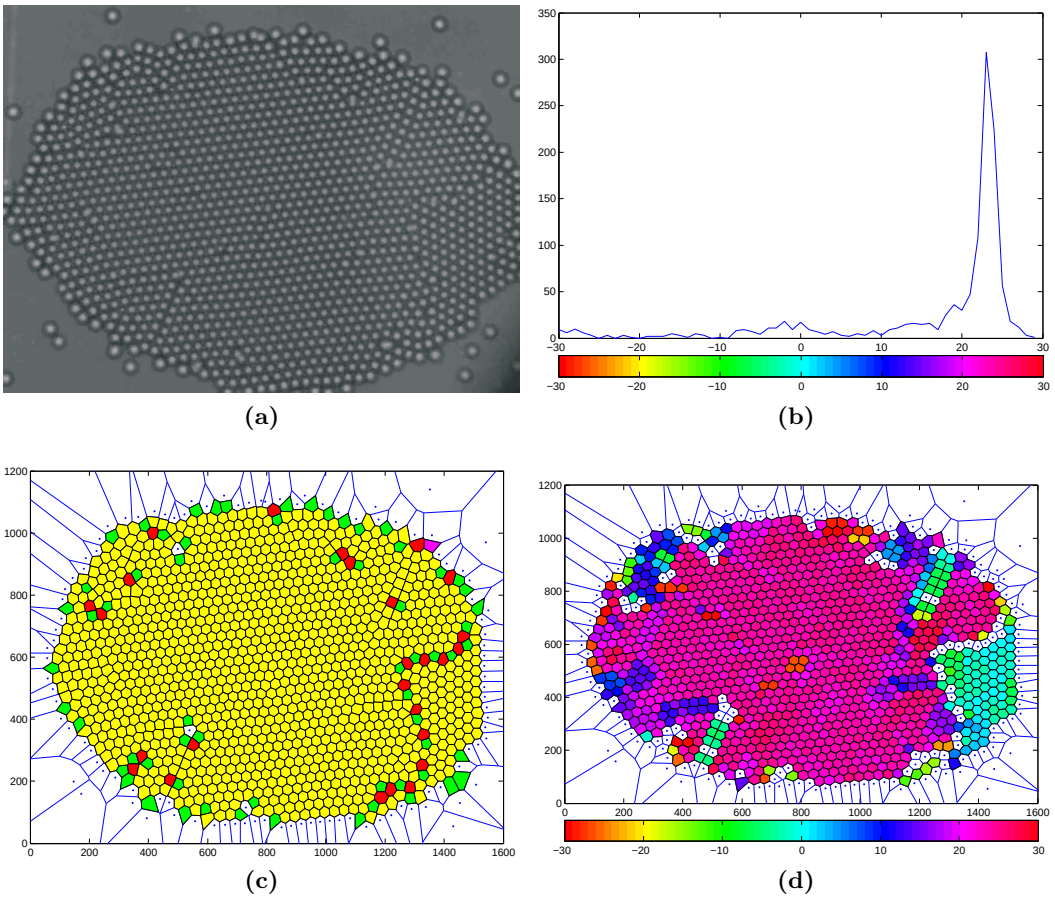

Figure 6.9: A large, low defect crystal with a single orientation, grown using a line of heating spots. The crystal is approximately 200 µm in diameter.

This technique may be utilized to grow large crystals with a single orientation, for example by using the SLM to place an array of nucleation sites across the gold surface. An example is shown in Figure 6.9, where a crystal is grown by placing 8 laser spots on the surface, each spot separated by 10.5 µm. Further experiments could involve growing crystals with nucleation sites positioned along more than one axis, to generate multiple grain boundaries and further investigate annealing dynamics. This could then be extended to randomly generated nucleation points, as a model system for nanocrystal growth. Experimentally, this will be quite challenging due to the difficulties of generating multiple arrays which have a low number of defects, which would negatively impact upon annealing lifetimes.

6.5 Conclusions

A colloidal system has been utilized as an analogue of nanocrystals to investigate the annealing dynamics of grain boundaries. A spatial light modulator was used to generate precisely

controlled nucleation spots for the individual grains, which were formed by the absorption of visible laser radiation on a gold coated surface through a combination of thermophoresis and convection currents. The variation of annealing lifetime with the separation of nucleation sites was investigated for the simplest case of two grains. Grain rotation induced grain coalescence was observed, with the average lifetimes of the annealing process found to be in good agreement with theoretical predictions for nanocrystal growth. Both grains were observed to rotate during the annealing process, with the final orientation of the crystal lying between the initial values of the grain orientations. Minimal particle rearrangement at the grain boundary was observed for small grains, while for the larger grains local surface melting was more prominent.

Chapter 7

Evanescent wave broadband cavity enhanced absorption spectroscopy

This chapter moves right away from the use of lasers as tools to manipulate condensed phase systems, and instead focuses upon spectroscopic analysis of interfacial systems, a topic related to the studies of WGMs of Chapters 4 and 5. Those previous chapters performed spectroscopy utilizing a microcavity, formed by a droplet whose dimensions were on the order of microns. In this chapter, a bulk fused silica/water interface is probed using an evanescent wave generated upon total internal reflection of light at the interface. Specifically, a supercontinuum light source is utilized for illumination, owing to its attractive properties which blend the spatial coherence and high intensities of a narrowband laser, with the wide spectral range offered by a broadband source. This chapter shall examine the adsorption of cytochrome c, a well characterised molecule, to the prism surface utilizing the SC for detection.

7.1 Introduction

Absorption spectroscopy (Section 4.7) is a widely used technique in analytical chemistry, owing to its specifity and absolute nature. For liquid phase samples, the Beer Lambert law is usually expressed as:

$$A = \log_{10} \frac{I_0}{I} = \epsilon C L \tag{7.1}$$

where I and I_0 refer to the intensities of the radiation in the presence and absence of absorbing species respectively, ϵ is the decadic molar absorption coefficient, C is the concentration of absorbing species and L is the pathlength through which the radiation travels. A serious

limitiation of conventional absorption spectroscopy is a lack of sensitivity, due to the difficulty in detecting small changes upon a large background signal. One method of increasing the sensitivity is to increase the pathlength, for instance utilizing a multipass cell. Another method for achieving enhanced pathlengths is to construct an optical cavity around the sample cell, such that the light undergoes multiple reflections before leaking out of the cavity and onto a detector. There are two primary methods by which this can be achieved. The first is known as *cavity ring down spectroscopy* (CRDS) [253]. In CRDS, a laser is coupled into a high finesse optical cavity, and when the laser radiation is on resonance with a cavity mode, a build up of intensity occurs within the cavity due to constructive interference. The source is then switched off, and the time dependence of the intensity decay is recorded. The *ring down time* (RDT) is defined as the time taken for the intensity to fall to $1/e$ of its initial value and is related to the loss mechanisms within the cavity (for example, scattering and absorption). Thus, it is possible to obtain the absolute absorption coefficient of a species simply by comparing the RDT in the presence and absence of absorbing species. The second related technique is known as *cavity enhanced absorption spectroscopy* (CEAS), where the time integrated transmitted intensity is measured [254]. Unlike CRDS, CEAS is not absolute and it is not possible to directly correlate the measured signal with the concentration of absorbing species without knowledge of the mirror reflectivity and other cavity losses. However, the technique does not require a fast optical switch and, from a technical viewpoint, is significantly less challenging than CRDS. When an optical cavity, consisting of two mirrors with reflectivity R, is constructed around the absorbing sample, the Beer-Lambert law is modified to read [255]:

$$\frac{I_0}{I} - 1 = \frac{\epsilon C \ell \ln 10}{1 - R} \tag{7.2}$$

where the notation given is for condensed phase samples. Cavity enhancement techniques are widely used for gas phase detection and typically employ mirrors of $R > 0.999$, thereby giving enhanced pathlengths on the order of a few km within a cell of length $\sim 1\,\mathrm{m}$.

However, there are several challenges that present themselves when cavity enhancement techniques are applied to studies of the condensed phase, all of which lead to reduced pathlength enhancements. For example, cavity enhanced absorption studies of liquids could be conducted by completely filling the optical cavity with liquid [256], however problems can arise due to molecules adsorbing to the surfaces within the cavity; in addition there is potential for mirror reflectivity degradation. Such liquid phase measurements will also demonstrate increased losses due to Rayleigh scattering from solvent molecules. Alternatively, a cuvette can be introduced into the cavity, either at Brewster's angle [257], or at normal incidence [258]; this will again lead to increased losses due to scattering from the cuvette surface. A rapidly developing technique for condensed phase studies utilises a total

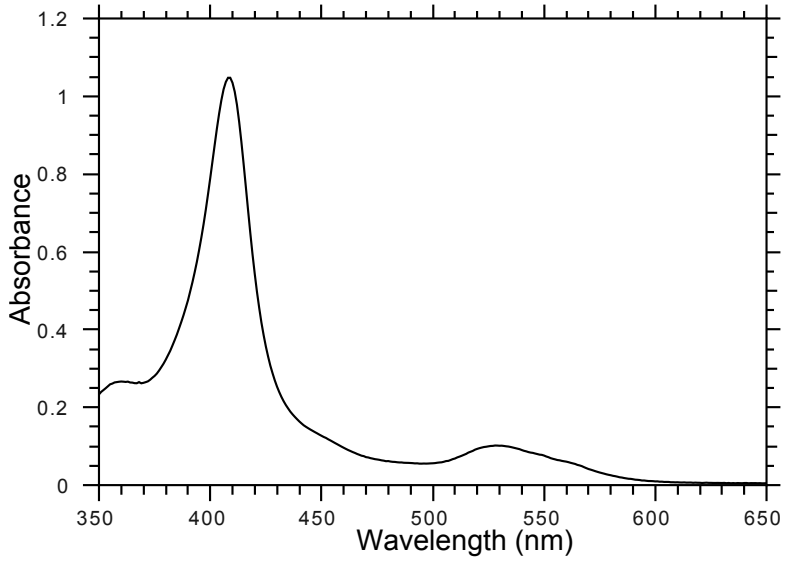

Figure 7.1: Absorption spectrum of a 10 µM solution of cyt c in KPB buffer.

internal reflection (TIR) event within the optical cavity to generate an evanescent wave (in a similar fashion to attenuated total reflection spectroscopy [259]), which is used to probe the sample [260]. These techniques are known as evanescent wave cavity ringdown spectroscopy (EW-CRDS) [261] and evanescent wave cavity enhanced absorption spectroscopy (EW-CEAS) [262].

One obvious disadvantage of using cavity enhancement techniques for surface/condensed phase measurements with narrowband lasers is the reduced specifity encountered because of the broad spectral features associated with surface and liquid phase species. A broadband source (for example, a light emitting diode [263] or a supercontinuum source [264]) coupled with highly reflective broadband cavity mirrors, overcomes this limitation when combined with a spectrograph to obtain a wavelength-resolved spectrum. Supercontinuum (SC) sources are particularly attractive for such studies due to their high spectral brilliance [265], as well as maintaining the spatial coherence of a laser beam. In this chapter, evanescent wave broadband cavity enhanced absorption spectroscopy (EW-BBCEAS) is used to study the adsorption of cytochrome c (cyt c) to the surface of a fused silica prism. Cyt c is a small, globular protein with a net positive charge at pH 7.4 and is widely used as a benchmark molecule [266–268]. The charge distribution in cyt c is highly asymmetric (measured dipole of > 300 D) [269], and thus will be attracted to the negatively charged prism surface. The visible absorption spectrum shows two main bands: a strong absorption known as the Soret band ($\lambda_{max} = 409$ nm) and the weaker Q band ($\lambda_{max} = 529$ nm), shown in Figure 7.1 for a 10 µM solution. This experiment utilizes an SC source operating between 450 nm to 700 nm, allowing the entirety of the Q band to be observed. The source

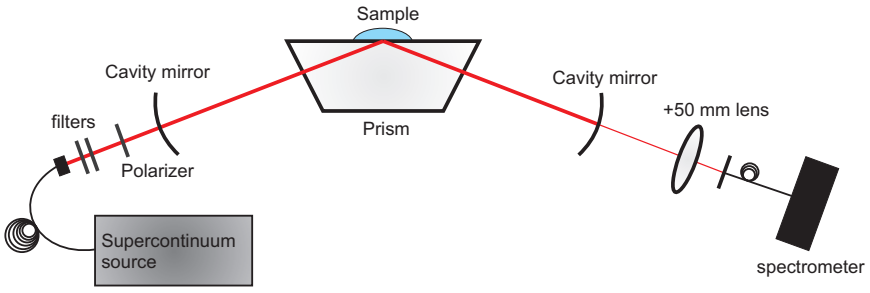

Figure 7.2: Schematic of the experimental setup, showing the sample carrying prism bound by two cavity mirrors. The filters remove the unwanted near-IR radiation from the SC source.

is selectively polarized, which can be used to give information about the orientation of the molecule.

7.2 Materials and Methods

A supercontinuum source (Fianium SC-450-4) is used as the broad band illumination for the experiment and has a maximum output power of 4 W over the 450–2000 nm range. The output of the source is directed through a series of filters (consisting of a pair of cold mirrors (Thorlabs FM03) and a 667 nm shortpass filter) to attenuate the unwanted near-infrared radiation. The resulting visible radiation (ranging from 450–700 nm) is then directed into a custom made Heraeus Suprasil 311 prism (Tower Optical) at normal incidence, undergoing total internal reflection at the prism/water interface with an angle of incidence of 70° (which greater than the critical angle for a fused silica/water interface of $\sim 67°$ at visible wavelengths). A broadband antireflection coating is present on the entrance and exit faces of the prism, in order to minimize reflection losses. An optical cavity is constructed around this prism using a pair of concave high reflectivity broadband cavity mirrors (0.9985–0.9998 from 400–700 nm) with a radius of curvature of 500 mm (Layertec). Light leaking out of the cavity is focused with a +50 mm lens into a fiber coupled spectrometer (Ocean Optics USB 2000). The SC output is randomly polarized, hence the output is selectively polarized using a Glan Laser Polarizer (Laser Lab Components) housed in a precision rotation mount (Newport); experiments have been conducted with this polarizer both pre-cavity and post-cavity. A schematic of the experimental setup is detailed in Figure 7.2.

Optical losses within the cavity will be dominated by those from the prism, hence Equation 7.2 should be modified to take into account these losses. This is quantified by defining a *cavity enhancement factor* (CEF), which is related to the enhancement due to the reflectivity of the mirrors composing the cavity and the losses as a result of the prism. Equation 7.2

is thus modified to:

$$\frac{I_0}{I} - 1 = \epsilon C d_e \ln 10 \times \text{CEF} \tag{7.3}$$

where d_e is the effective penetration depth of the evanescent wave, which is defined for a given polarization by Equations 7.4 and 7.5. The CEF is an experimentally determined factor, and must be determined on a daily basis. This is performed by measuring absorption spectra of known concentrations of aqueous dye solutions, and performing a linear regression on the measured value of $I_0/I - 1$ vs concentration. The dye solution used for calibration of the absorption spectrum is a mixture of Sunset Yellow FCF (Sigma) and Acid Red 27 (Sigma) dissolved in Milli-Q water (Millipore), each of concentration 1 mM. Calibration samples were prepared by accurately placing 40 µL of Milli-Q over the TIR footprint of the source on the prism surface. A spectrum for each polarization is recorded, corresponding to I_0. 10 µL aliquots of the calibration dye are then added to this droplet, the resulting solution is well mixed by multiple aspirations of the pipette. Again, a spectrum is recorded for each polarization and concentration of dye, giving the value of I. In between calibrations, the prism surface is thoroughly cleaned using high grade methanol and 50% sulfuric acid solution. As both dyes are negatively charged, it is assumed that adsorption of the dyes to the prism surface is negligible. To confirm that the cavity alignment is not altered between calibrations, care is taken to ensure that the signal observed on the spectrometer returns to its initial value after cleaning.

Cyt c from equine heart (Sigma, C7752) is dissolved in a 10 mM KPB buffer solution (pH 7.4) to give a stock solution with a concentration of 1 mM. This is then further diluted using KPB buffer to give stock solutions with concentrations ranging from 1 µM to 100 µM. Spectra of cyt c are recorded in a similar fashion to that of the calibration dye. In this instance, the value of I_0 is obtained by measuring the spectrum of a 40 µL droplet of KPB buffer solution on the prism surface. After a 10 µL aliquot of cyt c stock is added to the droplet, the system is left for 5 minutes to allow time for the cyt c adsorption to reach equilibrium before recording a spectrum for each polarization. Between measurements, 50% sulfuric acid solution is added to the TIR surface and left for 30 minutes; the prism is then cleaned using high grade and methanol and lens tissue. Again, confirmation that the alignment had not changed is obtained by noting that the spectrometer signal returns to its initial value; furthermore this suggests that all adsorbed cyt c has been removed from the prism surface. The prism surface is regularly purged of any residual organic matter by adding a 3:1 mixture of concentrated sulphuric acid:hydrogen peroxide solution (30%) to the TIR surface, followed by thorough rinsing with Milli-Q water and cleaning with high grade methanol/lens tissue.

7.3 Results and discussion

An example of the CEAS signals observed for the calibration dye with S and P polarized radiation is shown in Figure 7.3. The spectra show clear oscillations on top of the broad absorption band and are due to wavelength dependent variations in the CEF values. This highlights the need to correct the data for such variations in (principally) mirror reflectivity across the spectral range. Note that the spectra are considerably noisier at wavelengths $< 450\,\text{nm}$, owing to the very low levels of supercontinuum light. The effective penetration depth in Equation 7.3 is given by the equations formulated by Harrick, and is the equivalent pathlength that would give the same signal in a absorption measured by conventional transmission techniques. For S polarized radiation, this depth is given by [270]:

$$d_{e,s} = \frac{n_{21}\lambda_0 \cos\theta}{n_1 \pi (1 - n_{21}^2)(\sin^2\theta - n_{21}^2)^{1/2}} \tag{7.4}$$

while for P polarized radiation, the effective penetration depth is given by [270]:

$$d_{e,p} = \frac{n_{21}\lambda_0 \cos\theta (2\sin^2\theta - n_{21}^2)}{n_1 \pi (1 - n_{21}^2)[(1 + n_{21}^2)\sin^2\theta - n_{21}^2](\sin^2\theta - n_{21}^2)^{1/2}} \tag{7.5}$$

where n_2 and n_1 refer to the refractive indices of the aqueous phase and the prism respectively, and n_{21} is the ratio of the two. The value of the molar absorptivity of the calibration dye was determined by taking a single pass measurement of a 10 µM mixture of the dyes in a UV-Vis spectrophotometer (Cary 100, Varian). The CEAS signal is then plotted against concentration of the dye mixture in the droplet, and a linear regression is performed to obtain the CEF, as described by Equation 7.3. The resulting CEF values are shown in Figure 7.4, varying between 200–400. This is consistent with expectations for a cavity consisting of mirrors of $R \sim 0.999$ (giving a CEF of 1000) and additional intracavity losses due to the prism. P polarized light shows a lower CEF due to the increase in reflection losses. The CEF structure mirrors the dips in the CEAS signals in Figure 7.3, corresponding to the fluctuations in the mirror reflectivity. The general trend is an increase in the CEF towards the red end of the spectrum, due to the wavelength dependence of scattering losses. Variations in the exact structure are due to slightly different cavity alignments.

The CEAS signal of the cyt c solutions are converted to the equivalent value of the single pass absorbance of cyt c, via:

$$A = \frac{I_0/I - 1}{\ln 10 \times \text{CEF}} \tag{7.6}$$

The resulting spectra at a series of bulk cyt c concentrations are shown in Figure 7.5 for each polarization. The whole of the Q band is clearly visible between 500 and 590 nm. The absorption seen in Figure 7.5 at approximately 450 nm to 490 nm is due to the Soret band; this is a much stronger transition than the Q band, with a maximum absorbance at 409 nm

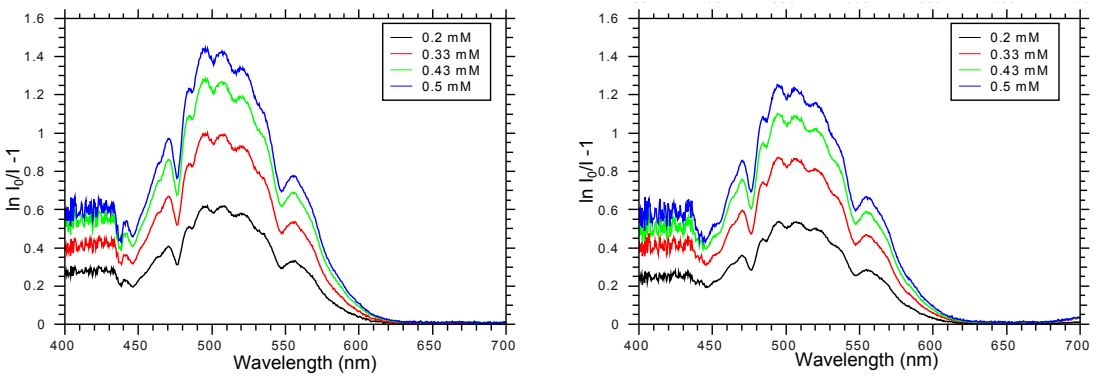

(a) P polarized **(b)** S Polarized

Figure 7.3: CEAS spectra of the dyes used to calibrate the CEF. For each wavelength, the measured signal is plotted against concentration. The CEF is then extracted by performing a linear regression, thus negating any changes in the mirror reflectivity across the spectrum.

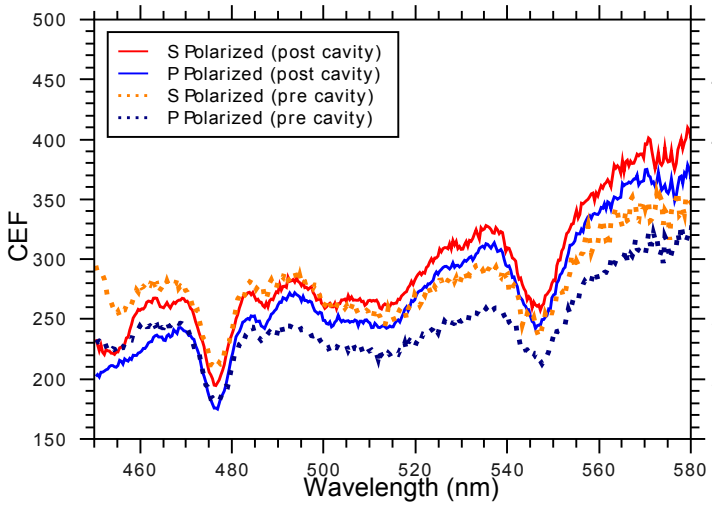

Figure 7.4: Examples of measured cavity enhancement factors obtained from performing a linear regression on the spectra in Figure 7.3. The solid lines correspond to the polarizer being placed after the cavity, while the dotted lines correspond to the polarizer being placed prior to the cavity.

(lying outside the range of the SC). Equation 7.2 can be used to estimate what the expected value of a CEAS signal would be for a bulk cyt c solution. The decadic molar absorption coefficient ϵ was found by taking a single pass absorption spectrum of a 10 µM solution of cyt c in KPB buffer, and was found to be 1.01×10^{6} M^{-1} m^{-1} at 532 nm. Using the CEF for S polarized light shown in Figure 7.4, a bulk CEAS signal of 0.0075 is predicted for a 10 µM solution. The measured CEAS signal is on the order of 0.65, so we conclude the signal detected is due to absorption of radiation from molecules situated at the interface.

The effective single pass absorbance values shown in Figure 7.5 are therefore due to surface adsorbed species only.

The absorption spectrum is integrated between 500 and 590 nm for each concentration in Figure 7.5; three repeat measurements are performed and the integrated absorbance averaged. This integrated absorbance is then plotted against concentration, shown in Figure 7.6 and the data is fitted to a Langmuir isotherm of the form:

$$A = \frac{A_{\max} KC}{1 + KC} \tag{7.7}$$

where $A_{\max}$ corresponds to the maximum absorbance and K is the equilibrium constant for adsorption of the protein. The parameters obtained from the plot are presented in Table 7.1. It is of interest to note that the equilibrium constants returned from the fit are an order of magnitude larger than those previously reported for the adsorption of cyt c under similar conditions [271], however equilibrium constants of the order of 10^6 M^{-1} have been reported for adsorption of cyt c to Coring 0211 glass surfaces [272]. This may be due to the cleaning method employed; the mixture of sulphuric acid and hydrogen peroxide is known to hydroxylate silica surfaces, and so providing more adsorption sites for the cty c molecules.

The assumptions made in the derivation of the Langmuir isotherm are that only one type of adsorption site is present, and that monolayer coverage is achieved. The first assumption is certainly invalid in the case of adsorption to hydrophilic silica as it is known that two silanol sites exist [273]. A fit to a multi-adsorption site isotherm was attempted but this did not yield sensible values for the maximum absorbance and the equilibrium constants.

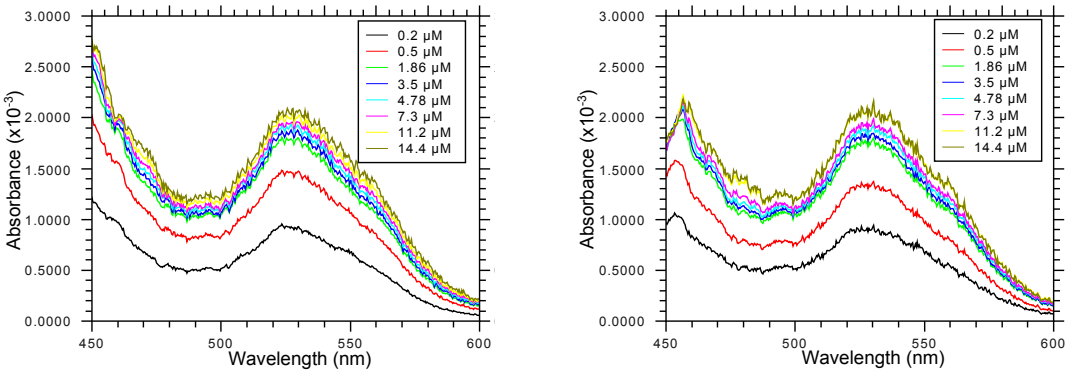

(a) P polarized **(b)** S Polarized

Figure 7.5: Absorption spectra of cyt c, determined by dividing the CEAS signal by the measured CEF. The Q band is clearly visible, while the peak of the Soret band lies outside of the SC spectral range.

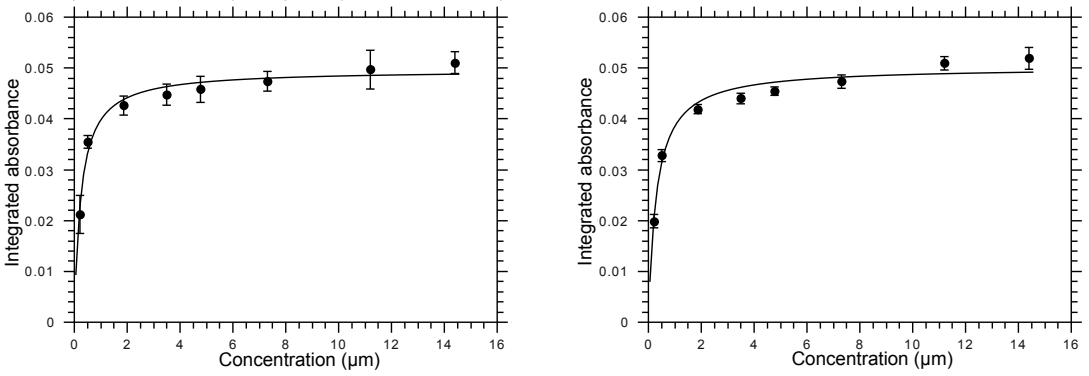

(a) P polarized **(b)** S Polarized

Figure 7.6: Integrated absorbance vs bulk concentration of cyt c. The black line corresponds to a fit of to the Langmuir isotherm in Equation 7.7.

Table 7.1: Parameters determined from the fitting of the Langmuir isotherm in Equation 7.7 to the data in Figure 7.6. R^2 is the squared regression coefficient and reflects the goodness of the fit to the data.

Parameter	Value (S Polarized)	Value (P Polarized)
$A_{\max}$	0.05 ± 0.0009	0.05 ± 0.0009
K ($\times 10^6$ M^{-1})	3.30 ± 0.45	4.04 ± 0.49
ΔG (kJ mol^{-1})	-36.6 ± 0.14	-37.1 ± 0.12
R^2	0.970	0.972

A second assumption is that monolayer coverage is obtained. An estimate of the expected absorbance due to monolayer coverage can be obtained via the dimensions of cyt c and the area of the laser spot. The dimensions of a cyt c molecule are (25 × 25 × 37) Å and the area of the laser spot is approximately 6 mm^2. A rough estimate of the amount of cyt c in a monolayer on the laser spot is approximately 1.26×10^{-12} mol; using the molar absorptivity of cyt c determined from a single pass absorption measurements implies that this monolayer should have an integrated absorbance of 0.016 over the range 500 nm to 590 nm. The measured maximum absorbance is 0.05, so it is concluded that ∼3 monolayers are present on the surface at the highest concentration. This is consistent with previous measurements using EW-CRDS [271].

The orientation of the cyt c adsorbed to the surface can be probed by measuring the differences in absorbance with different polarizations. This is quantified by the *dichroic ratio*, i.e. the ratio of the absorbances of S and P polarized light and may be evaluated via [274]:

$$\rho = \frac{A_s}{A_p} = \frac{|E_y|^2}{|E_x|^2 + 2|E_z|^2 \cot^2\langle\alpha\rangle} \tag{7.8}$$

where $|E_i|$ is the amplitude of the ith component of the electric field of the evanescent wave, and $\langle\alpha\rangle$ is the mean angle of the transition dipole moment with respect to the surface normal. A non-unity value of ρ suggests some form of orientational order of the adsorbed cyt c. The dichroic ratio was determined using the pre-cavity polarizer data, and three repeats were performed for each measurement, to give a wavelength-resolved average dichroic ratio. This result was then averaged over the entire wavelength range of the Q band, giving a resulting dichroic ratio was 0.85 ± 0.1.

To extract the tilt angle of the transition dipole moment, the electric field amplitudes are calculated via [274]

$$E_x = \frac{2(\sin^2\theta_i - n_{21}^2)^{1/2}\cos\theta_i}{(1-n_{21}^2)^{1/2}[(1+n_{21}^2)\sin^2\theta_i - n_{21}^2]^{1/2}} \tag{7.9}$$

$$E_y = \frac{2\cos\theta_i}{(1-n_{21}^2)^{1/2}} \tag{7.10}$$

$$E_z = \frac{2\sin\theta_i\cos\theta_i}{(1-n_{21}^2)^{1/2}[(1+n_{21}^2)\sin^2\theta_i - n_{21}^2]^{1/2}} \tag{7.11}$$

For example, at 525 nm these equations give the electric field amplitudes to be $|E_x| = 0.4156$, $|E_y| = 1.6853$ and $|E_z| = 1.7872$, which lead to an average angle of the transition dipole moment 54.8 ± 1.7° for the dichroic ratio quoted above. Representative angles for each measurement (at low and high bulk concentration) are presented in Table 7.2. Note that previous work by Edmiston *et al.* for adsorption of cyt c to a hydrophilic surface reported a tilt angle of 12 ± 33° [267]. The broad orientation distribution reported for a hydrophilic surface (where the quoted uncertainty is the standard deviation in the orientation distribution) was attributed to competing interactions resulting in a relatively disordered film on the surface. A more recent study by Cheng *et al.*, probing the Soret band, measured a tilt angle of 41° (no quoted uncertainty) [268].

The measured value of $\langle\alpha\rangle$ appears to be independent of bulk concentration, and is approximately the same as the magic angle (the angle for which $3\cos^2\theta - 1 = 0$), which takes the value of 54.7° i.e. the sample is isotropically distributed along the interface. There is likely to be additional uncertainty in these measurements as the polarization scrambling due to stress-induced birefringence in the cavity mirrors is not fully characterised. Furthermore, the use of tilted mirrors to direct the SC source into the prism is likely to introduce a degree of elliptical polarisation to the beam, which would result in additional ambiguity when measuring the absorbances for the different polarisations. Future measurements should fibre couple the filtered output of the SC source, with the output coupler mounted directly infront of the cavity at the correct orientation. Furthermore, two polarizers of the same orientation should be utilized pre- and post-cavity, to ensure that the same type of polarisation used to probe the molecules is detected by the spectrometer.

Table 7.2: Mean angle between the surface normal and the transition dipole moment determined from the dichroic ratios measured using a linear polarizer pre-cavity. The uncertainty quoted arises from taking the deviation of the dichroic ratio over the spectral range.

0.5 µM	$\langle\alpha\rangle$	14.4 µM	$\langle\alpha\rangle$
1	$54.5 \pm 0.7°$	1	$55.5 \pm 0.7°$
2	$56.4 \pm 0.7°$	2	$56.0 \pm 0.7°$
3	$53.0 \pm 0.7°$	3	$52.7 \pm 0.7°$

7.4 Conclusions

This chapter has demonstrated the application of evanescent wave broadband cavity enhanced absorption spectroscopy (EW-BBCEAS) to the study of cytochrome c adsorbing to a prism surface. Cavity enhancement factors on the order of 300 were measured by utilizing known concentrations of absorbing dye on the prism surface. The broadband nature of the SC source allowed the whole of the Q band to be observed and its integrated absorbance was measured as a function of bulk cyt c concentration. The data is well fit by a Langmuir isotherm, with a large value of the equilibrium constant K indicative of the high degree of adsorption, although the limiting value of the absorbance suggests that approximately three monolayers have adsorbed to the surface. A linear polarizer was used to selectively polarize the SC output, with the aim of obtaining information about the orientation of cyt c to be determined. A mean orientation of the transition dipole moment was found to be $54.8° \pm 1.7$, similar to the magic angle.

Chapter 8

General Conclusions

The work presented in this thesis has covered a wide range of topics relating to the dynamics and spectroscopy of colloidal particles, aerosols and other interfacial systems.

The bulk of the work presented relied upon the construction and characterisation of a dynamic holographic optical tweezers experiment, allowing precise manipulation of microscopic matter. This tweezers system was coupled with a high resolution spectrograph, to allow spectroscopic measurements to be carried out in tandem with sample tweezing.

The system was applied to the study of salt water aerosols; the 532 nm radiation utilized in the tweezers acts as the excitation source for Raman scattering from the water molecules comprising the aerosols. Whispering Gallery Modes observed within the Raman spectrum were assigned utilizing a custom written MATLAB script, returning accurate measurements of the aerosol size and composition. The mechanism of droplet "locking" due to resonant absorption of the trapping laser when trapped with a Gaussian beam was explored. The spatial light modulator (SLM) was utilized to investigate how the WGM spectrum of the droplet is altered by changing from a conventional Gaussian trapping beam to a Laguerre Gaussian geometry. Higher values of the topological charge of the LG mode were demonstrated to give much more intense resonant modes within the SRS spectrum, with diameters concomitant with a WGM at the trapping laser wavelength. In order to appreciate the relative humidity within the aerosol cell, diode laser absorption spectroscopy was utilized to measure the concentration of water molecules, demonstrating that high relative humidities can be achieved even with unsealed cells lacking active RH regulation.

The first known demonstration of the optical tweezing of ionic liquid solutions was performed. Droplets comprising the ionic liquid ethylammonium nitrate and water were generated and trapped using a conventional optical tweezers. These droplets were spectroscopically interrogated using broadband Mie scattering, with the location of the morphology

dependent resonances within the scattered spectrum used to assign the droplet size and refractive index (and hence determine composition). The response of these droplets to low, ambient and high RH environments was also investigated, with an ultimate aim of trapping droplets of pure ionic liquid in order to assess their purity, and uptake of gaseous species.

The SLM setup was utilized with a low numerical aperture microscope objective to heat the surface of a gold-coated microscope slide at precisely defined locations. When a colloidal sample was placed onto this slide, the combination of thermophoresis and convection currents induced formation of two dimensional colloidal crystals. The SLM allowed multiple heating spots to be generated, allowing the interaction of two crystals to be observed. At the simplest level of two crystals of a different orientation, they merge to form a grain boundary, then both crystals rotate to anneal this boundary and form a crystal with a single orientation. The scaling behaviour of this interaction agrees very well with theoretical predictions from nanocrystal growth, and direct observations utilizing video microscopy provided information about the real time mechanism of grain rotation.

Finally, an alternative method of probing an interfacial system, using evanescent waves, was demonstrated. An optical cavity was constructed around a fused silica prism, upon which a supercontinuum source was incident. This cavity enhancement technique increases the sensitivity of conventional absorption spectroscopy (or attenuated total reflection spectroscopy) by increasing the pathlength through which the radiation travels. The evanescent wave generated upon total internal reflection was utilized to probe the adsorption of cytochrome c molecules to the prism surface, with selective polarisation utilized to elucidate the orientation of the adsorbed molecules. A strong degree of adsorption to the prism surface was measured, inferred to be due to the presence of ~ 3 monolayers of cyt c.

The nebulization of pure ionic liquids offers exciting future development for this work. Spectroscopic characterisation can be utilized to assess their purity, but a much more interesting investigation is the potential of droplets to sequester greenhouse gases, and compare the efficiency of droplets to the bulk phase. The uptake of CO_2 by the droplet could be monitored by spectroscopic techniques (such as Raman spectroscopy). If this process is feasible, then the possibility of *in situ* reduction of CO_2 (using the droplet itself as a microreactor) could be explored. For instance, homogeneous hydrogenation of CO_2 to CH_3OH was reported by Ashley *et al.* [275]; if future reagents were developed that were compatible with ILs and suitably reactive at ambient temperature and pressure, then the benefits that would be offered to the carbon economy would be enormous.

References

[1] P. Atkins and J. de Paulo. *Atkins' Physical Chemistry*. Oxford University Press (2002).

[2] D. J. McClements and E. Dickinson. *Advances In Food Colloids*. Advances in Food Colloids. Springer (1996).
http://books.google.co.uk/books?id=YFC2CF63qr4C

[3] T. F. Tadros. *Colloids in Paints: Colloids and Interface Science*. Number v. 6 in Colloids and Interface Science. Wiley (2011).
http://books.google.co.uk/books?id=A5v_YJbRMPgC

[4] C. A. Murray and D. G. Grier. "Video Microscopy of Monodisperse Colloidal Systems". *Annual Review of Physical Chemistry*, **47**, 421–462 (1996).
http://dx.doi.org/10.1146/annurev.physchem.47.1.421

[5] V. Prasad, D. Semwogerere and E. R. Weeks. "Confocal microscopy of colloids". *Journal of Physics: Condensed Matter*, **19**, 113102 (2007).
http://dx.doi.org/10.1088/0953-8984/19/11/113102

[6] P. N. Pusey and W. van Megen. "Phase behaviour of concentrated suspensions of nearly hard colloidal spheres". *Nature*, **320**, 340 (1986).
http://dx.doi.org/10.1038/320340a0

[7] A. Yethiraj. "Tunable colloids: control of colloidal phase transitions with tunable interactions". *Soft Matter*, **3**, 1099 (2007).
http://dx.doi.org/10.1039/b704251p

[8] D. G. Grier and C. A. Murray. "The microscopic dynamics of freezing in supercooled colloidal fluids". *The Journal of Chemical Physics*, **100**, 9088 (1994).
http://dx.doi.org/10.1063/1.466662

[9] U. Gasser, E. R. Weeks, A. Schofield, P. N. Pusey and D. A. Weitz. "Real-space imaging of nucleation and growth in colloidal crystallization." *Science*, **292**, 258–62 (2001).
http://dx.doi.org/10.1126/science.1058457

[10] D. G. A. L. Aarts, M. Schmidt and H. N. W. Lekkerkerker. "Direct visual observation of thermal capillary waves." *Science*, **304**, 847–50 (2004). http://dx.doi.org/10.1126/science.1097116

[11] R. Dullens, D. Aarts and W. Kegel. "Dynamic Broadening of the Crystal-Fluid Interface of Colloidal Hard Spheres". *Physical Review Letters*, **97**, 2–5 (2006). http://dx.doi.org/10.1103/PhysRevLett.97.228301

[12] W. Poon. "Colloids as big atoms." *Science*, **304**, 830–1 (2004). http://dx.doi.org/10.1126/science.1097964

[13] A. Ashkin, J. M. Dziedzic, J. E. Bjorkholm and S. Chu. "Observation of a single-beam gradient force optical trap for dielectric particles". *Optics Letters*, **11**, 288 (1986). http://dx.doi.org/10.1364/OL.11.000288

[14] E. Hecht. *Optics*. Addison Wesley, San Francisco, fourth edition (2002).

[15] A. Ashkin. *Optical Trapping and Manipulation of Neutral Particles Using Lasers*. World Scientific, Singapore (2006). http://books.google.co.uk/books?id=N0x_QgAACAAJ

[16] A. Ashkin. "Acceleration and Trapping of Particles by Radiation Pressure". *Physical Review Letters*, **24**, 156–159 (1970). http://dx.doi.org/10.1103/PhysRevLett.24.156

[17] A. Ashkin and D. Dziedzic. "Optical Levitation by Radiation Pressure". *Applied Physics Letters*, **19**, 283 (1971). http://dx.doi.org/10.1063/1.1653919

[18] A. Ashkin and J. M. Dziedzic. "Stability of optical levitation by radiation pressure". *Applied Physics Letters*, **24**, 586 (1974). http://dx.doi.org/10.1063/1.1655064

[19] A. Ashkin and J. M. Dziedzic. "Feedback stabilization of optically levitated particles". *Applied Physics Letters*, **30**, 202 (1977). http://dx.doi.org/10.1063/1.89335

[20] A. Ashkin and J. M. Dziedzic. "Observation of Resonances in the Radiation Pressure on Dielectric Spheres". *Physical Review Letters*, **38**, 1351–1354 (1977). http://dx.doi.org/10.1103/PhysRevLett.38.1351

[21] A. Ashkin and J. M. Dziedzic. "Observation of optical resonances of dielectric spheres by light scattering". *Applied Optics*, **20**, 1803–1814 (1981). http://dx.doi.org/10.1364/AO.20.001803

[22] A. Ashkin. "Optical trapping and manipulation of neutral particles using lasers". *Proceedings of the National Academy of*, **94**, 4853–4860 (1997).
http://dx.doi.org/10.1073/pnas.94.10.4853

[23] A. Ashkin. "Trapping of Atoms by Resonance Radiation Pressure". **40**, 729–732 (1978).
http://dx.doi.org/10.1103/PhysRevLett.40.729

[24] A. Ashkin and J. M. Dziedzic. "Optical trapping and manipulation of viruses and bacteria ". *Science*, **235**, 1517–1520 (1987).
http://dx.doi.org/10.1126/science.3547653

[25] S. Block, D. Blair and H. Berg. "Compliance of bacterial flagella measured with optical tweezers". *Nature*, **338**, 514 (1989).
http://dx.doi.org/10.1038/338514a0

[26] K. Svoboda and S. M. Block. "Biological Applications of Optical Forces". *Annual Review of Biophysics and Biomolecular Structure*, **23**, 247–285 (1994).
http://dx.doi.org/10.1146/annurev.bb.23.060194.001335

[27] U. Bockelmann, P. Thomen, B. Essevaz-Roulet, V. Viasnoff and F. Heslot. "Unzipping DNA with optical tweezers: high sequence sensitivity and force flips." *Biophysical journal*, **82**, 1537–53 (2002).
http://dx.doi.org/10.1016/S0006-3495(02)75506-9

[28] U. Bockelmann, B. Essevaz-Roulet and F. Heslot. "Molecular Stick-Slip Motion Revealed by Opening DNA with Piconewton Forces". *Physical Review Letters*, **79**, 4489–4492 (1997).
http://dx.doi.org/10.1103/PhysRevLett.79.4489

[29] J. Finer, R. Simmons and J. Spudich. "Single myosin molecule mechanics: piconewton forces and nanometre steps". *Nature* (1994).
http://dx.doi.org/10.1038/368113a0

[30] S. Block, L. Goldstein and B. Schnapp. "Bead movement by single kinesin molecules studied with optical tweezers". *Nature*, **348**, 348 (1990).
http://dx.doi.org/10.1038/348348a0

[31] C. Shingyoji, H. Higuchi, M. Yoshimura, E. Katayama and T. Yanagida. "Dynein arms are oscillating force generators." *Nature*, **393**, 711–4 (1998).
http://dx.doi.org/10.1038/31520

[32] J. E. Molloy and M. J. Padgett. "Lights, action: Optical tweezers". *Contemporary Physics*, **43**, 241–258 (2002).
http://dx.doi.org/10.1080/00107510110116051

[33] T. Perkins. "Optical traps for single molecule biophysics: a primer". *Laser and Photonics Review*, **3**, 203–220 (2009).
http://dx.doi.org/10.1002/lpor.200810014

[34] P. Korda, G. C. Spalding, E. R. Dufresne and D. G. Grier. "Nanofabrication with holographic optical tweezers". *Review of Scientific Instruments*, **73**, 1956 (2002).
http://dx.doi.org/10.1063/1.1455136

[35] D. C. Benito, D. M. Carberry, J. Hildmann, E. G. Edwards, S. H. Simpson, G. M. Gibson, M. J. Padgett, J. G. Rarity, M. Kuball, M. J. Miles and S. Hanna. "Fabrication of photonic crystal templates using holographic optical tweezers and adhesion via entropic attraction". *Proceedings of SPIE*, **7038**, 70380K–70380K–9 (2008).
http://dx.doi.org/10.1117/12.795070

[36] D. C. Benito, D. M. Carberry, S. H. Simpson, G. M. Gibson, M. J. Padgett, J. G. Rarity, M. J. Miles and S. Hanna. "Constructing 3D crystal templates for photonic band gap materials using holographic optical tweezers." *Optics Express*, **16**, 13005–15 (2008).
http://dx.doi.org/10.1364/OE.16.013005

[37] R. Agarwal, K. Ladavac, Y. Roichman, G. Yu, C. Lieber and D. Grier. "Manipulation and assembly of nanowires with holographic optical traps." *Optics Express*, **13**, 8906–12 (2005).
http://dx.doi.org/10.1364/OPEX.13.008906

[38] M. E. J. Friese, H. Rubinsztein-Dunlop, J. Gold, P. Hagberg and D. Hanstorp. "Optically driven micromachine elements". *Applied Physics Letters*, **78**, 547 (2001).
http://dx.doi.org/10.1063/1.1339995

[39] D. M. Carberry, S. H. Simpson, J. a. Grieve, Y. Wang, H. Schäfer, M. Steinhart, R. Bowman, G. M. Gibson, M. J. Padgett, S. Hanna and M. J. Miles. "Calibration of optically trapped nanotools." *Nanotechnology*, **21**, 175501 (2010).
http://dx.doi.org/10.1088/0957-4484/21/17/175501

[40] D. B. Phillips, D. M. Carberry, S. H. Simpson, H. Schäfer, M. Steinhart, R. Bowman, G. M. Gibson, M. J. Padgett, S. Hanna and M. J. Miles. "Optimizing the optical trapping stiffness of holographically trapped microrods using high-speed video tracking". *Journal of Optics*, **13**, 044023 (2011).
http://dx.doi.org/10.1088/2040-8978/13/4/044023

[41] A. Yao, M. Tassieri, M. Padgett and J. Cooper. "Microrheology with optical tweezers." *Lab on a chip*, **9**, 2568–75 (2009).
http://dx.doi.org/10.1039/b907992k

[42] E. M. Furst. "Applications of laser tweezers in complex fluid rheology". *Current Opinion in Colloid & Interface Science*, **10**, 79–86 (2005). http://dx.doi.org/10.1016/j.cocis.2005.04.001

[43] C. Hertlein, L. Helden, a. Gambassi, S. Dietrich and C. Bechinger. "Direct measurement of critical Casimir forces." *Nature*, **451**, 172–5 (2008). http://dx.doi.org/10.1038/nature06443

[44] M. Ozkan, M. Wang and C. Ozkan. "Optical manipulation of objects and biological cells in microfluidic devices". *Biomedical Microdevices*, **5**, 61–67 (2003). http://dx.doi.org/10.1023/A:1024467417471

[45] J. Enger, M. Goksör, K. Ramser, P. Hagberg and D. Hanstorp. "Optical tweezers applied to a microfluidic system." *Lab on a chip*, **4**, 196–200 (2004). http://dx.doi.org/10.1039/b307960k

[46] E. Eriksson, J. Enger, B. Nordlander, N. Erjavec, K. Ramser, M. Goksör, S. Hohmann, T. Nyström and D. Hanstorp. "A microfluidic system in combination with optical tweezers for analyzing rapid and reversible cytological alterations in single cells upon environmental changes." *Lab on a chip*, **7**, 71–6 (2007). http://dx.doi.org/10.1039/b613650h

[47] M. Padgett and R. Di Leonardo. "Holographic optical tweezers and their relevance to lab on chip devices." *Lab on a chip*, **11**, 1196–205 (2011). http://dx.doi.org/10.1039/c0lc00526f

[48] D. G. Grier. "Optical tweezers in colloid and interface science". *Current Opinion in Colloid & Interface Science*, **2**, 264–270 (1997). http://dx.doi.org/10.1016/S1359-0294(97)80034-9

[49] P. T. Korda and D. G. Grier. "Annealing thin colloidal crystals with optical gradient forces". *The Journal of Chemical Physics*, **114**, 7570 (2001). http://dx.doi.org/10.1063/1.1359741

[50] L. Belloni. "Colloidal interactions". *Journal of Physics: Condensed Matter*, **549** (2000). http://dx.doi.org/10.1088/0953-8984/12/46/201

[51] J. C. Crocker and D. G. Grier. "Microscopic measurement of the pair interaction potential of charge-stabilized colloid". *Physical Review Letters*, **73**, 352–356 (1994). http://dx.doi.org/10.1103/PhysRevLett.73.352

[52] J. C. Crocker and D. G. Grier. "When Like Charges Attract: The Effects of Geometrical Confinement on Long-Range Colloidal Interactions." *Physical Review Letters*,

77, 1897–1900 (1996).
http://dx.doi.org/10.1103/PhysRevLett.77.1897

[53] E. R. Dufresne, T. M. Squires, M. P. Brenner and D. G. Grier. "Hydrodynamic coupling of two brownian spheres to a planar surface." *Physical Review Letters*, **85**, 3317–20 (2000).
http://dx.doi.org/10.1103/PhysRevLett.85.3317

[54] S. Henderson, S. Mitchell and P. Bartlett. "Position correlation microscopy: probing single particle dynamics in colloidal suspensions". *Colloids and Surfaces A: Physicochemical and Engineering Aspects*, **190**, 81–88 (2001).
http://dx.doi.org/10.1016/S0927-7757(01)00667-7

[55] S. Kulin, R. Kishore, K. Helmerson and L. Locascio. "Optical manipulation and fusion of liposomes as microreactors". *Langmuir*, pp. 8206–8210 (2003).
http://dx.doi.org/10.1021/la0344433

[56] J. E. Reiner, A. M. Crawford, R. B. Kishore, L. S. Goldner, K. Helmerson and M. K. Gilson. "Optically trapped aqueous droplets for single molecule studies". *Applied Physics Letters*, **89**, 13904 (2006).
http://dx.doi.org/10.1063/1.2219977

[57] S. Kawata and T. Sugiura. "Movement of micrometer-sized particles in the evanescent field of a laser beam". *Optics Letters*, **17**, 772–774 (1992).
http://dx.doi.org/10.1364/OL.17.000772

[58] V. Garces-Chavez, K. Dholakia and G. C. Spalding. "Extended-area optically induced organization of microparticles on a surface". *Applied Physics Letters*, **86**, 031106 (2005).
http://dx.doi.org/10.1063/1.1843283

[59] C. D. Mellor, C. D. Bain and J. Lekner. "Pattern formation in evanescent wave optical traps". *Proc SPIE*, **5930**, 352 (2005).
http://dx.doi.org/10.1117/12.616474

[60] C. D. Mellor and C. D. Bain. "Array formation in evanescent waves." *ChemPhysChem*, **7**, 329–32 (2006).
http://dx.doi.org/10.1002/cphc.200500348

[61] M. Šiler, T. Čižmár, M. Šerý and P. Zemánek. "Optical forces generated by evanescent standing waves and their usage for sub-micron particle delivery". *Applied Physics B*, **84**, 157–165 (2006).
http://dx.doi.org/10.1007/s00340-006-2235-9

[62] K. Dholakia. "Colloquium: Gripped by light: Optical binding". *Reviews of Modern Physics*, **82**, 1767–1791 (2010).
http://dx.doi.org/10.1103/RevModPhys.82.1767

[63] M. Burns, J. M. Fournier and J. A. Golovchenko. "Optical binding". *Physical Review Letters*, **63**, 1233–1236 (1989).
http://dx.doi.org/10.1103/PhysRevLett.63.1233

[64] P. J. Reece, V. Garces-Chavez and K. Dholakia. "Near-field optical micromanipulation with cavity enhanced evanescent waves". *Applied Physics Letters*, **88**, 221116 (2006).
http://dx.doi.org/10.1063/1.2208272

[65] N. J. van Leeuwen, L. J. Moore, W. D. Partridge, R. Peverall, G. A. D. Ritchie and M. D. Summers. "Near-field optical trapping with an actively locked cavity". *Journal of Optics*, **13**, 044007 (2011).
http://dx.doi.org/10.1088/2040-8978/13/4/044007

[66] M. D. Summers, R. D. Dear, J. M. Taylor and G. A. D. Ritchie. "Directed assembly of optically bound matter". *Optics Express*, **20**, 1001 (2012).
http://dx.doi.org/10.1364/OE.20.001001

[67] A. Constable, J. Kim, J. Mervis, F. Zarinetchi and M. Prentiss. "Demonstration of a fiber-optical light-force trap." *Optics Letters*, **18**, 1867–9 (1993).
http://dx.doi.org/10.1364/OL.18.001867

[68] J. Guck, R. Ananthakrishnan, H. Mahmood, T. J. Moon, C. C. Cunningham and J. Käs. "The optical stretcher: a novel laser tool to micromanipulate cells." *Biophysical journal*, **81**, 767–84 (2001).
http://dx.doi.org/10.1016/S0006-3495(01)75740-2

[69] J. Guck, S. Schinkinger, B. Lincoln, F. Wottawah, S. Ebert, M. Romeyke, D. Lenz, H. M. Erickson, R. Ananthakrishnan, D. Mitchell, J. Käs, S. Ulvick and C. Bilby. "Optical deformability as an inherent cell marker for testing malignant transformation and metastatic competence." *Biophysical journal*, **88**, 3689–98 (2005).
http://dx.doi.org/10.1529/biophysj.104.045476

[70] P. Y. Chiou, A. T. Ohta and M. C. Wu. "Massively parallel manipulation of single cells and microparticles using optical images." *Nature*, **436**, 370–2 (2005).
http://dx.doi.org/10.1038/nature03831

[71] M. C. Wu. "Optoelectronic Tweezers". *Nature Photonics*, **5**, 322–324 (2011).
http://dx.doi.org/10.1038/nphoton.2011.98

[72] H.-y. Hsu, A. T. Ohta, P.-Y. Chiou, A. Jamshidi, S. L. Neale and M. C. Wu. "Phototransistor-based optoelectronic tweezers for dynamic cell manipulation in cell culture media." *Lab on a chip*, **10**, 165–72 (2010).
http://dx.doi.org/10.1039/b906593h

[73] A. T. Ohta, M. Garcia, J. K. Valley, L. Banie, H.-Y. Hsu, A. Jamshidi, S. L. Neale, T. Lue and M. C. Wu. "Motile and non-motile sperm diagnostic manipulation using optoelectronic tweezers." *Lab on a chip*, **10**, 3213–7 (2010).
http://dx.doi.org/10.1039/c0lc00072h

[74] A. Ashkin. "Forces of a single-beam gradient laser trap on a dielectric sphere in the ray optics regime." *Methods in cell biology*, **55**, 1–27 (1992).
http://dx.doi.org/10.1016/S0006-3495(92)81860-X

[75] K. C. Neuman and S. M. Block. "Optical trapping". *Review of Scientific Instruments*, **75**, 2787–2809 (2004).
http://dx.doi.org/10.1063/1.1785844

[76] G. Gouesbet. "Generalized Lorenz-Mie theory and applications". *Particle & Particle Systems Characterization*, **11**, 22–34 (1994).
http://dx.doi.org/10.1002/ppsc.19940110105

[77] K. F. Ren, G. Gréha and G. Gouesbet. "Radiation pressure forces exerted on a particle arbitrarily located in a Gaussian beam by using the generalized Lorenz-Mie theory, and associated resonance effects". *Optics Communications*, **4018**, 343–354 (1994).
http://dx.doi.org/10.1016/0030-4018(94)90673-4

[78] A. Mazolli, P. A. Maia Neto and H. M. Nussenzveig. "Theory of trapping forces in optical tweezers". *Proceedings of the Royal Society A: Mathematical, Physical and Engineering Sciences*, **459**, 3021–3041 (2003).
http://dx.doi.org/10.1098/rspa.2003.1164

[79] N. B. Viana, A. Mazolli, P. a. Maia Neto, H. M. Nussenzveig, M. S. Rocha and O. N. Mesquita. "Absolute calibration of optical tweezers". *Applied Physics Letters*, **88**, 131110 (2006).
http://dx.doi.org/10.1063/1.2189148

[80] N. B. Viana, M. S. Rocha, O. N. Mesquita, a. Mazolli, P. a. Maia Neto and H. M. Nussenzveig. "Towards absolute calibration of optical tweezers". *Physical Review E*, **75**, 1–14 (2007).
http://dx.doi.org/10.1103/PhysRevE.75.021914

[81] L. P. Ghislain, N. A. Switz and W. W. Webb. "Measurement of small forces using an optical trap". *Review of Scientific Instruments*, **65**, 2762 (1994). http://dx.doi.org/10.1063/1.1144613

[82] S. Chandrasekhar. "Stochastic problems in physics and astronomy". *Reviews of Modern Physics*, **15**, 1 (1943). http://dx.doi.org/10.1103/RevModPhys.15.1

[83] R. D. Leonardo, G. Ruocco, J. Leach, M. J. Padgett, A. J. Wright, J. M. Girkin, D. R. Burnham and D. McGloin. "Parametric resonance of optically trapped aerosols". *Physical Review Letters*, **010601**, 1–4 (2007). http://dx.doi.org/10.1103/PhysRevLett.99.010601

[84] S. Keen, J. Leach, G. Gibson and M. J. Padgett. "Comparison of a high-speed camera and a quadrant detector for measuring displacements in optical tweezers". *Journal of Optics A: Pure and Applied Optics*, **9**, S264–S266 (2007). http://dx.doi.org/10.1088/1464-4258/9/8/S21

[85] K. Berg-Sø rensen and H. Flyvbjerg. "Power spectrum analysis for optical tweezers". *Review of Scientific Instruments*, **75**, 594 (2004). http://dx.doi.org/10.1063/1.1645654

[86] G. Pesce, a. C. De Luca, G. Rusciano, P. a. Netti, S. Fusco and a. Sasso. "Microrheology of complex fluids using optical tweezers: a comparison with macrorheological measurements". *Journal of Optics A: Pure and Applied Optics*, **11**, 034016 (2009). http://dx.doi.org/10.1088/1464-4258/11/3/034016

[87] W. M. Lee, P. J. Reece, R. F. Marchington, N. K. Metzger and K. Dholakia. "Construction and calibration of an optical trap on a fluorescence optical microscope". *Nature Protocols*, **2**, 3226–3238 (2007). http://dx.doi.org/10.1038/nprot.2007.446

[88] S. Block. "Optical tweezers: a new tool for biophysics". In J. K. Foskett and S. Grinstein, editors, "Non-invasive techniques in Cell Biology", volume 9, chapter 15 (1990). http://www.stanford.edu/group/blocklab/Block1990Noninvasive-tech.pdf

[89] "Numerical Aperture and Image Resolution". http://www.microscopyu.com/tutorials/java/imageformation/airyna/index.html

[90] K. T. Gahagan and G. a. Swartzlander. "Trapping of low-index microparticles in an optical vortex". *Journal of the Optical Society of America B*, **15**, 524 (1998). http://dx.doi.org/10.1364/JOSAB.15.000524

[91] P. Prentice, M. Macdonald, T. Frank, A. Cuschier, G. Spalding, W. Sibbett, P. Campbell and K. Dholakia. "Manipulation and filtration of low index particles with holographic Laguerre-Gaussian optical trap arrays." *Optics Express*, **12**, 593–600 (2004). http://dx.doi.org/10.1364/OPEX.12.000593

[92] W. M. Lee, B. P. S. Ahluwalia, X.-C. Yuan, W. C. Cheong and K. Dholakia. "Optical steering of high and low index microparticles by manipulating an off-axis optical vortex". *Journal of Optics A: Pure and Applied Optics*, **7**, 1–6 (2005). http://dx.doi.org/10.1088/1464-4258/7/1/001

[93] N. B. Simpson, D. McGloin, K. Dholakia, L. Allen and M. J. Padgett. "Optical tweezers with increased axial trapping efficiency". *Journal of Modern Optics*, pp. 37–41 (1998). http://dx.doi.org/10.1080/09500349808231712

[94] H. Felgner, O. Müller and M. Schliwa. "Calibration of light forces in optical tweezers." *Applied Optics*, **34**, 977–82 (1995). http://dx.doi.org/10.1364/AO.34.000977

[95] M. D. Summers. *Optical Micromanipulation of Aerosols*. PhD, St Andrews (2009). http://hdl.handle.net/10023/779

[96] E. Fällman and O. Axner. "Design for fully steerable dual-trap optical tweezers". *Applied Optics*, **36**, 2107–2113 (1997). http://dx.doi.org/10.1364/AO.36.002107

[97] M. Mammen, K. Helmerson, R. Kishore, S. K. Choi, W. D. Phillips and G. M. Whitesides. "Optically controlled collisions of biological objects to evaluate potent polyvalent inhibitors of virus-cell adhesion." *Chemistry & Biology*, **3**, 757–63 (1996). http://dx.doi.org/10.1016/S1074-5521(96)90252-5

[98] J. Sung, S. Sivaramakrishnan, A. R. Dunn and J. a. Spudich. *Single-molecule dual-beam optical trap analysis of protein structure and function.*, volume 475. Elsevier Inc., 1 edition (2010). http://dx.doi.org/10.1016/S0076-6879(10)75014-X

[99] J. Buajarern, L. Mitchem, A. D. Ward, N. H. Nahler, D. McGloin and J. P. Reid. "Controlling and characterizing the coagulation of liquid aerosol droplets." *The Journal of chemical physics*, **125**, 114506 (2006). http://dx.doi.org/10.1063/1.2336772

[100] K. J. Knox and J. P. Reid. "Ultrasensitive absorption spectroscopy of optically-trapped aerosol droplets." *The Journal of Physical Chemistry A*, **112**, 10439–41

(2008).
http://dx.doi.org/10.1021/jp807418g

[101] K. Visscher, S. P. Gross and S. M. Block. "Construction of Multiple-Beam Optical Traps with Nanometer-Resolution Position Sensing". *IEEE Journal of Selected Topics in Quantum Electronics*, **2**, 1066–1076 (1996).
http://dx.doi.org/10.1109/2944.577338

[102] M. J. Lang, C. L. Asbury, J. W. Shaevitz and S. M. Block. "An automated two-dimensional optical force clamp for single molecule studies." *Biophysical journal*, **83**, 491–501 (2002).
http://dx.doi.org/10.1016/S0006-3495(02)75185-0

[103] E. Dufresne. "Optical tweezer arrays and optical substrates created with diffractive optics". *Review of Scientific Instruments*, **69**, 1974–1977 (1998).
http://scholar.google.com/scholar?hl=en&btnG=Search&q=intitle:Optical+tweezer+arrays+and+optical+substrates+created+with+diffractive+optics#0

[104] M. Beijersbergen, R. Coerwinkel, M. Kristensen and J. Woerdman. "Helical-wavefront laser beams produced with a spiral phaseplate". *Optics Communications*, **112**, 321–327 (1994).
http://dx.doi.org/10.1016/0030-4018(94)90638-6

[105] J. E. Curtis, B. A. Koss and D. G. Grier. "Dynamic holographic optical tweezers". *Optics Communications*, **207**, 169–175 (2002).
http://dx.doi.org/10.1016/S0030-4018(02)01524-9

[106] J. A. Grieve, A. Ulcinas, S. Subramanian, G. M. Gibson, M. J. Padgett, D. M. Carberry and M. J. Miles. "Hands-on with optical tweezers: a multitouch interface for holographic optical trapping." *Optics Express*, **17**, 3595–602 (2009).
http://dx.doi.org/10.1364/OE.17.003595

[107] R. W. Bowman, G. Gibson, D. Carberry, L. Picco, M. J. Miles and M. J. Padgett. "iTweezers: optical micromanipulation controlled by an Apple iPad". *Journal of Optics*, **13**, 044002 (2011).
http://dx.doi.org/10.1088/2040-8978/13/4/044002

[108] D. R. Burnham. *Microscopic Applications of Holographic Beam Shaping and Studies of Optically Trapped Aerosols*. Ph.D thesis, University of St Andrews (2009).
http://hdl.handle.net/10023/699

[109] W. H. de Jeu. *Physical Properties of Liquid Crystalline Materials*. Gordon and Breach Science Publishers (1980).

[110] S. M. Kelly. *Flat Panel Displays: Advanced Organic Materials*. Royal Society of Chemistry (2000).
http://dx.doi.org/10.1039/9781847550828

[111] J. Liesener, M. Reicherter, T. Haist and H. J. Tiziani. "Multi-functional optical tweezers using computer-generated holograms". *Optics Communications*, **185**, 77–82 (2000).
http://dx.doi.org/10.1016/S0030-4018(00)00990-1

[112] R. Di Leonardo, F. Ianni and G. Ruocco. "Computer generation of optimal holograms for optical trap arrays." *Optics Express*, **15**, 1913–22 (2007).
http://dx.doi.org/10.1364/OE.15.001913

[113] M. Born, E. Wolf, A. B. Bhatia, P. C. Clemmow, D. Gabor, A. R. Stokes, A. M. Taylor, P. A. Wayman and W. L. Wilcock. *Principles of Optics: Electromagnetic Theory of Propagation, Interference and Diffraction of Light*. Cambridge University Press (1999).
http://books.google.co.uk/books?id=nUHGpfNsGyUC

[114] K. D. Wulff, D. G. Cole, R. L. Clark, R. Dileonardo, J. Leach, J. Cooper, G. Gibson and M. J. Padgett. "Aberration correction in holographic optical tweezers." *Optics Express*, **14**, 4170–5 (2006).
http://dx.doi.org/10.1364/OE.14.004170

[115] J. E. Curtis and D. G. Grier. "Structure of Optical Vortices". *Phys. Rev. Lett.*, **90**, 133901 (2003).
http://dx.doi.org/10.1103/PhysRevLett.90.133901

[116] L. Allen, M. Beijersbergen, R. Spreeuw and J. Woerdman. "Orbital angular momentum of light and the transformation of Laguerre-Gaussian laser modes". *Physical Review A*, **45** (1992).
10.1103/PhysRevA.45.8185

[117] M. J. Padgett and L. Allen. "The Poynting vector in Laguerre-Gaussian laser modes". *Optics Communications*, **121**, 36–40 (1995).
http://dx.doi.org/10.1016/0030-4018(95)00455-H

[118] N. B. Simpson, K. Dholakia, L. Allen and M. J. Padgett. "Mechanical equivalence of spin and orbital angular momentum of light: an optical spanner." *Optics Letters*, **22**, 52–4 (1997).
http://dx.doi.org/10.1364/OL.22.000052

[119] K. Ladavac and D. Grier. "Microoptomechanical pumps assembled and driven by holographic optical vortex arrays." *Optics Express*, **12**, 1144–9 (2004).
http://dx.doi.org/10.1364/OPEX.12.001144

[120] M. Lee, A. Curran, G. Gibson, M. Tassieri, N. R. Heckenberg and M. J. Padgett. "Optical shield: measuring viscosity of turbid fluids using optical tweezers". *Optics Express*, **20**, 12127–12132 (2012).
http://dx.doi.org/10.1364/OE.20.012127

[121] N. Chattrapiban, E. a. Rogers, D. Cofield, W. T. Hill and R. Roy. "Generation of nondiffracting Bessel beams by use of a spatial light modulator." *Optics Letters*, **28**, 2183–5 (2003).
http://dx.doi.org/10.1364/OL.28.002183

[122] G. Milne. *Optical Sorting and Manipulation of Microscopic Particles*. Ph.D, University of St Andrew (2007).
http://grahammilne.com/Graham_Milne_Thesis.pdf

[123] D. R. Burnham, G. D. Wright, N. D. Read and D. McGloin. "Holographic and single beam optical manipulation of hyphal growth in filamentous fungi". *Journal of Optics A: Pure and Applied Optics*, **9**, S172–S179 (2007).
http://dx.doi.org/10.1088/1464-4258/9/8/S09

[124] M. L. Cordero, D. R. Burnham, C. N. Baroud and D. McGloin. "Thermocapillary manipulation of droplets using holographic beam shaping: Microfluidic pin ball". *Applied Physics Letters*, **93**, 034107 (2008).
http://dx.doi.org/10.1063/1.2952374

[125] A. Jesacher, A. Schwaighofer, S. Fürhapter, C. Maurer, S. Bernet and M. Ritsch-Marte. "Wavefront correction of spatial light modulators using an optical vortex image." *Optics Express*, **15**, 5801–8 (2007).
http://dx.doi.org/10.1364/OE.15.005801

[126] N. Logan. "Survey of some early studies of the scattering of plane waves by a sphere". *Proceedings of the IEEE*, **53**, 773–785 (1965).
http://dx.doi.org/10.1109/PROC.1965.4055

[127] P. Debye. "Der lichtdruck auf kugeln von beliebigem material". *Annalen der Physik* (1909).
http://dx.doi.org/doi/10.1002/andp.19093351103

[128] G. Mie. "Beiträge zur Optik trüber Medien, speziell kolloidaler Metallösungen". *Annalen der Physik* (1908).
http://dx.doi.org/10.1002/andp.19083300302

[129] G. Gouesbet and G. Gréhan. *Generalized Lorenz-Mie Theories*. Springer (2011). http://goo.gl/BqL33

[130] C. F. Bohren and D. R. Huffman. *Absorption and Scattering of Light by Small Particles*. Wiley Scientific, New York (1983).

[131] H. van de Hulst. *Light Scattering by Small Particles*. Dover Publications Inc., Mineola (1957).

[132] C. Mätzler. "MATLAB Functions for Mie scattering and absorption". *IAP Res. Rep* (2002). http://goo.gl/TnndW

[133] P. Barber and R. Chang, editors. *Optical Effects Associated With Small Particles*. World Scientific Publishing Co. Pte. Ltd., Singapore (1998).

[134] R. Dobbins and T. Eklund. "Ripple structure of the extinction coefficient". *Applied Optics*, **16**, 281–282 (1977). http://dx.doi.org/10.1364/AO.16.000281

[135] J. Cole III, R. Dobbins and H. Semerjian. "Time-Resolved Measurement of Droplet Size and Concentration in Cloud Chambers." *Journal of Applied Meteorology*, **9**, 684–689 (1970). http://dx.doi.org/10.1175/1520-0450(1970)009<0684:TRMODS>2.0.CO;2

[136] P. Chylek, J. Kiehl, M. Ko and P. Chỳlek. "Optical levitation and partial-wave resonances". *Physical Review A*, **18**, 2229–2233 (1978). http://dx.doi.org/10.1103/PhysRevA.18.2229

[137] K. D. Möller. *Optics*. University Science Books (1988).

[138] Lord Rayleigh. "The Problem of the Whispering Gallery". *Philosophical Magazine*, **XX**, 1001–1004 (1910). http://goo.gl/sn6C6

[139] R. Symes, R. M. Sayer and J. P. Reid. "Cavity enhanced droplet spectroscopy: Principles, perspectives and prospects". *Physical Chemistry Chemical Physics*, **6**, 474–487 (2004). http://dx.doi.org/10.1039/b313370b

[140] H. Lin, A. Huston, J. Eversole, A. Campillo and P. Chỳlek. "Internal scattering effects on microdroplet resonant emission structure". *Optics Letters*, **17**, 970–972 (1992). http://dx.doi.org/10.1364/OL.17.000970

[141] T. Ioppolo, N. Das and M. V. Otugen. "Whispering gallery modes of microspheres in the presence of a changing surrounding medium: A new ray-tracing analysis and sensor experiment". *Journal of Applied Physics*, **107**, 103105 (2010).
http://dx.doi.org/10.1063/1.3425790

[142] V. Datsyuk. "Optics of microdroplets". *Journal of Molecular Liquids*, **93**, 159–175 (2001).
http://dx.doi.org/10.1016/S0167-7322(01)00225-2

[143] L. Collot, V. Lefevre-Seguin, M. Brune, J. Raimond and S. Haroche. "Very high-Q whispering-gallery mode resonances observed on fused silica microspheres". *EPL (Europhysics Letters)*, **23**, 327 (1993).
http://dx.doi.org/10.1209/0295-5075/23/5/005

[144] M. Guillon, R. E. H. Miles, J. P. Reid and D. McGloin. "Thermo-optical resonance locking of an optically trapped salt-water microdroplet". *New Journal of Physics*, **11**, 103041 (2009).
http://dx.doi.org/10.1088/1367-2630/11/10/103041

[145] H. Chew. "Transition rates of atoms near spherical surfaces". *The Journal of Chemical Physics*, **87**, 1355 (1987).
http://dx.doi.org/10.1063/1.453317

[146] H. Chew. "Radiation and lifetimes of atoms inside dielectric particles". *Physical Review A*, **38**, 3410 (1988).
http://dx.doi.org/10.1103/PhysRevA.38.3410

[147] A. Weller, F. Liu, R. Dahint and M. Himmelhaus. "Whispering gallery mode biosensors in the low-Q limit". *Applied Physics B*, **90**, 561–567 (2008).
http://dx.doi.org/10.1007/s00340-007-2893-2

[148] P. Chýlek. "Resonance structure of Mie scattering: distance between resonances". *Journal of the Optical Society of America A*, **7**, 1609 (1990).
http://dx.doi.org/10.1364/JOSAA.7.001609

[149] X. Quan and E. S. Fry. "Empirical equation for the index of refraction of seawater." *Applied Optics*, **34**, 3477–80 (1995).
http://dx.doi.org/10.1364/AO.34.003477

[150] C. C. Lam, P. T. Leung and K. Young. "Explicit asymptotic formulas for the positions, widths, and strengths of resonances in Mie scattering". *Journal of the Optical Society of America B*, **9**, 1585 (1992).
http://dx.doi.org/10.1364/JOSAB.9.001585

[151] N. R. Labiris and M. B. Dolovich. "Pulmonary drug delivery. Part II: The role of inhalant delivery devices and drug formulations in therapeutic effectiveness of aerosolized medications". *British Journal of Clinical Pharmacology*, **56**, 600–612 (2003).
http://dx.doi.org/10.1046/j.1365-2125.2003.01893.x

[152] M. Andreae and P. Crutzen. "Atmospheric aerosols: Biogeochemical sources and role in atmospheric chemistry". *Science*, **276**, 1052–1058 (1997).
http://dx.doi.org/10.1126/science.276.5315.1052

[153] P. Forster, V. Ramaswamy, P. Artaxo, T. Berntsen, R. Betts, D. Fahey, J. Haywood, J. Lean, D. Lowe, G. Myhre, J. Nganga, R. Prinn, G. Raga, S. M and R. Van Dorland. "Changes in Atmospheric Constituents and in Radiative Forcing". In "Climate Change 2007: The Physical Science Basis. Contribution of Working Group I to the Fourth Assessment Report of the Intergovernmental Panel on Climate Change", Cambridge University Press, Cambridge, United Kingdom and New York, NY, USA (2007).
http://en.scientificcommons.org/23467316

[154] B. J. Mason, S.-J. King, R. E. H. Miles, K. M. Manfred, A. M. J. Rickards, J. Kim, J. P. Reid and A. J. Orr-Ewing. "Comparison of the Accuracy of Aerosol Refractive Index Measurements from Single Particle and Ensemble Techniques." *The Journal of Physical Chemistry A* (2012).
http://dx.doi.org/10.1021/jp3049668

[155] A. Ansmann, M. Riebesell and C. Weitkamp. "Measurement of atmospheric aerosol extinction profiles with a Raman lidar". *Optics Letters*, **15**, 746–748 (1990).
http://dx.doi.org/10.1364/OL.15.000746

[156] A. D. Sappey, E. S. Hill, T. Settersten and M. A. Linne. "Fixed-frequency cavity ringdown diagnostic for atmospheric particulate matter." *Optics Letters*, **23**, 954–6 (1998).
http://dx.doi.org/10.1364/OL.23.000954

[157] R. E. H. Miles, S. Rudić, A. J. Orr-Ewing and J. P. Reid. "Measurements of the wavelength dependent extinction of aerosols by cavity ring down spectroscopy." *Physical Chemistry Chemical Physics: PCCP*, **12**, 3914–20 (2010).
http://dx.doi.org/10.1039/b923758e

[158] R. J. Hopkins, L. Mitchem, A. D. Ward and J. P. Reid. "Control and characterisation of a single aerosol droplet in a single-beam gradient-force optical trap". *Phys. Chem. Chem. Phys.*, **6**, 4924 (2004).
http://dx.doi.org/10.1039/b414459g

[159] D. McGloin, D. R. Burnham, M. D. Summers, D. Rudd, N. Dewar and S. Anand. "Optical manipulation of airborne particles: techniques and applications". *Faraday Discussions*, **137**, 335 (2008).
http://dx.doi.org/10.1039/b702153d

[160] E. Davis. "A history of single aerosol particle levitation". *Aerosol science and technology* (1997).
http://dx.doi.org/10.1080/02786829708965426

[161] J. P. Reid. "Particle levitation and laboratory scattering". *Journal of Quantitative Spectroscopy and Radiative Transfer*, **110**, 1293–1306 (2009).
http://dx.doi.org/10.1016/j.jqsrt.2009.02.019

[162] J. H. Seinfeld and S. M. Pandis. *Atmospheric Chemistry and Physics: From Air Pollution to Climate Change*. Wiley-Blackwell (1998).

[163] H. Meresman, J. B. Wills, M. Summers, D. McGloin and J. P. Reid. "Manipulation and characterisation of accumulation and coarse mode aerosol particles using a Bessel beam trap." *Physical chemistry chemical physics : PCCP*, **11**, 11333–9 (2009).
http://dx.doi.org/10.1039/b914165k

[164] A. E. Carruthers, J. P. Reid and A. J. Orr-Ewing. "Longitudinal optical trapping and sizing of aerosol droplets." *Optics Express*, **18**, 14238–44 (2010).
http://dx.doi.org/10.1364/OE.18.014238

[165] A. E. Carruthers, J. S. Walker, A. Casey, A. J. Orr-Ewing and J. P. Reid. "Selection and characterization of aerosol particle size using a bessel beam optical trap for single particle analysis." *Physical Chemistry Chemical Physics: PCCP*, pp. 6741–6748 (2012).
http://dx.doi.org/10.1039/c2cp40371d

[166] R. D. Dear, D. R. Burnham, M. D. Summers, D. McGloin and G. A. D. Ritchie. "Single aerosol trapping with an annular beam: Improved particle localisation". *Phys. Chem. Chem. Phys.*, **14**, 15826–15831 (2012).
http://dx.doi.org/10.1039/C2CP42925J

[167] D. R. Burnham and D. McGloin. "Modeling of optical traps for aerosols". *Journal of the Optical Society of America B*, **28**, 2856 (2011).
http://dx.doi.org/10.1364/JOSAB.28.002856

[168] J. Wedding and J. Stukel. "Operational limits of vibrating orifice aerosol generator". *Environmental Science & Technology*, pp. 456–457 (1974).
http://dx.doi.org/10.1021/es60090a008

[169] V. Fassel and B. Bear. "Ultrasonic nebulization of liquid samples for analytical inductively coupled plasma-atomic spectroscopy: an update". *Spectrochimica Acta Part B: Atomic Spectroscopy*, **488** (1986).
http://dx.doi.org/10.1016/0584-8547(86)80129-X

[170] D. Burnham, P. Reece and D. McGloin. "Parameter exploration of optically trapped liquid aerosols". *Physical Review E*, **82**, 1–9 (2010).
http://dx.doi.org/10.1103/PhysRevE.82.051123

[171] H. R. Pruppacher and J. D. Klett. *Microphysics of Clouds and Precipitation*. Atmospheric and Oceanographic Sciences Library. Springer (1996).
http://books.google.co.uk/books?id=kQ18q7wtP6gC

[172] D. R. Lide. *CRC Handbook of Chemistry and Physics: A Ready-reference Book of Chemical and Physical Data*. CRC Handbook of Chemistry and Physics, 85th Ed. CRC Press (2004).
http://books.google.co.uk/books?id=WDll8hA006AC

[173] R. E. H. Miles, M. Guillon, L. Mitchem, D. McGloin and J. P. Reid. "The influence of resonant absorption and heating on the equilibrium size of aqueous-solute aerosol droplets." *Physical chemistry chemical physics : PCCP*, **11**, 7312–7 (2009).
http://dx.doi.org/10.1039/b904690a

[174] H. Rosen and T. Novakov. "Raman scattering and the characterisation of atmospheric aerosol particles". *Nature*, **266**, 708 (1977).
http://dx.doi.org/10.1038/266708a0

[175] R. Vehring. "Linear Raman spectroscopy on aqueous aerosols: influence of nonlinear effects on detection limits". *Journal of Aerosol Science*, **29**, 65–79 (1998).
http://dx.doi.org/10.1016/S0021-8502(97)00292-9

[176] R. W. Boyd. *Nonlinear Optics*. Elsevier Science, second edition (2002).
http://books.google.co.uk/books?id=30t9VmOmOGsC

[177] J. B. Snow, S. X. Qian and R. K. Chang. "Stimulated Raman scattering from individual water and ethanol droplets at morphology-dependent resonances." *Optics Letters*, **10**, 37–9 (1985).
http://dx.doi.org/10.1364/OL.10.000037

[178] S. C. Hill and R. E. Benner. "Morphology-dependent resonances associated with stimulated processes in microspheres". *Journal of the Optical Society of America B*, **3**, 1509 (1986).
http://dx.doi.org/10.1364/JOSAB.3.001509

[179] H. Yokoyama and S. D. Brorson. "Rate equation analysis of microcavity lasers". *Journal of Applied Physics*, **66**, 4801 (1989).
http://dx.doi.org/10.1063/1.343793

[180] H. Lin and A. Campillo. "CW nonlinear optics in droplet microcavities displaying enhanced gain". *Physical Review Letters*, **73**, 2440–2443 (1994).
http://dx.doi.org/10.1103/PhysRevLett.73.2440

[181] R. M. Sayer, R. D. B. Gatherer, R. J. J. Gilham and J. P. Reid. "Determination and validation of water droplet size distributions probed by cavity enhanced Raman scattering". *Physical Chemistry Chemical Physics*, **5**, 3732 (2003).
http://dx.doi.org/10.1039/b304599d

[182] D. M. Carey and G. M. Korenowski. "Measurement of the Raman spectrum of liquid water". *The Journal of Chemical Physics*, **108**, 2669 (1998).
http://dx.doi.org/10.1063/1.475659

[183] L. Mitchem, R. J. Hopkins, J. Buajarern, A. D. Ward and J. P. Reid. "Comparative measurements of aerosol droplet growth". *Chemical Physics Letters*, **432**, 362–366 (2006).
http://dx.doi.org/10.1016/j.cplett.2006.10.053

[184] J. P. Reid and L. Mitchem. "Laser probing of single-aerosol droplet dynamics." *Annual Review of Physical Chemistry*, **57**, 245–71 (2006).
http://dx.doi.org/10.1146/annurev.physchem.57.032905.104621

[185] J. Reid, H. Meresman, L. Mitchem and R. Symes. "Spectroscopic studies of the size and composition of single aerosol droplets". *International Reviews in Physical Chemistry*, **26**, 139–192 (2007).
http://dx.doi.org/10.1080/01442350601081899

[186] R. E. H. Miles, J. S. Walker, D. R. Burnham and J. P. Reid. "Retrieval of the complex refractive index of aerosol droplets from optical tweezers measurements." *Physical chemistry chemical physics : PCCP*, **14**, 3037–3047 (2012).
http://dx.doi.org/10.1039/c2cp23999j

[187] S. Elliott. *Sensitive Laser Absorption Studies of Electronegative Oxygen Plasmas*. MChem, University of Oxford (2007).

[188] D. R. Burnham and D. McGloin. "Holographic optical trapping of aerosol droplets". *Optics Express*, **14**, 196–200 (2006).
http://dx.doi.org/10.1364/OE.14.004175

[189] K. J. Knox, D. R. Burnham, L. I. McCann, S. L. Murphy, D. McGloin and J. P. Reid. "Observation of bistability of trapping position in aerosol optical tweezers". *JOSA B*, **27**, 582–591 (2010).
http://dx.doi.org/10.1364/JOSAB.27.000582

[190] L. Mitchem, J. Buajarern, R. J. Hopkins, A. D. Ward, R. J. J. Gilham, R. L. Johnston and J. P. Reid. "Spectroscopy of growing and evaporating water droplets: exploring the variation in equilibrium droplet size with relative humidity." *The journal of physical chemistry. A*, **110**, 8116–25 (2006).
http://dx.doi.org/10.1021/jp061135f

[191] J. R. Butler, L. Mitchem, K. L. Hanford, L. Treuel and J. P. Reid. "In situ comparative measurements of the properties of aerosol droplets of different chemical composition". *Faraday Discussions*, **137**, 351 (2008).
http://dx.doi.org/10.1039/b706770b

[192] P. W. Atkins and R. S. Friedman. *Molecular Quantum Mechanics*. OUP Oxford (2010).
http://books.google.co.uk/books?id=yk7lRAAACAAJ

[193] W. Demtröder. *Atoms, Molecules and Photons: An Introduction to Atomic-, Molecular- and Quantum Physics*. Graduate Texts in Physics. Springer (2011).
http://books.google.co.uk/books?id=vbc5mA7OEuYC

[194] W. Demtröder. *Laser Spectroscopy: Basic Concepts and Instrumentation*. Advanced Texts in Physics. Springer (2002).
http://books.google.co.uk/books?id=dNx1OLgn1xcC

[195] B. Cummings, M. L. Hamilton, L. Ciaffoni, T. R. Pragnell, G. A. D. Ritchie, G. Hancock, P. A. Robbins and R. Peverall. "Laser-based absorption spectroscopy as a technique for rapid in-line analysis of respired gas concentrations of O_2 and CO_2". *Journal of Applied Physiology*, **111**, 303–307 (2011).
http://dx.doi.org/10.1152/japplphysiol.00119.2011

[196] B. L. Cummings. *Applications of infrared laser spectroscopy to breath analysis*. DPhil thesis, University of Oxford (2011).

[197] P. R. Lowe and J. M. Ficke. "The Computation of Saturation Vapor Pressure" (1974).
http://goo.gl/Hr68W

[198] P. Walden. "Ueber die MolekulargroÌsse und elektrische LeitfaÌhigkeit einiger geschmolzenen Salze". *Bulletin de lAcadémie Impériale des Sciences de St.-Pétersbourg*, **469**, 405 (1914).
http://www.mathnet.ru/rus/im6491

[199] E. M. Arnett and J. F. Wolf. "Electrochemical scrutiny of organometallic iron complexes and hexamethylbenzene in a room temperature molten salt". *Journal of the American Chemical Society*, **3264**, 3264–3265 (1975).
http://dx.doi.org/10.1021/ja00844a081

[200] J. Wilkes and J. Levisky. "Dialkylimidazolium chloroaluminate melts: a new class of room-temperature ionic liquids for electrochemistry, spectroscopy and synthesis". *Inorganic Chemistry*, **237**, 1263–1264 (1982).
http://dx.doi.org/10.1021/ic00133a078

[201] S. S. Moganty and R. E. Baltus. "Regular Solution Theory for Low Pressure Carbon Dioxide Solubility in Room Temperature Ionic Liquids: Ionic Liquid Solubility Parameter from Activation Energy of Viscosity". *Industrial & Engineering Chemistry Research*, **49**, 5846–5853 (2010).
http://dx.doi.org/10.1021/ie901837k

[202] M. J. Earle and K. R. Seddon. "Ionic liquids. Green solvents for the future". *Pure and Applied Chemistry*, **72**, 1391–1398 (2000).
http://dx.doi.org/10.1351/pac200072071391

[203] C. F. Poole and S. K. Poole. "Extraction of organic compounds with room temperature ionic liquids." *Journal of Chromatography. A*, **1217**, 2268–86 (2010).
http://dx.doi.org/10.1016/j.chroma.2009.09.011

[204] H. Zhao, S. Xia and P. Ma. "Use of ionic liquids as green solvents for extractions". *Journal of Chemical Technology & Biotechnology*, **80**, 1089–1096 (2005).
http://dx.doi.org/10.1002/jctb.1333

[205] N. V. Plechkova and K. R. Seddon. "Ionic Liquids: Designer Solvents for Green Chemistry". In "Methods and Reagents for Green Chemistry: An Introduction", John Wiley & Sons, Inc, Hoboken, NJ (2007).
http://dx.doi.org/10.1002/9780470124086.ch5

[206] J. F. Brennecke and E. J. Maginn. "Ionic liquids: Innovative fluids for chemical processing". *AIChE Journal*, **47**, 2384–2389 (2001).
http://dx.doi.org/10.1002/aic.690471102

[207] M. Freemantle. "Ionic liquids may boost clean technology development". *Chemical & Engineering News*, **76**, 32–37 (1997).
http://dx.doi.org/10.1021/cen-v076n013.p032

[208] J. Holbrey and K. Seddon. "The phase behaviour of 1-alkyl-3-methylimidazolium tetrafluoroborates; ionic liquids and ionic liquid crystals". *Journal of the Chemical*

Society, Dalton Transactions, pp. 2133–2139 (1999).
http://dx.doi.org/10.1039/A902818H

[209] S. Sowmiah, V. Srinivasadesikan, M.-C. Tseng and Y.-H. Chu. "On the chemical stabilities of ionic liquids." *Molecules*, **14**, 3780–813 (2009).
http://dx.doi.org/10.3390/molecules14093780

[210] M. Estruga, C. Domingo, X. Domènech and J. a. Ayllón. "Zirconium-doped and silicon-doped TiO_2 photocatalysts synthesis from ionic-liquid-like precursors." *Journal of colloid and interface science*, **344**, 327–33 (2010).
http://dx.doi.org/10.1016/j.jcis.2009.12.063

[211] M.-D. Bermúdez, A.-E. Jiménez, J. Sanes and F.-J. Carrión. "Ionic liquids as advanced lubricant fluids." *Molecules*, **14**, 2888–908 (2009).
http://dx.doi.org/10.3390/molecules14082888

[212] B. T. Torimoto, T. Tsuda, K.-i. Okazaki and S. Kuwabata. "New Frontiers in Materials Science Opened by Ionic Liquids". **0871**, 1196–1221 (2010).
http://dx.doi.org/10.1002/adma.200902184

[213] C. Cadena, J. L. Anthony, J. K. Shah, T. I. Morrow, J. F. Brennecke and E. J. Maginn. "Why Is CO_2 so soluble in imidazolium-based ionic liquids?" *Journal of the American Chemical Society*, **126**, 5300–8 (2004).
http://dx.doi.org/10.1021/ja039615x

[214] J. Huang and T. Rüther. "Why are ionic liquids attractive for CO_2 absorption? An overview". *Australian Journal of Chemistry*, pp. 298–308 (2009).
http://dx.doi.org/10.1071/CH08559

[215] B. F. Goodrich, J. C. de la Fuente, B. E. Gurkan, Z. K. Lopez, E. a. Price, Y. Huang and J. F. Brennecke. "Effect of water and temperature on absorption of CO_2 by amine-functionalized anion-tethered ionic liquids." *The Journal of Physical Chemistry B*, **115**, 9140–50 (2011).
http://dx.doi.org/10.1021/jp2015534

[216] J. Huang, A. Riisager, P. Wasserscheid and R. Fehrmann. "Reversible physical absorption of SO_2 by ionic liquids." *Chemical communications (Cambridge, England)*, pp. 4027–9 (2006).
http://dx.doi.org/10.1039/b609714f

[217] A.-L. Revelli, F. Mutelet and J.-N. Jaubert. "Reducing of nitrous oxide emissions using ionic liquids." *The Journal of Physical Chemistry B*, **114**, 8199–206 (2010).
http://dx.doi.org/10.1021/jp103734c

[218] A. Kokorin, editor. *Ionic Liquids: Applications and Perspectives*. InTech (2011). http://dx.doi.org/10.5772/1782

[219] A. Kokorin, editor. *Ionic Liquids: Theory, Properties, New Approaches*. InTech (2011). http://dx.doi.org/10.5772/603

[220] P. J. Scammells, J. L. Scott and R. D. Singer. "Ionic Liquids: The Neglected Issues". *Australian Journal of Chemistry*, **58**, 155 (2005). http://dx.doi.org/10.1071/CH04272

[221] M. M. Elmahdy, C. Gutsche and F. Kremer. "Forces within Single Pairs of Charged Colloids in Aqueous Solutions of Ionic Liquids as Studied by Optical Tweezers". *The Journal of Physical Chemistry C*, **114**, 19452–19458 (2010). http://dx.doi.org/10.1021/jp107673f

[222] W. Gault. *Optical Studies of Colloidal Systems*. MChem thesis, University of Oxford (2012).

[223] C. Poole, B. Kersten, S. Ho, M. Coddens and K. Furton. "Organic salts, liquid at room temperature, as mobile phases in liquid chromatography". *Journal of Chromatography*, **352**, 407–425 (1986). http://www.sciencedirect.com/science/article/pii/S0021967301833975

[224] O. Cabeza, S. García-Garabal, L. Segade, M. Domínguez-Pérez, E. Rilo and L. M. Varela. "Physical Properties of Binary Mixtures of ILs with Water and Ethanol. A Review." In "Ionic Liquids: Theory, Properties, New Approaches", (2011). http://dx.doi.org/10.5772/14848

[225] M. Allen and D. Evans. "Thermodynamic properties of the ethylammonium nitrate+ water system: partial molar volumes, heat capacities, and expansivities". *Journal of solution chemistry*, **14**, 549–560 (1985). http://dx.doi.org/10.1007/BF00649520

[226] A. D. Ward, M. Zhang and O. Hunt. "Broadband Mie scattering from optically levitated aerosol droplets using a white LED". *Optics Express*, **16**, 16390 (2008). http://dx.doi.org/10.1364/OE.16.016390

[227] K. Tang and A. Gomez. "Generation by electrospray of monodisperse water droplets for targeted drug delivery by inhalation". *Journal of Aerosol Science*, **25**, 1237–1249 (1994). http://dx.doi.org/10.1016/0021-8502(94)90212-7

[228] J. Fenn, M. Mann, C. Meng, S. F. Wong and C. M. Whitehouse. "Electrospray ionization for mass spectrometry of large biomolecules". *Science*, **246**, 64–71 (1989). http://dx.doi.org/10.1126/science.2675315

[229] T. Makino. "In situ Raman study of dissolved carbon-dioxide induced changes of imidazolium-based ionic liquids". *Journal of Physics: Conference Series*, **215**, 012068 (2010). http://dx.doi.org/10.1088/1742-6596/215/1/012068

[230] L. J. Moore, R. D. Dear, M. D. Summers, R. P. A. Dullens and G. A. D. Ritchie. "Direct Observation of Grain Rotation-Induced Grain Coalescence in Two-Dimensional Colloidal Crystals". *Nano Letters*, **10**, 4266–4272 (2010). http://dx.doi.org/10.1021/nl102786k

[231] R. Piazza and A. Parola. "Thermophoresis in colloidal suspensions". *Journal of Physics: Condensed Matter*, **20**, 153102 (2008). http://dx.doi.org/10.1088/0953-8984/20/15/153102

[232] D. Braun and A. Libchaber. "Trapping of DNA by Thermophoretic Depletion and Convection". *Physical Review Letters*, **89**, 2–5 (2002). http://dx.doi.org/10.1103/PhysRevLett.89.188103

[233] S. Duhr and D. Braun. "Two-dimensional colloidal crystals formed by thermophoresis and convection". *Applied Physics Letters*, **86**, 131921 (2005). http://dx.doi.org/10.1063/1.1888036

[234] F. Weinert and D. Braun. "Observation of Slip Flow in Thermophoresis". *Physical Review Letters*, **101**, 15–18 (2008). http://dx.doi.org/10.1103/PhysRevLett.101.168301

[235] R. Di Leonardo, F. Ianni and G. Ruocco. "Colloidal attraction induced by a temperature gradient." *Langmuir: the ACS Journal of Surfaces and Colloids*, **25**, 4247–50 (2009). http://dx.doi.org/10.1021/la8038335

[236] T. M. Squires. "Effective pseudo-potentials of hydrodynamic origin". *Journal of Fluid Mechanics*, **443**, 403–412 (2001). http://dx.doi.org/10.1017/S0022112001005432

[237] C. Burda, X. Chen, R. Narayanan and M. A. El-Sayed. "Chemistry and properties of nanocrystals of different shapes." *Chemical reviews*, **105**, 1025–102 (2005). http://dx.doi.org/10.1021/cr030063a

[238] W. Ostwald. "". *Z. Phys. Chem.*, **34**, 495 (1900).

[239] J. Zhang, F. Huang and Z. Lin. "Progress of nanocrystalline growth kinetics based on oriented attachment". *Nanoscale*, **2**, 18 (2010).
http://dx.doi.org/10.1039/b9nr00047j

[240] R. L. Penn. "Imperfect Oriented Attachment: Dislocation Generation in Defect-Free Nanocrystals". *Science*, **281**, 969–971 (1998).
http://dx.doi.org/10.1126/science.281.5379.969

[241] R. L. Penn and J. F. Banfield. "Oriented attachment and growth, twinning, polytypism, and formation of metastable phases: Insights from nanocrystalline TiO_2". *American Mineralogist*, **83**, 1077–1082 (1998).
http://www.minsocam.org/msa/AmMin/Toc/Articles_Free/1998/Penn_p1077-1082_98.pdf

[242] D. Moldovan, V. Yamakov, D. Wolf and S. Phillpot. "Scaling Behavior of Grain-Rotation-Induced Grain Growth". *Physical Review Letters*, **89**, 206101 (2002).
http://dx.doi.org/10.1103/PhysRevLett.89.206101

[243] E. J. Lee, C. Ribeiro, E. Longo and E. R. Leite. "Growth kinetics of tin oxide nanocrystals in colloidal suspensions under hydrothermal conditions". *Chemical Physics*, **328**, 229–235 (2006).
http://dx.doi.org/10.1016/j.chemphys.2006.06.032

[244] C. Ribeiro, E. Longo and E. R. Leite. "Tailoring of heterostructures in a SnO_2 / TiO_2 system by the oriented attachment mechanism". *Applied Physics Letters*, **91**, 103105 (2007).
http://dx.doi.org/10.1063/1.2779932

[245] Z. Zhuang, J. Zhang, F. Huang, Y. Wang and Z. Lin. "Pure multistep oriented attachment growth kinetics of surfactant-free SnO_2 nanocrystals". *Physical Chemistry Chemical Physics*, **11**, 8516–8521 (2009).
http://dx.doi.org/10.1039/b907967j

[246] R. Piazza and A. Guarino. "Soret Effect in Interacting Micellar Solutions". *Physical Review Letters*, **88**, 208302 (2002).
http://dx.doi.org/10.1103/PhysRevLett.88.208302

[247] J. Crocker and D. Grier. "Methods of digital video microscopy for colloidal studies". *Journal of Colloid and Interface Science*, **179**, 298–310 (1996).
http://dx.doi.org/10.1006/jcis.1996.0217

[248] J. Weiss, D. Oxtoby, D. Grier and C. Murray. "Martensitic transition in a confined colloidal suspension". *The Journal of Chemical Physics*, **103**, 1180 (1995).
http://dx.doi.org/10.1063/1.469828

[249] V. W. A. D. Villeneuve, D. Verboekend, R. P. A. Dullens, D. G. A. L. Aarts, W. K. Kegel and H. N. W. Lekkerkerker. "Hard sphere crystal nucleation and growth near large spherical impurities". *Journal of Physics: Condensed Matter*, **17**, S3371–S3378 (2005).
http://dx.doi.org/10.1088/0953-8984/17/45/024

[250] S. M. Anthony, M. Kim and S. Granick. "Translation-rotation decoupling of colloidal clusters of various symmetries." *The Journal of Chemical Physics*, **129**, 244701 (2008).
http://dx.doi.org/10.1063/1.3043443

[251] K. E. Harris, V. Singh and A. King. "Grain rotation in thin films of gold". *Acta Materialia*, **46**, 2623–2633 (1998).
http://dx.doi.org/10.1016/S1359-6454(97)00467-9

[252] D. Moldovan, D. Wolf and S. R. Phillpot. "Theory of diffusion-accommodated grain rotation in columnar polycrystalline microstructures". *Acta Materialia*, **49**, 3521–3532 (2001).
http://dx.doi.org/10.1016/S1359-6454(01)00240-3

[253] A. OKeefe and D. A. G. Deacon. "Cavity ring-down optical spectrometer for absorption measurements using pulsed laser sources". *Review of Scientific Instruments*, **59**, 2544 (1988).
http://dx.doi.org/10.1063/1.1139895

[254] R. Engeln, G. Berden, R. Peeters and G. Meijer. "Cavity enhanced absorption and cavity enhanced magnetic rotation spectroscopy". *Review of Scientific Instruments*, **69**, 3763 (1998).
http://dx.doi.org/10.1063/1.1149176

[255] M. Mazurenka, A. J. Orr-Ewing, R. Peverall and G. A. D. Ritchie. "Cavity ring-down and cavity enhanced spectroscopy using diode lasers". *Annual Reports Section C (Physical Chemistry)*, **101**, 100 (2005).
http://dx.doi.org/10.1039/b408909j

[256] A. J. Hallock, E. S. F. Berman and R. N. Zare. "Direct monitoring of absorption in solution by cavity ring-down spectroscopy." *Analytical Chemistry*, **74**, 1741–3 (2002).
http://dx.doi.org/10.1021/ac011103i

[257] K. L. Snyder and R. N. Zare. "Cavity Ring-Down Spectroscopy as a Detector for Liquid Chromatography". *Analytical Chemistry*, **75**, 3086–3091 (2003).
http://dx.doi.org/10.1021/ac0340152

[258] L. van Der Sneppen, F. Ariese, C. Gooijer and W. Ubachs. "Cavity ring-down spectroscopy for detection in liquid chromatography at UV wavelengths using standard cuvettes in a normal incidence geometry." *Journal of chromatography. A*, **1148**, 184–8 (2007).
http://dx.doi.org/10.1016/j.chroma.2007.03.028

[259] F. M. Mirabella. *Internal Reflection Spectroscopy: Theory and Applications*. Practical Spectroscopy. Taylor & Francis (1992).
http://books.google.co.uk/books?id=Cb5dewIqHzsC

[260] A. C. R. Pipino, J. W. Hudgens and R. E. Huie. "Evanescent wave cavity ring-down spectroscopy with a total-internal-reflection minicavity". *Review of Scientific Instruments*, **68**, 2978 (1997).
http://dx.doi.org/10.1063/1.1148230

[261] A. Pipino, J. Hudgens and R. Huie. "Evanescent wave cavity ring-down spectroscopy for probing surface processes". *Chemical Physics Letters*, pp. 104–112 (1997).
http://dx.doi.org/10.1016/S0009-2614(97)01080-4

[262] L. van der Sneppen, G. Hancock, C. Kaminski, T. Laurila, S. R. Mackenzie, S. R. T. Neil, R. Peverall, G. a. D. Ritchie, M. Schnippering and P. R. Unwin. "Following interfacial kinetics in real time using broadband evanescent wave cavity-enhanced absorption spectroscopy: a comparison of light-emitting diodes and supercontinuum sources." *The Analyst*, **135**, 133–9 (2010).
http://dx.doi.org/10.1039/b916712a

[263] S. M. Ball, J. M. Langridge and R. L. Jones. "Broadband cavity enhanced absorption spectroscopy using light emitting diodes". *Chemical Physics Letters*, **398**, 68–74 (2004).
http://dx.doi.org/10.1016/j.cplett.2004.08.144

[264] J. M. Langridge, T. Laurila, R. S. Watt, R. L. Jones, C. F. Kaminski and J. Hult. "Cavity enhanced absorption spectroscopy of multiple trace gas species using a supercontinuum radiation source". *Optics Express*, **16**, 10178 (2008).
http://dx.doi.org/10.1364/OE.16.010178

[265] M. Schnippering, P. Unwin, J. Hult, T. Laurila, C. Kaminski, J. Langridge, R. Jones, M. Mazurenka and S. Mackenzie. "Evanescent wave broadband cavity enhanced absorption spectroscopy using supercontinuum radiation: A new probe of electrochemical processes". *Electrochemistry Communications*, **10**, 1827–1830 (2008).
http://dx.doi.org/10.1016/j.elecom.2008.09.014

[266] J. Lee and S. Saavedra. "Molecular orientation in heme protein films adsorbed to hydrophilic and hydrophobic glass surfaces". *Langmuir*, **12**, 4025–4032 (1996).
http://dx.doi.org/10.1021/la960253z

[267] P. L. Edmiston, J. E. Lee, S.-S. Cheng and S. S. Saavedra. "Molecular Orientation Distributions in Protein Films. 1. Cytochrome c Adsorbed to Substrates of Variable Surface Chemistry". *Journal of the American Chemical Society*, **119**, 560–570 (1997).
http://dx.doi.org/10.1021/ja962366a

[268] Y.-Y. Cheng, S. H. Lin, H.-C. Chang and M.-C. Su. "Probing Adsorption, Orientation and Conformational Changes of Cytochrome c on Fused Silica Surfaces with the Soret Band ". *The Journal of Physical Chemistry A*, **107**, 10687–10694 (2003).
http://dx.doi.org/10.1021/jp0305178

[269] W. Koppenol and E. Margoliash. "The asymmetric distribution of charges on the surface of horse cytochrome c. Functional implications". *J. Biol. Chem.*, **257**, 4426–4437 (1982).
http://www.jbc.org/cgi/content/abstract/257/8/4426

[270] N. J. Harrick. "Electric Field Strengths at Totally Reflecting Interfaces". *Journal of the Optical Society of America*, **55**, 851 (1965).
http://dx.doi.org/10.1364/JOSA.55.000851

[271] L. van der Sneppen, C. Gooijer, W. Ubachs and F. Ariese. "Evanescent-wave cavity ring-down detection of cytochrome c on surface-modified prisms". *Sensors and Actuators B: Chemical*, **139**, 505–510 (2009).
http://dx.doi.org/10.1016/j.snb.2009.03.048

[272] I. E. Araci, S. B. Mendes, N. Yurt, S. Honkanen and N. Peyghambarian. "Highly sensitive spectroscopic detection of heme-protein submonolayer films by channel integrated optical waveguide". *Optics Express*, **15**, 5595 (2007).
http://dx.doi.org/10.1364/OE.15.005595

[273] H.-F. Fan, F. Li, R. N. Zare and K.-C. Lin. "Characterization of two types of silanol groups on fused-silica surfaces using evanescent-wave cavity ring-down spectroscopy". *Analytical Chemistry*, **79**, 3654–61 (2007).
http://dx.doi.org/10.1021/ac062386n

[274] D. M. D. Cropek and P. W. P. Bohn. "Surface molecular orientations determined by electronic linear dichroism in optical waveguide structures". *The Journal of Physical Chemistry*, **94**, 6452–6457 (1990).
http://dx.doi.org/10.1021/j100379a054

[275] A. E. Ashley, A. L. Thompson and D. O'Hare. "Non-metal-mediated homogeneous hydrogenation of CO_2 to CH_3OH." *Angewandte Chemie (International ed. in English)*, **48**, 9839–43 (2009).
http://dx.doi.org/10.1002/anie.200905466